MATHEMATICAL MODELLING OF PERMANENT-MAGNET BRUSHLESS DC MOTOR DRIVES

by

KHALID SALIH MOHAMMAD AL-HADITHI

A Doctoral Thesis

Submitted in partial fulfilment of the requirements

for the award of the degree of

Doctor of Philosophy

of

Loughborough University of Technology

1992

Supervisor

Mr. J. G. Kettleborough

Department of Electronic and Electrical Engineering

Dedicated To

My Mother and Father

ACKNOWLEDGEMENT

I wish to express my deepest gratitude to both Professor I. R. Smith and Mr. J. G. Kettleborough for their invaluable guidance and advice throughout the course of the research and the preparation of this thesis.

I would like to thank Mr. Keith Gregory and Dr. V. V. Vadher for their assistance and the many useful discussions that we had.

I am thankful to the technicians for their assistance.

My sincere thanks go to my parents for their hard work and the great support they have contributed towards the building of my career.

My brothers deserve special thanks for their constant encouragement and support.

I want to thank the Ministry of Higher Education and Scientific Research in IRAQ for sponsoring me while I undertook this research.

Finally, my thanks to the staff in the Computer Centre at Loughborough University for their help and co-operation, particularly Mr. David Thomas and Mr. Geoff Harris.

ABSTRACT

Brushless dc motor drives have become increasingly popular, following recent developments in rare-earth permanent-magnet materials and the semiconductor devices used to control the stator input power and to sense the rotor position. They are now frequently used in applications such as flight control systems and robot actuators, and for drives which require high reliability, long life, little maintenance and a high torque-to-weight ratio. In many motor drives the presence of torque and speed ripples, especially at low speed, is extremely undesirable. The mathematical model developed in this thesis was used to investigate their occurrence in a typical brushless dc drive system, with the objective of establishing factors which effect their magnitude and ways by which they may be reduced. The model is based on the numerical solution of the differential equations for the system, with those for the motor being formulated in the phase reference frame. Tensor methods are used to account for both the varying topology and the discontinuous operation of the motor arising from changes in the conduction pattern of the inverter supply switches.

The thesis describes the design, construction and testing of an experimental voltage source PWM inverter, using MOSFET switching devices, to drive a 1.3 kW 3-phase brushless dc motor. A practical circuit is described which implements current profiling to minimize torque ripple, and the optimum phase current waveforms are established. The effect of changes in the firing angle of the inverter switches on the

torque ripple are also examined.

Throughout the thesis, theoretical predictions are verified by comparison with experimental results.

LIST OF PRINCIPAL SYMBOLS

B	flux-density (T)
B_i	intrinsic flux-density (T)
B_r	magnetic remanence (T)
C	branch / mesh transformation matrix
$\mathbf{C}^t$	transpose of C
D	viscous damping coefficient (Nm/krpm)
$\mathbf{E}_b$	branch induced voltage vector
e_k	induced voltage in winding k (V)
e_o	generated open-circuit phase voltage (V)
H	magnetic field intensity (A/m)
H_c	normal coercivity (A/m)
H_{ci}	intrinsic coercivity (A/m)
h	integration step length (s)
$\mathbf{I}_b$	branch current vector
$\mathbf{I}_m$	mesh current vector
i_k , I_k	current in winding k (A)
J	combined motor and load moment of inertia ($kg.m^2$)
J_m	motor moment of inertia ($kg.m^2$)
K_T	torque constant (Nm/A)
K_B	back emf constant (V/rps)
K_G	tachometer voltage constant (V/rps)
$\mathbf{L}_b$	branch inductance matrix
L_{kk}	self-inductance of winding k (H)
L_{kj}	mutual-inductance between windings k and j, $k \neq j$ (H)
$\mathbf{L}_m$	mesh inductance matrix
$\mathbf{L}_m^{-1}$	inverse of mesh inductance matrix
L_o	average value of L_{kk} (H)

L_2 coefficient of the second harmonic component of L_{kk} (H)

M_o average value of L_{kj} (H)

M_2 coefficient of the second harmonic component of L_{kj} (H)

P number of rotor pole pairs

p differential operator, d/dt

$\mathbf{R}_b$ branch resistance matrix

R_k resistance of winding k (Ω)

$\mathbf{R}_m$ mesh resistance matrix

T_e electromagnetic torque (Nm)

T_F frictional torque (Nm)

T_L load torque (Nm)

$\mathbf{V}_b$ impressed branch voltage vector

V_k voltage across winding k (V)

V_s dc supply voltage (V)

$\mathbf{V}_m$ impressed mesh voltage vector

θ_e angular displacement between the rotor and the axis of phase *a* in electrical degrees

θ_r angular displacement between the rotor and the axis of phase *a* in mechanical degrees

Ψ_b branch total flux linkage vector

ψ_k total flux linkage with winding k (Wb)

Ψ_{Pb} branch flux linkage vector due to the permanent-magnet rotor

ψ_{Prk} flux linkage with winding k due to the permanent-magnet rotor (Wb)

Ψ_m mesh total flux linkage vector

Ψ_{Pm} mesh flux linkage vector due to the permanent-magnet rotor

ω_e angular velocity of the rotor in electrical radians per second

ω_r angular velocity of the rotor in mechanical radians per second

μ_r relative permeability

μ_o permeability of free space (H/m)

CONTENTS

CHAPTER 1

INTRODUCTION

The number of applications for brushless dc motor drives has increased considerably during the last 20 years. This is due mainly to a number of substantial advances in brushless drive technology, brought about by improvements in power semiconductor switching devices and permanent-magnet materials. The high-power semiconductor devices which are now available enable large currents to be switched electronically, and the development of rare-earth permanent-magnet materials, in particular samarium-cobalt and neodymium-boron-iron, has made it possible to both reduce the size of the machine and improve its efficiency[1].

Prior to 1970, only Alnico alloy and Ferrite permanent-magnets were available, and machines using these materials could not compete seriously with induction or synchronous motors or dc servo drives. However, in March 1969, Buschow, Luiten and Westendrop[2] reported a rare-earth material with an energy density approaching 160kJm^{-3}, and in September 1969 this figure was confirmed for samarium-cobalt by Das[3]. Since then several such materials have become readily available, which has led to brushless machines becoming serious competitors to more traditional machines. The brushless motor was developed in the early sixties by the National Aeronautics and Space Administration (NASA) during its spacecraft research program, to replace brushed machines which were clearly unsuitable for this application[1]. In

recent years brushless drives have become attractive for robotic, aerospace and electric vehicle applications[1,4,5,6], mainly because their large torque producing capabilities can develop the high acceleration and deceleration which is often required. Moreover, the elimination of the commutator and brushgear reduces the maintenance requirements and allows the machines to operate at much higher speeds than brushed machines.

Brushless motors have a permanent-magnet rotor, single or multi-phase stator windings, a sensor to determine the rotor position and an inverter which feeds direct current to the stator windings. The inverter drive signals are generated from the output signals of the rotor-position sensor, so that synchronism between the stator field and the permanent-magnet field is ensured at all speeds. This construction improves the thermal characteristics of the motor, with the heat-generating windings being close to the stator surface[7].

The inverter supplying the brushless machine provides the required sequence of excitation to the motor windings and controls the power which is delivered to them. The commutation logic circuit turns on and off the appropriate switches and pulse-width-modulation (PWM) techniques control the power. By eliminating the need for extra control devices, the PWM inverter has an important advantage over other available techniques.

An efficient and reliable inverter design requires the switching devices to have adequate voltage and current ratings. Their switching speed must be fast to minimize the switching losses, and they should be robust and easy to drive

to reduce the complexity of the drive circuit. Consideration of the various different devices which are available led to power MOSFETs being chosen for the PWM inverter built during the course of this research.

An accurate system model is required to enable the design and performance of a brushless drive to be optimised. The model developed in this thesis consists of a set of differential equations, providing a convenient analytical tool for studying the overall performance of the drive. It is flexible and includes circuit discontinuities such as turn-on and turn-off of the inverter switches. In particular, the model can be used to predict the torque behaviour and the implementation of torque ripple minimization.

Interest in simulating brushless dc motor drives began several years ago, when their potential for aerospace applications was realised. In some early models[8] the rotor speed was assumed constant, although this is inappropriate at low speeds when torque ripple can be a particular problem. Most previous models have used either the highly idealized dqO or $\alpha\beta$O reference frames[9,10,11], which assume the machine windings to be sinusoidally distributed and the induced voltage to be sinusoidal. The machine phases are also assumed to be balanced, and considerable restrictions are thereby placed on the application of the analysis to torque ripple prediction[12]. In the phase reference frame these assumptions are unnecessary[13,14,15] and, since the brushless dc motor has a trapezoidal generated emf waveform and non-sinusoidal inductance variations with rotor position,

it provides a much better basis for any analytical studies. This approach also eliminates the complication of the transformations associated with the dqO and αβO reference frames. Moreover, use of the phase reference frame enables simulated and corresponding experimental results to be directly compared, since the actual machine voltages and currents are all readily available from the simulation. Although magnetic saturation may be included in any reference frame, its inclusion in the phase reference frame is essentially more correct, since it relates to the actual machine windings, whereas in both the dqO and αβO reference frames, it relates to saturation of fictitious windings.

At one time, an important disadvantage of the phase reference frame model was that a time-varying inductance matrix has to be inverted at each step of a numerical solution. However, this is of little significance with modern high-speed digital computers.

In this thesis, Kron's tensor methods[16,17] are used to obtain the differential equations for a brushless drive. The approach reduces the time required to solve the system equations, since it copes efficiently with the varying circuit topology due to the changing conduction pattern of the semiconductor switches. All possible topologies for the system are considered in the model, which provides a clear understanding of the behaviour of the drive.

An accurate model for the brushless motor requires the accurate representation of the permanent-magnet component of the stator winding flux linkage. The open-circuit voltage waveform of the machine was measured at 800 rpm and this was

used to determine an expression for the stator winding no-load flux linkage due to the permanent-magnet rotor. The mathematical model may be simplified considerably, without a significant loss of accuracy, if the flux produced by the permanent-magnet is assumed to remain constant due to the high coercivity of samarium-cobalt.

The mathematical model developed in the thesis is verified experimentally, with the good correlation obtained between simulated and experimental results giving a high degree of confidence in both the mathematical model developed and the modelling technique described.

The electromagnetic torque of a brushless motor at any speed is proportional to the product of the stator phase currents and the generated emfs[18]. To obtain a constant output torque, the stator phase current waveforms must be rectangular functions of the rotor position and the generated emfs must be trapezoidal with a 120°e flat-top. In practice, the currents do not rise instantaneously, due to the winding inductance, and the generated emfs are constant for less than 120°e due to fringing, which together result in an undesirable torque ripple for applications such as robotic and position control requiring smooth operation. The impact on the output torque of the deviations in the stator current and the generated emf waveforms is studied in this thesis, and the optimal stator current waveshape to minimize the torque ripple is determined. The effect on the torque ripple of advancing the current with respect to the generated emf, reducing the stator winding inductance and increasing the switching frequency of the PWM current controller are also

examined and other methods which minimize the torque ripple are presented. Since the ripple is synchronized to both the commutation events and the deviation and fluctuations of the generated emf waveforms, an incremental encoder is necessary to provide accurate information on the rotor position relative to the stator. In practice, compensation of the torque ripple is achieved using a PWM current controller and an EPROM to adjust the stator current waveform in relation to the rotor position and commutation instants.

The main objectives of this thesis are

(1) to provide a better understanding of the characteristics of the brushless dc motor drive.

(2) to develop an accurate mathematical model for the motor.

(3) to design and build a brushless drive suitable for validating the proposed mathematical model.

The organisation of the thesis is as follow :

Chapter 2 summarises the characteristics of permanent-magnets and the materials available for brushless dc motors. Chapter 3 presents a detailed description of a brushless dc motor drive and explains and discusses the theory of its operation and its torque-speed characteristics. Other types of brushless dc motors are also examined briefly. Chapter 4 deals specifically with the design of a voltage source MOSFET PWM inverter, together with the design details of the controller and power supplies for the brushless drive. Chapter 5 develops a mathematical model for a permanent-magnet 3-phase brushless drive, and explains its

implementation on a mainframe computer. Chapter 6 describes methods for the accurate measurement of the motor parameters and Chapter 7 presents a detailed investigation into the torque production of the drive using the model presented in Chapter 5. Particular attention is given to the output torque ripple and factors which effect this ripple. Practical implementation of current profiling is also presented in this chapter. The conclusions of this thesis and recommendations for further work are presented in Chapter 8.

CHAPTER 2

PERMANENT-MAGNET MATERIALS

Permanent-magnet materials produce a magnetic field which is maintained even in the presence of a large externally-applied field. They are frequently used in special-purpose rotating machines and other types of electromechanical devices.

2.1 PERMANENT-MAGNET CHARACTERISTICS

A typical hysteresis loop for a permanent-magnet material is shown in Figure 2.1. In most permanent-magnet devices the material operates in the second quadrant of its hysteresis loop, in which the magnetic field H and the flux-density B are opposed. That portion of the hysteresis loop which lies in the second quadrant is called the demagnetization characteristic[19,20]. In the typical B-H loop shown in Figure 2.1, and known as the normal hysteresis loop[21], the B-value includes the contributions from both the intrinsic flux-density of the material B_i and the flux-density $\mu_o H$ resulting from the applied field H. If only B_i is plotted against H, the resultant loop represents the intrinsic hysteresis loop shown in Figure 2.2. The intrinsic loop represents that proportion of the flux-density which is intrinsic to the magnetic material itself for a particular magnetic field H, and it is of use in the design of a permanent-magnet machine. The intrinsic flux-density B_i, the normal flux-density B and the magnetizing field intensity H

are related by the equation

$$B = \mu_o H + B_i$$

Several terms used in permanent-magnet studies are defined below.

2.1.1 MAGNETIC REMANENCE, B_r

If a magnetizing force is applied to an unmagnetized magnet and then removed, there remains a residual flux-density or remanence B_r due to the non-elastic displacement of the boundary walls between the magnetic domains[22]. The remanence is the same for both the B and B_i curves, since at this point H is zero, as shown in Figure 2.2.

2.1.2 NORMAL COERCIVITY, H_c

Increasing the negative magnetic field intensity H eventually reduces the normal flux-density B to zero. The value of the magnetic field intensity for this situation is termed the coercivity or coercive force H_c.

2.1.3 INTRINSIC COERCIVITY, H_{ci}

The intrinsic coercivity H_{ci} is the value of the magnetic field intensity at which the intrinsic flux-density B_i is zero. It is a measure of the ability of the magnetic material to withstand demagnetizing forces without permanent changes in its magnetization. The magnitude of H_{ci} may be several times greater than that of H_c[21,23].

2.1.4 RECOIL LINES

If the demagnetization field is reduced to the value H_b (see Figure 2.3) and then returned to zero, the B/H characteristic does not return along the original demagnetizing curve but rather along the lower half of a minor hysteresis loop. When H_b is re-applied the characteristic follows the upper half of the minor loop. This loop is very narrow and may be replaced by a straight line, termed the recoil line[20,21]. The slope of this line is specified as the recoil or permanent permeability of the material[20,22].

2.1.5 ENERGY PRODUCT AND MAXIMUM ENERGY PRODUCT

The energy product is the product of the flux-density and the magnetic field intensity at any point along the demagnetization curve. It is a measure of the energy stored in the permanent-magnet material, and the maximum value of the product indicates the strength of the permanent-magnet. Figure 2.4 shows typical demagnetization and energy product curves for a permanent-magnet material, with the flux-density and the coercive force corresponding to this maximum energy point being designated by B_d and H_d respectively. Along the recoil line the energy is obtained from the product of B and H at corresponding points on the line[19,21].

2.1.6 OPERATING LINE

The point Q in Figure 2.5(a) is the operating point of the magnet. The line intersecting the recoil line at this

point is the operating line, whose slope is the permeance of the magnetic circuit. The point P in Figure 2.4 is the ideal operating point, since it is here that maximum energy is available from the magnet. The operating point depends on the presence of any additional sources of reaction field. Rare-earth permanent-magnet materials have linear characteristics and their operating points are on the normal demagnetization curve, as shown in Figure 2.5(b).

2.1.7 CURIE TEMPERATURE

The Curie temperature is that temperature at which all ferromagnetic properties are lost and it is clearly important that a magnetic circuit is not subjected to a temperature approaching this value.

2.2 PERMANENT-MAGNET TYPES

The main features of the three types of permanent-magnet materials used in small rotating machines are briefly summarized below.

(a) Ceramic-ferrite magnets

These have a relatively linear demagnetization characteristic, a low remanence of about 0.4T, a moderately high coercive force of up to 250kAm^{-1}, a maximum energy product of around 30kJm^{-3}[20,22] and an extremely high electrical resistivity of about 10^{10} μΩm. Ceramic magnets are relatively cheap and are used widely in small dc motors.

(b) Alnico magnet

This is a more expensive material than ceramic-ferrite. It has a non-linear demagnetization characteristic, a very high remanence of up to 1.2T, a low coercive force of below 120kAm^{-1}[20,22], a maximum energy product of around 60kJm^{-3} and a low electrical resistivity of about 0.5μΩm.

(c) Samarium-cobalt rare-earth magnet

This material has an almost linear demagnetization characteristics, a high remanence (up to 0.9T), a very high coercive force (up to 750kAm^{-1}) and a maximum energy product of around 400kJm^{-3} [20,22]. It has a maximum energy product greater than that of other materials, which is a great advantage on a volumetric basis. The disadvantage of the material is its high cost, and it was consequently first used only for aerospace and military equipment and for computer memory disks. Samarium-cobalt rare-earth magnets are now becoming increasingly used, as the availability of the material becomes widespread and its cost falls.

A comparison of the demagnetization curves of the above materials is given in Figure 2.6.

2.3 DEMAGNETIZATION AND STABILIZATION OF MAGNETS

When a permanent-magnet is used in a rotating machine, the operating flux may decrease due to factors such as armature reaction, over-load, or dismantling of the machine[22,23]. To ensure that the magnet is not easily demagnetized it is necessary for it to be stablized before use. The stabilization process consists of subjecting the

magnet to a demagnetizing effect slightly greater than that encountered during operation. This may be achieved by either momentary removal of the rotor from the stator or stalling the machine for a short period[23]. Repeating this process several times stablizes the magnet and ensures that it continues to operate along the recoil line. Permanent-magnet materials with a linear characteristics have a recoil line which almost coincides with their demagnetization curves, and they do not therefore need stabilizing. Other permanent-magnet materials, such as Alnico, have a highly non-linear characteristic and some form of stabilizing is then almost imperative.

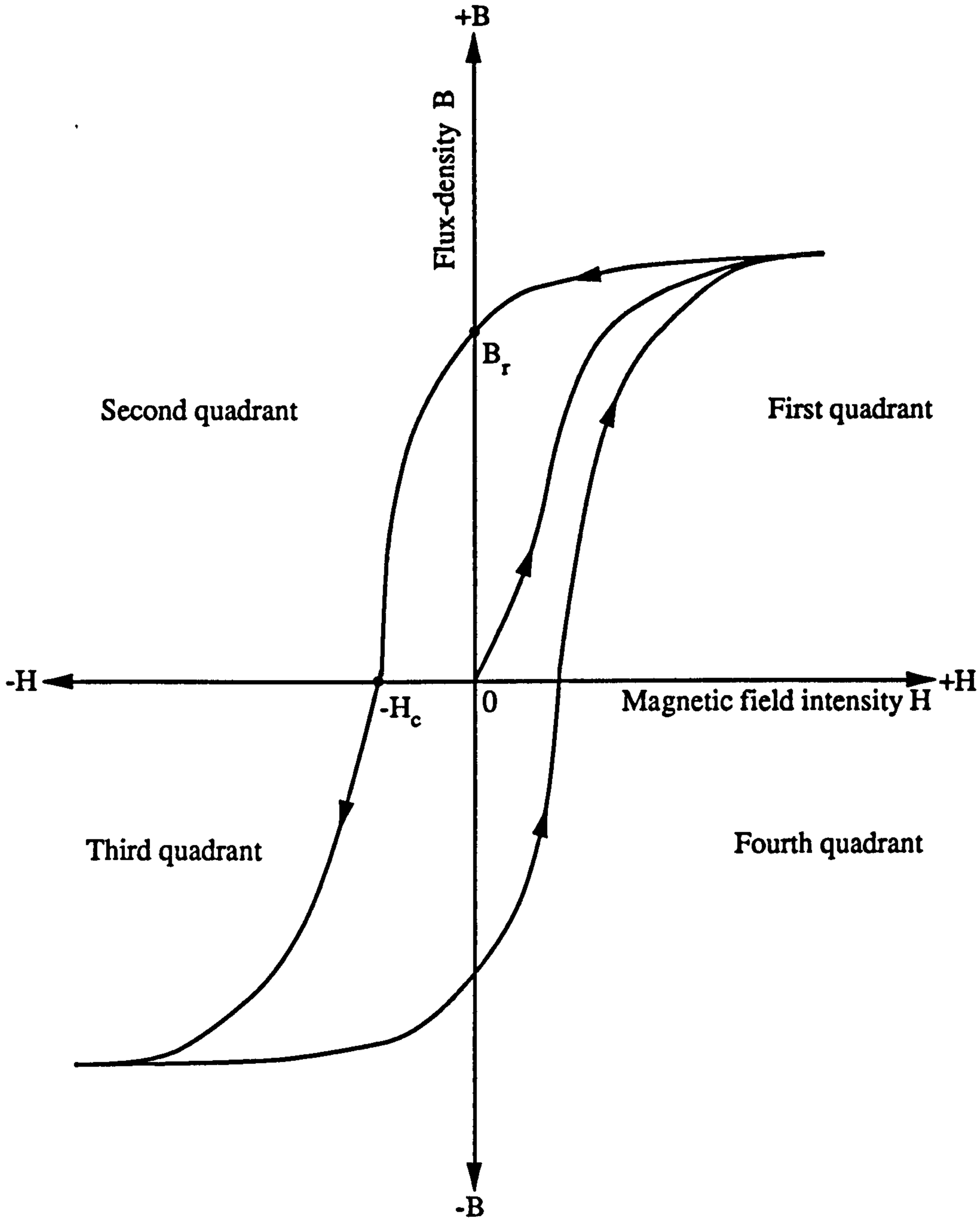

Figure 2.1 Hysteresis loop for a typical permanent-magnet material

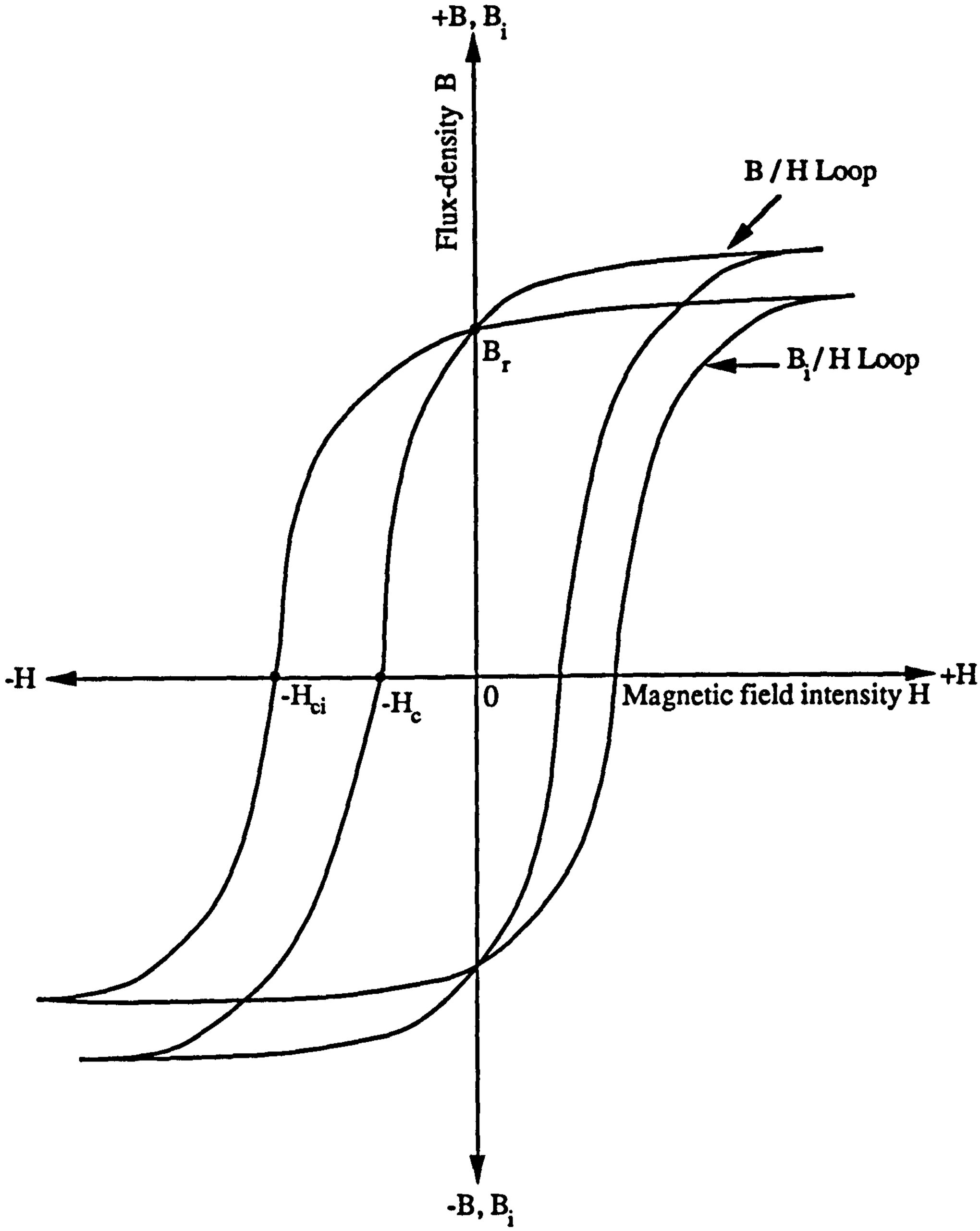

Figure 2.2 Normal and intrinsic hysteresis loops for a typical permanent-magnet material

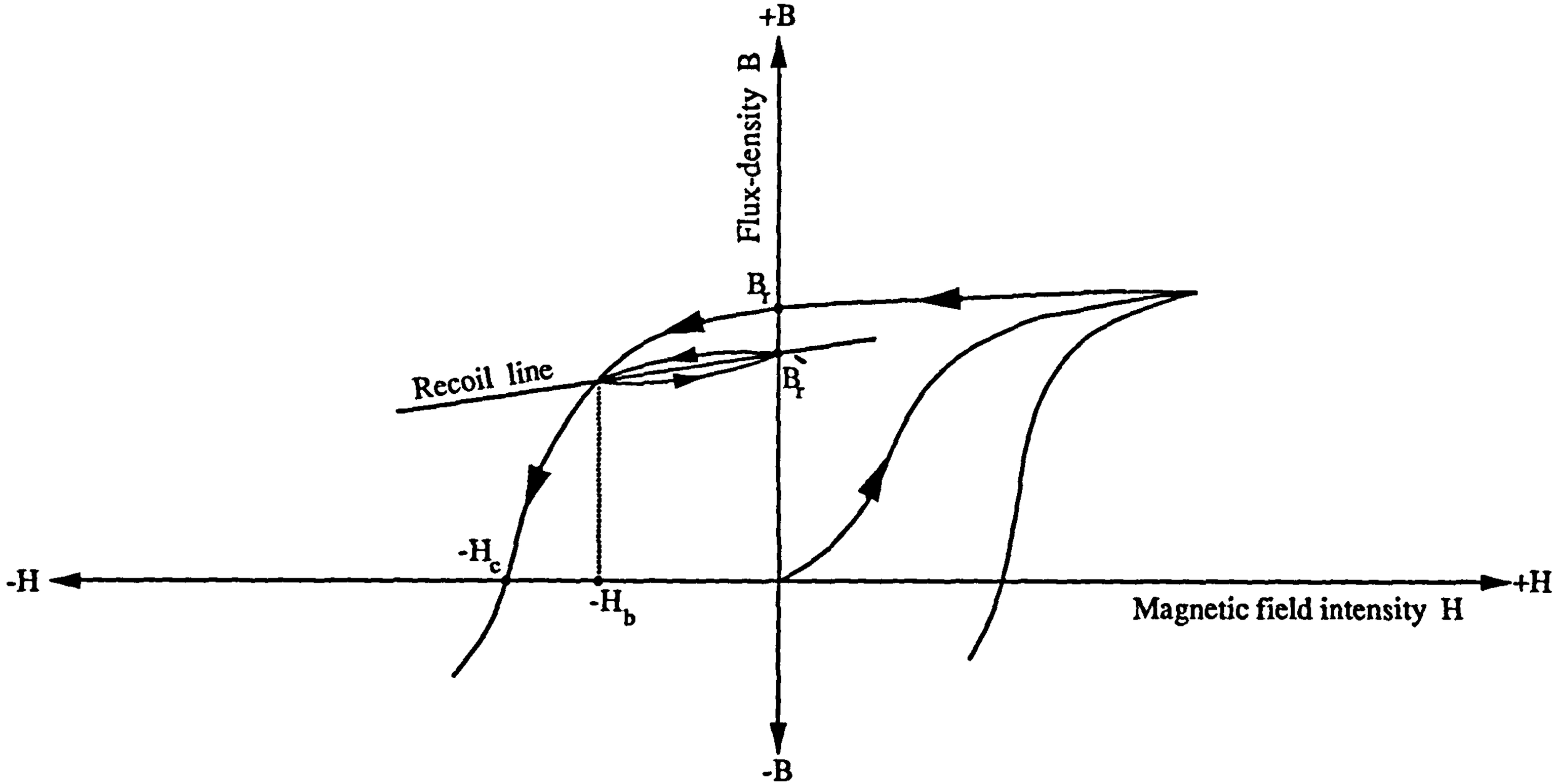

Figure 2.3 Permanent-magnet recoil line

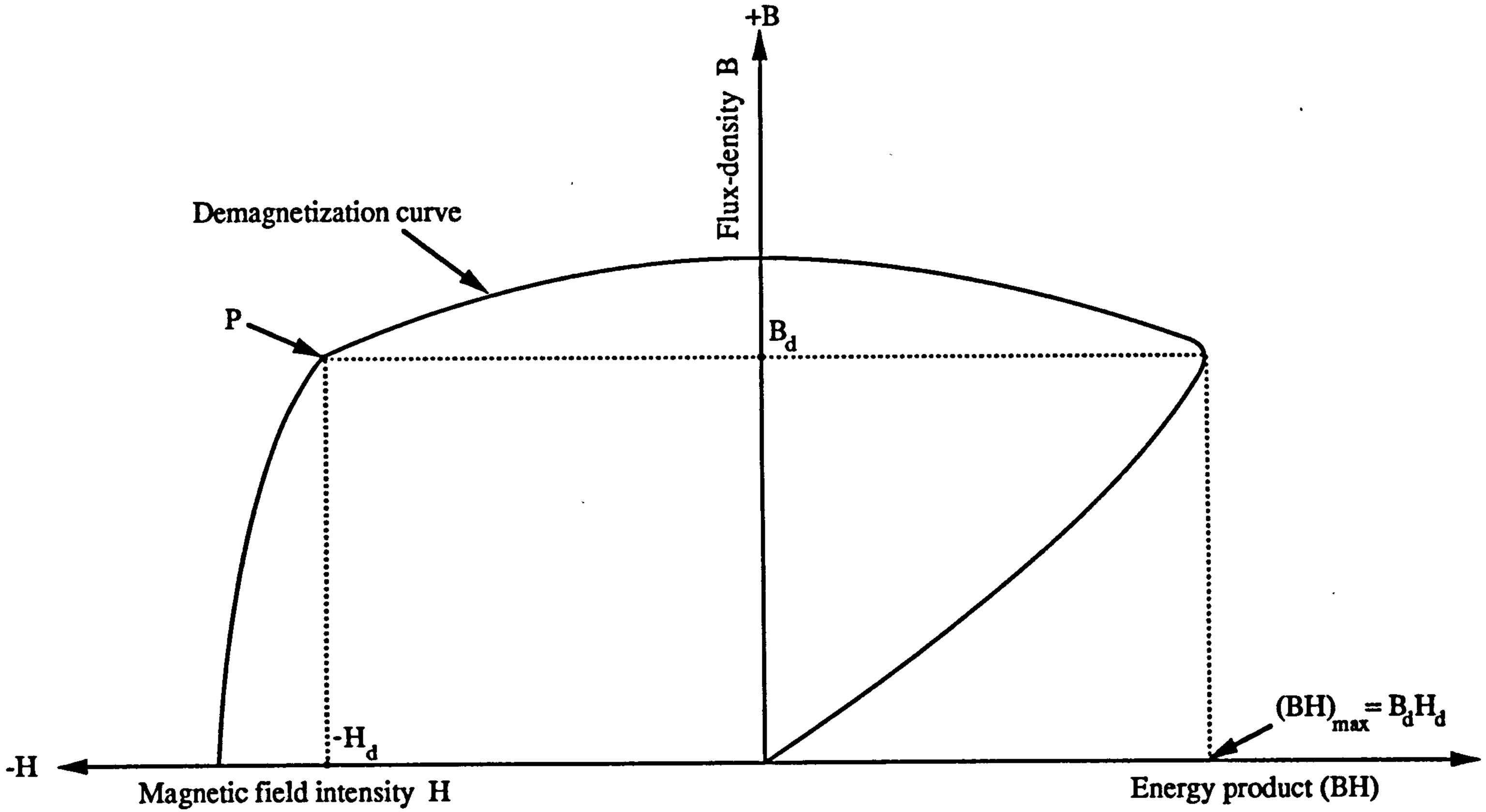

Figure 2.4 Typical demagnetization and energy product curves

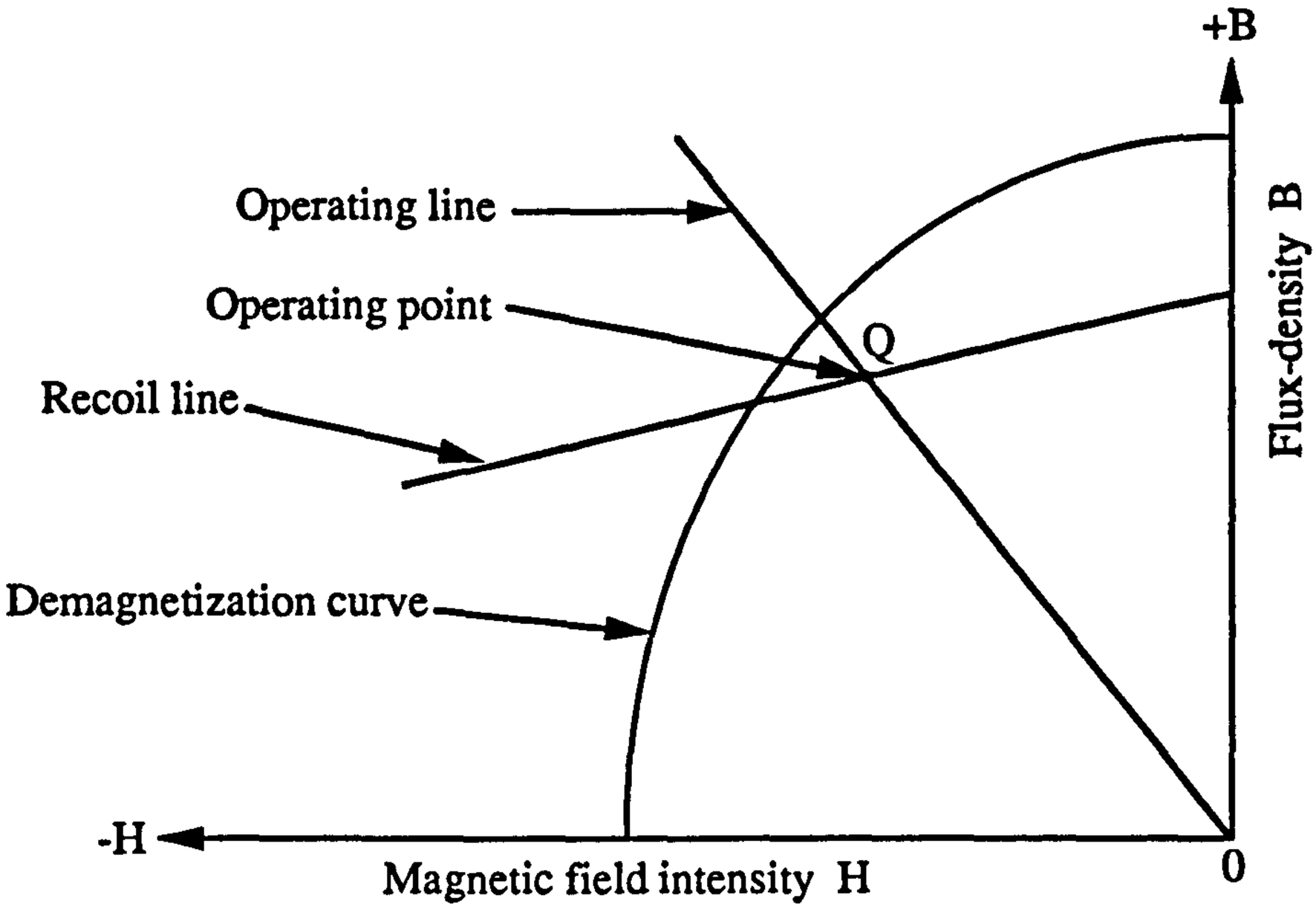

(a) A non-linear magnet

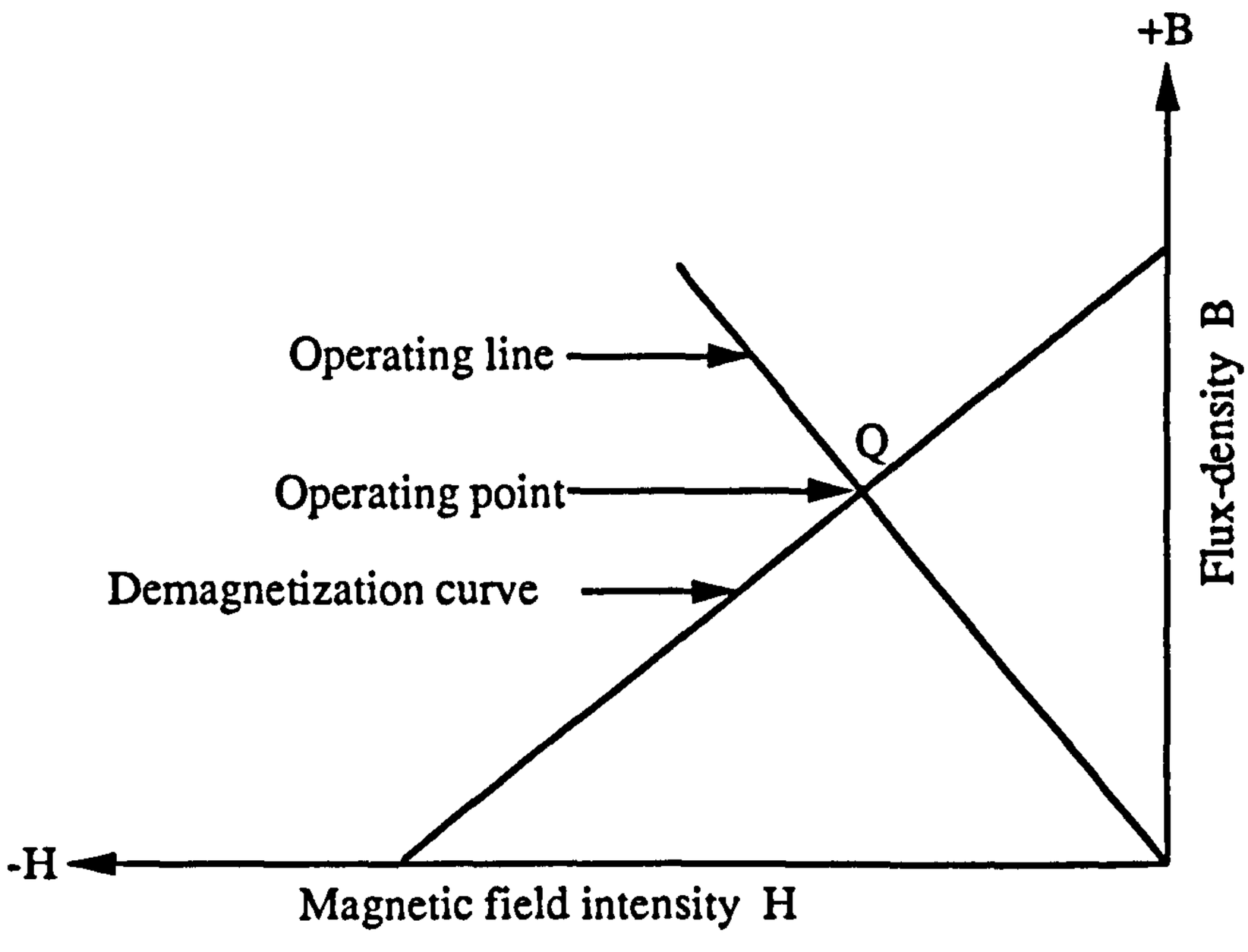

(b) A linear magnet

Figure 2.5 Demagnetization curve and operating line for permanent-magnet materials

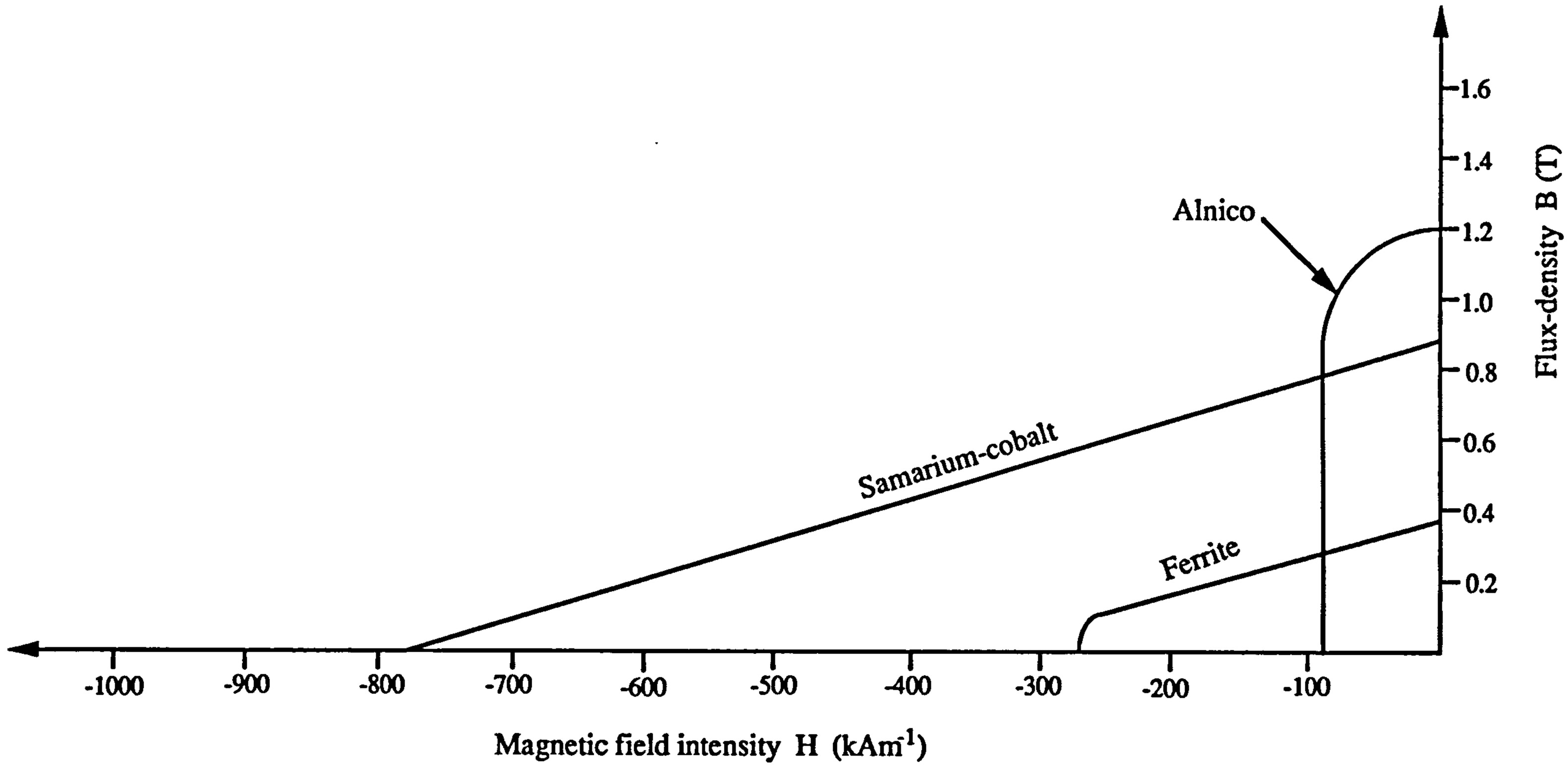

Figure 2.6 Demagnetization curves for some common permanent-magnet materials

CHAPTER 3

PERMANENT-MAGNET BRUSHLESS DC MOTOR DRIVES

The brushless dc motor has a linear torque-speed characteristic similar to that of a conventional separately-excited dc motor. Constructionally, it consists of a permanent-magnet rotor, a wound stator, a solid-state inverter and a rotor-position sensor. Motor operation is made self-synchronous when the rotor-position sensor controls the firing signals for the solid-state inverter. In response to these signals, the inverter directs current through the stator phase windings in the required sequence[24].

Developments in rare-earth magnetic materials and solid-state devices for both rotor position sensing and controlling the stator input power have led to significant improvements in the performance. This has greatly increased the range of applications for brushless dc motors in both aerospace applications and other high-performance drives.

3.1 EVOLUTION OF THE BRUSHLESS DC MOTOR

In a conventional dc motor, current is supplied to the armature winding through stationary brushes sliding on commutator segments connected to the armature coils. As a consequence of this, the armature field is stationary in space, with its axis in a direction determined by the brush position. When a commutator segment passes under a brush the corresponding armature coil is connected to either the

positive or the negative supply terminal, and to reproduce this with an electronic commutator requires each commutator segment to be replaced by a pair of semiconductor switches. Since a conventional dc motor has many segments the cost of the semiconductor switches would clearly be prohibitively high. Attempts to reduce the number of switches have led to the 3-phase brushless machine supplied by a six-switch inverter[25], with switching of each armature coil at the correct rotor position being achieved through the rotor-position sensor. It is clearly far more convenient to have stationary rather than rotating switches, so that the armature coils are located on the stator of the machine and the field poles on the rotor. Figure 3.1 illustrates the evolution from the conventional machine to the 3-phase brushless dc motor, where the commutator and brushgear have been replaced by electronic switches and the rotor-position sensor.

3.2 BRUSHLESS DC MOTOR CONFIGURATIONS

It is possible to envisage a number of different configurations of brushless dc motors by selection of the number of phases and the way that current is delivered to the windings by the semiconductor switches.

3.2.1 SINGLE-PHASE, HALF-WAVE BRUSHLESS DC MOTOR

As shown in Figure 3.2(a), this arrangement has a single-phase winding energized once per 360°e through the single semiconductor switch S1. Although the motor generates positive torque over only 180°e of the rotation, as shown in

Figure 3.2(b), the rotor inertia cause angular rotation to continue over the remaining 180°e[26].

3.2.2 SINGLE-PHASE, FULL-WAVE BRUSHLESS DC MOTOR

The single-phase, full-wave brushless dc motor of figure 3.3(a) is energized twice per 360°e by the two semiconductor switches S1 and S2. The stator winding is consequently 100% utilised, but the resulting torque is not continuous and as Figure 3.3(b) shows there are rotor positions at which the torque falls to zero.

3.2.3 TWO-PHASE, FULL-WAVE BRUSHLESS DC MOTOR

Figure 3.4 shows the arrangement with two phase windings mutually displaced by 90°e. The motor switching sequence given in Figure 3.5 indicates that only 50% of the available windings is used at any time.

3.2.4 THREE-PHASE, HALF-WAVE BRUSHLESS DC MOTOR

The star-connected stator phase windings of the 3-phase half-wave brushless dc motor shown in Figure 3.6 are mutually displaced by 120°e. A return path is made via the neutral point and the excitation pattern of Figure 3.7 illustrates that current flows in one phase only at any time. The main advantages of this scheme are its simplicity and the low cost of the electronic package. Its disadvantages are the low winding usage, with only one third of the available windings in use at any time, and the lack of free-wheeling diodes to provide an alternative path for the inductive current when a semiconductor switch turns off[7]. The motor has a very

limited potential for either high-performance systems or where the inductive winding energy is large. The torque characteristic and the required logic sequence are given in Figure 3.8.

3.2.5 FOUR-PHASE, HALF-WAVE BRUSHLESS DC MOTOR

The 4-phase half-wave brushless dc motor of Figure 3.9 has four windings on the stator mutually displaced by 90°e, only one of which is energized at any time, as shown in Figure 3.10. The motor needs only one power supply and gives a performance similar to that of the 2-phase, full-wave brushless motor which requires two power supplies[7].

3.2.6 THREE-PHASE, FULL-WAVE BRUSHLESS DC MOTOR

The 3-phase full-wave brushless dc motor shown in Figure 3.11 has a 3-phase star-connected stator winding energized by a 6-switch inverter. Feedback diodes are in parallel with each switch for inductive energy recovery. The utilization of the stator winding is 67% and the output torque is more than for the previous configurations[7]. The machine used in the present research has this configuration and is described in detail in the following section. The design of the associated 3-phase PWM inverter and the commutation control logic circuits are discussed later in chapter 4.

3.3 MACHINE DESCRIPTION

3.3.1 STRUCTURE OF THE ROTOR AND STATOR

The 3-phase 6-pole 1.3kW machine used in the present research has a rare-earth samarium-cobalt permanent-magnet

rotor. A non-magnetic stainless steel sleeve surrounds the rotor magnets to retain them in place in the presence of the large centrifugal forces arising during high-speed operation. The laminated stator core has 18 slots to house the 3-phase, star-connected winding. The winding is concentrated and the rotor poles are profiled such that the generated emf is trapezoidal[27]. A brushless dc tachometer provides a velocity signal.

3.3.2 ROTOR-POSITION SENSOR

Many methods are available for detecting the rotor position of a brushless dc motor, eg: absolute optical encoder, Hall-effect sensor, brushless resolver, capacitance transducer, photo diodes. A Hall-effect sensor, the most common of these devices, is fitted to the experimental machine, with Hall-effect elements spaced 20°m or 60°e apart around the airgap to sense the rotor position relative to the stator phases. The output of each sensor switches from logic high for a north magnetic pole to logic low for a south pole, or vice versa when the rotation of the rotor flux reverses. The output voltage of the Hall element is amplified, to give a signal of usable magnitude, and each Hall element with its associated electronic circuit is incorporated into a single chip. Figure 3.12(a) and (b) show respectively the block diagram for the chip and its output-voltage/flux-density characteristic.

3.3.3 THEORY OF OPERATION

In response to the rotor-position sensor signals the inverter of Figure 3.11 switches current to the stator windings, as indicated in Figure 3.13. The rotor-position signals are decoded by a commutation logic circuit to give six output signals, which control the inverter switches such that only two devices are on at any given instant and sequential switching from one pair of stator coils to the next occurs at intervals of 60°e of rotor position. The windings are thus energized in the commutation sequence of figure 3.14, tabulated in table 3.1. This particular switching sequence causes continuous clockwise rotation of the rotor and maximum torque output for a given phase current. The emfs generated in the motor phases are trapezoidal and the phase current waveforms are rectangular. Consequently the motor torque is also trapezoidal, with the 60°e flat-top shown in Figure 3.15[27,28]. The direction of rotation may be reversed by phase-shifting the sequence of electronic commutation by 180°e, rather than by reversing the power supply[1]. The commutation sequence and the corresponding current waveforms for reverse rotation are both given in Figure 3.16.

Only two phases are utilized at any given time, with each phase conducting for 120°e and being de-energized for 60°e. Due to this and the rectangular current waveform, the stator MMF moves in discrete steps of 60°e rather than as a smooth travelling wave[29]. The rotor MMF attempts to follow the motion of the stator MMF, to minimize the angle which separates them. This continues until the next switching

Rotor position ele. deg.	Position sensor signals			Drives						Stator phases		
	sensor 1	sensor 2	sensor 3	S1	S2	S3	S4	S5	S6	a	b	c
0---60	1	1	0	0	0	0	1	1	0	-1	0	+1
60---120	1	0	0	0	0	0	0	1	1	0	-1	+1
120---180	0	0	0	1	0	0	0	0	1	+1	-1	0
180---240	0	0	1	1	1	0	0	0	0	+1	0	-1
240---300	0	1	1	0	1	1	0	0	0	0	+1	-1
300---360	1	1	1	0	0	1	1	0	0	-1	+1	0

+1 = current source
-1 = current sink
0 = output off

Table 3.1 Six step switching truth table for a 3-phase, full-wave brushless dc motor

step, at which the stator MMF is advanced by 60°e and the process of rotor motion is continued.

A brushless dc motor has the same characteristics as a conventional permanent-magnet machine, with the speed proportional to the supply voltage, torque proportional to the stator current and a start/stall torque higher than the running torque[7,24]. The brushless motor produces a linear torque-speed characteristic as shown in figure 3.17. The characteristic is linear even when the motor is stalled, since the magnetic flux remains constant at all loads due to the high coercivity of the rare-earth permanent-magnet.

The motor speed is controlled by varying the average voltage applied to the stator winding. This is achieved using PWM techniques, whereby the switching devices are switched on and off several times per cycle to produce a chopped voltage. By changing the ratio of on-state to off-state time, the average voltage applied to the stator winding can be controlled[30].

3.4 ADVANTAGES OF BRUSHLESS DC MOTOR DRIVE

A brushless dc motor drive has several advantages arising from the stationary armature windings, the elimination of the brushes and commutator and the use of high energy-product permanent-magnets. These may be summarised as:

(a) Long life and reduced maintenance due to the lack of a commutator and brushgear.

(b) Elimination of the radio frequency interference (RFI) produced by commutation arcing.

(c) With the speed limitations imposed by the brushes

and commutator eliminated, the motor is capable of operation at a high speed and over a wide speed range [31,32].

(d) Operation both in an explosive environment and a hard vacuum is possible.

(e) A high torque-to-inertia ratio.

(f) A small frame size and a light weight for a given power output.

(g) Reduced input power and high efficiency, as the excitation is provided by the rotor magnet.

(h) A linear torque-speed characteristic.

(i) Improved heat dissipation, since the power windings are on the stator.

Due to its excellent performance characteristics, the brushless dc motor has replaced many brushed motors in applications such as flight control actuators, robotics, electric vehicles, medical systems and machine tools.

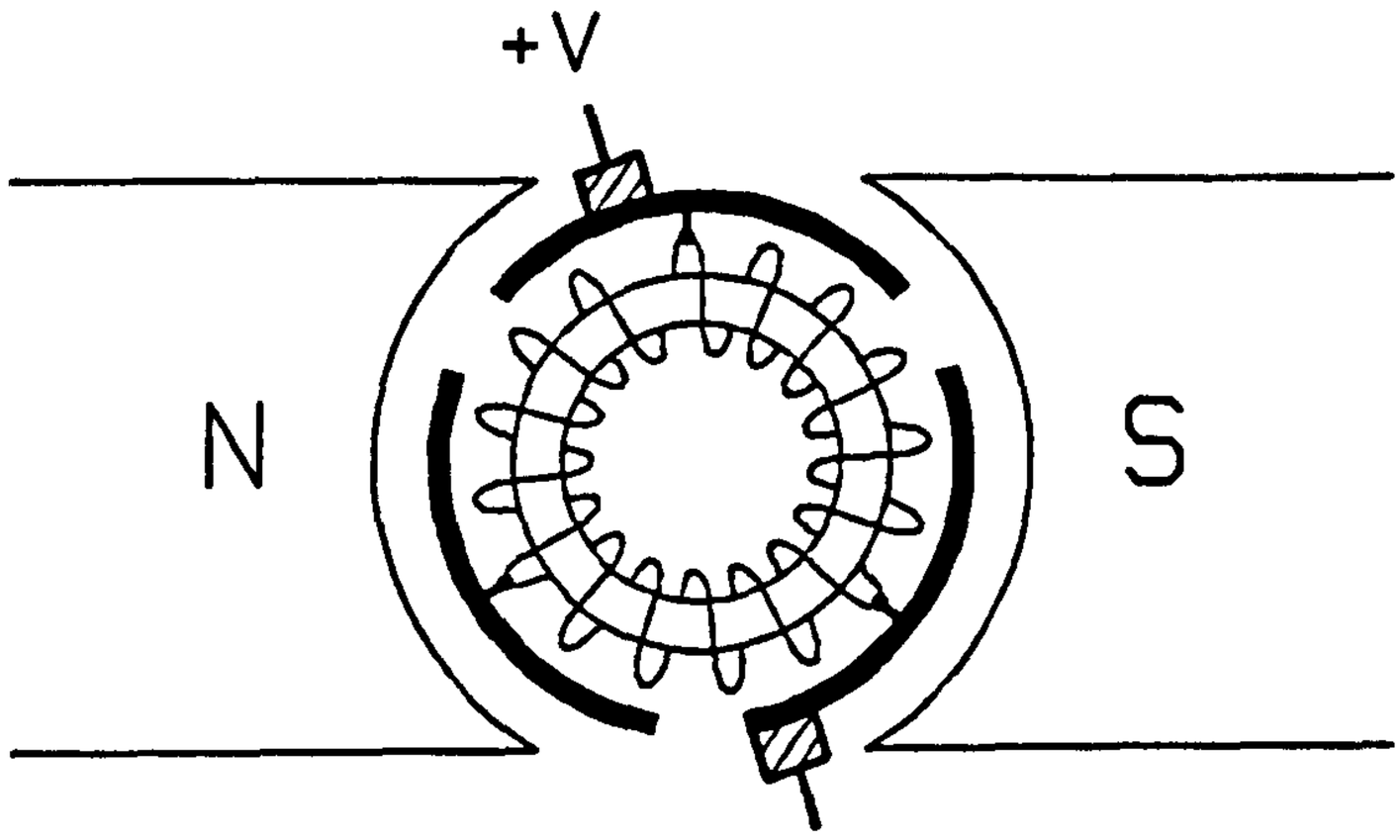

(a) permanent-magnet dc motor

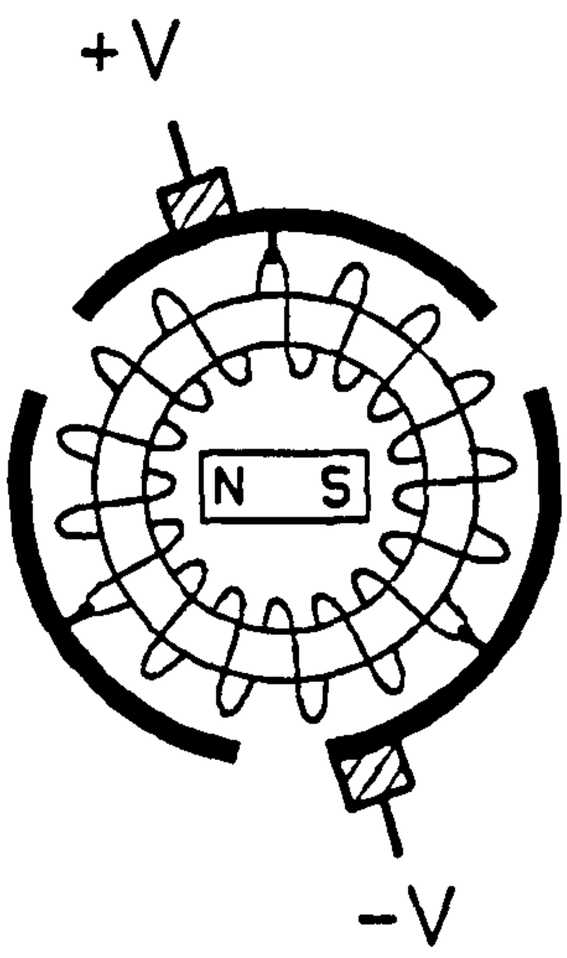

(b) inverted permanent-magnet dc motor

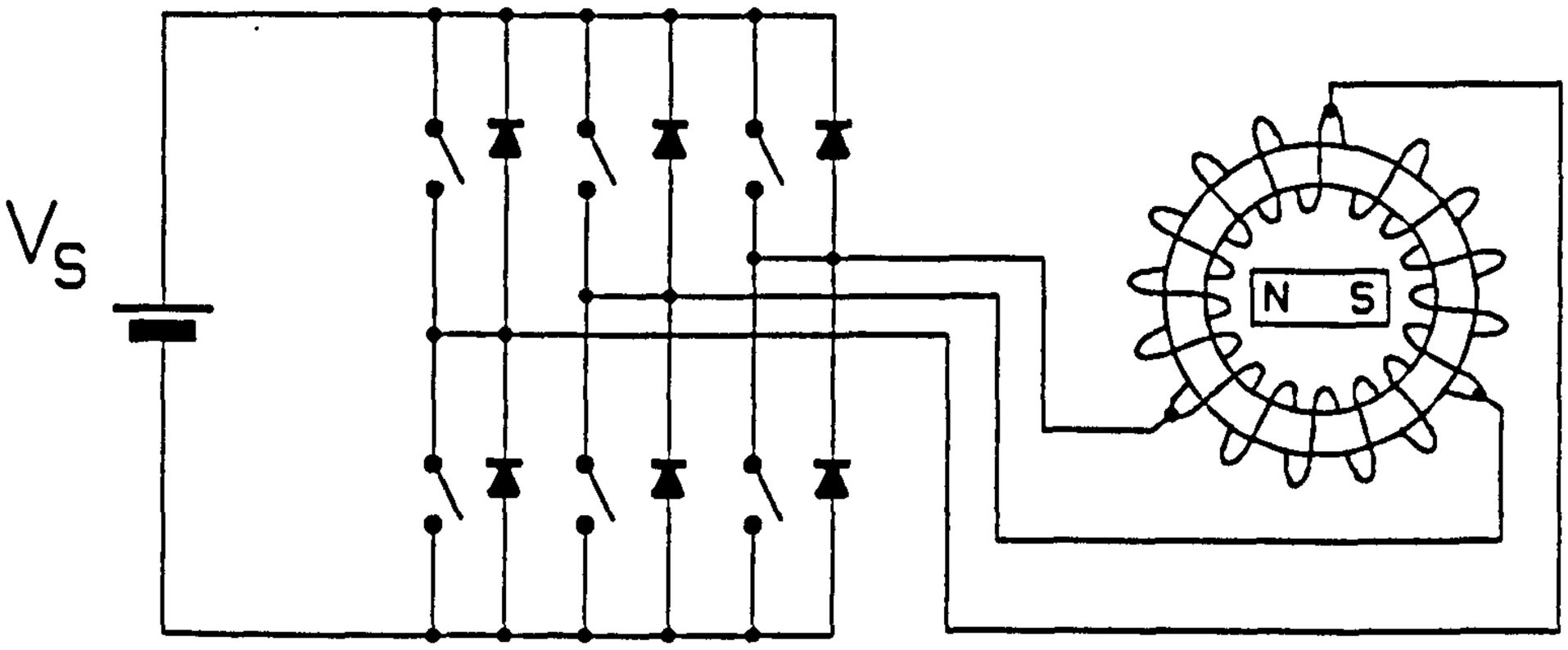

(c) replacement of mechanical commutator by elecrtronic switches

Figure 3.1 Evolution of brushless dc motor from commutator dc motor

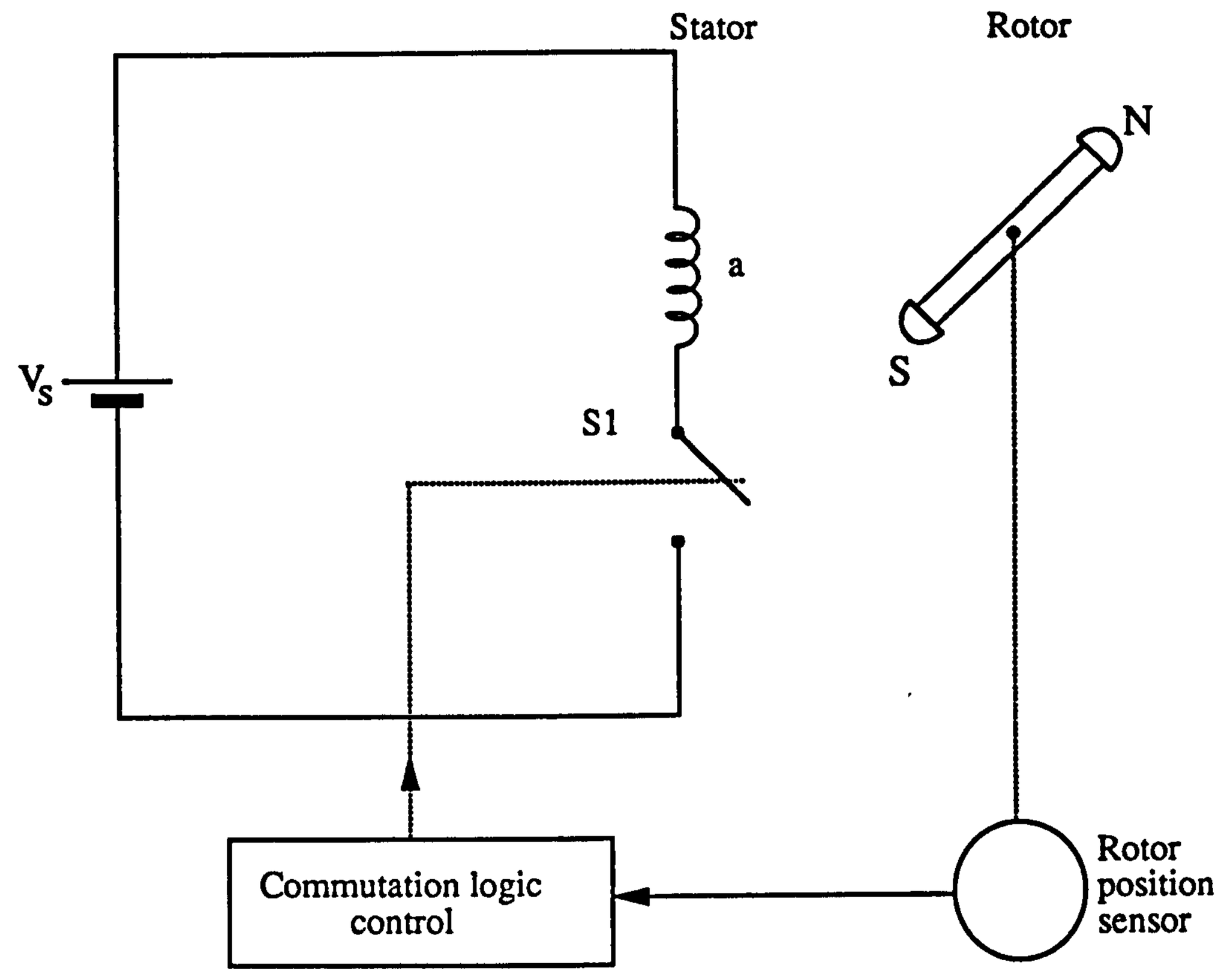

Figure 3.2 (a) Single-phase, half-wave brushless dc motor drive

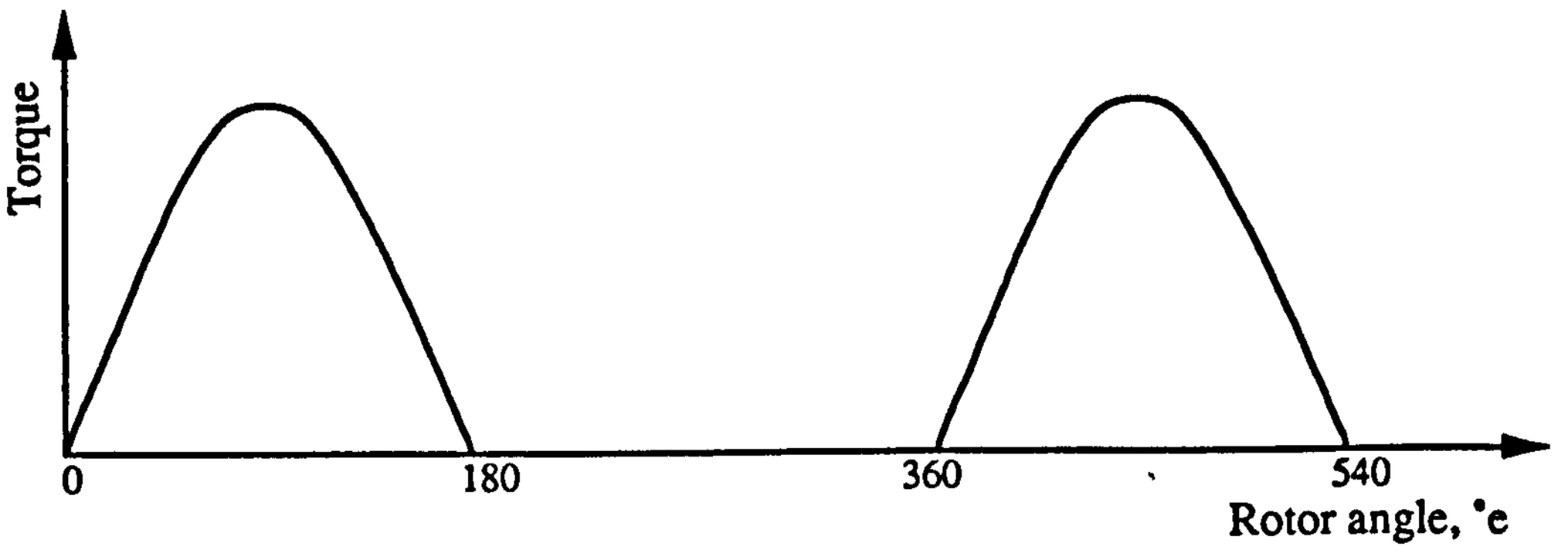

Figure 3.2 (b) Torque output for single-phase, half-wave brushless dc motor

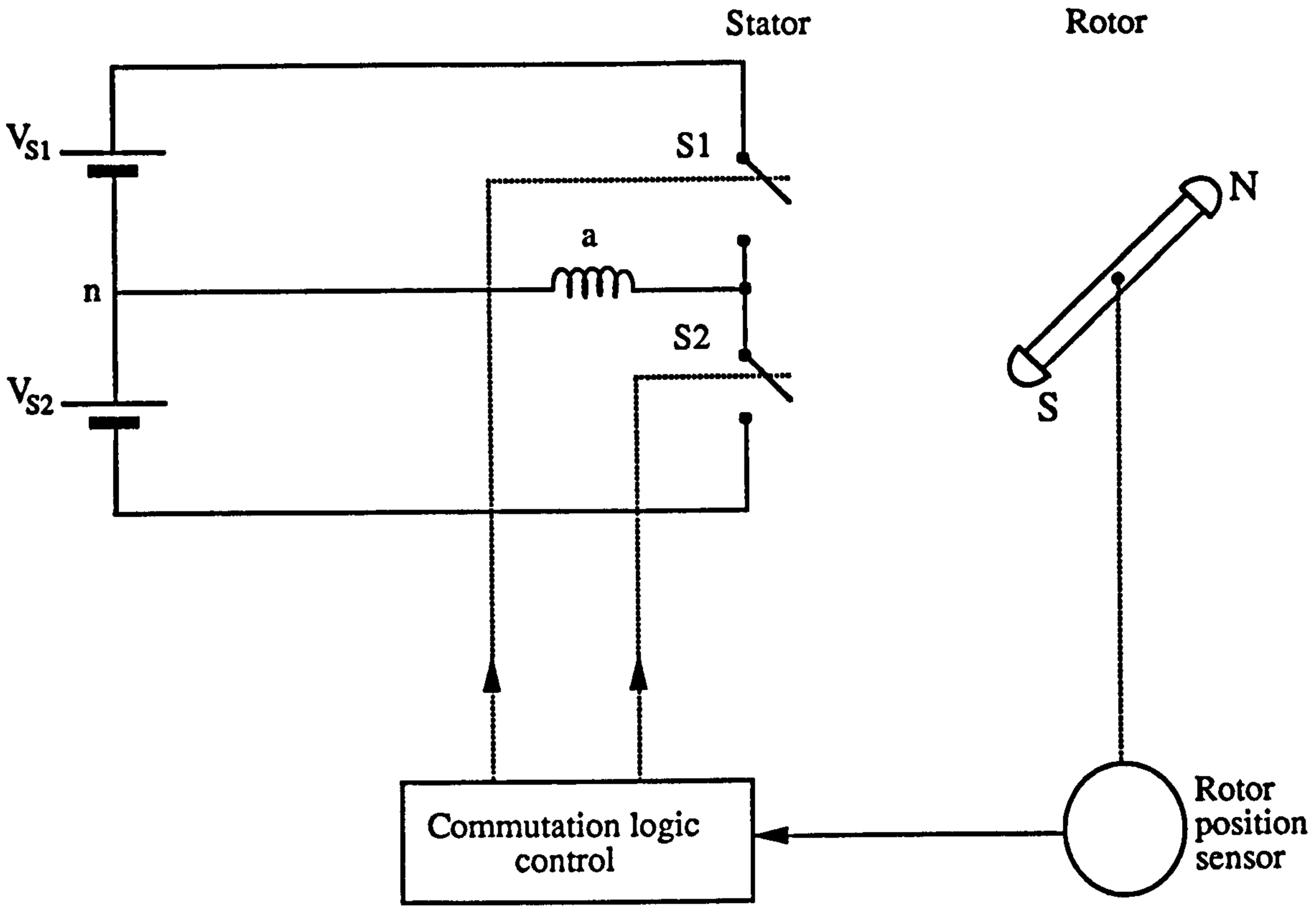

Figure 3.3 (a) Single-phase, full-wave brushless dc motor drive

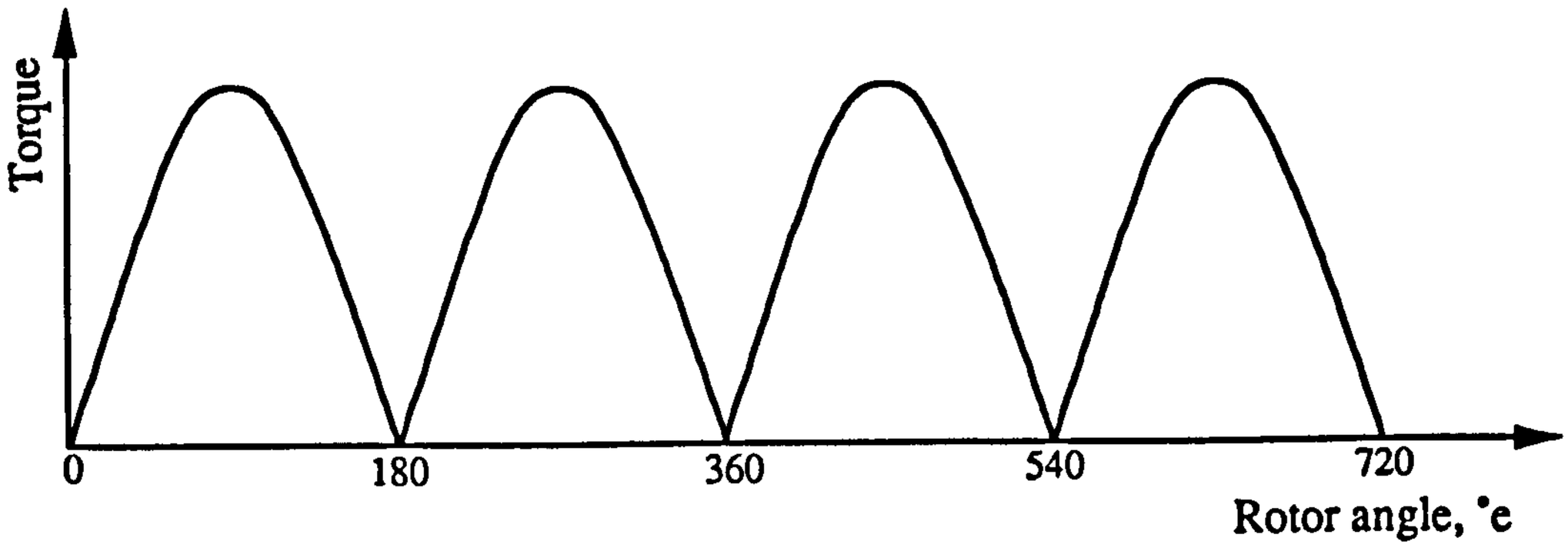

Figure 3.3 (b) Torque output for single-phase, full-wave brushless dc motor

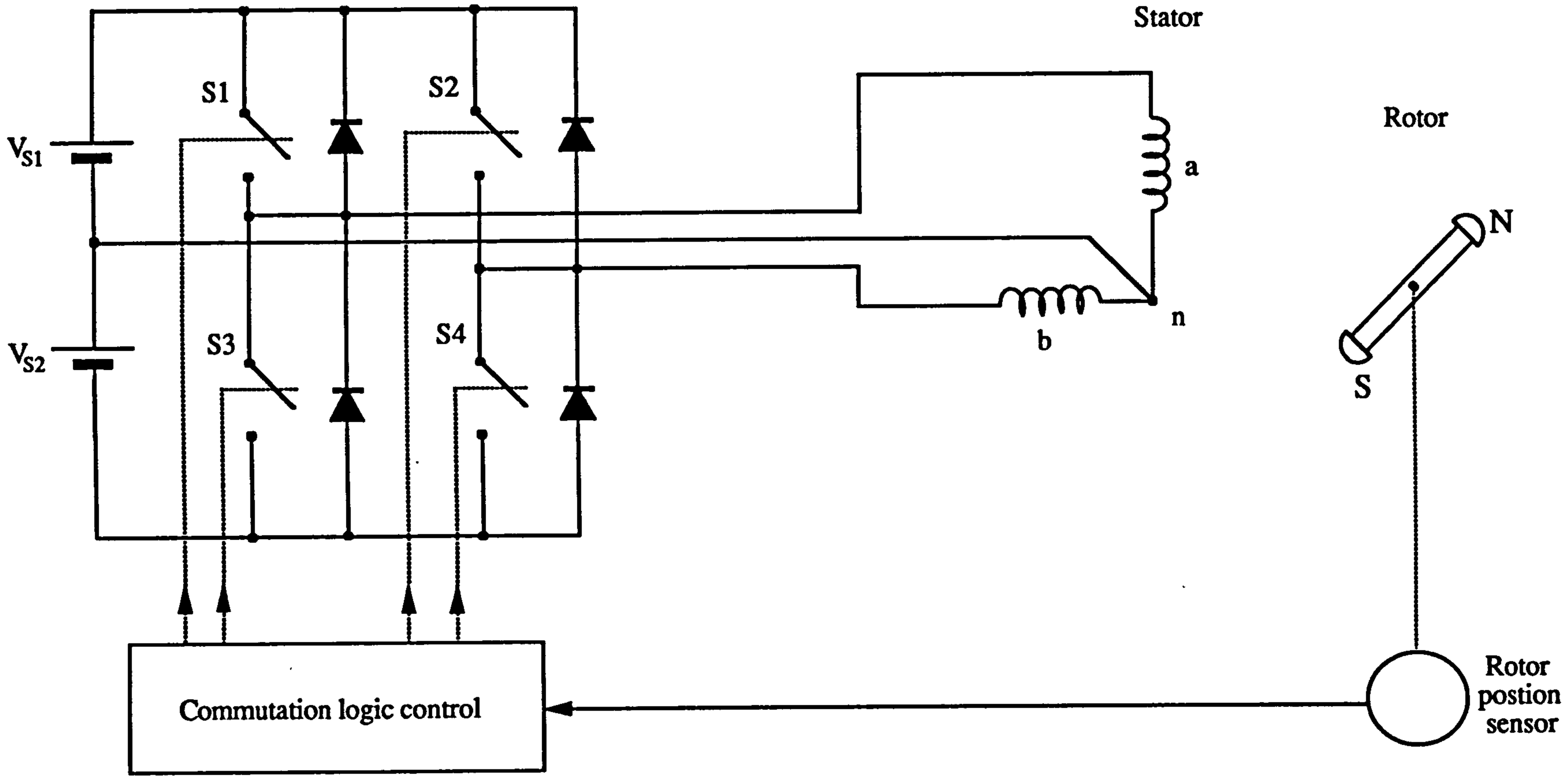

Figure 3.4 Two-phase, full-wave brushless dc motor drive

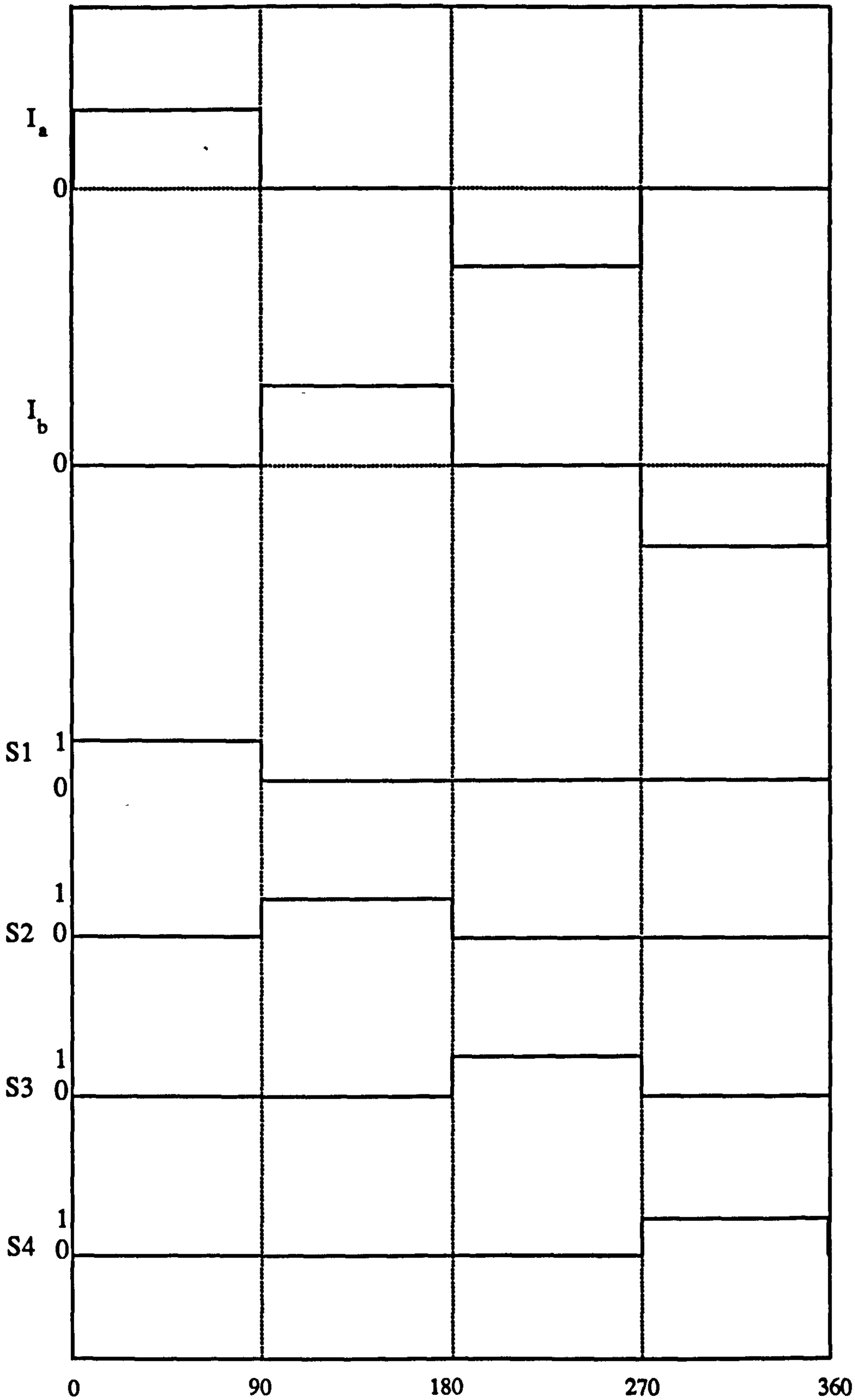

Figure 3.5 Switching sequence and corresponding phase current waveforms for 2-phase, full-wave brushless dc motor

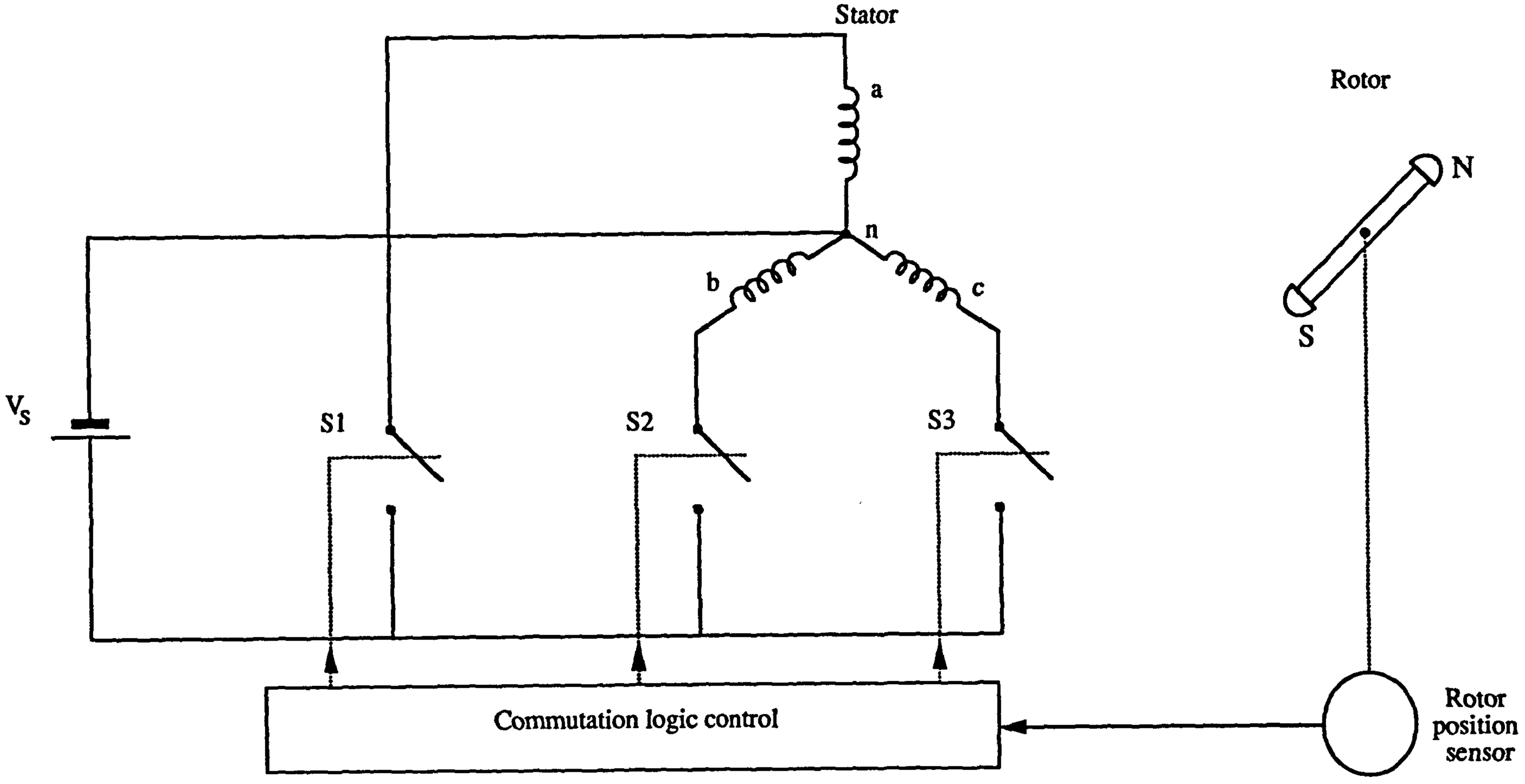

Figure 3.6 Three-phase, half-wave brushless dc motor drive

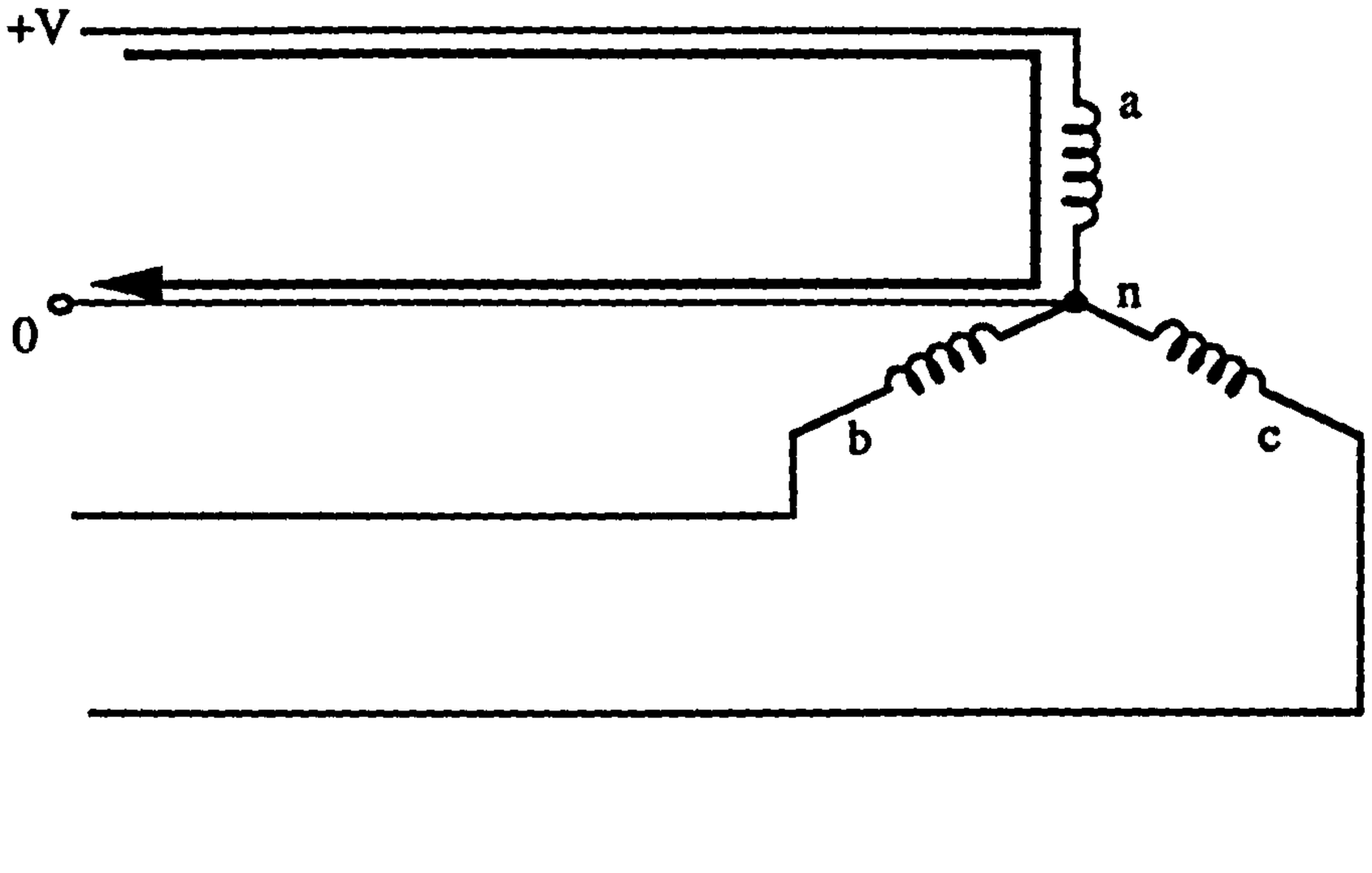

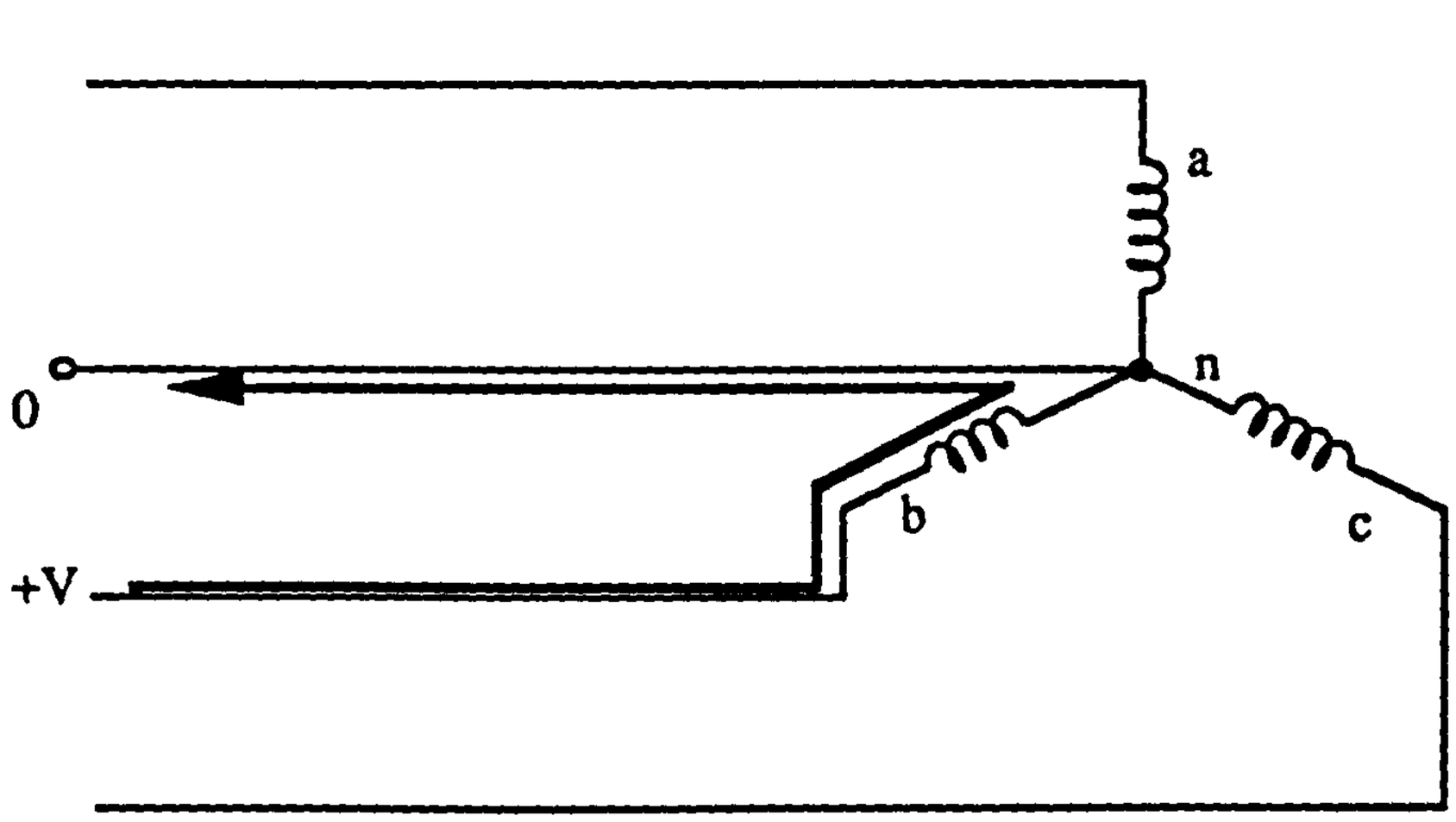

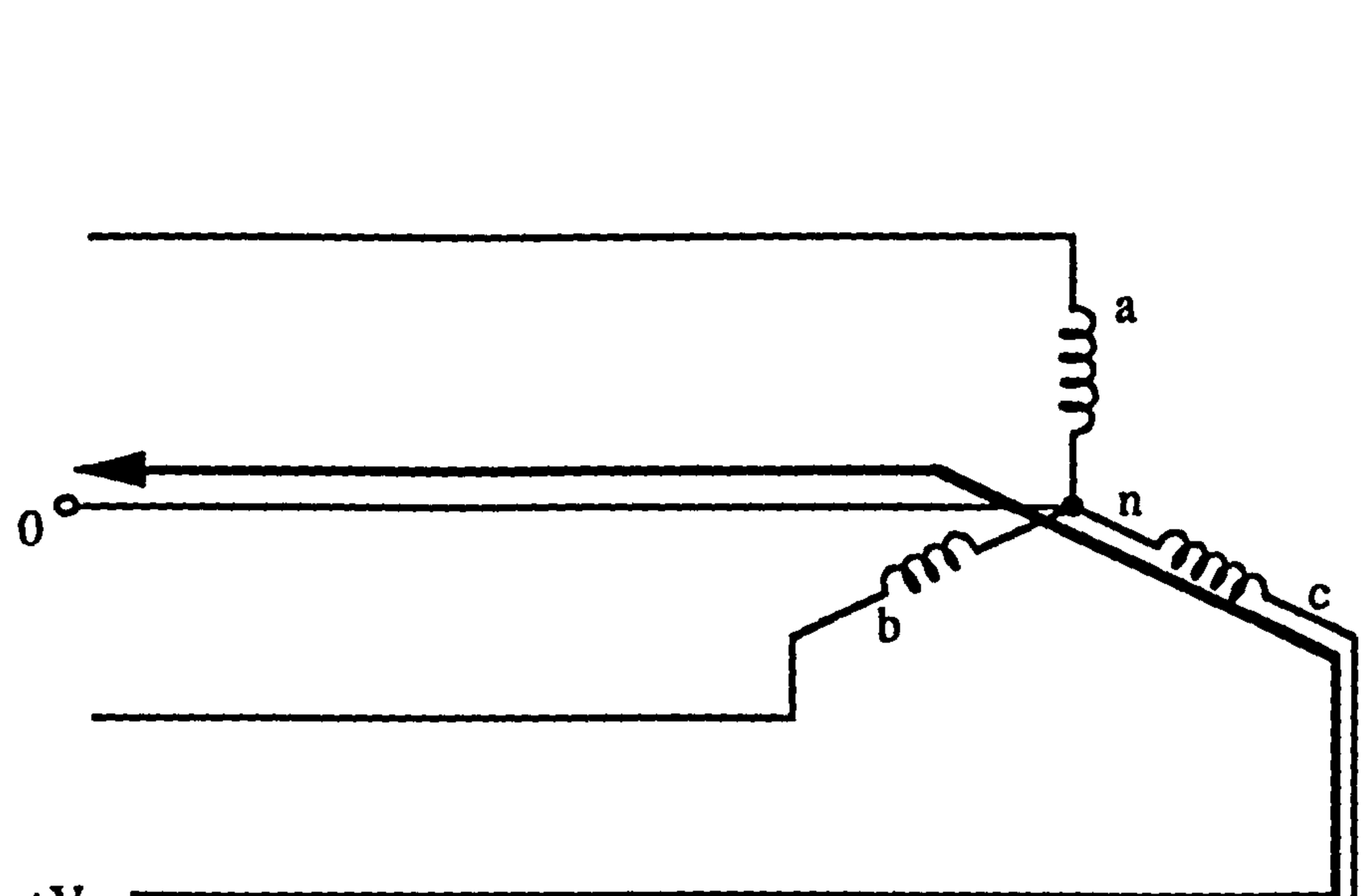

Figure 3.7 Switching sequence for 3-phase, half-wave brushless dc motor

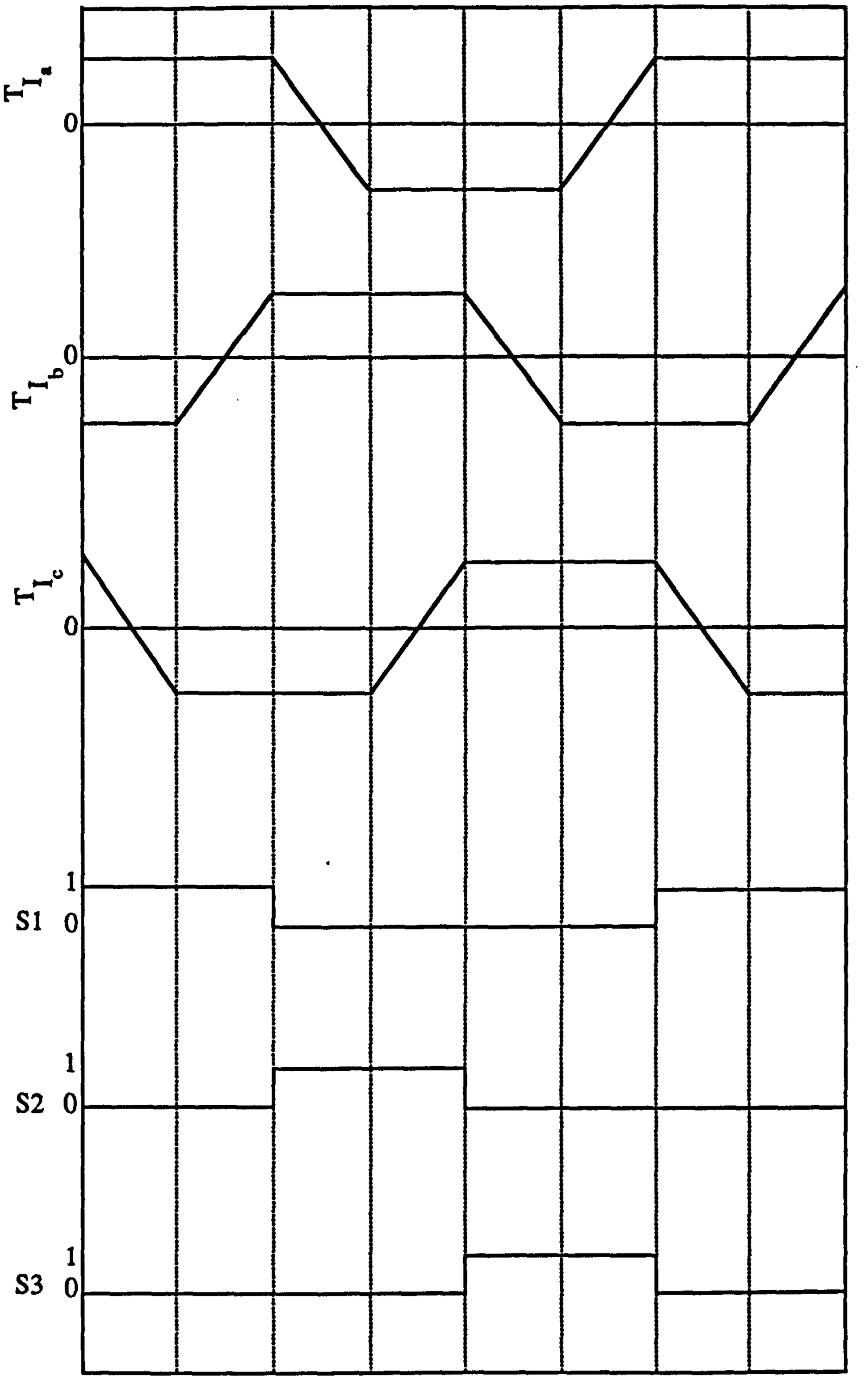

"1" = S ON , " 0 " = S OFF

Figure 3. 8 Switching sequence and idealized torque profile for 3-phase, half-wave brushless dc motor

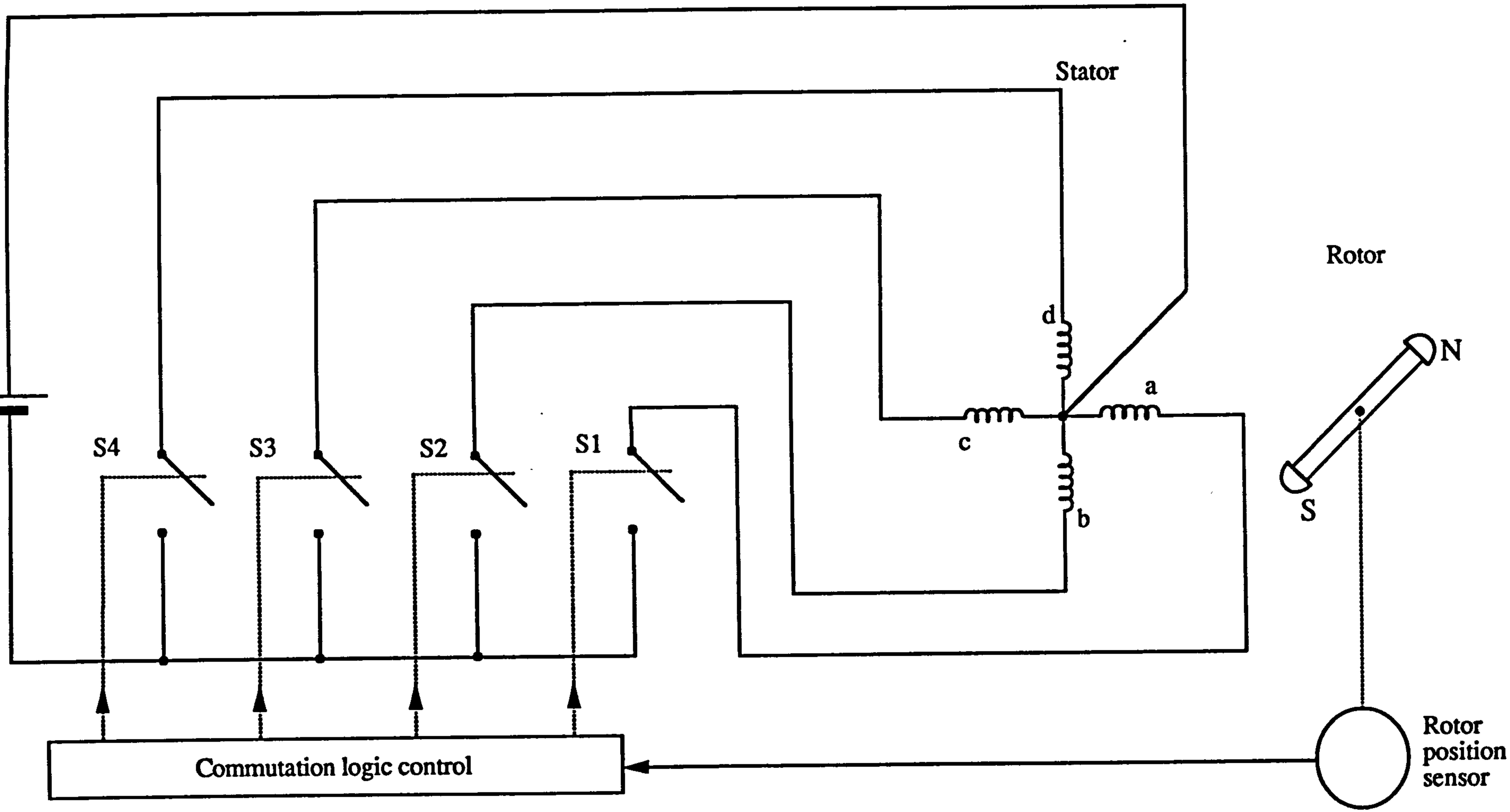

Figure 3.9 Four-phase, half-wave brushless dc motor drive

Step 1

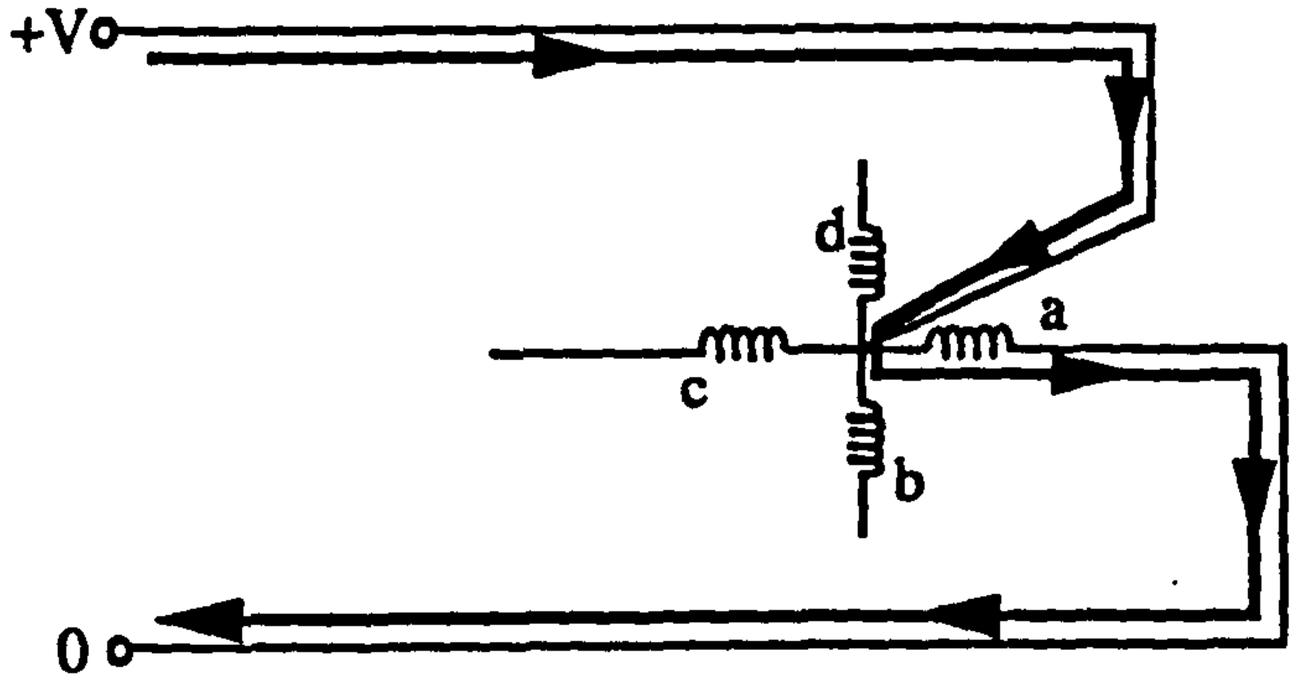

Step 2

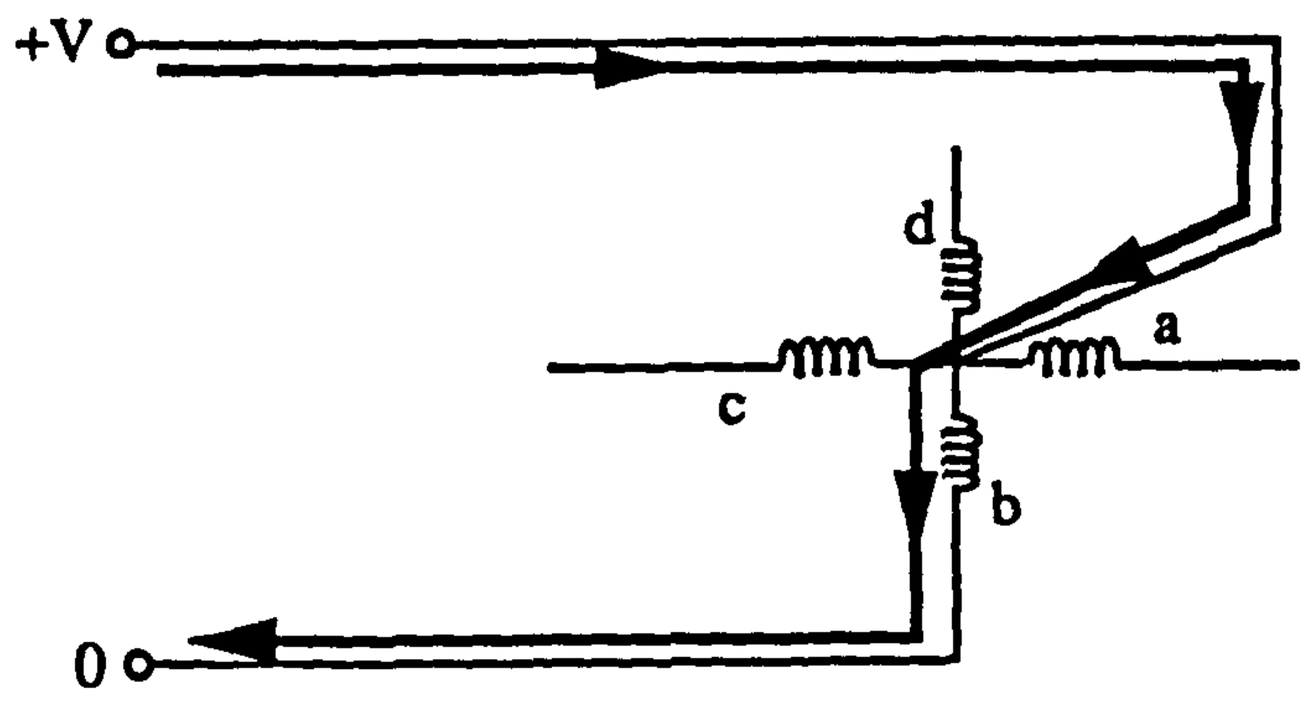

Step 3

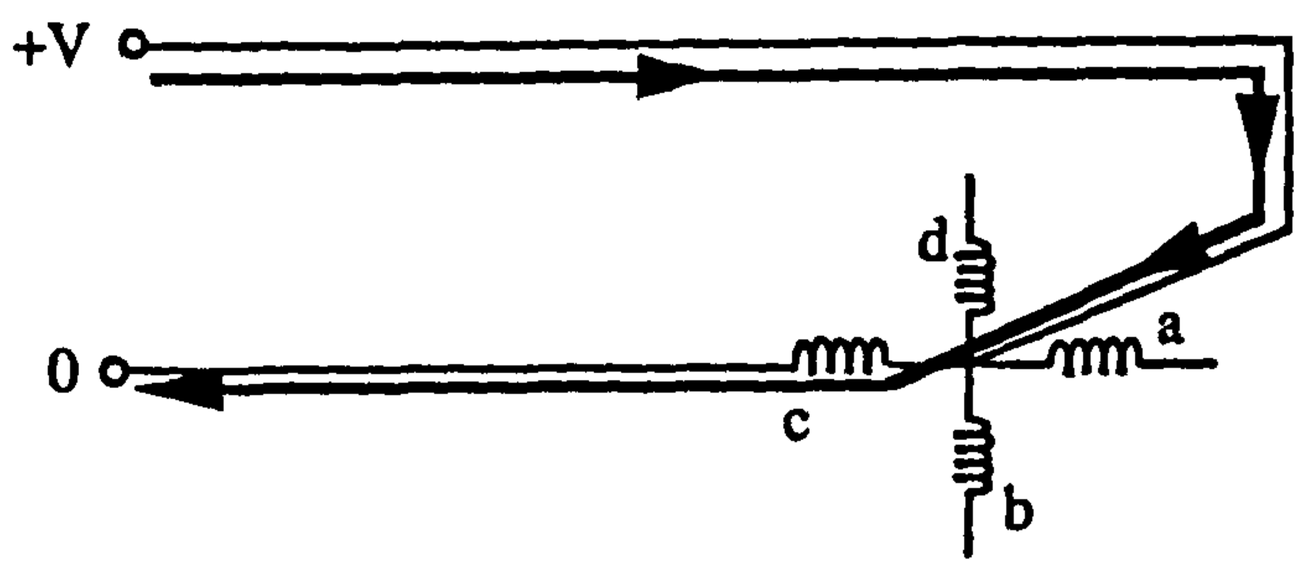

Step 4

Figure 3.10 Switching sequence for 4-phase, half-wave brushless dc motor

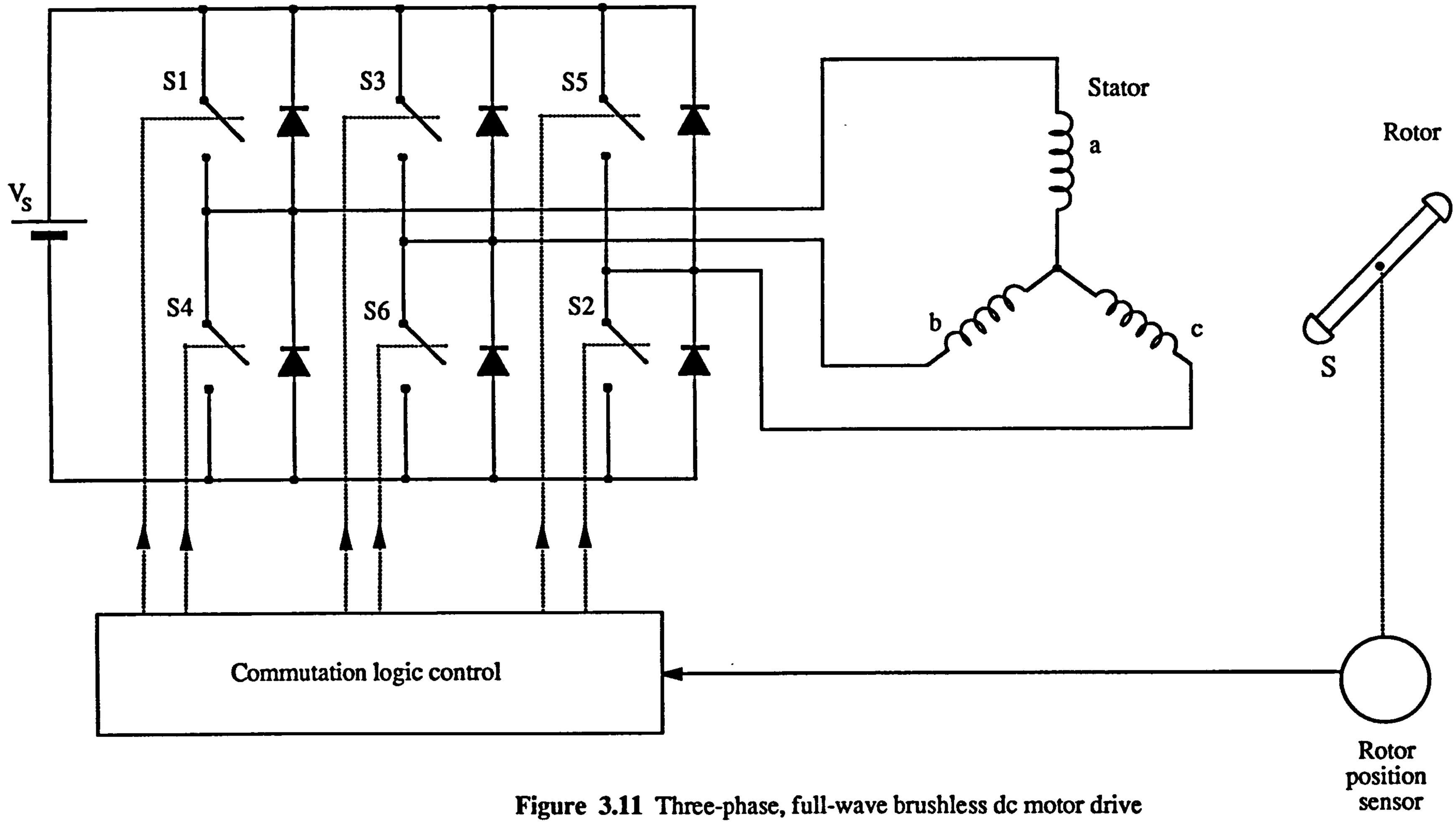

Figure 3.11 Three-phase, full-wave brushless dc motor drive

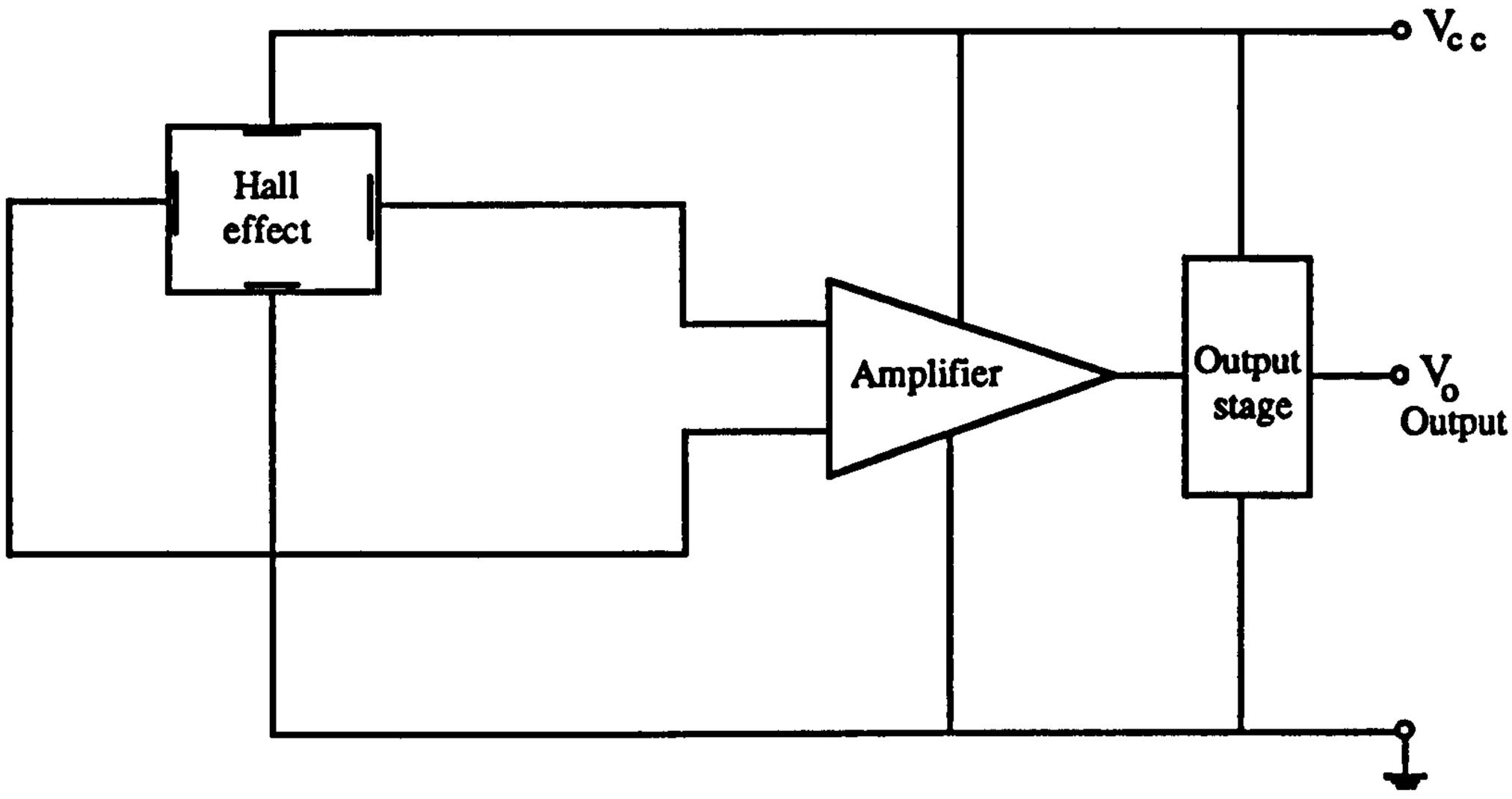

Figure 3.12 (a) Block diagram of Hall-effect integrated-circuit

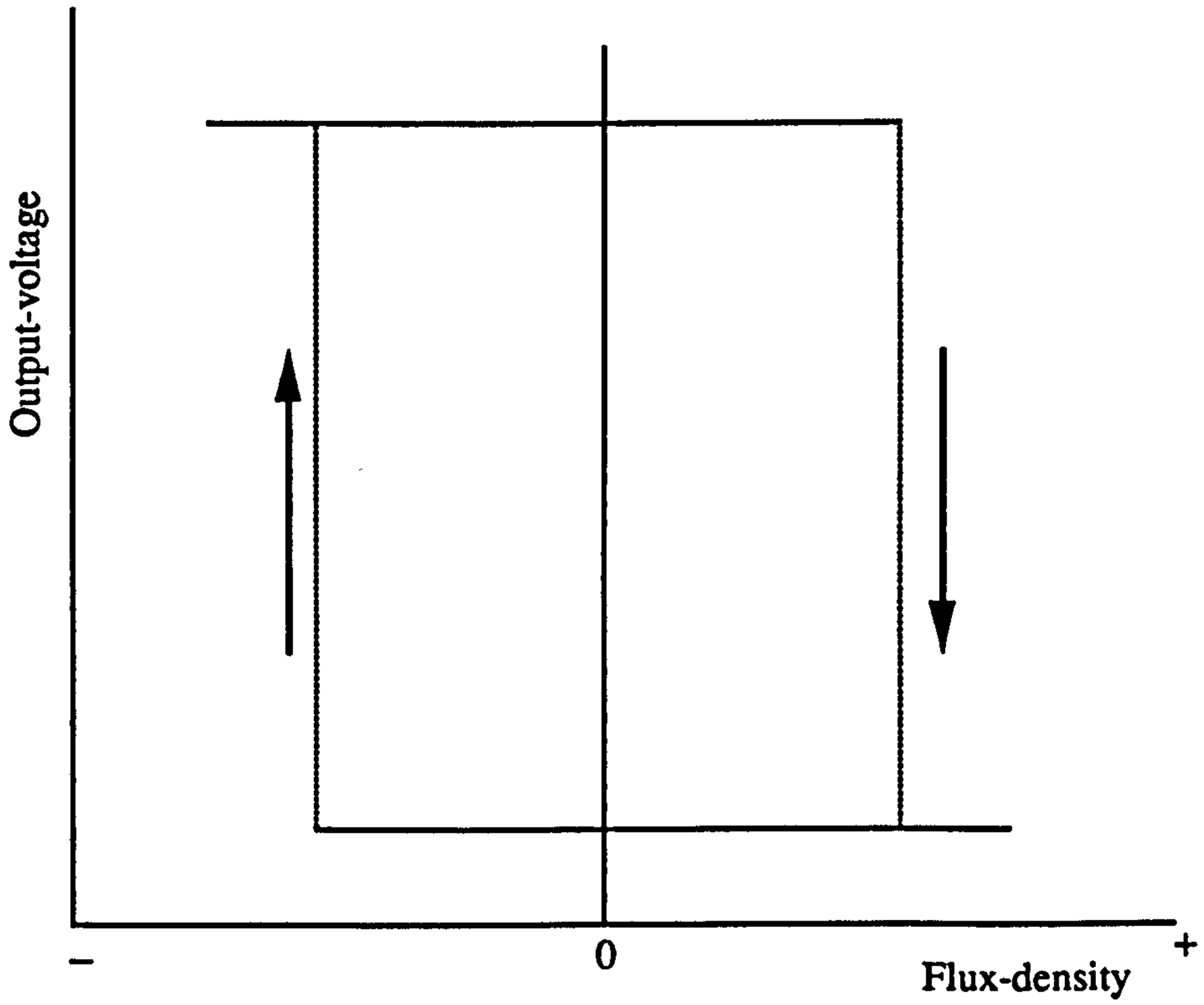

Figure 3.12(b) Characteristics of Hall integrated-circuit

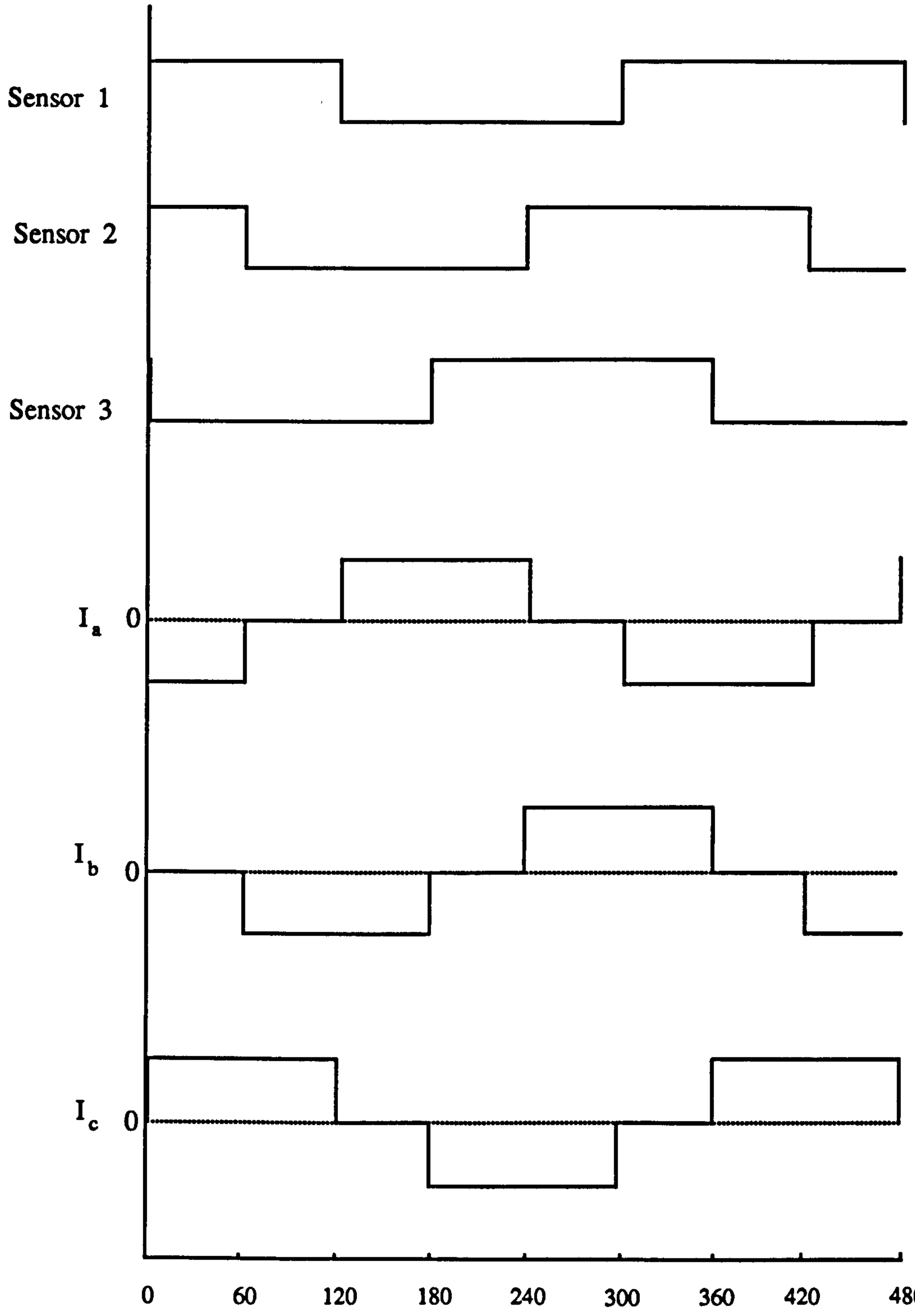

Figure 3.13 Hall-effect sensor signals and corresponding phase current waveforms for 3-phase, full-wave brushless dc motor

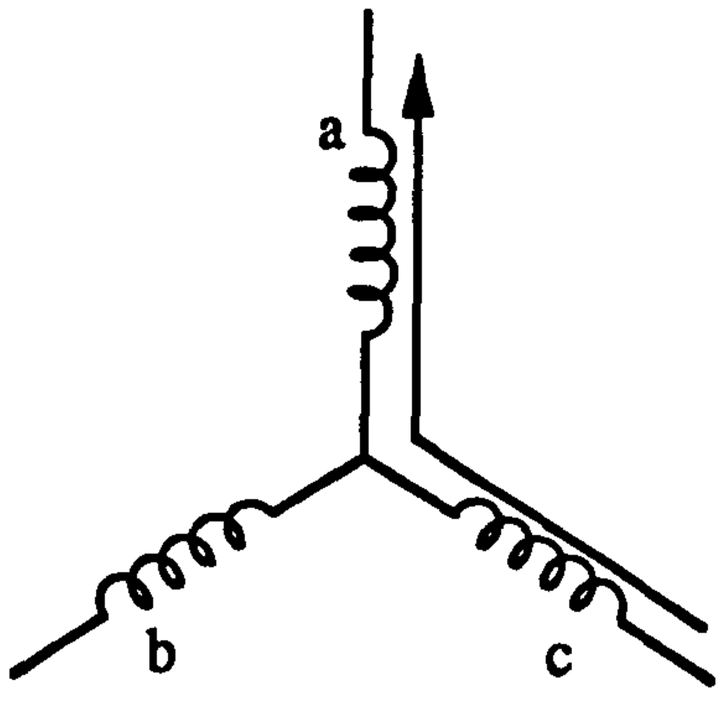

step 1

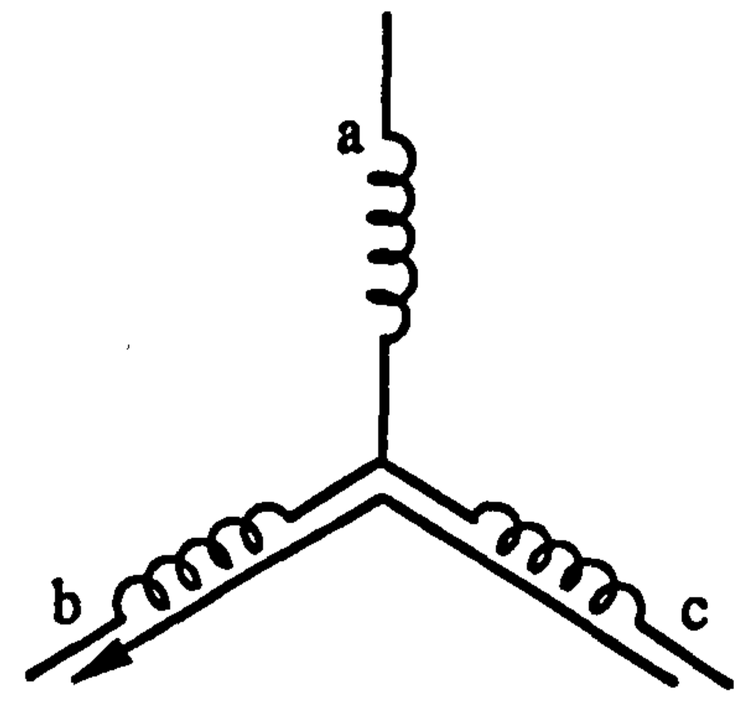

step 2

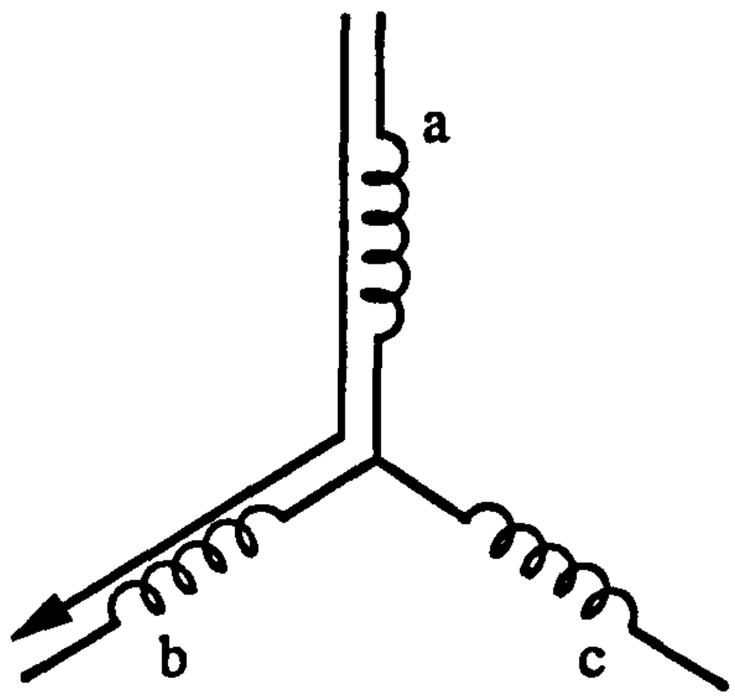

step 3

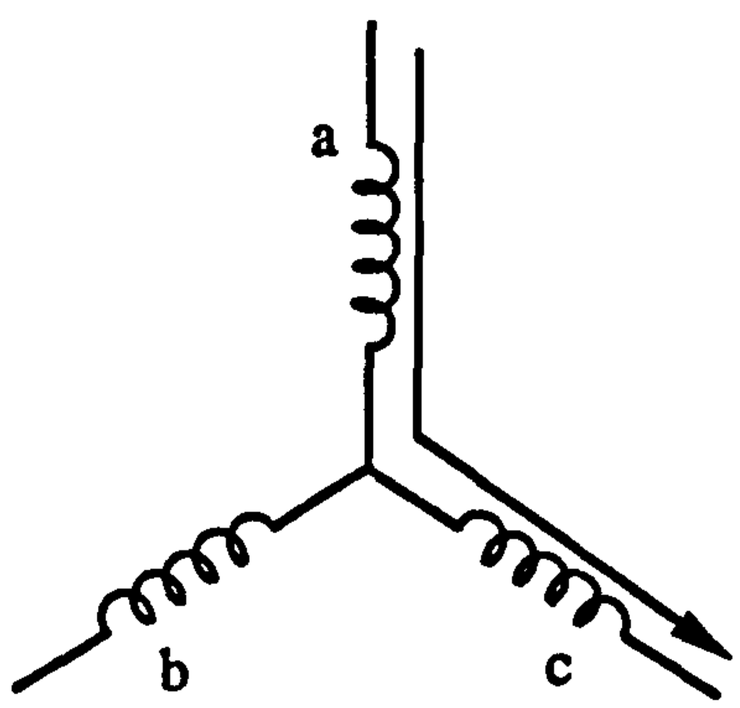

step 4

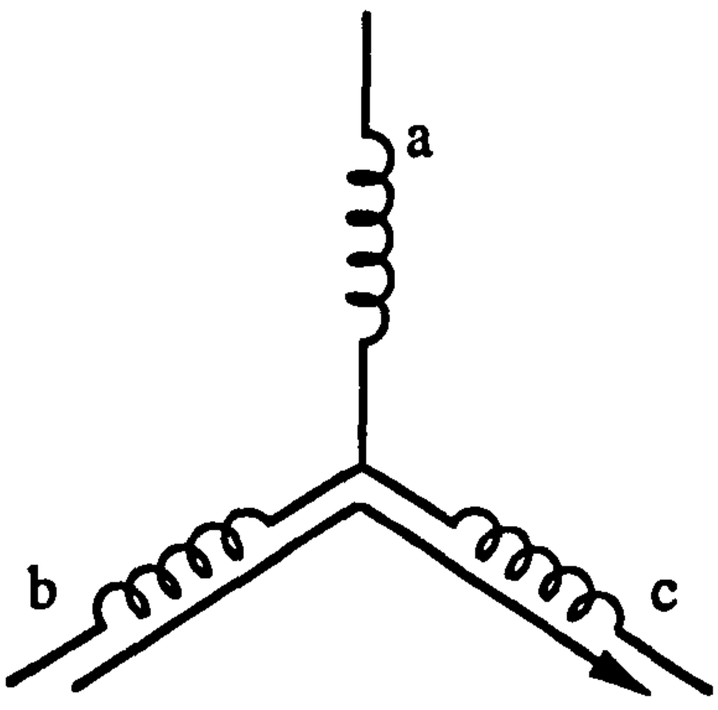

step 5

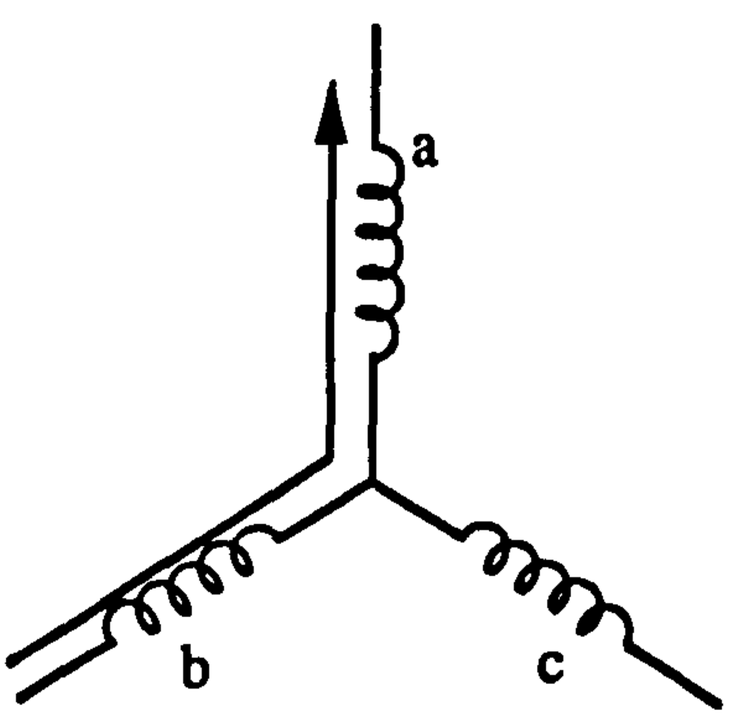

step 6

Figure 3.14 Switching sequence for 3-phase, full-wave brushless dc motor

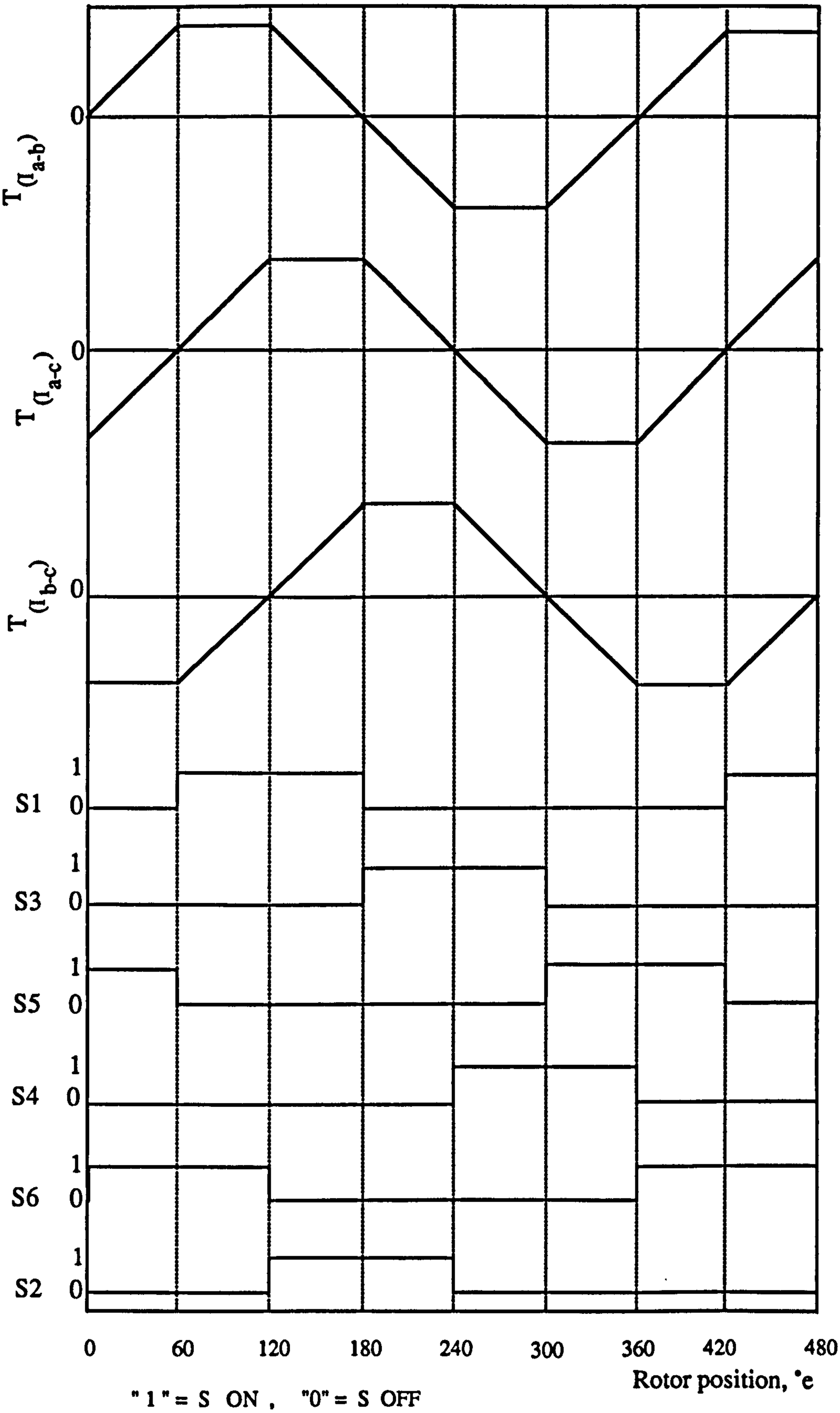

Figure 3.15 Switching sequence and idealized torque profile for 3-phase, full-wave brushless dc motor

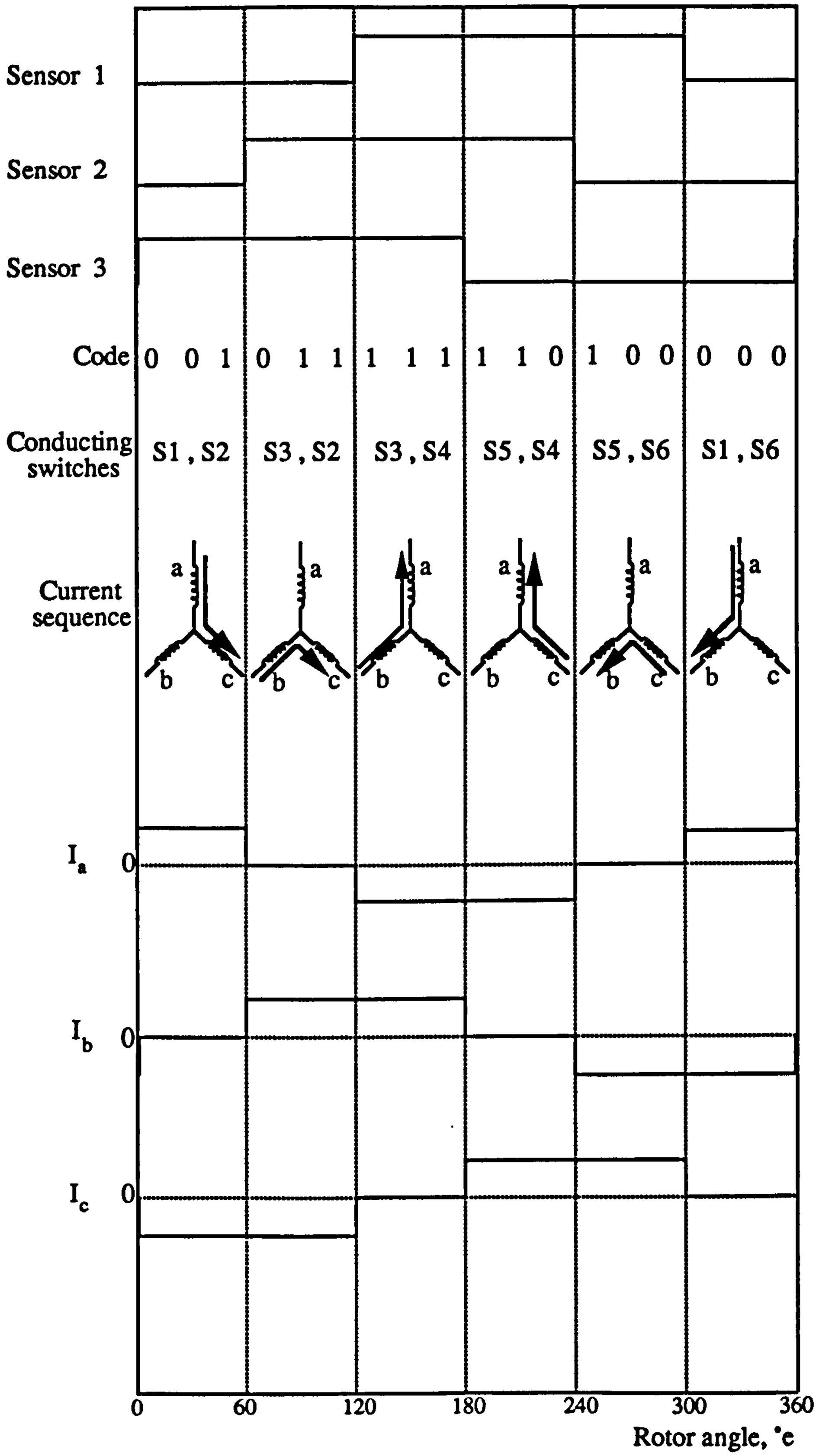

Figure 3.16 Switching sequence and corresponding phase current waveforms for reverse operation of 3-phase brushless dc motor.

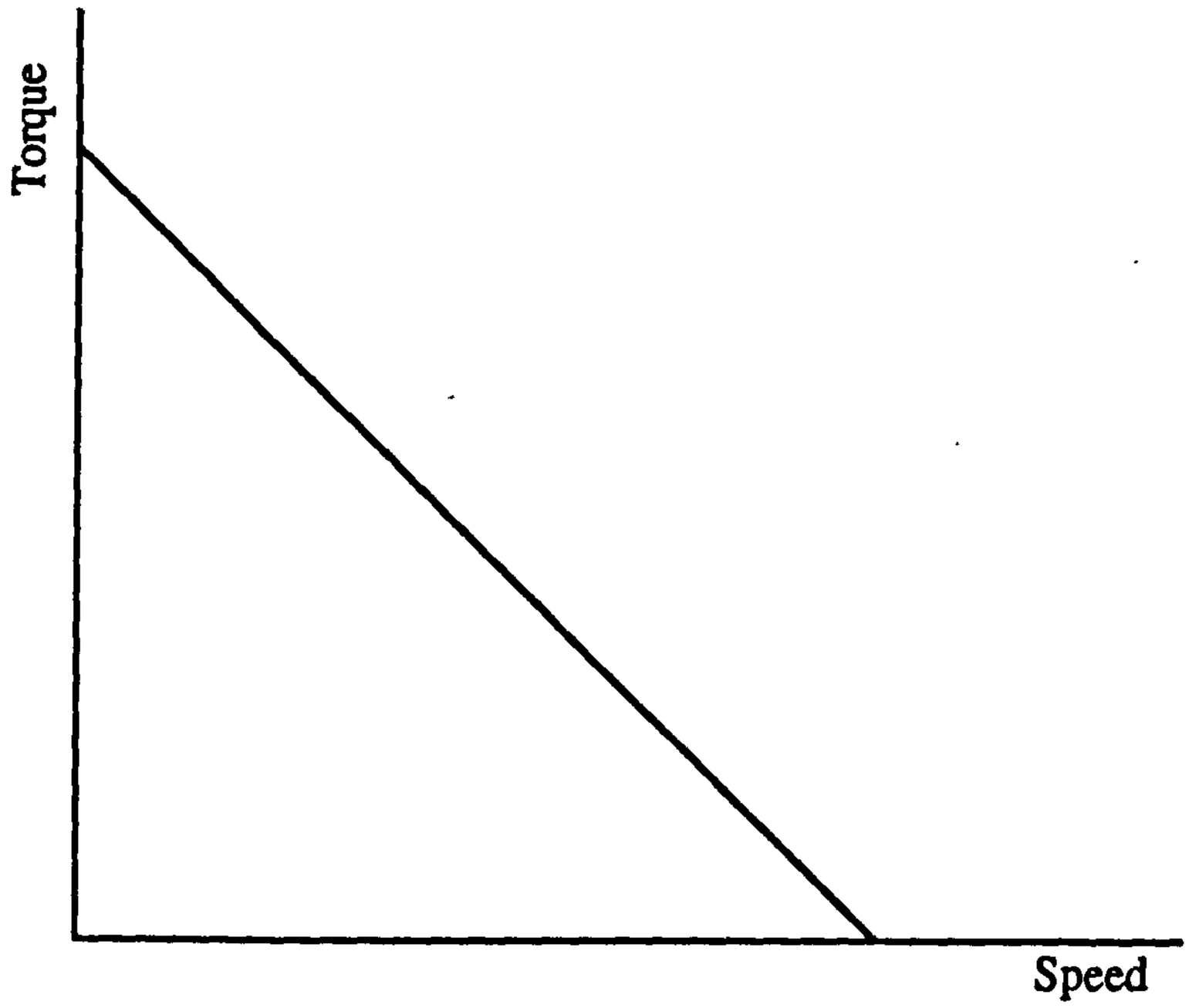

Figure 3.17 Typical torque-speed characteristic for brushless dc motor

CHAPTER 4

INVERTER AND CONTROL CIRCUIT DESIGN

The overall block diagram for the inverter and control circuit shown in Figure 4.1 comprises four main parts; an uncontrolled bridge rectifier which provides a smooth dc supply, a 3-phase inverter to apply the dc supply sequentially to the motor stator windings, a control circuit to provide drive signals for the inverter switches and low-voltage isolated power supplies for the switch drive and control circuits. Each of these circuits is described in detail below.

4.1 DIODE BRIDGE

The dc supply is obtained from a 3-phase auto-transformer whose output is rectified by a full-wave uncontrolled diode bridge and smoothed using a parallel capacitor, as shown in Figure 4.2. A 10 kΩ discharge resistor connected across the dc supply discharges the smoothing capacitor when the supply is removed and dissipates the energy released during regenerative braking.

The power diodes of Figure 4.2 should be capable of withstanding both the peak line voltage, with a safety margin in case of regeneration, and the maximum expected load current. For a supply voltage of 222V rms, the peak line voltage is therefore[30]

$$V_{Line(pk)} = 222\sqrt{2}$$

$$= 314V$$

During regenerative braking, the dc supply voltage can rise above $V_{Line(pk)}$. If the permitted rise is 50%, the diode should be capable of withstanding 470V and of carrying a current of 25A, which is the maximum allowable motor current. On this basis, the power diode M41 800R, with a peak reverse voltage capability of 800V and a peak forward current of 41A, was used in the rectifier bridge.

4.2 POWER SWITCH SELECTION

The four main types of power switching device used in power electronics inverters are summarised below.

4.2.1 CONVENTIONAL THYRISTOR

The thyristor is a four-layer, P-N-P-N switching device. It has three external terminals; the anode, cathode and gate. The contact electrode to the outer P-layer is the anode and that to the outer N-layer the cathode. The anode and cathode are the main current connections, while the gate provides a contact to the inner P-region and carries the control current which determines the thyristor forward resistance[30,33]. A short positive pulse on the gate causes this resistance to fall to a low value and thereby turns the device into the on-state. With no gate current applied the forward resistance is very high, and the thyristor is in the off-state. An increased gate current improves the turn-on time, but the maximum acceptable gate power dissipation must

not be exceeded. The overload rating of generally available thyristors is considerably higher than that of transistors. However, an auxiliary commutation circuit is required to turn-off the device[34,35].

4.2.2 GATE-TURN-OFF THYRISTOR

The gate-turn-off thyristor (GTO) is a four layer P-N-P-N 3-terminal switching device, similar in construction to the conventional thyristor. However, the GTO is more versatile because it can be turned-off by a brief pulse of negative current at the gate terminal. This facility allows the construction of inverter circuits without the bulky and expensive forced commutating components associated with conventional thyristor circuitry[24]. A GTO is turned-on by application of a positive pulse of current to the gate. To ensure a reduction in the on-state voltage and hence in the conduction losses, some manufacturers recommend a continuous gating current during the entire conduction period[24,33]. Like a conventional thyristor, the GTO can pass a high forward current when turned-on and block a high forward voltage when turned-off but, unlike a thyristor, it is unable to block reverse voltage. Its switching speed is faster than that of the thyristor[24,30].

4.2.3 BIPOLAR TRANSISTOR

The bipolar transistor is a 3-layer semiconductor device with three terminals; the emitter, base and collector. To turn the transistor on, a continuous base current is required to take the device into saturation and, to turn it off, the

base current must be reduced to zero. The instantaneous power loss in the transistor during each on or off transition is a function of the product of the instantaneous value of the collector current and the collector-emitter voltage. To reduce the power dissipation, the high initial base current necessary to reduce the turn-on time should be reduced as rapidly as possible after turn-on. The transistor has a second breakdown phenomenon[34,35], which limits the rate at which base current can be reduced, and following turn-off the base current must be reduced at a rate which the collector current can follow. The bipolar transistor is relatively inexpensive and can switch considerably faster than the thyristor[33], with switching times of less than 1 to 2μs being possible.

4.2.4 POWER MOSFET

The power MOSFET is a very fast switching device, with extremely short turn-on and turn-off times. The drive circuit is relatively simple, since it is a voltage-controlled device with a very high gain. The device has three terminals; the source, drain and gate, and the circuit symbol for an N-channel MOSFET is shown in Figure 4.3. The power loss for a given drain current depends on the on-state resistance, which increases with temperature and approximately doubles over the range 25°C to 200°C[34]. The MOSFET has a positive temperature coefficient, which acts in a self protective manner by forcing current to be uniformly distributed through the silicon die, so that it does not display the second breakdown phenomenon of the bipolar

transistor. Moreover, MOSFETs are easy to parallel, because their positive temperature coefficient forces current sharing among the paralleled devices[34,36].

Due to these advantages, and to the ready availability of high voltage, high current devices, the MOSFET was chosen for the PWM inverter built in the course of this research.

Although both P and N-channel MOSFETs are available, the description which follows is restricted to the N-channel devices used for the present work. The structure of an N-channel device is shown in Figure 4.4, with the semiconductor body being of P-type material and the source and drain of N-type material[30]. The gate is isolated electrically from the source by the layer of silicon oxide, and the structure contains an internal reverse diode with the same current rating as the transistor itself. The MOSFET is a voltage-controlled device, such that, with zero voltage applied to the gate/source, the drain/source impedance is very high and only a small leakage current flows in the drain[36]. When a positive gate voltage greater than the threshold voltage is applied, a drain current flows[34,36]. The typical switching waveforms given in Figure 4.5 show that, under these conditions, an increase in drain/source voltage produces an increase in drain current, until the channel pinch-off voltage is reached and the drain current assumes the constant value shown in Figure 4.6.

The switching devices must be capable of handling the maximum dc supply voltage and the worst case peak current expected in the system, as well as the rms value of the normal operating current. As explained in section 4.1, the

maximum dc supply voltage is 470V and, since the motor rated and maximum currents are 5.5A and 25A respectively, an IRF 450 power MOSFET which has a continuous drain current of 13A, a pulsed drain current of 52A and a drain-to-source breakdown voltage of 500V was selected for the inverter.

4.3 INVERTER POWER CIRCUIT

Figure 4.7 shows a schematic diagram of the inverter circuit. Each inverter arm contains a MOSFET and its drive and snubber circuits, with a fast recovery free-wheeling diode connected in anti-parallel with the MOSFET and a series fast recovery diode used to prevent the MOSFET body drain diode from conducting. The complete inverter board diagram is shown in Figure 4.8.

4.3.1 MOSFET DRIVE CIRCUIT

Since the MOSFET is a voltage-controlled device, a voltage must be applied to the gate/source terminals to produce a flow of drain current. The switching speed is proportional to the rate at which the input capacitance (typically about 2nF) can be charged and discharged, and the gate drive circuit must be capable of supplying sufficient current to charge this capacitance during turn-on in the shortest possible time. During turn-off the gate drive circuit has to discharge the capacitance rapidly, and it must therefore have a very low sink impedance. These conditions ensure that the turn-on and turn-off times are both very short, and that the switching losses are consequently small[36].

In the gate drive circuit of Figure 4.9, the isolating pulse transformer T1 has tightly coupled windings with very low leakage reactances, and the output of the transformer is consequently a differentiated version of the input i.e. a square-wave input produces alternate positive and negative spikes at the output. The resistance divider R3 and R4 usually holds the input voltage to IC1 at half the supply voltage (7.5V). When the PWM control signal goes high, the resulting positive voltage spike, added to the 7.5V bias, switches the output of IC1 to low. The output of IC2 goes high and, since this is fed back via R5 to the input of IC1, the output of IC1 is held low. For this condition the output of IC3 is high, which produces a low at the output of the buffer formed by IC4 to IC6. This signal is applied to the C3/R6 combination, which acts to speed up the turn-on of transistor TR2. Transistor TR3 of the push/pull transistor pair is turned-on and charge is withdrawn from the MOSFET gate, to turn-off the device. When the control signal goes low, the negative spike appearing at the transformer secondary causes the input of IC1 to drop below the threshold. The output of IC1 goes high and is latched by IC2 as explained previously. The outputs of IC4 to IC6 are now high. Transistor TR2 turns-on, applying +15V to the MOSFET gate to turn the device on[37].

4.3.2 FREE-WHEELING AND REVERSE RECOVERY DIODES

The inverter is switched at intervals of 60°e and during every step two MOSFETs conduct, each for 120°. At the end of each conducting period, one device turns-off and a second

turns-on. The inductive energy stored in the winding connected to the device which is switched off produces a potentially damaging voltage spike and, to avoid this, free-wheeling diodes provide current paths during the switching operations. For the case illustrated by Figure 4.10, the diode in parallel with S3 begins conduction when S6 is turned-off and ceases conduction when the current I_1 has decreased to zero. The free-wheeling diodes allow the current to decay in a controlled way.

As shown in Figure 4.3, the MOSFET contains an internal reverse diode with the same current rating as the transistor. However, the recovery time of the diode is slow compared with the switching time of the MOSFET, so that an external fast recovery anti-parallel diode is used with each device. To prevent reverse current flow through the internal diode, a further external diode shown in Figure 4.11 is inserted in series with the MOSFET.

4.3.3 VOLTAGE TRANSIENT SNUBBER

The clamping diode shown in Figure 4.11 may not provide an instantaneous clamping action due to its forward recovery characteristic, and stray circuit inductance may cause an increased voltage spike. The snubber circuit of Figure 4.12 comprising a resistor, a diode and a capacitor, is therefore connected across the device. This circuit has two time constants, a very short one through the diode and a much longer one through the resistor, and Figure 4.13 shows typical voltage and current waveforms at turn-off, with and without a snubber circuit. As the MOSFET turns-off, load

current is diverted into the snubber capacitor via the diode while the drain current decreases. The drain/source voltage V_{DS} is held at a low value by the snubber capacitor, which require a finite time to charge, and V_{DS} is still quite low when the drain current has collapsed. Load current continues to flow into the snubber capacitor until V_{DS} reaches the supply rail level, when the free-wheeling diode becomes forward biased and conducts the load current[30].

4.4 CONTROL AND MOSFET DRIVE CIRCUIT POWER SUPPLIES

Since the source terminals of the six MOSFETs shown in Figure 4.8 are not all at the same potential, isolated power supplies are required. The three upper MOSFET drive circuits are provided with individual floating power supplies, but the three lower circuits share a common power supply. The control circuit requires a further floating power supply. The multiple power supply shown in Figure 4.14 has a 60kHz 12V square-wave oscillator IC1, which switches TR1 on and off, energizing pulse transformer T1 which is connected to other pulse transformers T2 to T6. The five secondary outputs are rectified by a single diode to provide the individual 15V supplies for the drives and control circuit[37].

4.5 LOGIC CONTROLLER OPERATION

In response to the motor position-sensor signals, the controller IC LS7261 of Figure 4.15 generates six signals which control the inverter. The controller provides PWM control of the motor current using an external control

voltage and a saw-tooth oscillator, with an over-current sensor providing protection for the motor windings and the MOSFET drive circuits. Figure 4.16 shows the controller circuit.

4.5.1 MOTOR SPEED CONTROL

A saw-tooth signal used in conjunction with the external control voltage applied to pin 13 provides the variable voltage PWM and consequently speed control for the motor. The timing components for the saw-tooth generator comprise the RC network connected to pin 14, as shown in Figure 4.16. When the level of the control signal to pin 13 is more negative than that of the saw-tooth signal at pin 14 the output control signals becomes high, causing the switches to turn-on. Conversely, when the level of the control signal is more positive than that of the saw-tooth signal, the output control signal becomes low and the switches turn-off. By varying the level of the control signal, the switch on and off durations can be adjusted, as in Figure 4.17, and the average voltage applied to the motor stator winding and consequently its speed are controlled.

4.5.2 OVER CURRENT PROTECTION

In order to protect the motor windings and the MOSFET switches from overload, a 0.5Ω resistor is inserted between the dc rail and the common source of the three lower MOSFETs. The motor current flowing through this resistor creates a voltage which is applied to potentiometer pt1 connected to the over current sensor (pin 12). When the voltage at the

over current sensor is more than half V_{SS}, the six output control signals are disabled and the motor is disconnected from the supply. The current limit value may be changed by adjustment of the potentiometer pt1.

Dynamic braking of the motor is provided by applying +15V to the brake input (pin 9). The output control signals 1, 2 and 3 turn-off and the output control signals 4, 5 and 6 turn-on, which effectively shorts the windings together.

4.5.3 MOTOR COMMUTATION

The controller IC LS7261 responds to changes of the motor position sensors, to provide commutation of the motor windings. The commutation select inputs (pins 1 and 20) are used to select the correct sequence of the output control signals, based on electrical separation of the motor position sensors. Options are available for separations of 60°, 120°, 240° and 300°e between the position sensors. The motor used in this research has three position sensors, mutually separated by 60°e, so that both pin 1 and 20 are connected to 0V, to achieve the correct switching sequence of Table 4.1.

Pin (19) of the commutator IC determines the rotor direction by changing the output sequence. Forward direction is selected by applying +15V to pin (19) and reverse direction is obtained by applying 0V.

4.6 DISCUSSION OF RESULTS

A selection of experimental results are presented in this section. Figure 4.18 shows the effect of varying the control signal on the mark-to-space ratio of the PWM signal. It is

Rotor-Position Sensor Signals			Forward Operation					Reverse Operation				
			Output Control Signals		Motor Windings			Output Control Signals		Motor Windings		
S1	S2	S3			A	B	C			A	B	C
0	0	0	01	05	+	-	OFF	02	04	-	+	OFF
1	0	0	03	05	OFF	-	+	02	06	OFF	+	-
1	1	0	03	04	-	OFF	+	01	06	+	OFF	-
1	1	1	02	04	-	+	OFF	01	05	+	-	OFF
0	1	1	02	06	OFF	+	-	03	05	OFF	-	+
0	0	1	01	06	+	OFF	-	03	04	-	OFF	+

1 2 3 4 5 6

1 3 5 4 6 2

Table 4.1 Output commutation sequence

clear that the duty cycle may be varied, which in turn will vary the output voltage applied to the motor stator windings. Figure 4.19 shows the effect of varying the sawtooth signal frequency on the switching frequency of the PWM signal. The PWM controller designed in the course of this research is capable of operating at high switching frequency (up to 50kHz). An increased switching frequency considerably reduces the current ripple amplitude and consequently the high-frequency torque ripple, as will be shown in chapter 7. This high switching frequency results in a 20µs switching time period which, for a 50% duty cycle, results in a 10µs on-time and a 10µs off-time. This requires that the switching devices have very fast turn-on and turn-off times. Since the MOSFET has a very short switching time (less than 60ns), it is possible to operate at such a high switching frequency in order to reduce the current ripple amplitude and at the same time keep the switching power loss in the device from being excessive. Generally, frequencies below 15kHz are to be avoided because of possible acoustic noise generation. The output signals of the rotor-position sensors at different speeds are given in Figure 4.20, and it can be seen that the frequency of these is a function of the rotor speed. Thus synchronism between the stator field and the permanent-magnet field is ensured at all speeds. Figure 4.21 shows the waveforms of the current for the free-wheeling diode D6 and the drain/source voltage of MOSFET S3 when MOSFET S1 turns-on and MOSFET S3 turns-off. These waveforms confirm that the current of the outgoing phase falls to zero through the free-wheel path of the anti-parallel diode in each inverter

leg and that the free-wheeling diode conducts from the moment the drain/source voltage reaches the supply rail level. Before this instant, the current flows into the snubber capacitor. Figure 4.22 shows the generated no-load phase emf waveforms at different speeds and it is evident that it has a trapezoidal shape. Figure 4.23 shows the phase and line voltage waveforms for the drive with a 50V supply voltage, 1.6Nm load torque, a steady-state speed of 420rpm and without PWM control. It is clear that there are voltage spikes on these voltage waveforms, and these are due to the sudden change in the phase current at the instants of commutation as shown in Figure 4.24. The motor supply current waveform for the same conditions described above is shown in Figure 4.25. Figure 4.26 shows the phase current and voltage and line voltage waveforms with a 70V supply voltage, 1Nm load torque, a steady-state speed of 300rpm and with PWM control set to 70% duty cycle at 20kHz switching frequency. The effect of the chopping action of the PWM controller on these waveforms is evident. Voltage spikes can be seen on the voltage waveforms and these are due to the same reason mentioned previously. Figure 4.27 shows the phase current and speed waveforms when a load having a torque of 0.7Nm and a moment of inertia of 0.003 $kg.m^2$ is applied and the motor is started from rest and run-up to a steady-state speed of 222rpm. It is apparent .that the starting current is about three times the running current and that the motor speed response during the start-up period is relatively smooth and linear. A detailed analytical study for these waveforms and their effect on the drive output performance is given later in chapters 5 and 7.

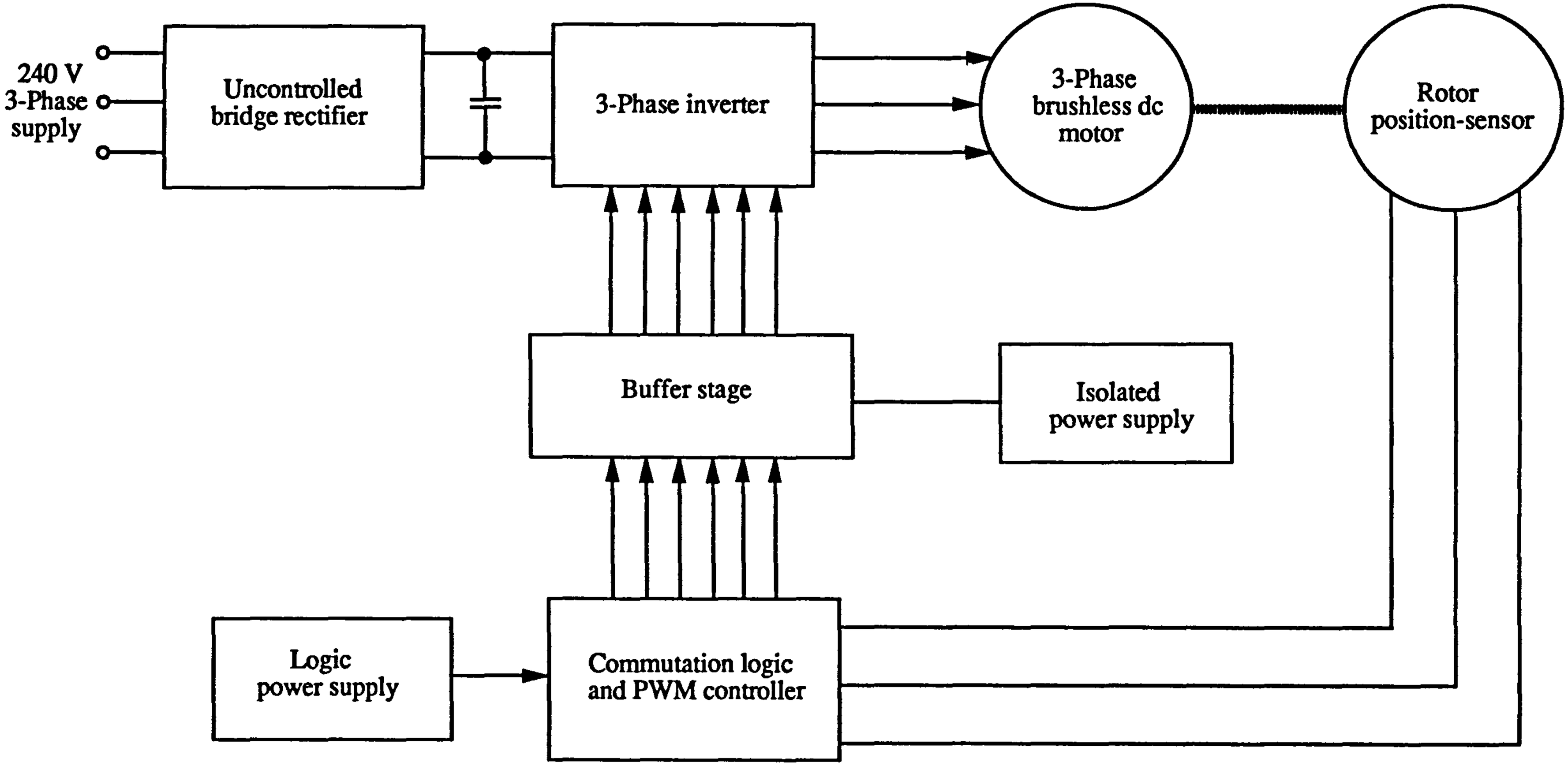

Figure 4.1 System block diagram

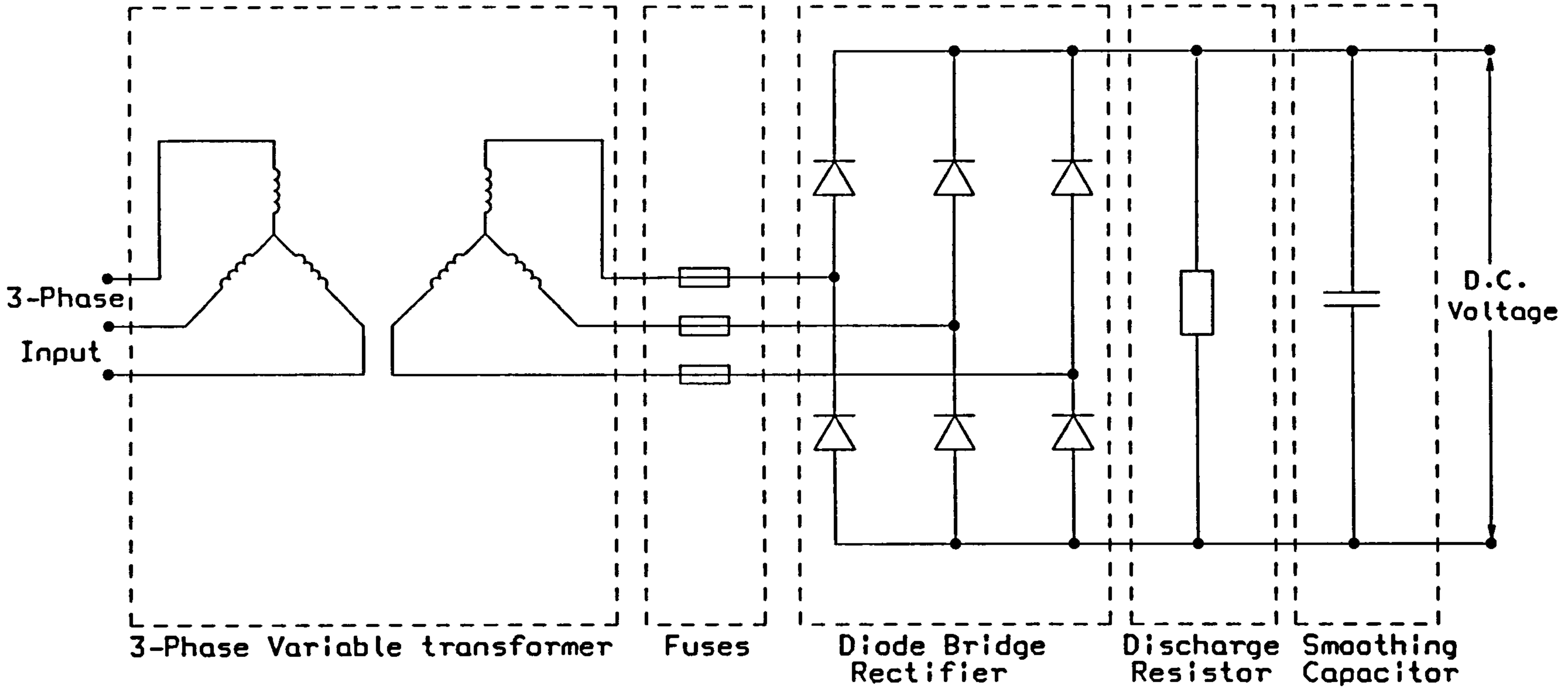

Figure 4.2 Voltage supply

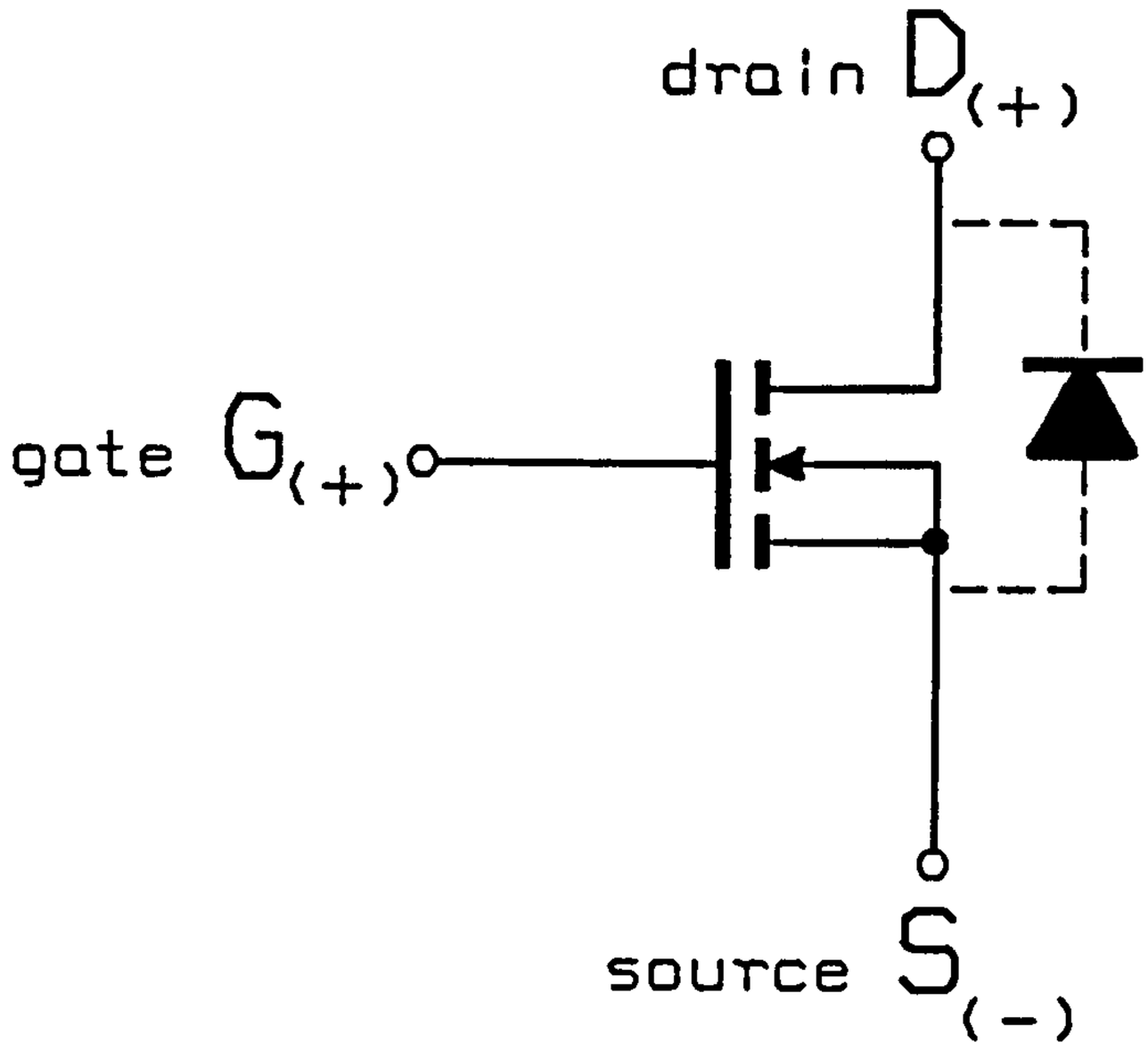

Figure 4.3 Symbol for an N-channel power MOSFET

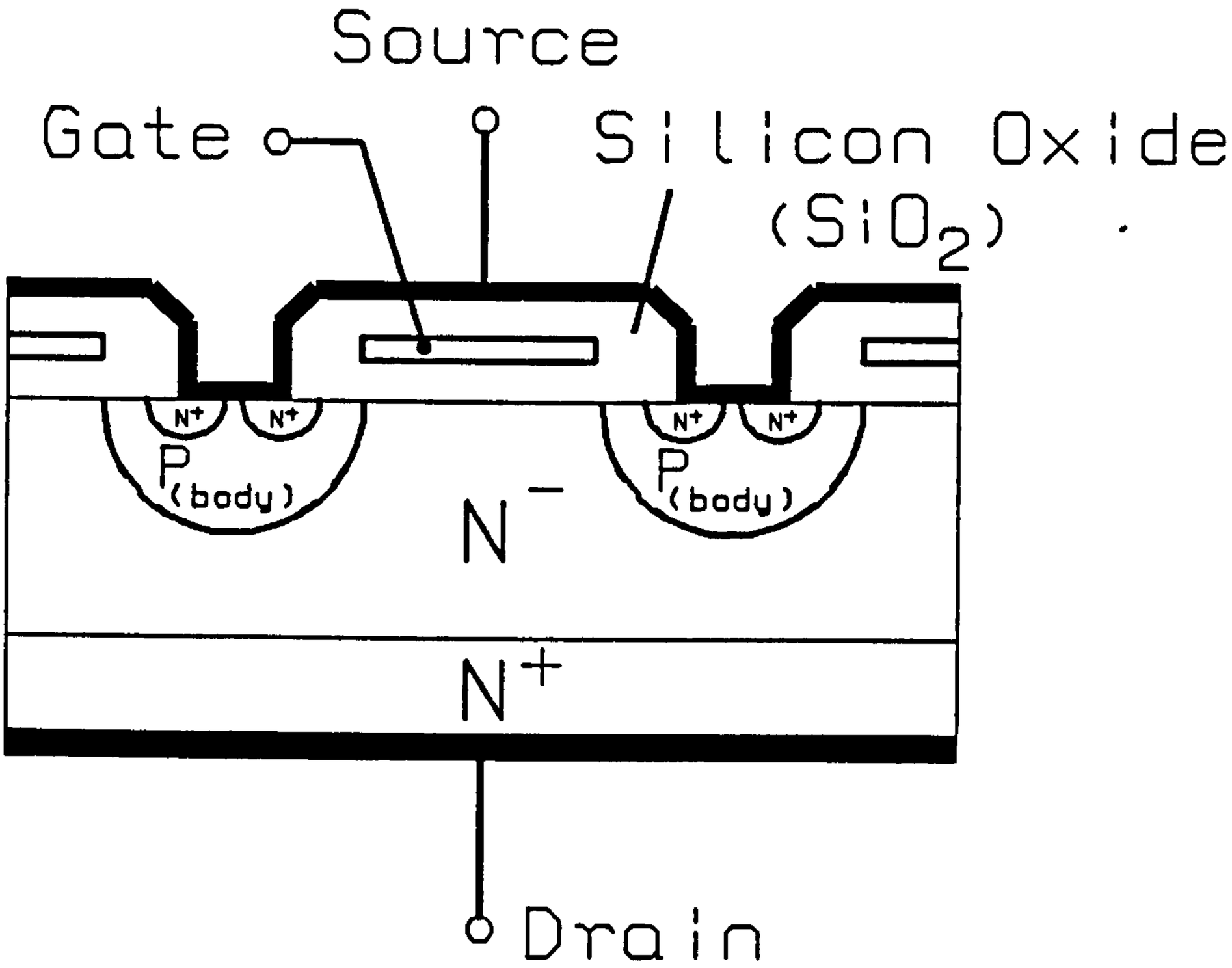

Figure 4.4 Basic N-channel MOSFET cross-sectional structure

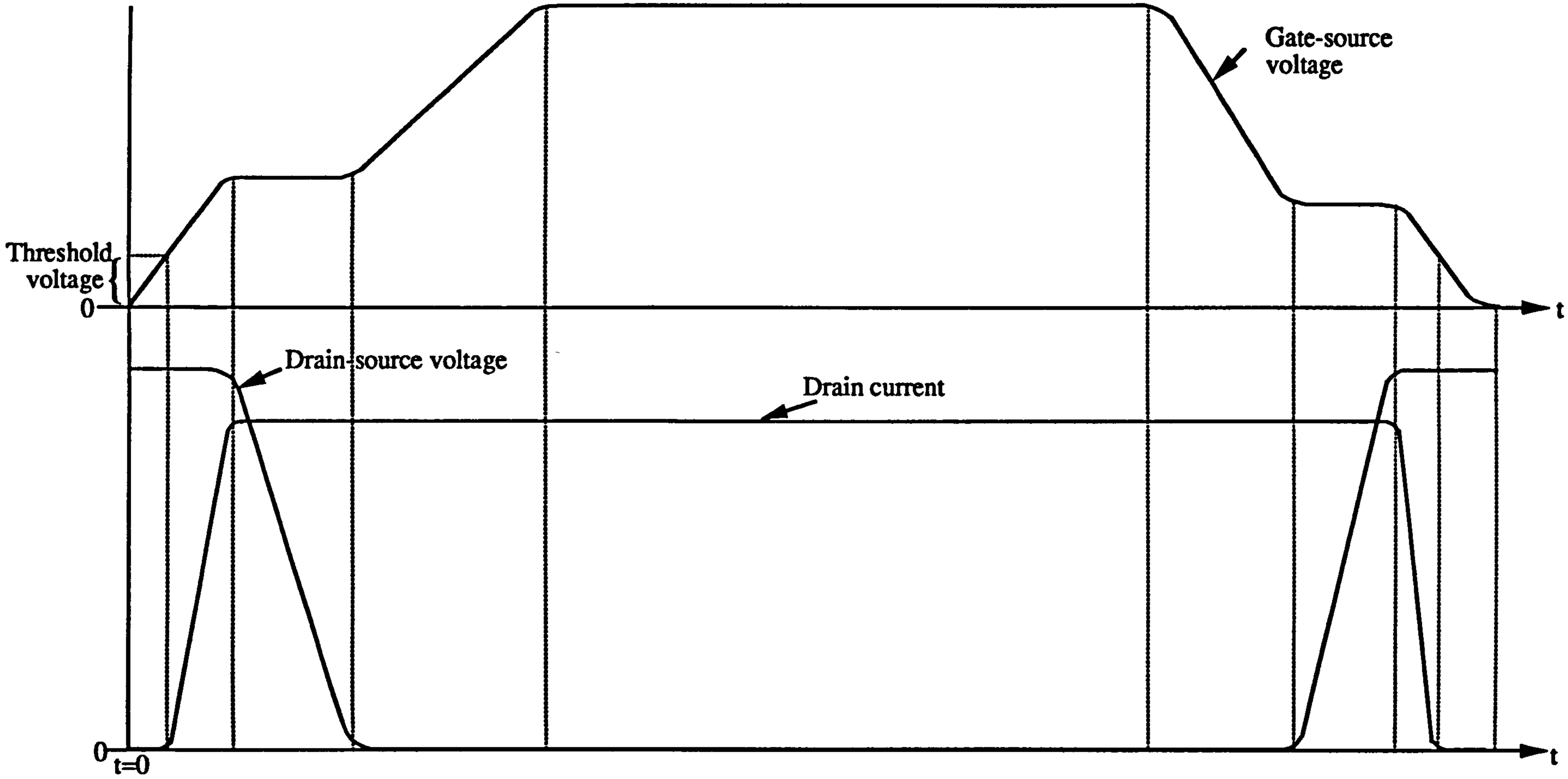

Figure 4.5 Switching waveforms for a MOSFET

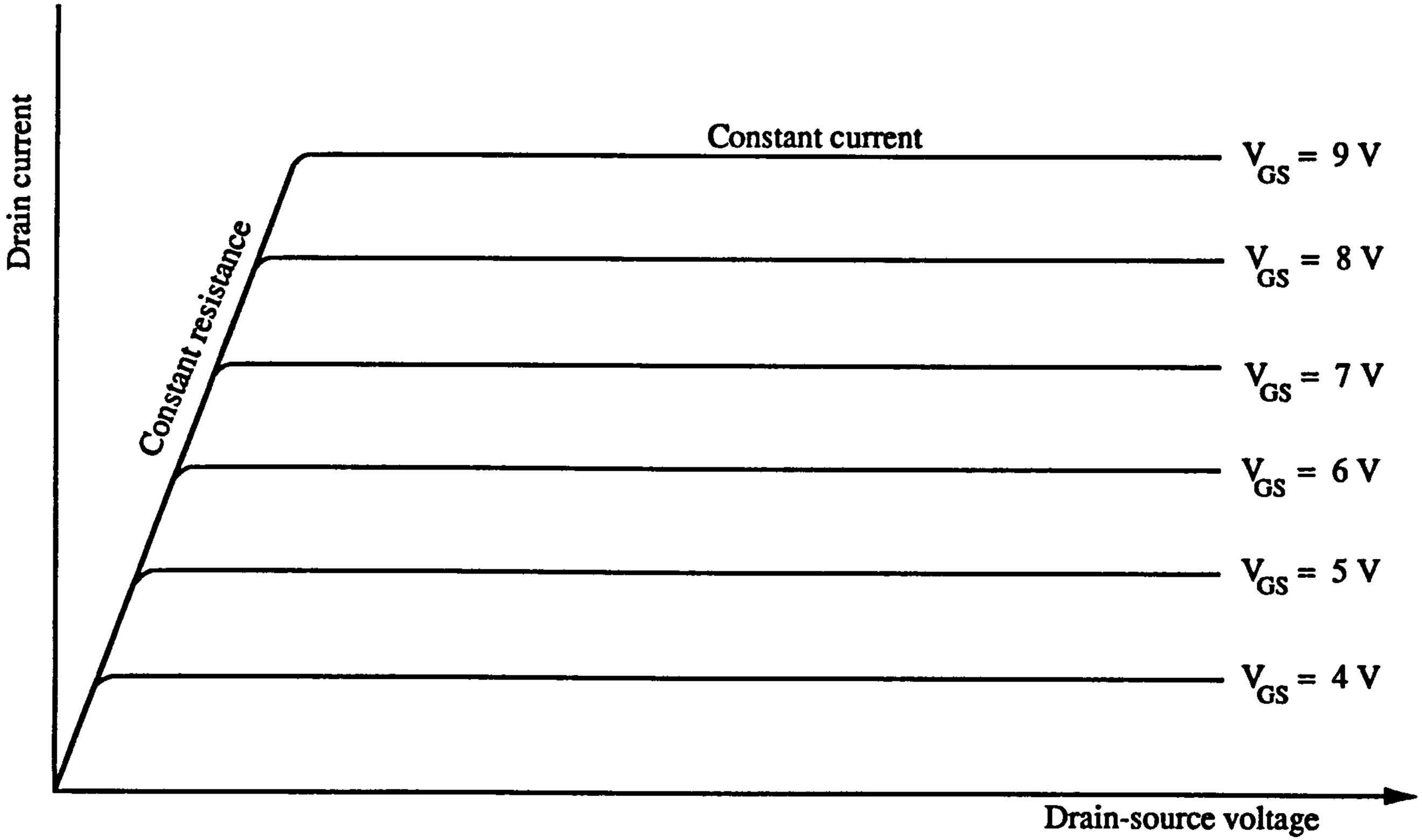

Figure 4.6 Idealized output characteristics of MOSFET

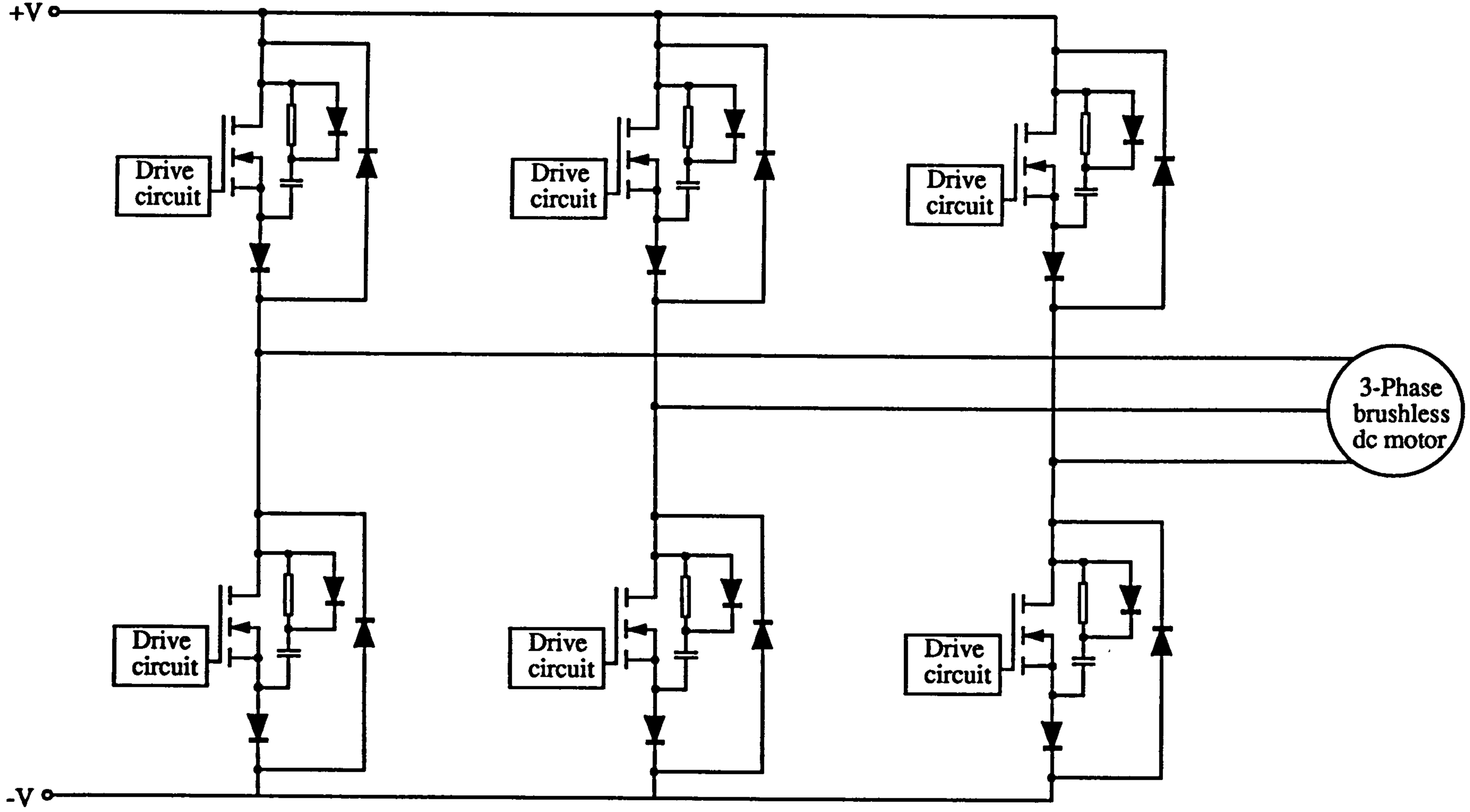

Figure 4.7 Block diagram of the power MOSFET inverter

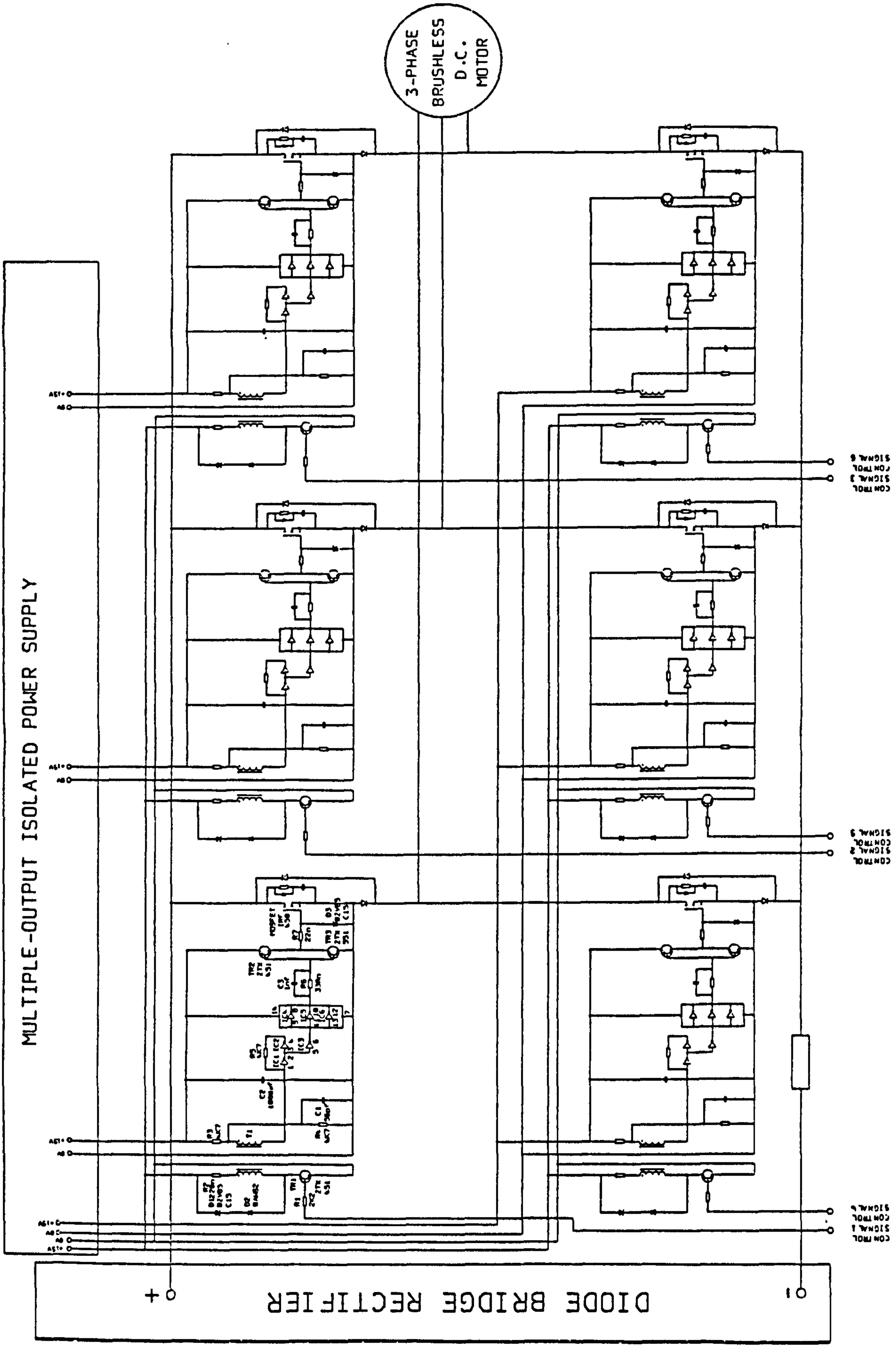

Figure 4.8 Inverter board

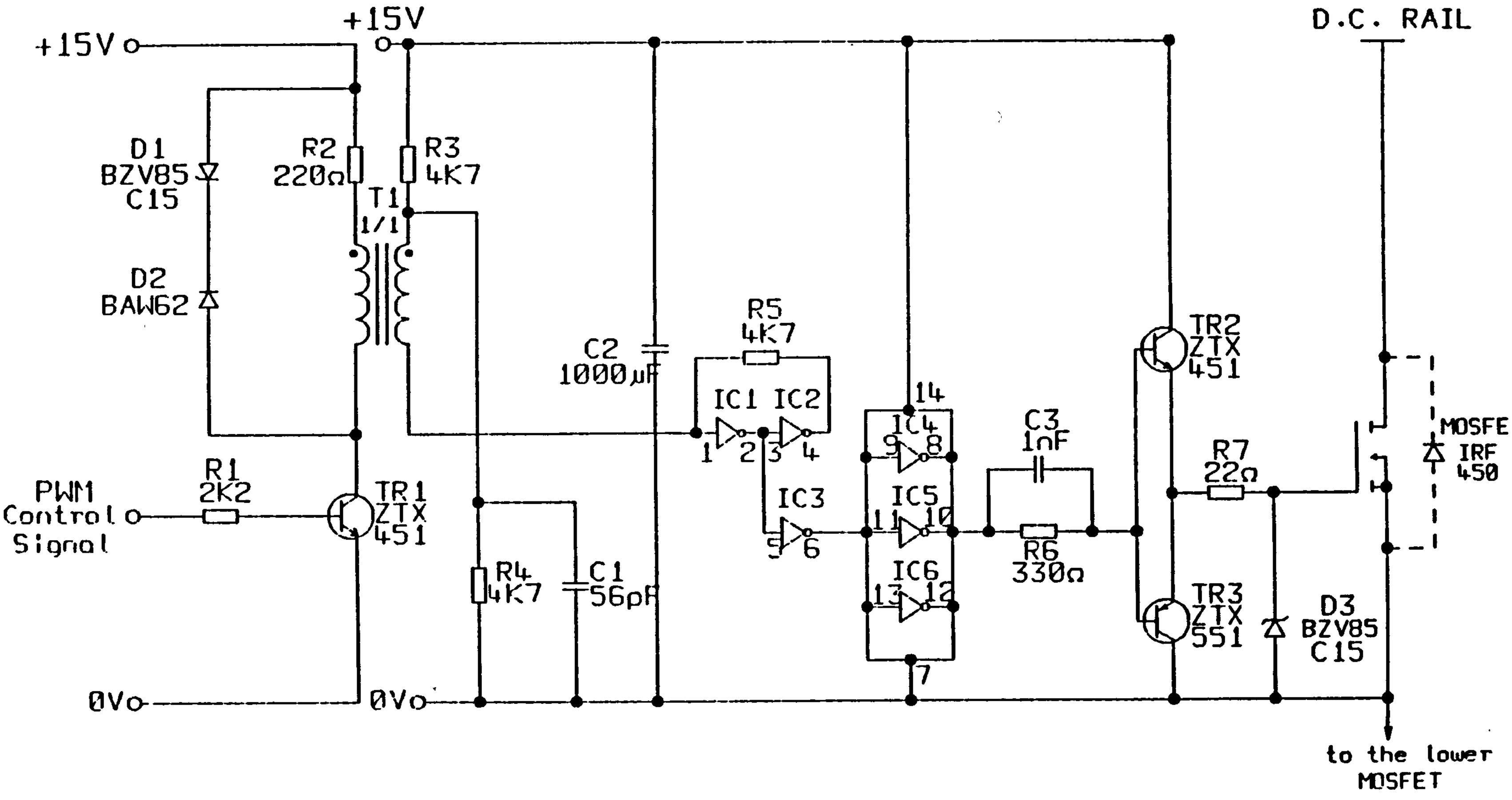

Figure 4.9 MOSFET drive circuit

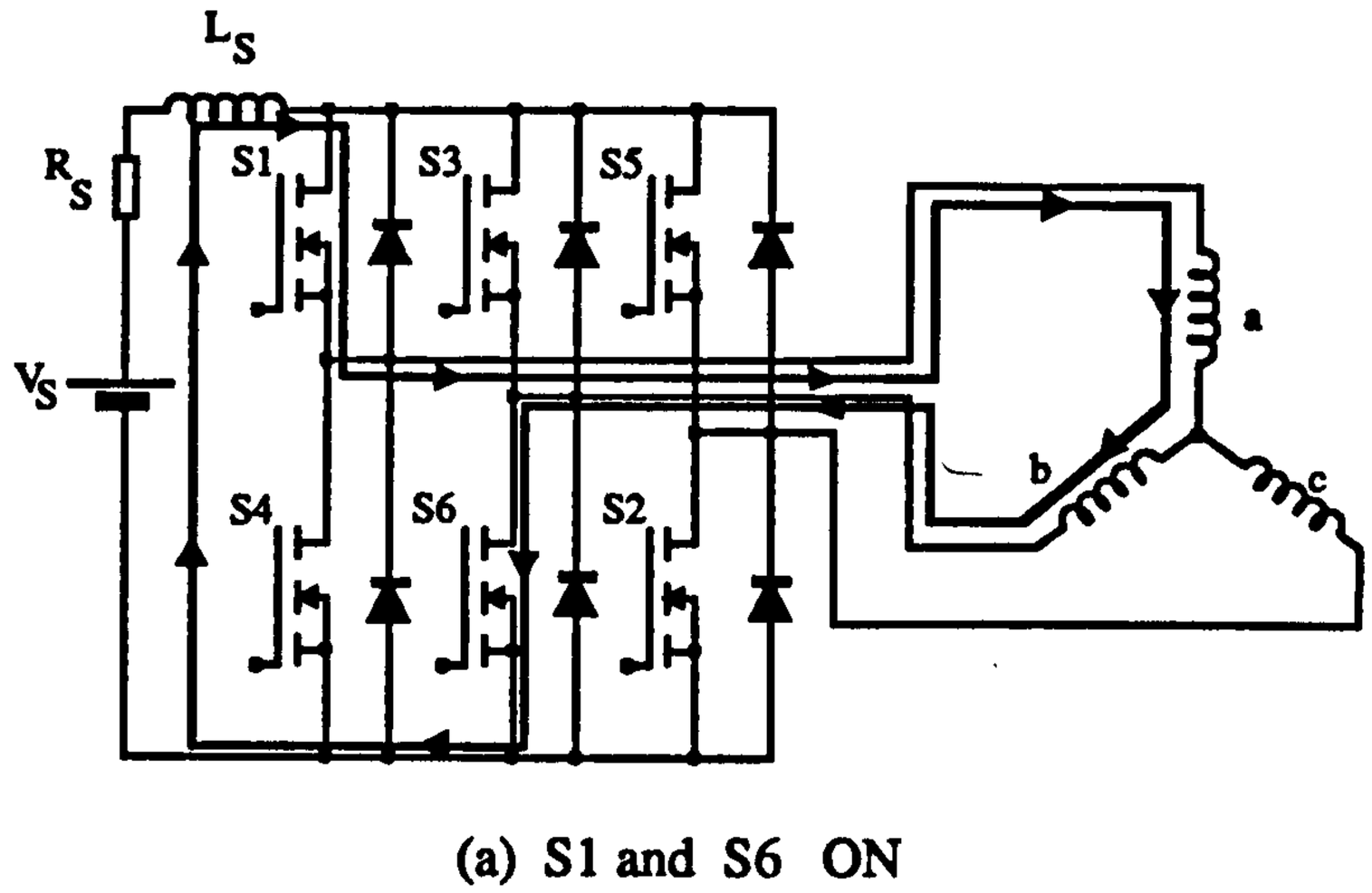

(a) S1 and S6 ON

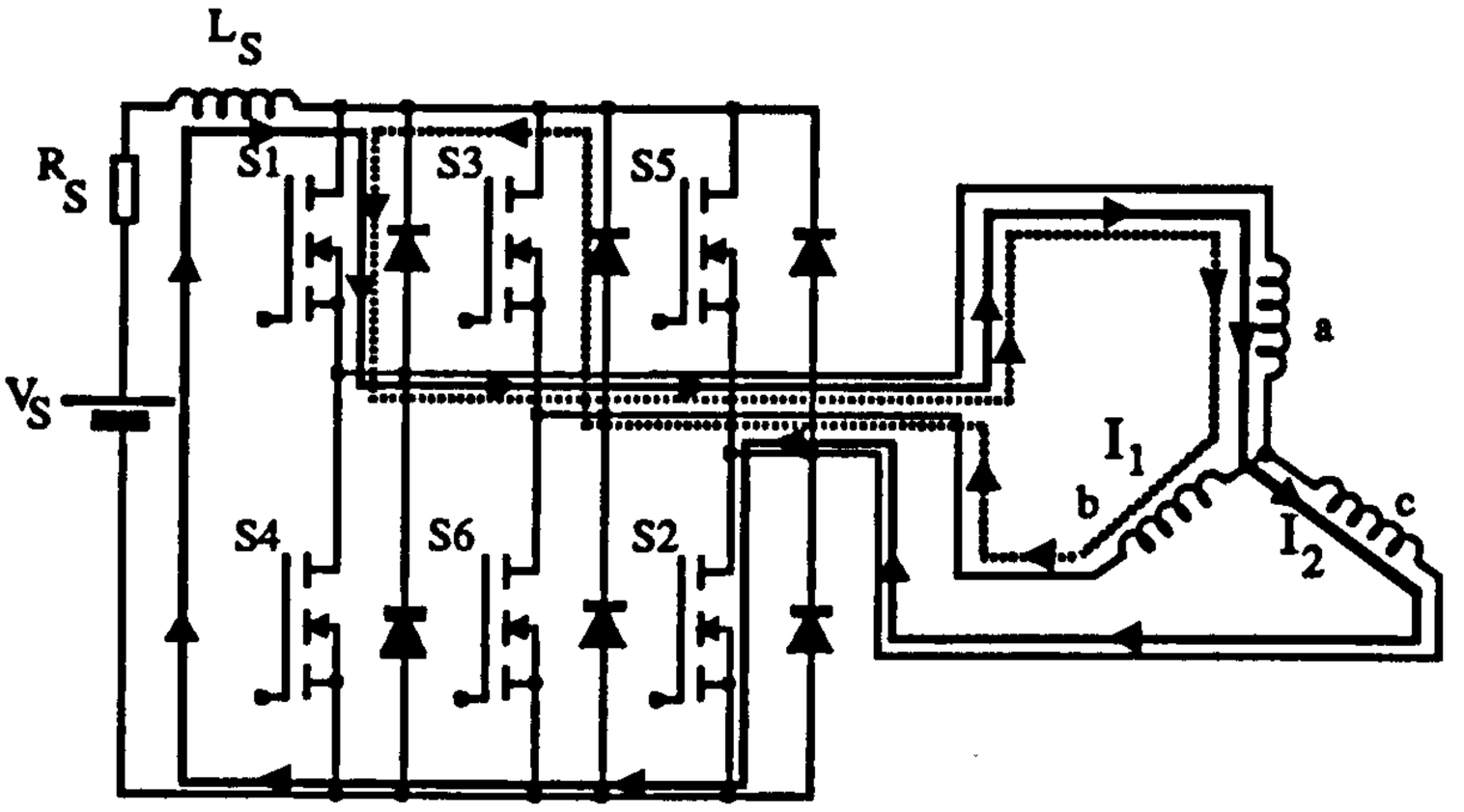

(b) S1 , S2 and D3 ON

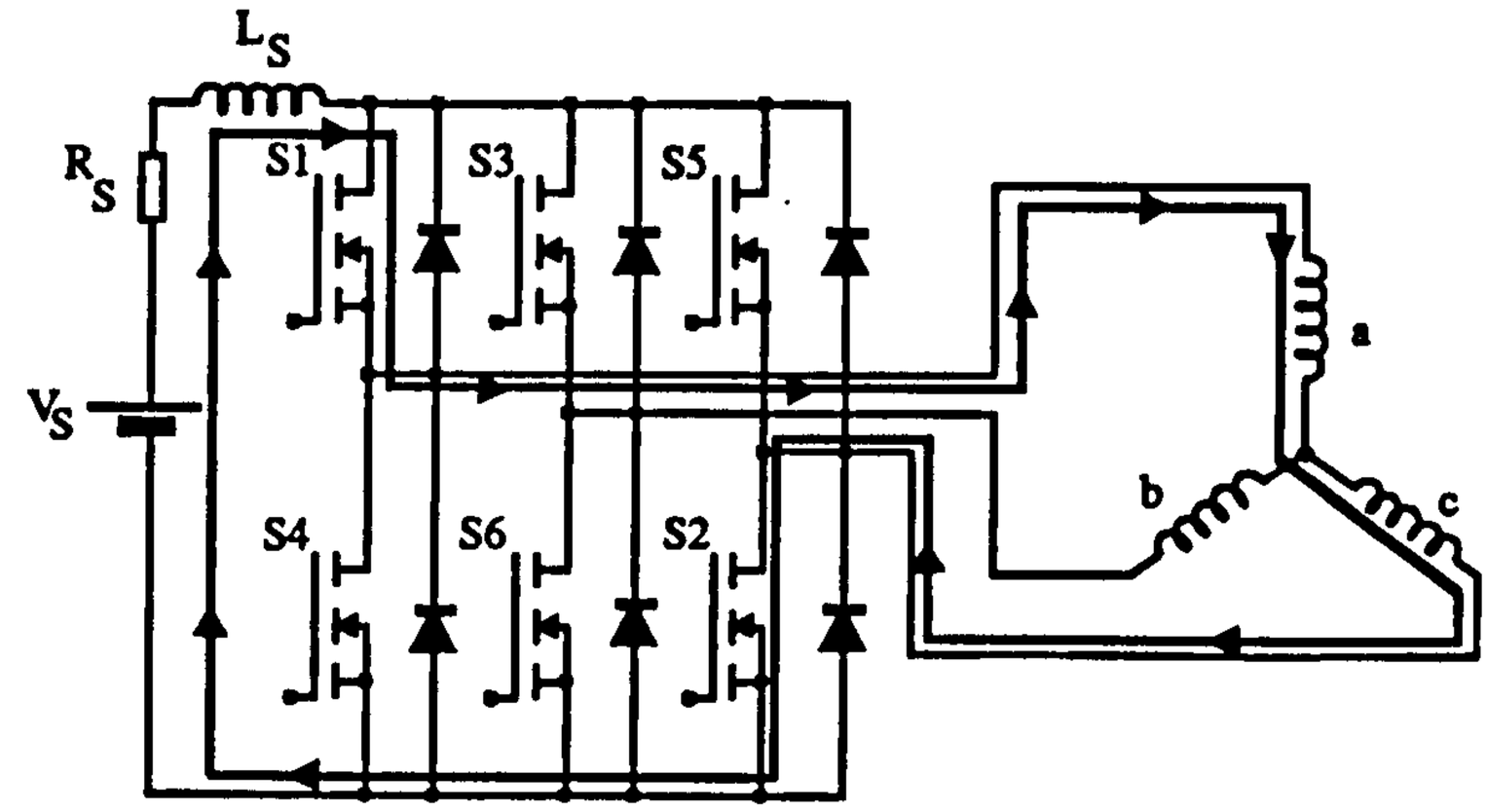

(c) S1 and S2 ON

Figure 4.10 Free-wheeling diode operation

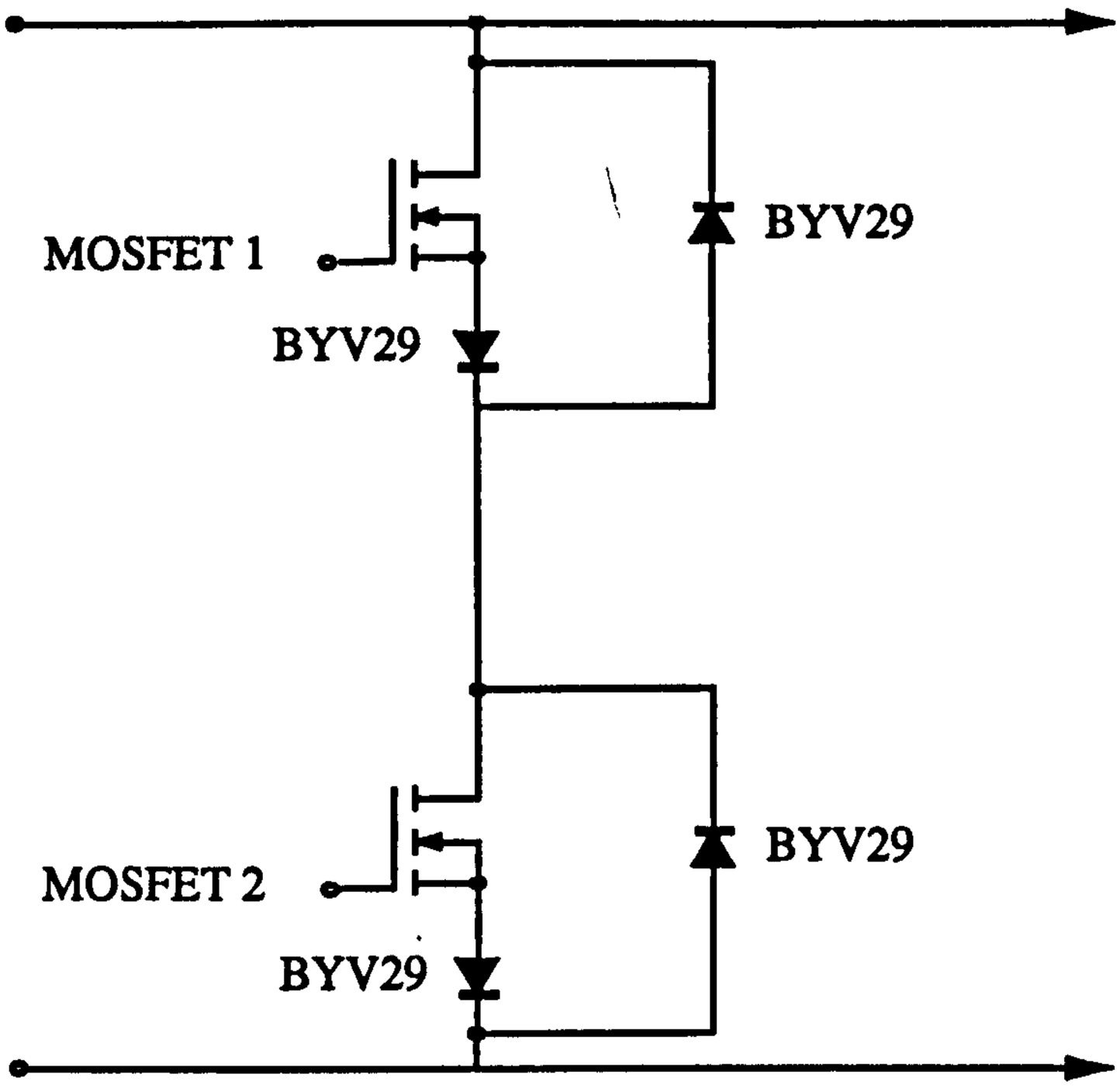

Figure 4.11 MOSFETs with external free wheeling-diodes

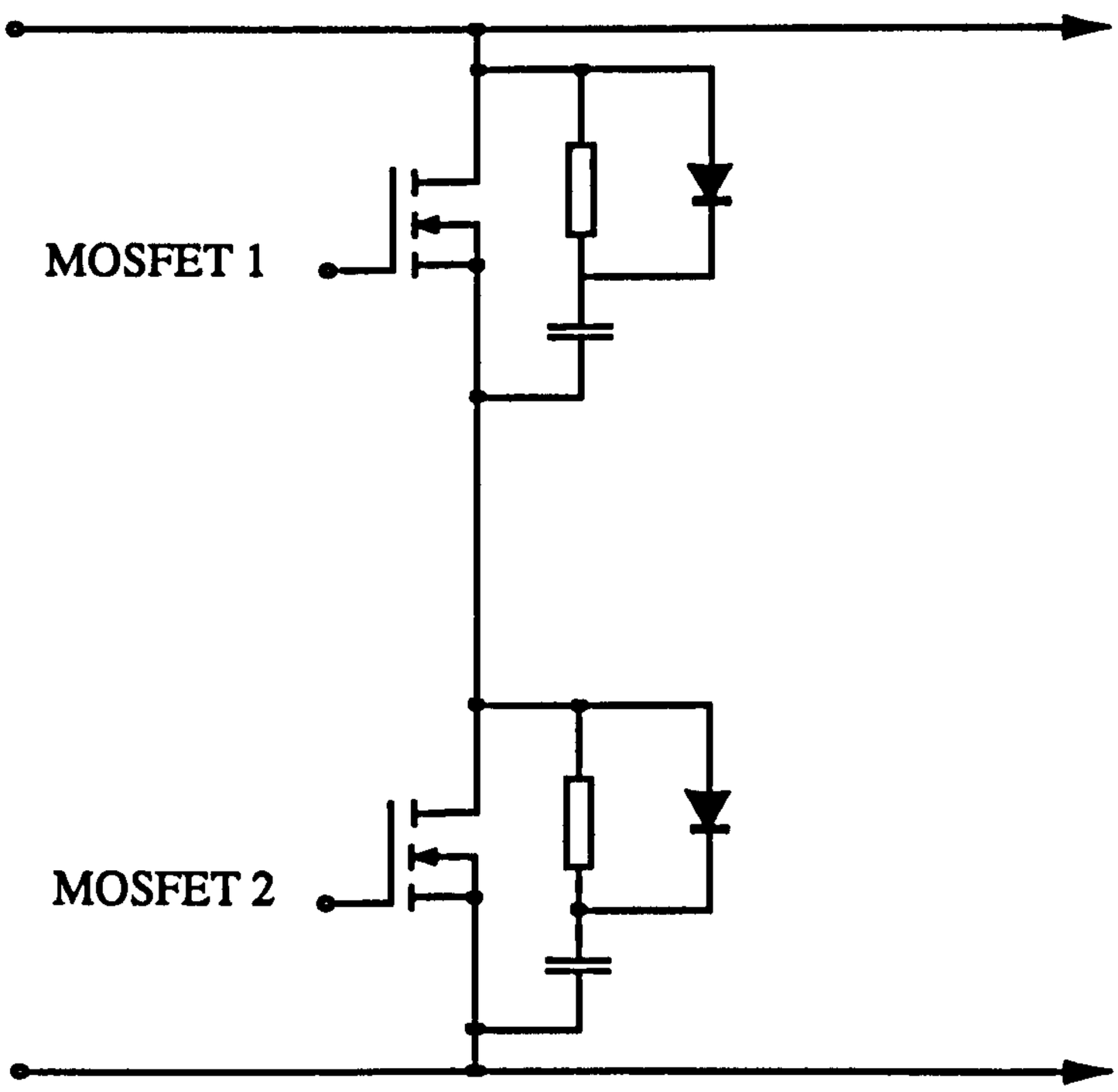

Figure 4.12 MOSFETs with snubber circuits

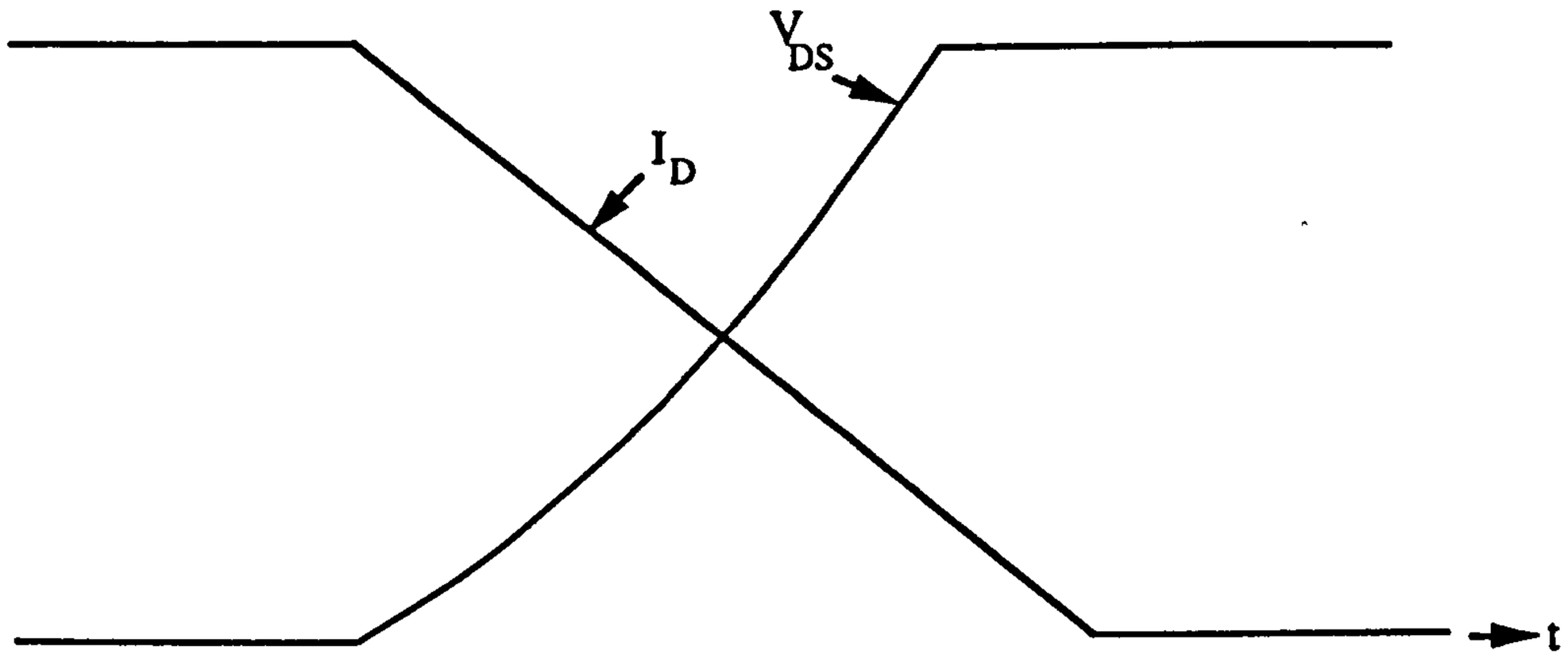

(a)

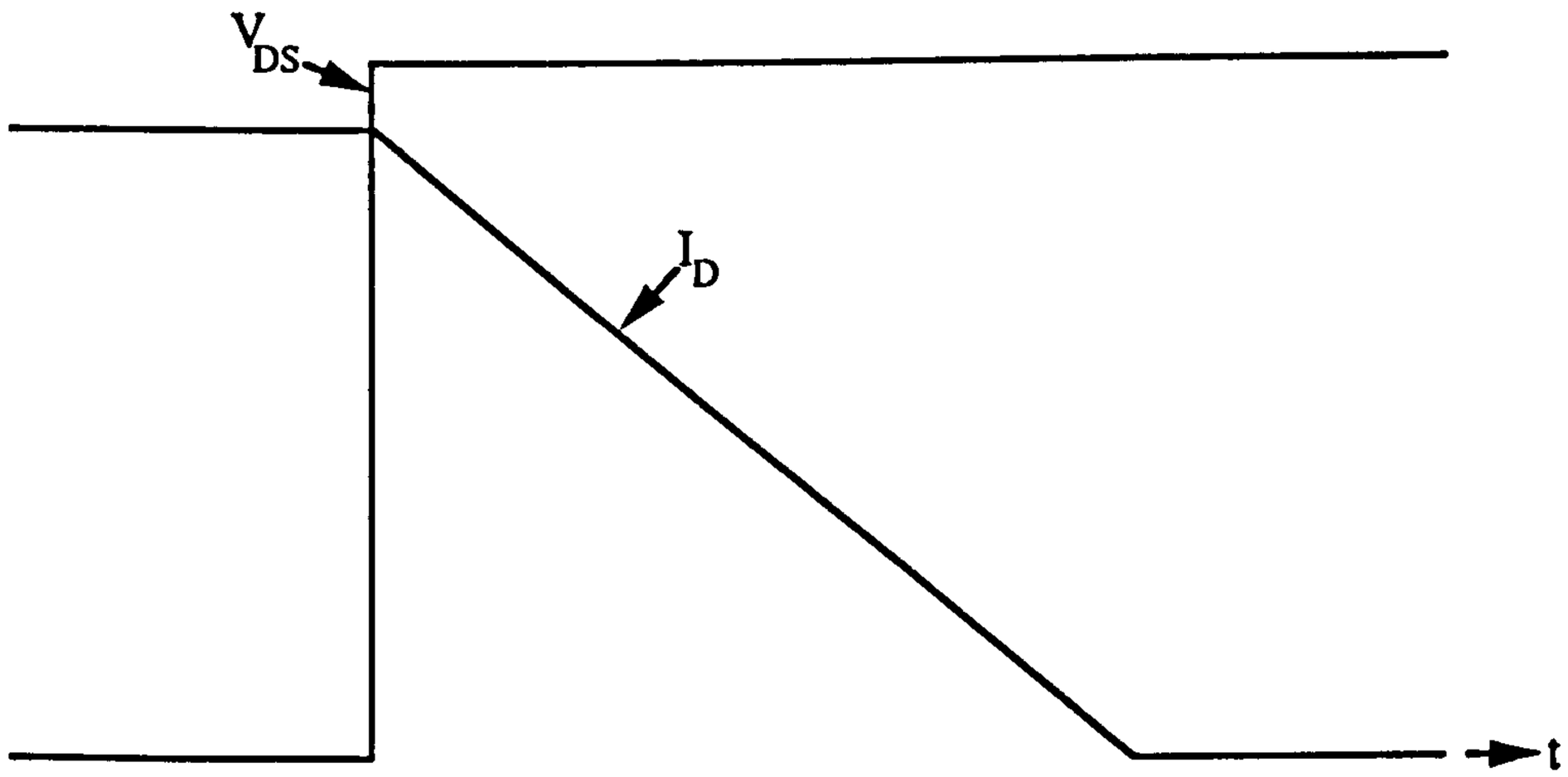

(b)

Figure 4.13 MOSFET turn-off waveforms (a) with snubber circuit (b) without snubber circuit

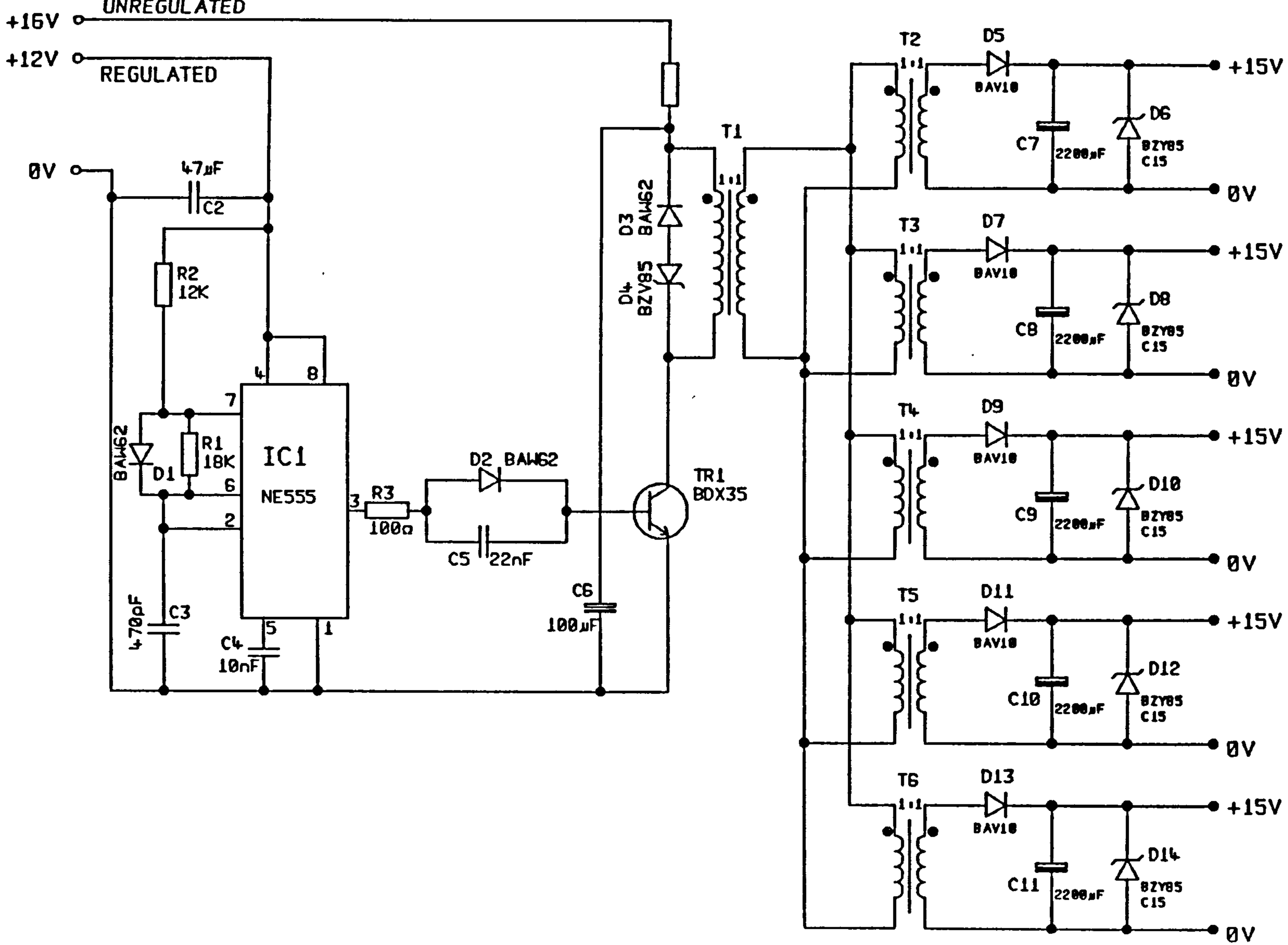

Figure 4.14 Multiple-output isolated power supply

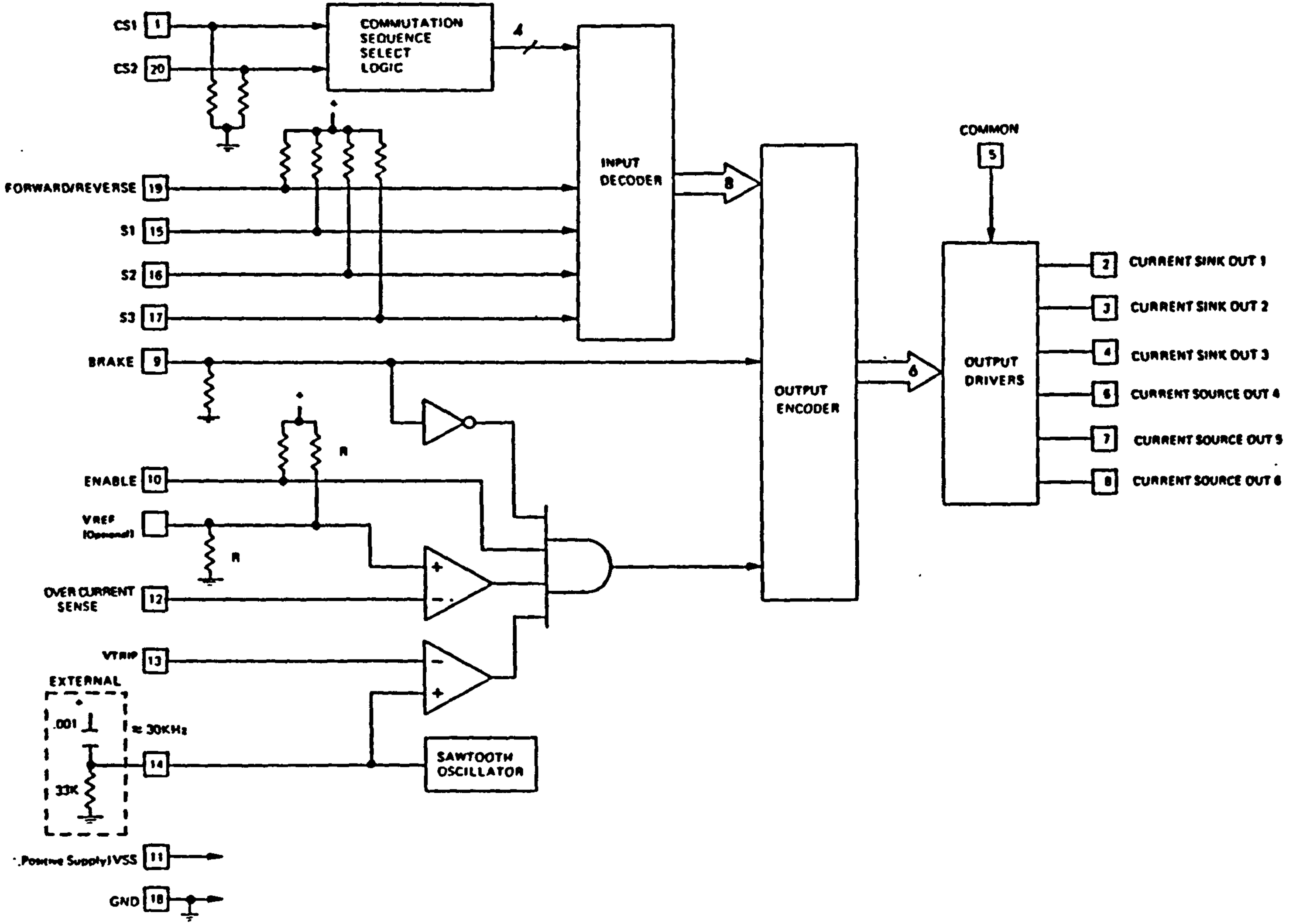

Figure 4.15 LS7261 block diagram

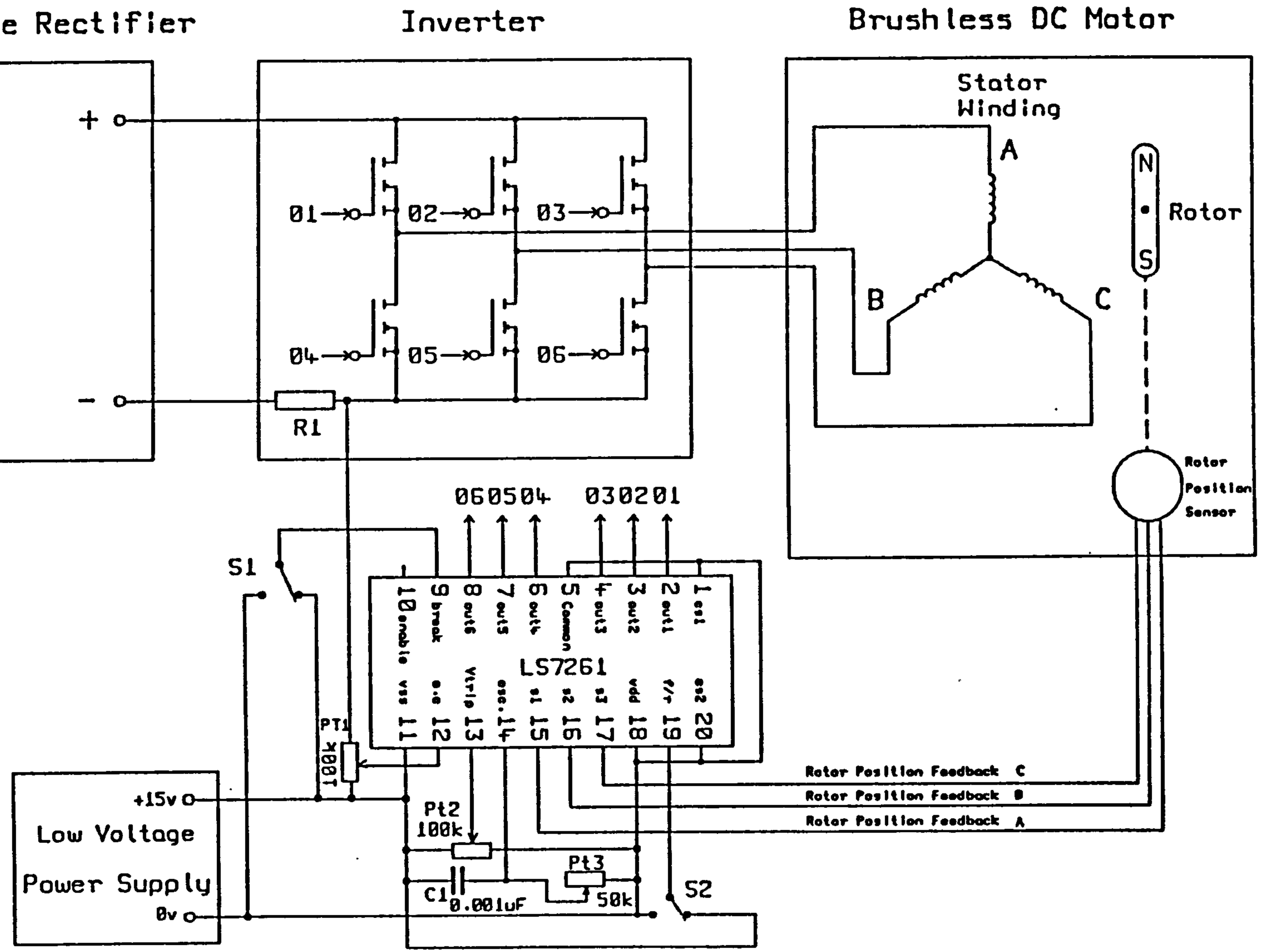

Figure 4.16 LS7261 interfacing configuration

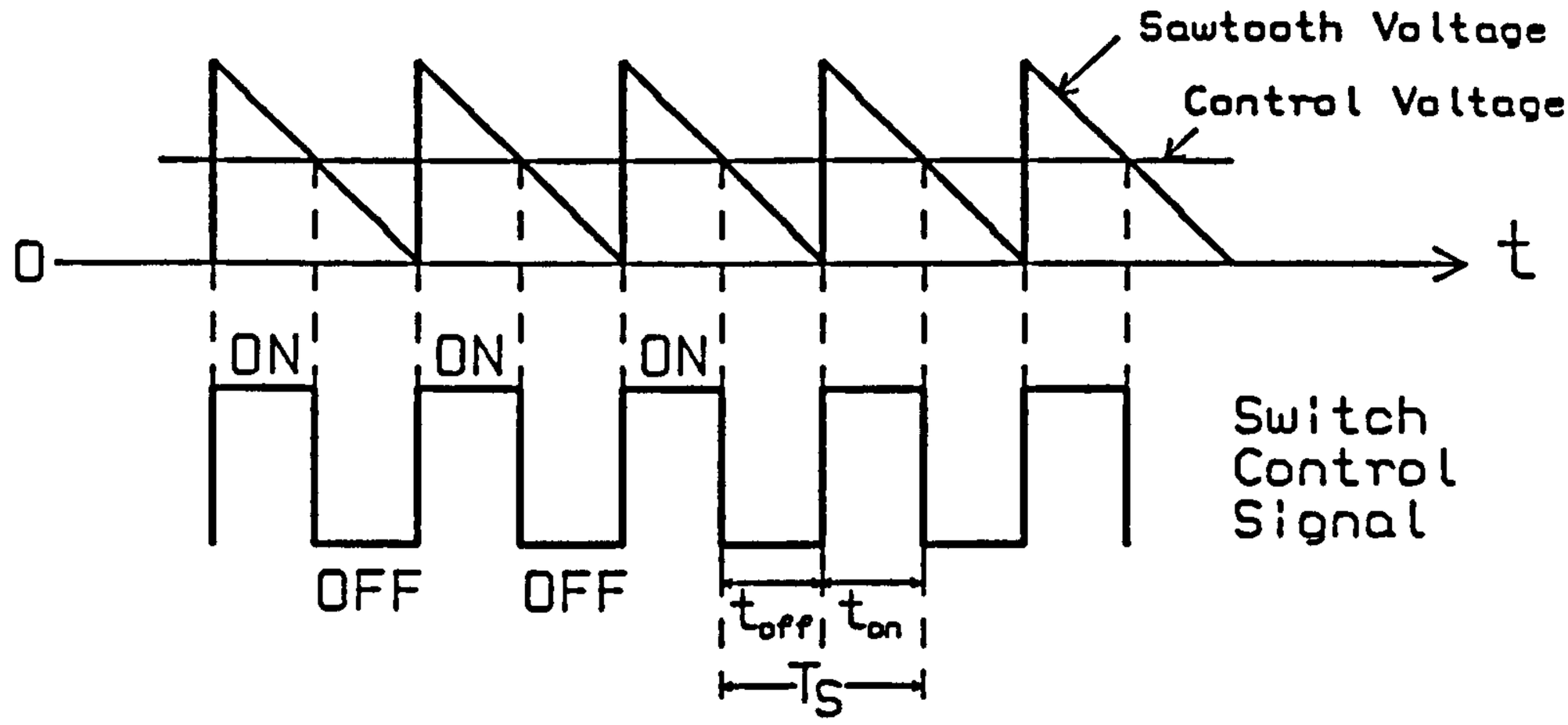

(a)

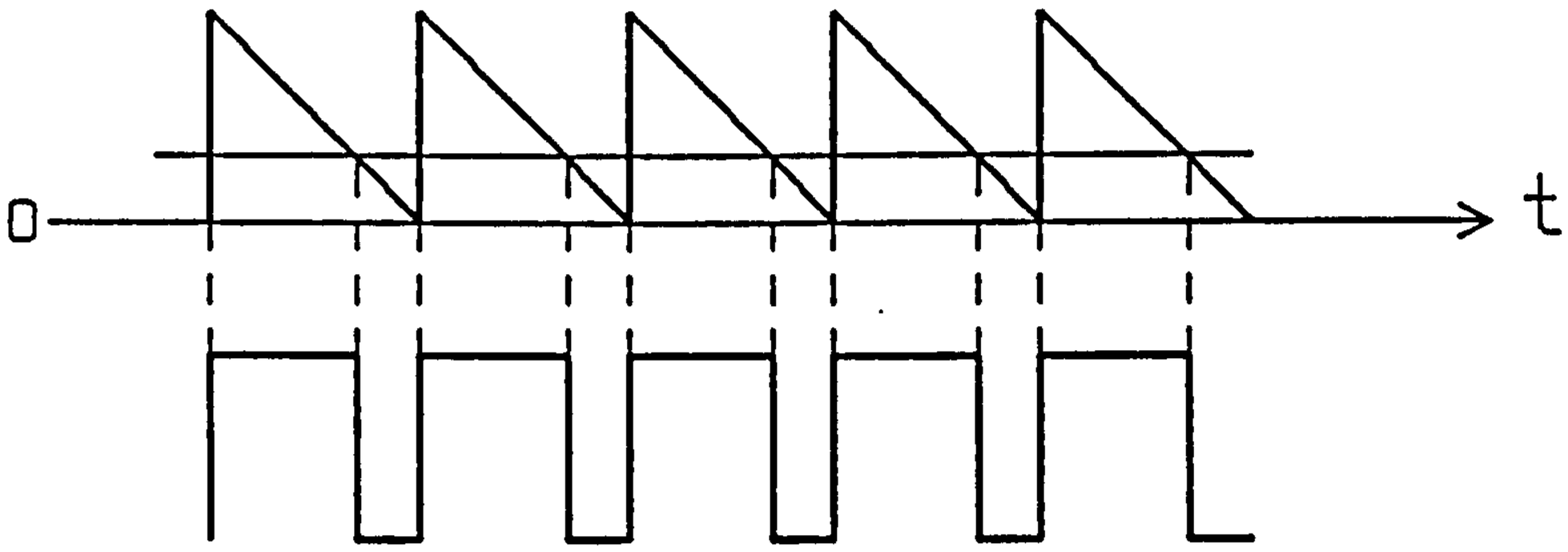

(b)

Figure 4.17 Modulation behaviour (a) with a high control voltage (b) with a low control voltage

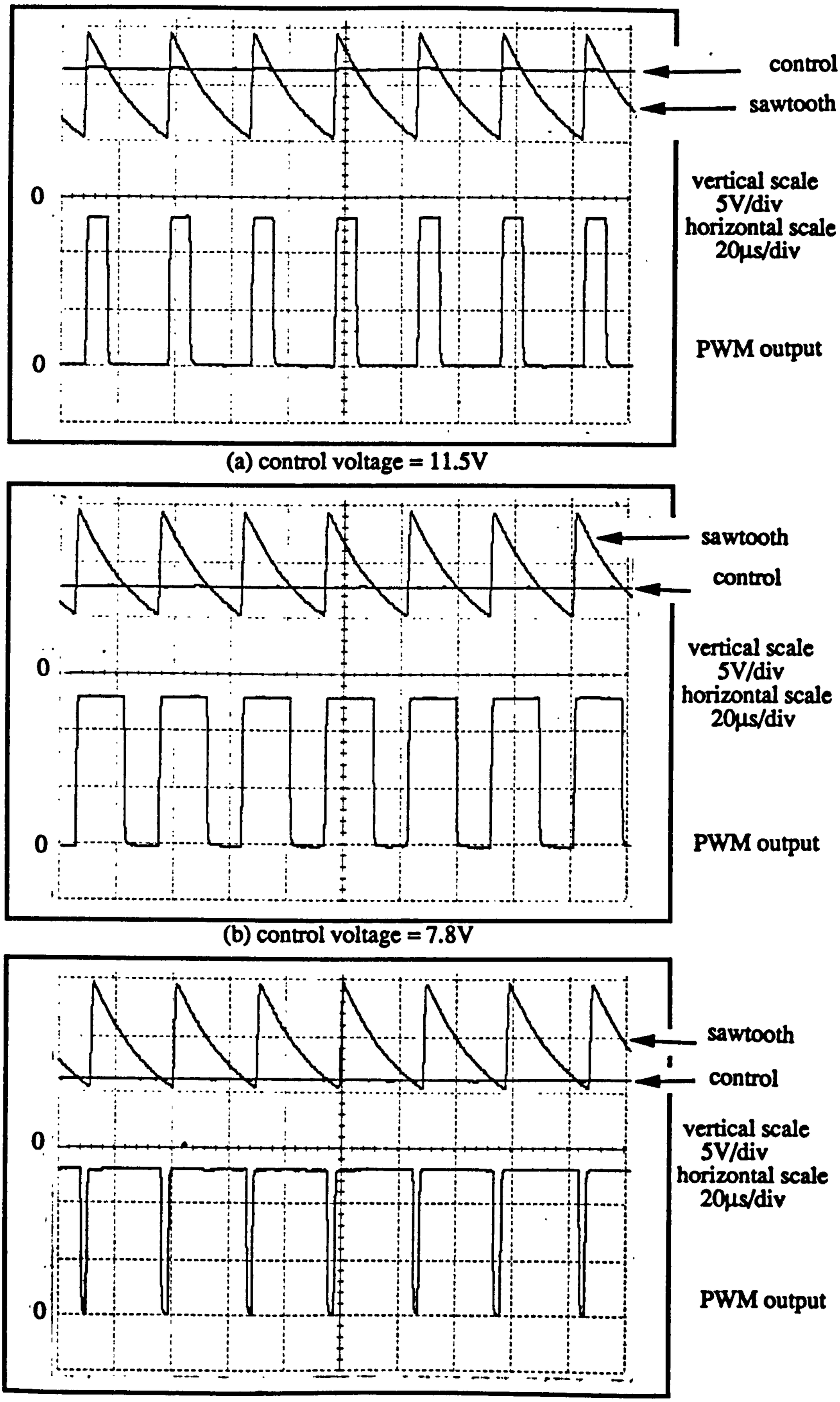

(a) control voltage = 11.5V

(b) control voltage = 7.8V

(c) control voltage = 6V

Figure 4.18 Modulation behaviour with different control voltage levels

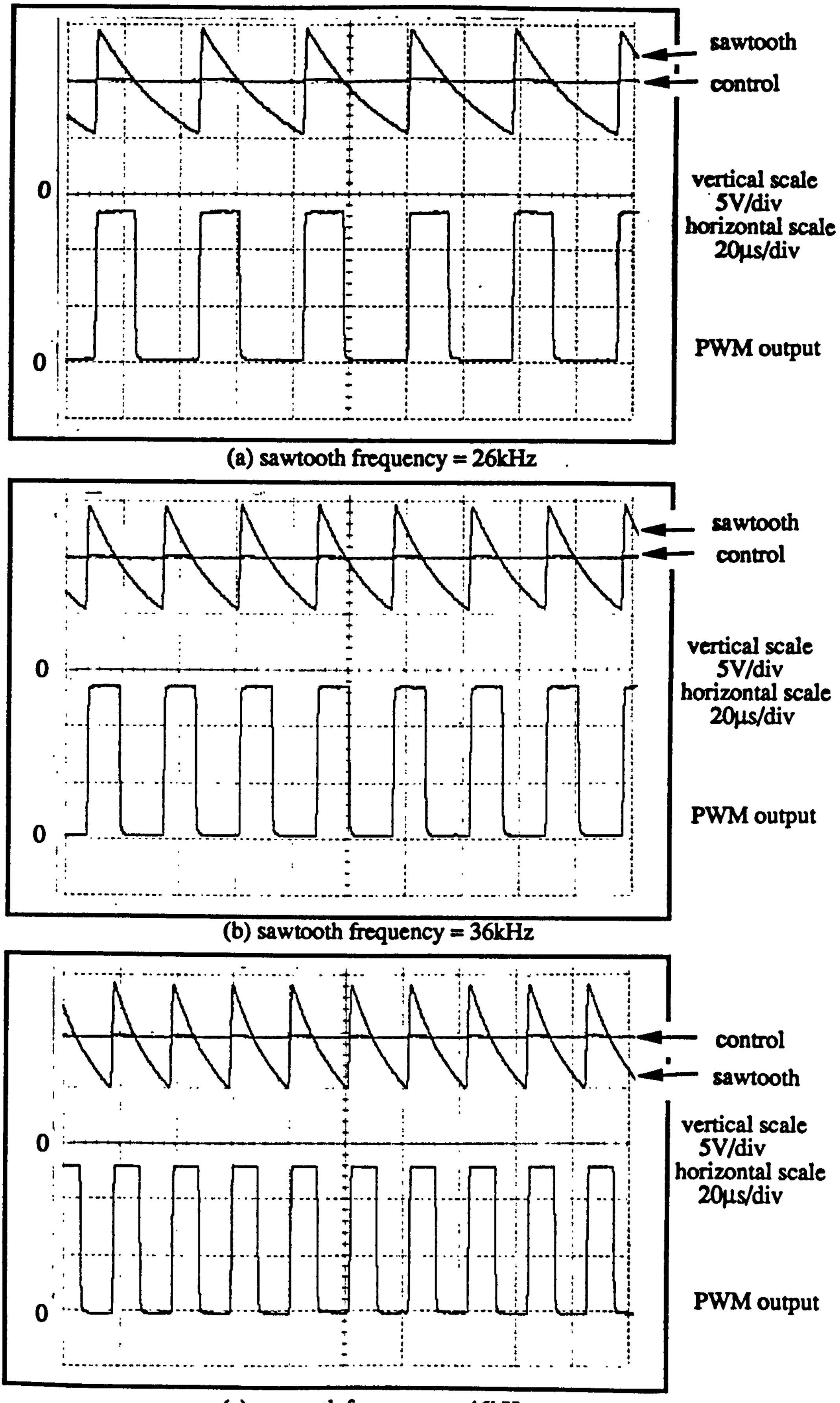

Figure 4.19 Modulation behaviour with different sawtooth frequencies

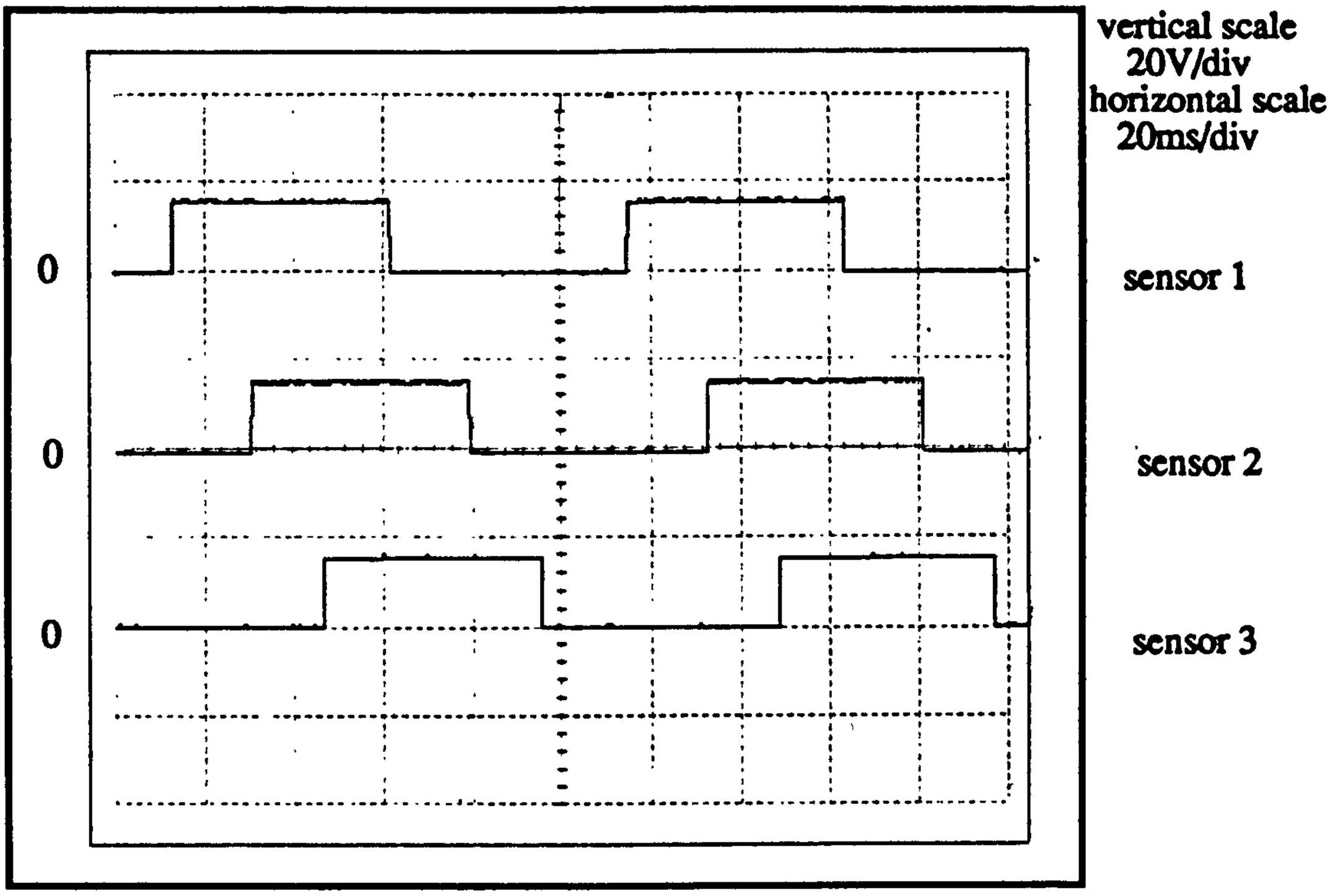

(a) speed = 200 rpm

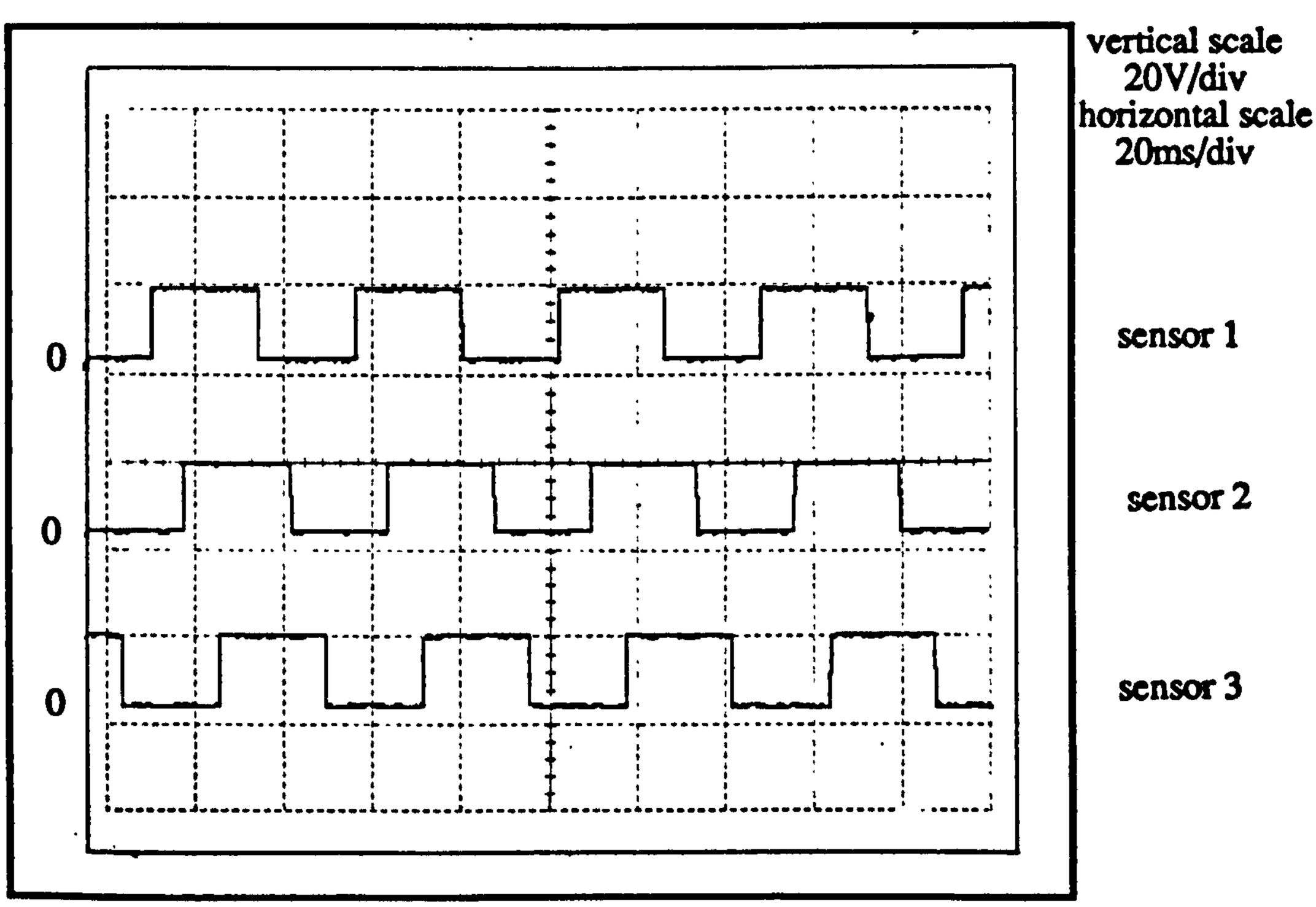

(b) speed = 425 rpm

Figure 4.20 Rotor-position sensor signals at different speeds

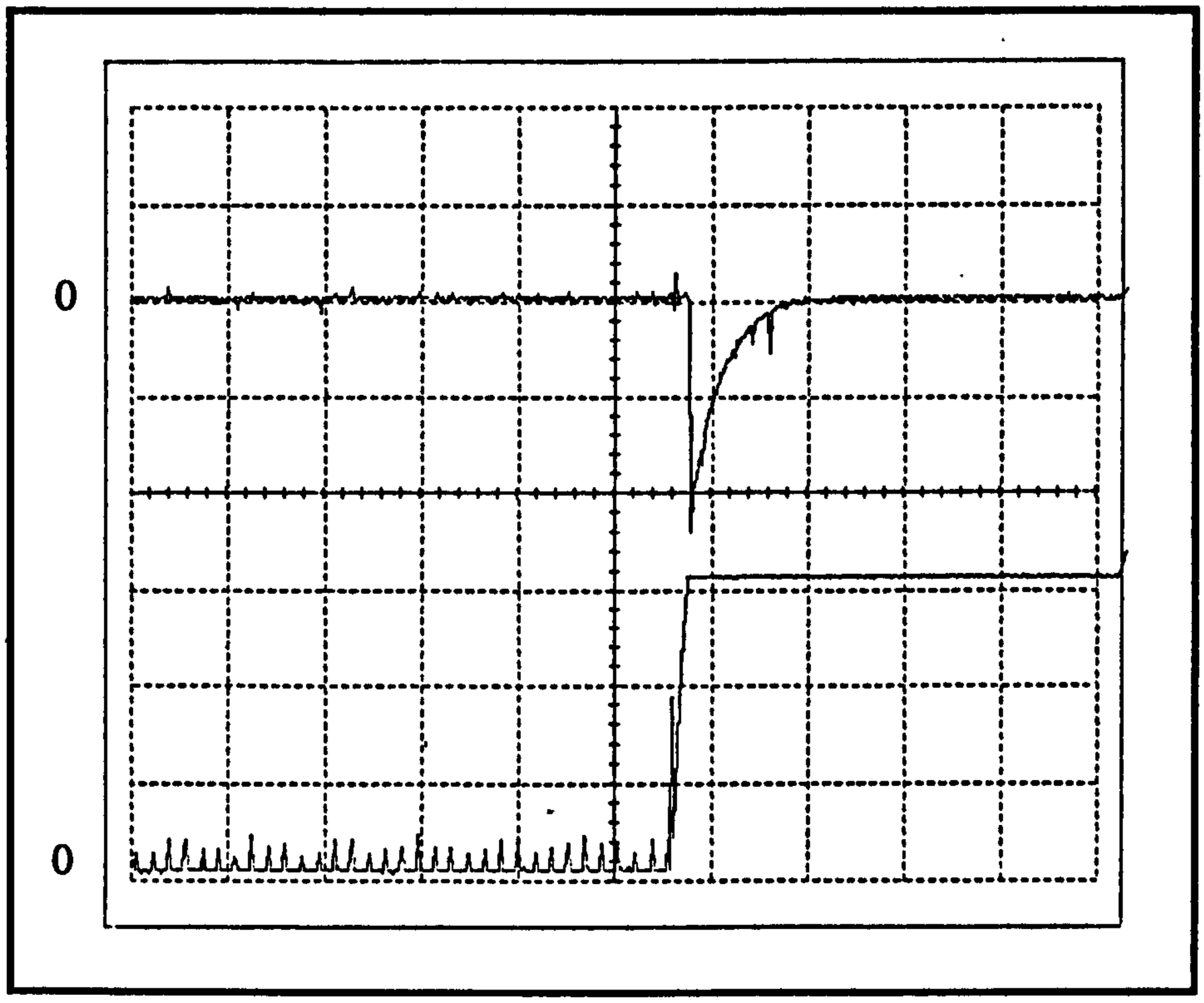

Figure 4.21 Free-wheeling diode (D6) current and power MOSFET (S3) drain-source voltage waveforms

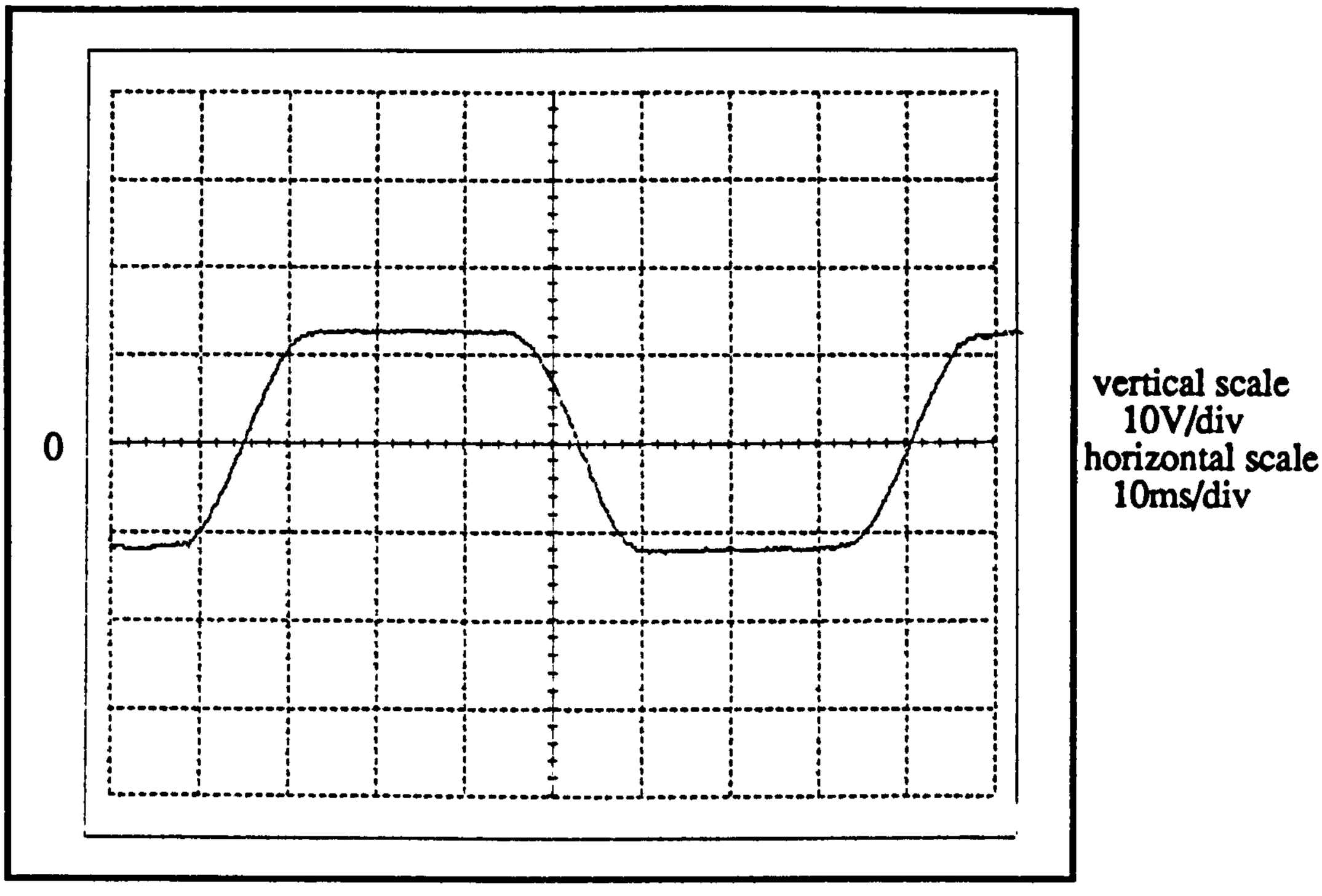

(a) speed = 265 rpm

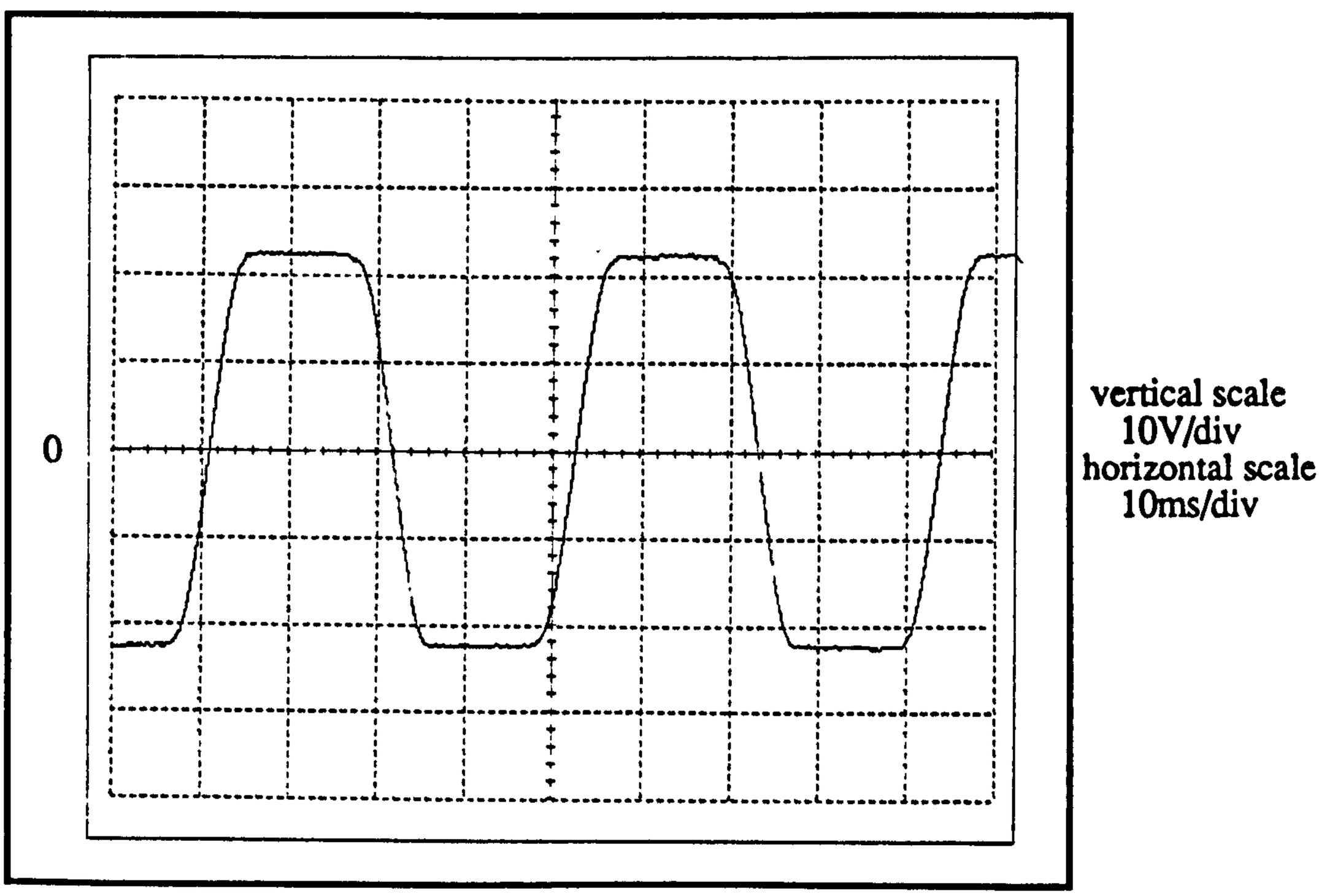

(b) speed = 500 rpm

Figure 4.22 Generated phase emf waveforms for different speeds (No-load condition)

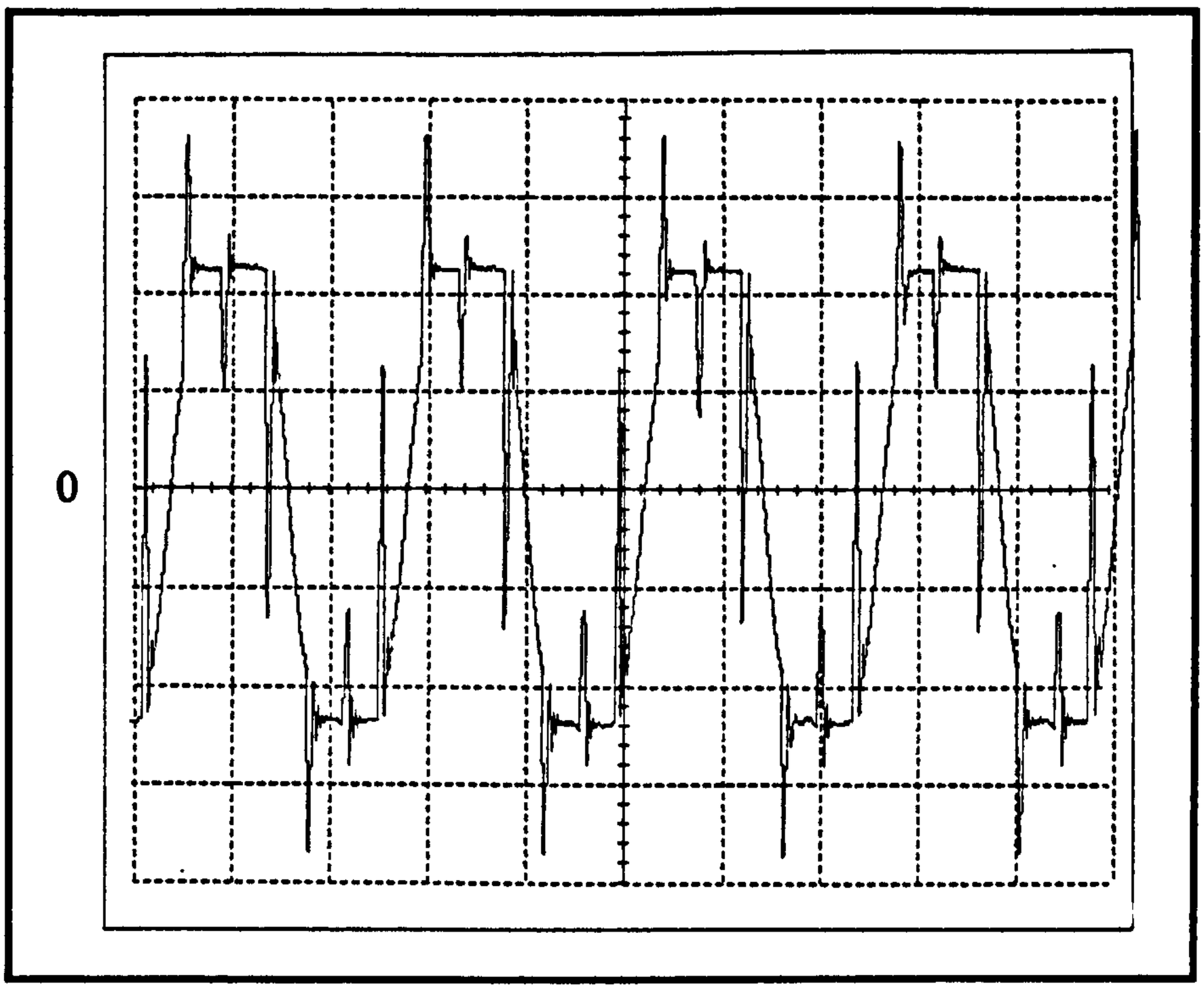

(a) phase voltage

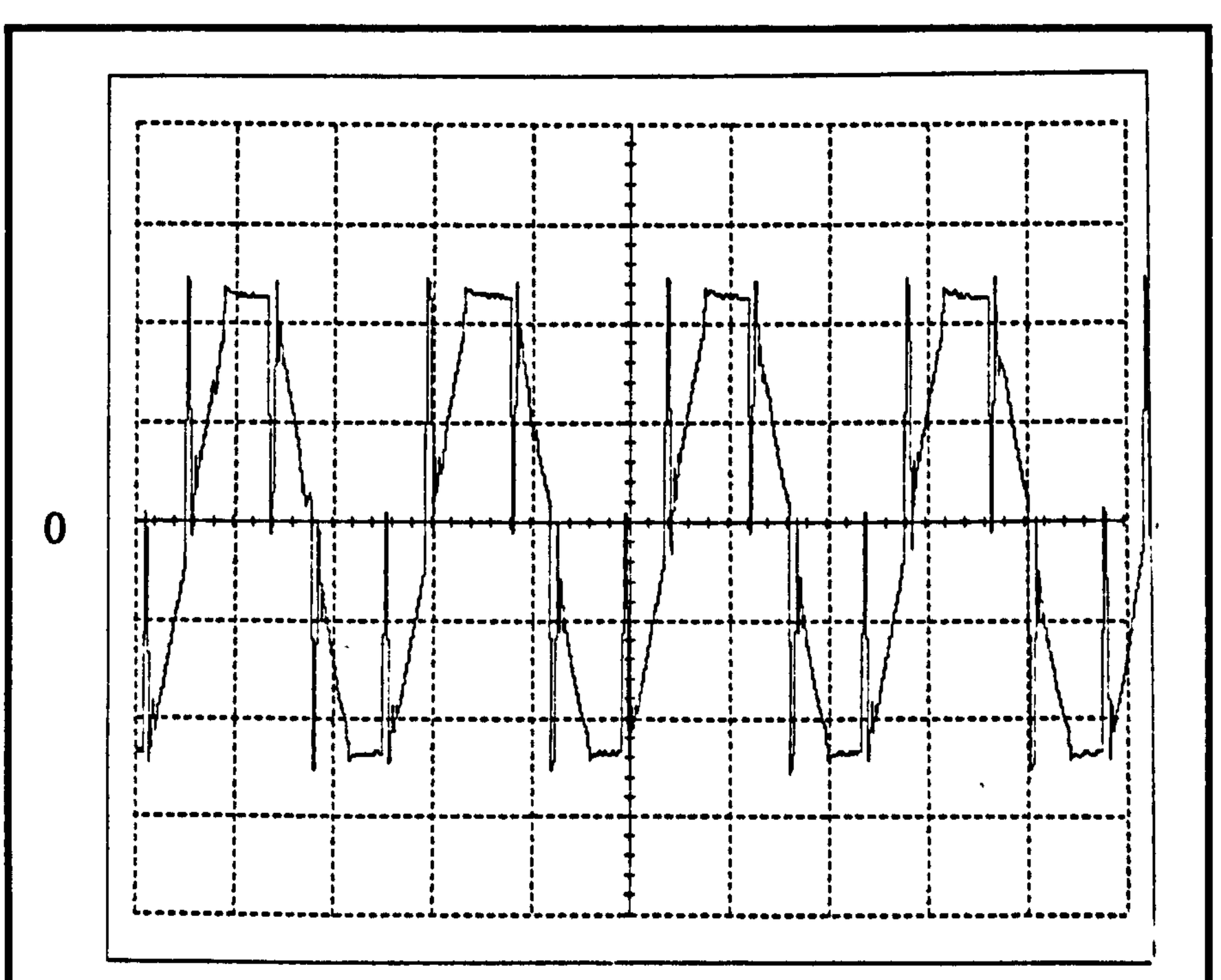

(b) line voltage

Figure 4.23 Phase and line voltage waveforms without PWM control (Load condition : 1.6Nm at 420rpm)

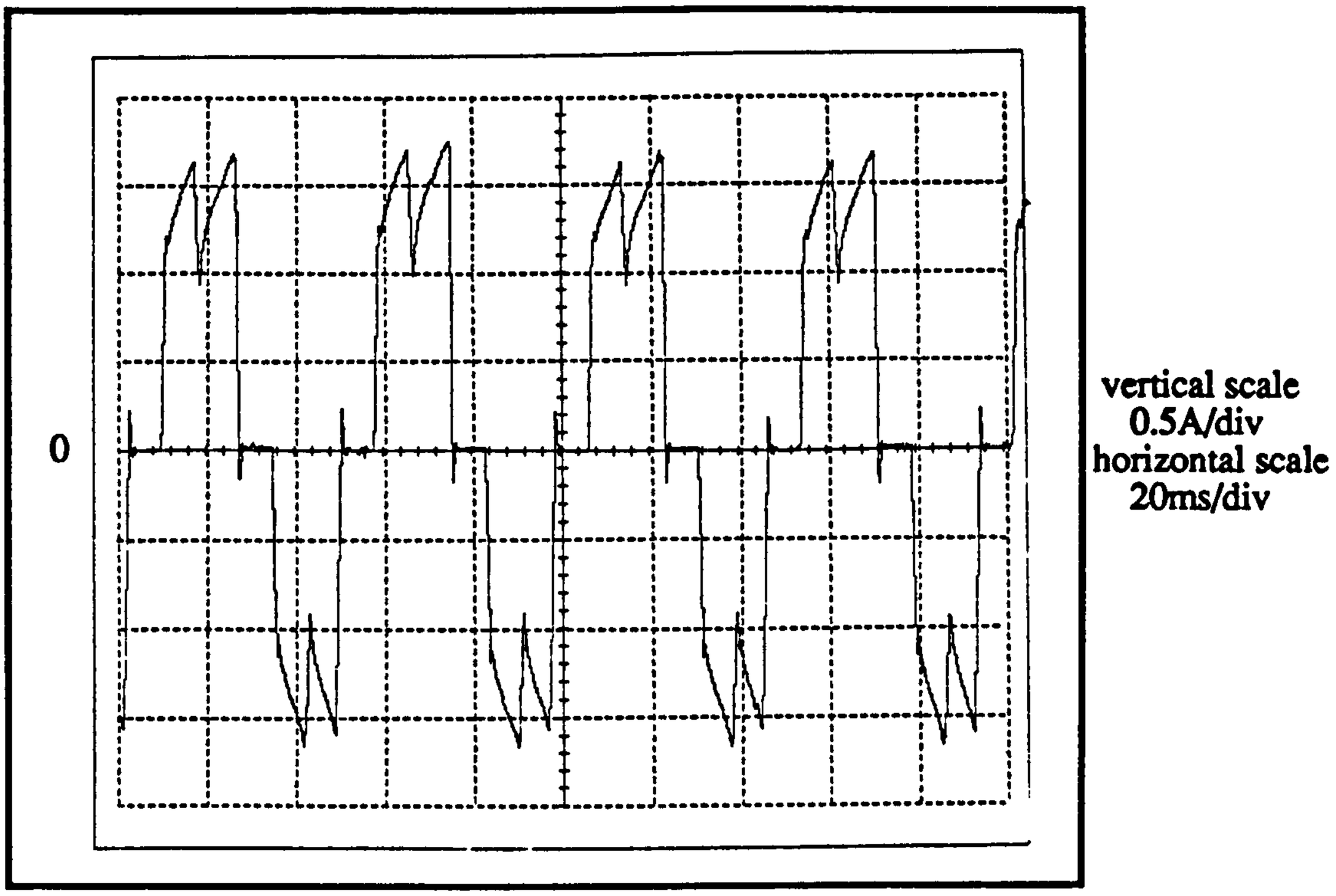

Figure 4.24 Phase current waveform without PWM control
(Load condition : 1.6Nm at 420rpm)

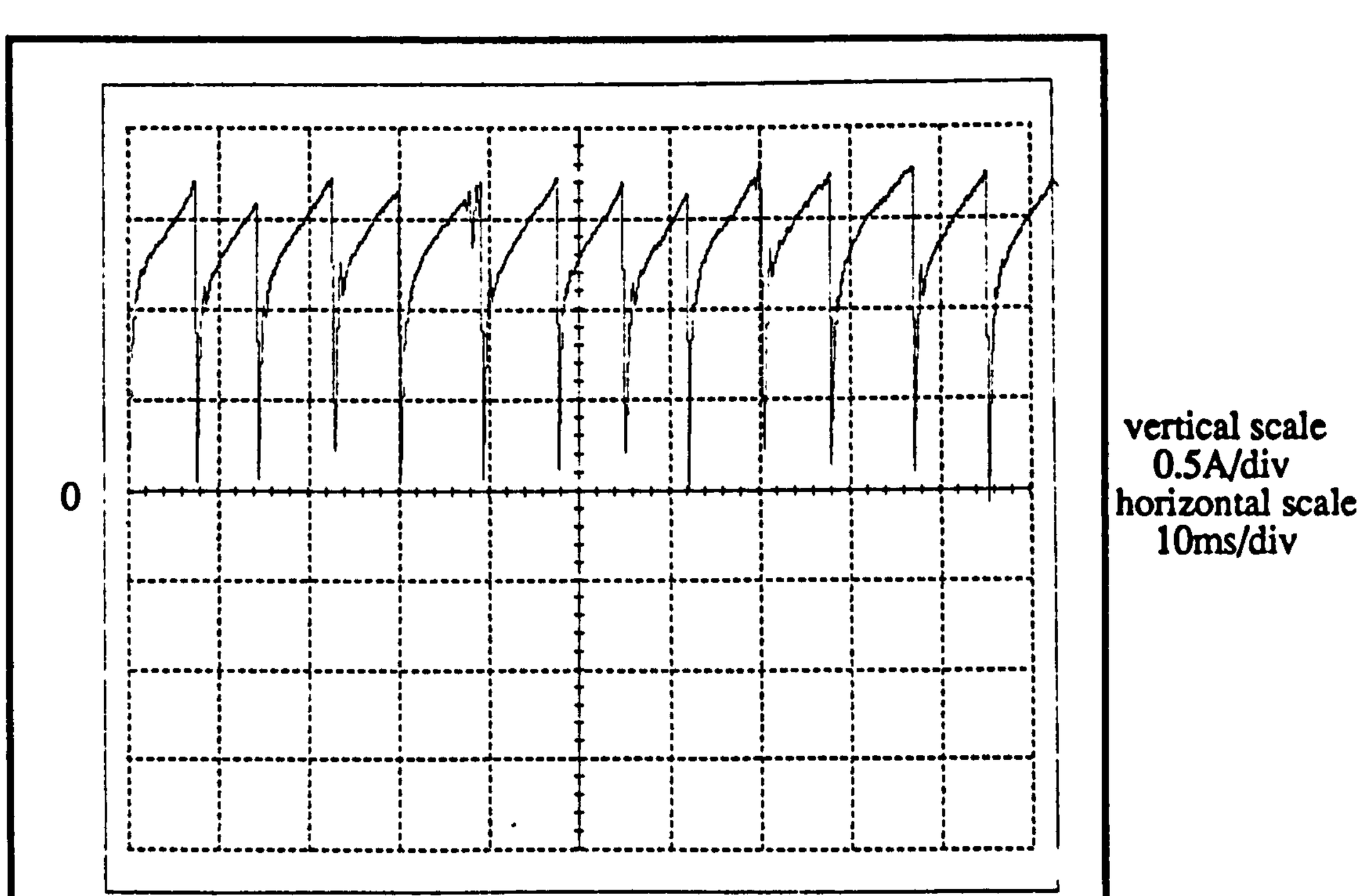

Figure 4.25 Supply current waveform without PWM control
(Load condition : 1.6Nm at 420rpm)

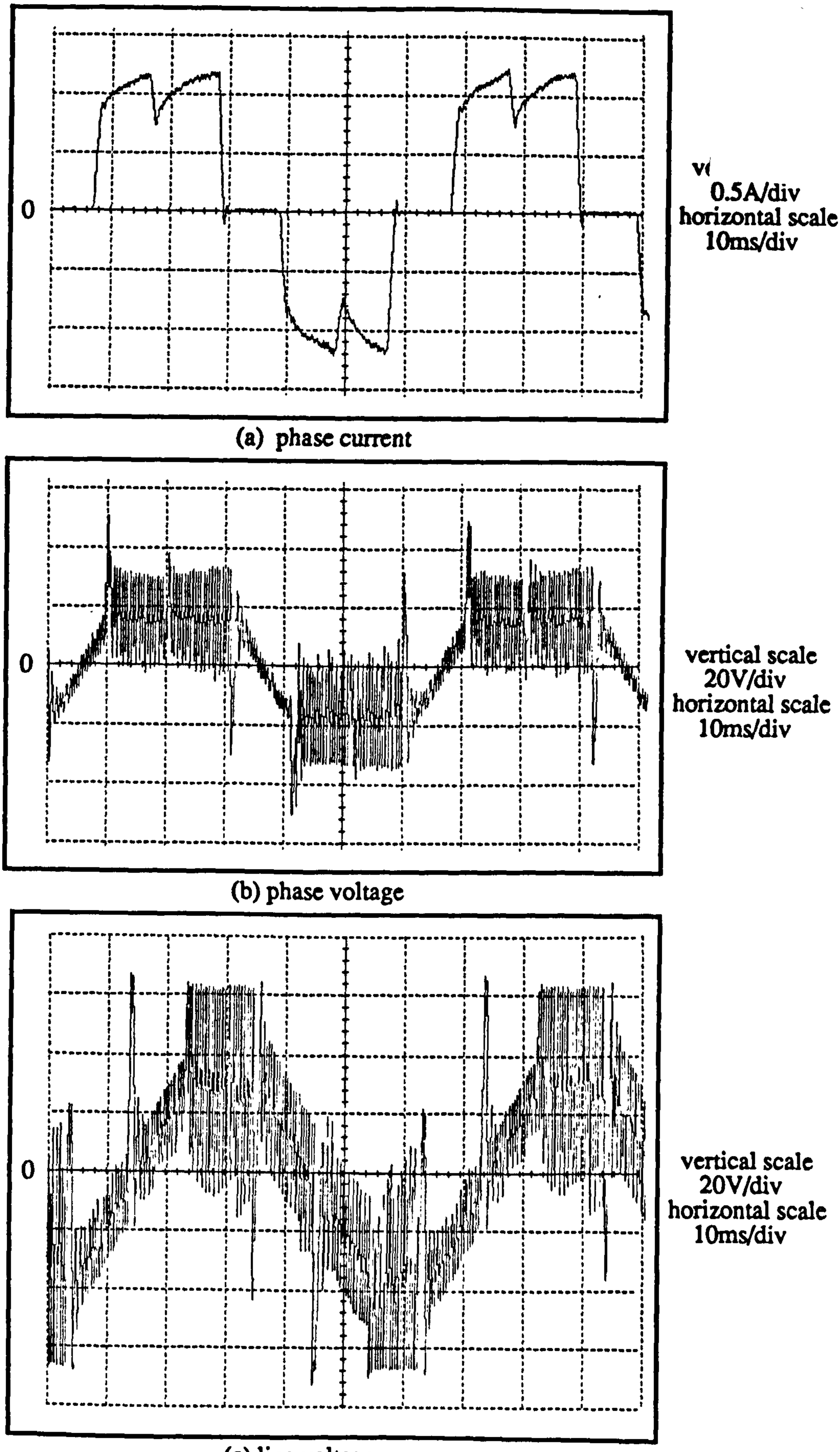

(a) phase current

(b) phase voltage

(c) line voltage

Figure 4.26 Phase current, phase voltage and line voltage waveforms with PWM control (Load condition : 1Nm at 300rpm)

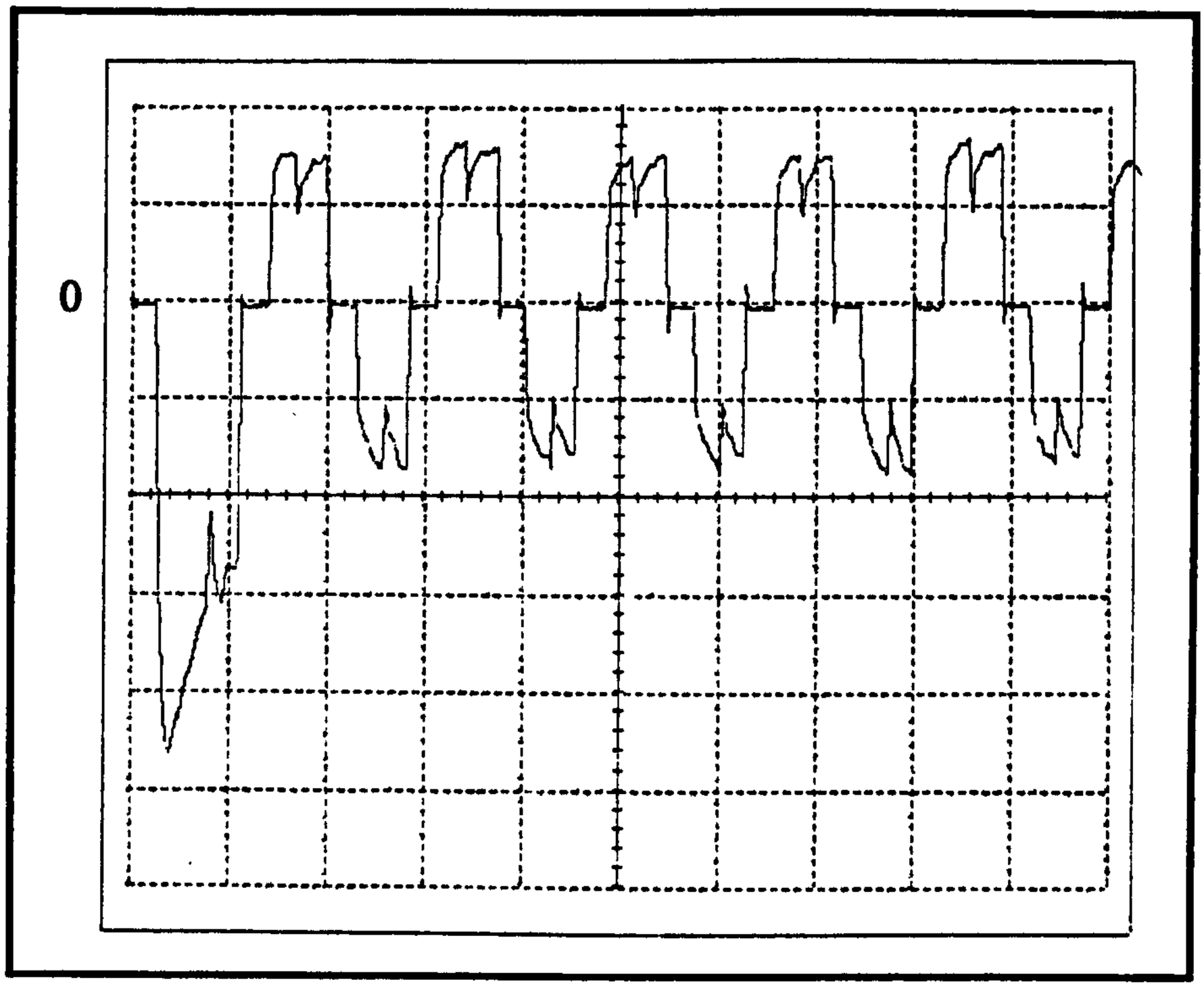

(a) phase current

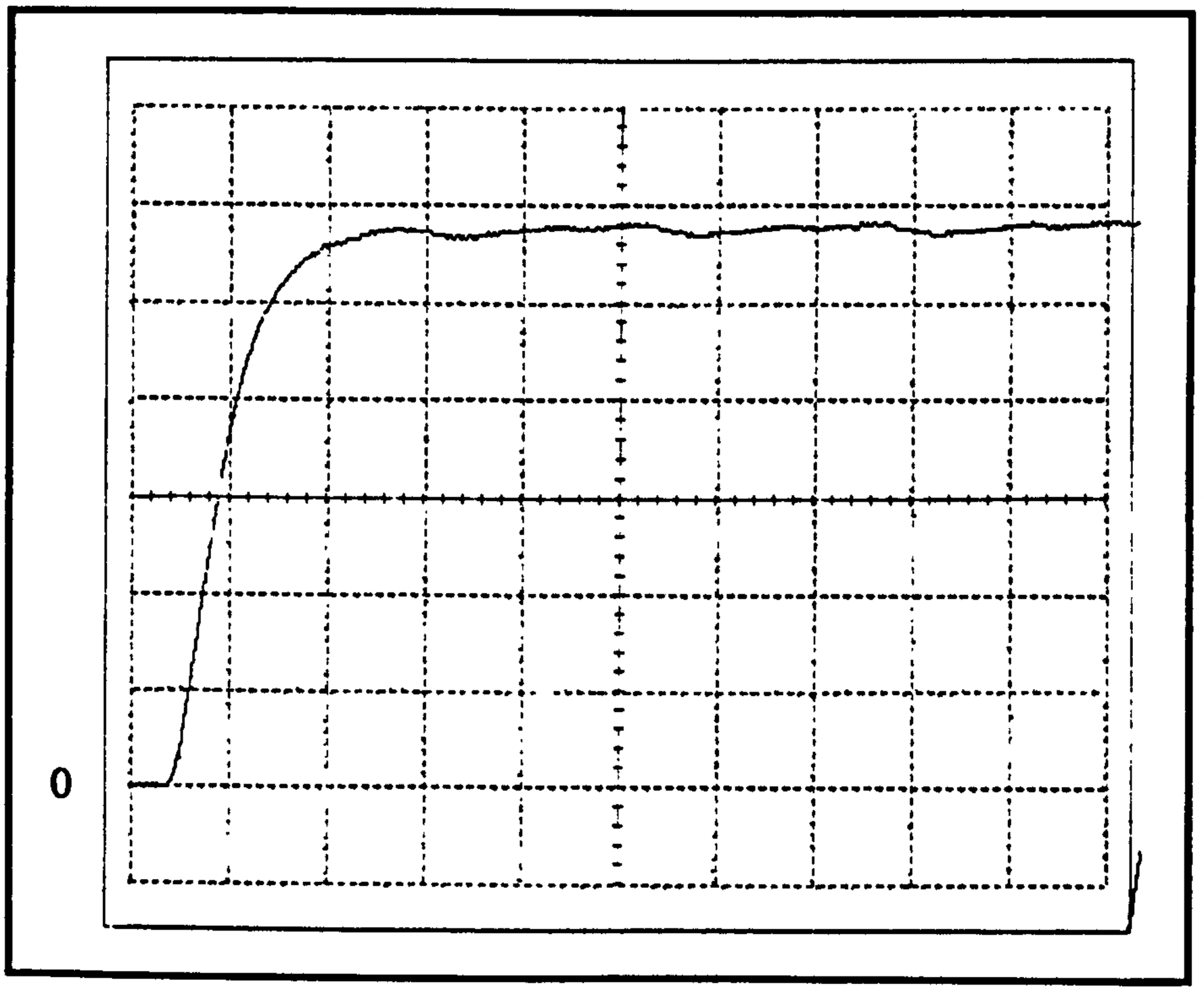

(b) motor speed

Figure 4.27 Experimental transient performance
(Load condition : 0.7Nm at 222 rpm)

CHAPTER 5

MATHEMATICAL MODEL FOR A 3-PHASE BRUSHLESS DC MOTOR DRIVE

This chapter describes a mathematical model for the brushless dc motor and its accompanying power-conditioning unit. The representation of the motor is based on the phase reference frame model shown in Figure 5.1, where coils a, b, c, d and q correspond respectively to the three stator phases and the two equivalent rotor damper windings. Although the experimental motor has no explicit damper windings, the provision for the inclusion of damping effects may be useful in subsequent research.

Under normal working the magnetic circuit operates in the linear region of its demagnetization characteristic, with the very high reluctance of the rare-earth magnets having a linearising effect similar to that of an airgap. Magnetic saturation can however be included by expressing the stator winding flux linkages as functions of both the rotor angle and the machine currents[38,39]. To simplify the analysis which follows, slot effects and saturation, hysteresis and eddy currents in the magnetic circuits are all neglected. The influence of the permanent-magnet rotor on the machine performance is determined by considerations of the rate-of-change of flux linkages seen by the stator phases. Actual machine parameters are used in the model, and these were measured as described in chapter 6. The required data could, of course, be calculated if only design data was

available. Although the inverter switching devices are assumed to be ideal, with no impedance or forward voltage drop when conducting and an infinite impedance when non-conducting, the software developed is sufficiently flexible to incorporate alternative representations, as well as the turn-on and turn-off times of the devices.

A tensor approach[16,17] is used in the present study, to define automatically the new circuit topology[40,41] as the conduction pattern of the inverter changes and therefore also the different circuit equations which apply.

The system equations are solved by numerical integration, as described in Appendix A2[42,43], to obtain the time variation of the flux linkages and currents in the mesh reference frame. The corresponding branch currents and voltages are then obtained by further tensor transformations. The use of tensors necessitates the definition of both branch and mesh reference frames, and a transformation between the two frames as explained below.

5.1 BRANCH REFERENCE FRAME

The branch reference frame is concerned with the disconnected branches of the system shown in Figure 5.2. The corresponding matrix equation, given in full in equation 5.1, may be written in the abbreviated form

$$\mathbf{V_b} = \mathbf{R_b}\,\mathbf{I_b} + p\boldsymbol{\Psi}_b \qquad (5.2)$$

where

$\mathbf{V_b}$ is the impressed branch voltage vector,

$\mathbf{I_b}$ the branch current vector,

$\mathbf{R_b}$ the branch resistance matrix,

$$\begin{bmatrix} V_a \\ V_b \\ V_c \\ V_d \\ V_q \\ V_s \end{bmatrix} = \begin{bmatrix} R_a & 0 & 0 & 0 & 0 & 0 \\ 0 & R_b & 0 & 0 & 0 & 0 \\ 0 & 0 & R_c & 0 & 0 & 0 \\ 0 & 0 & 0 & R_d & 0 & 0 \\ 0 & 0 & 0 & 0 & R_q & 0 \\ 0 & 0 & 0 & 0 & 0 & R_s \end{bmatrix} \begin{bmatrix} I_a \\ I_b \\ I_c \\ I_d \\ I_q \\ I_s \end{bmatrix} + p \begin{bmatrix} \psi_a \\ \psi_b \\ \psi_c \\ \psi_d \\ \psi_q \\ \psi_s \end{bmatrix} \qquad (5.1)$$

Matrix branch reference frame voltage equation

Ψ_b the branch total flux linkage vector, and

p the operator d/dt.

The total winding flux linkages $\psi_a, \psi_b, \psi_c, \psi_d$ and ψ_q are functions of the winding currents, the rotor position, and the flux linkages due to the permanent-magnet rotor[39]. The rotor position at any instant is specified with reference to the *a*-phase axis by the electrical angle $\theta_e = P\theta_r$, where θ_r is the mechanical angle and P the number of pole pairs.

The various flux linkages due to the permanent-magnet rotor were measured, as described in chapter 6, and their spatial variation expressed as

$$\psi_{Pra} = \psi_o (\cos\theta_e + 0.0763 \cos 3\theta_e + 0.0114 \cos 5\theta_e)$$

$$\psi_{Prb} = \psi_o \{\cos (\theta_e + 120^\circ) + 0.0763 \cos 3(\theta_e + 120^\circ) + 0.0114 \cos 5(\theta_e + 120^\circ)\}$$

$$\psi_{Prc} = \psi_o \{\cos (\theta_e - 120^\circ) + 0.0763 \cos 3(\theta_e - 120^\circ) + 0.0114 \cos 5(\theta_e - 120^\circ)\}$$

$$\psi_{Prd} = \psi_{od} (\cos 0^\circ + 0.0763 \cos 0^\circ + 0.0114 \cos 0^\circ)$$

and $\psi_{Prq} = 0$ (5.3)

where

ψ_o is the coefficient of the fundamental component of the no-load flux linkage with the stator windings due to the permanent-magnet rotor,

ψ_{od} the coefficient of the fundamental component of the no-load flux linkage with the d-axis damper winding due to the permanent-magnet rotor, and

ψ_{Prk} the flux linkage with winding k due to the permanent-magnet rotor, where k can be a, b, c, d or q.

The total flux linkages for the various windings are

$$\Psi_a = L_{aa} i_a + L_{ab} i_b + L_{ac} i_c + L_{ad} i_d + L_{aq} i_q + \Psi_{Pra}$$

$$\Psi_b = L_{ba} i_a + L_{bb} i_b + L_{bc} i_c + L_{bd} i_d + L_{bq} i_q + \Psi_{Prb}$$

$$\Psi_c = L_{ca} i_a + L_{cb} i_b + L_{cc} i_c + L_{cd} i_d + L_{cq} i_q + \Psi_{Prc}$$

$$\Psi_d = L_{da} i_a + L_{db} i_b + L_{dc} i_c + L_{dd} i_d + \Psi_{Prd}$$

$$\Psi_q = L_{qa} i_a + L_{qb} i_b + L_{qc} i_c + L_{qq} i_q$$

and $$\Psi_s = L_{ss} i_s \qquad (5.4)$$

Equation 5.4 may be re-stated in the abbreviated form

$$\Psi_b = L_b I_b + \Psi_{Pb} \qquad (5.5)$$

where

L_b is the branch inductance matrix, and

Ψ_{Pb} is a vector containing the branch flux linkage of the windings due to the permanent-magnet rotor.

The inductance coefficients of equation (5.4) are functions of rotor position and consequently of time, and the induced stator winding voltage vector E_b due to the rate-of-change of the total flux linkage vector Ψ_b is

$$E_b = L_b p I_b + p L_b I_b + p\Psi_{Pb} \qquad (5.6)$$

Equation 5.6 may be re-written as

$$E_b = L_b p I_b + \frac{dL_b}{d\theta_e} \omega_e I_b + \frac{d\Psi_{Pb}}{d\theta_e} \omega_e \qquad (5.7)$$

where ω_e is the angular velocity of the rotor in electrical radians per second.

The first term on the right-hand side of equation 5.7 represents the transformer voltage components and the second term the rotational voltages due to the inductance variation as a result of rotor angular variation with time[20]. The final term represents the no-load rotational voltages due to the permanent-magnet[44]. The final two terms are significant, since they appear in the expression for electromagnetic torque developed later. Equation 5.7 is given in full in equation 5.8, from which it can be seen that the induced voltages are functions of rotor position and speed, stator phase currents and magnetic properties. From equation 5.5, the branch current vector is

$$\mathbf{I_b} = \mathbf{L_b^{-1}} \left(\Psi_b - \Psi_{Pb}\right) \tag{5.9}$$

which is given in full in equation 5.10. Substituting equation 5.9 into equation 5.2 yields

$$\mathbf{V_b} = \mathbf{R_b}\, \mathbf{L_b^{-1}} \left(\Psi_b - \Psi_{Pb}\right) + p\Psi_b \tag{5.11}$$

which is given in full in equation 5.12.

5.2 MESH REFERENCE FRAME

The mesh reference frame is concerned with the meshes formed when conducting switches connect the stator phases of the motor to the dc supply. During normal operation, six discrete switching patterns occur in a defined sequence, for each period of which only two switches of the inverter bridge are conducting. A typical conduction pattern is shown in Figure 5.3, with the switching states for the six different patterns being given in Table 5.1. The system mesh differential equations may be written as

$$\begin{bmatrix} e_a \\ e_b \\ e_c \\ e_d \\ e_q \\ e_s \end{bmatrix} = \begin{bmatrix} L_{aa} & L_{ab} & L_{ac} & L_{ad} & L_{aq} & 0 \\ L_{ba} & L_{bb} & L_{bc} & L_{bd} & L_{bq} & 0 \\ L_{ca} & L_{cb} & L_{cc} & L_{cd} & L_{cq} & 0 \\ L_{da} & L_{db} & L_{dc} & L_{dd} & 0 & 0 \\ L_{qa} & L_{qb} & L_{qc} & 0 & L_{qq} & 0 \\ 0 & 0 & 0 & 0 & 0 & L_{ss} \end{bmatrix} p \begin{bmatrix} I_a \\ I_b \\ I_c \\ I_d \\ I_q \\ I_s \end{bmatrix} + \left\{ \frac{d}{d\theta_e} \begin{bmatrix} L_{aa} & L_{ab} & L_{ac} & L_{ad} & L_{aq} & 0 \\ L_{ba} & L_{bb} & L_{bc} & L_{bd} & L_{bq} & 0 \\ L_{ca} & L_{cb} & L_{cc} & L_{cd} & L_{cq} & 0 \\ L_{da} & L_{db} & L_{dc} & L_{dd} & 0 & 0 \\ L_{qa} & L_{qb} & L_{qc} & 0 & L_{qq} & 0 \\ 0 & 0 & 0 & 0 & 0 & L_{ss} \end{bmatrix} \right\} \omega_e \begin{bmatrix} I_a \\ I_b \\ I_c \\ I_d \\ I_q \\ I_s \end{bmatrix} + \left\{ \frac{d}{d\theta_e} \begin{bmatrix} \psi_{Pra} \\ \psi_{Prb} \\ \psi_{Prc} \\ \psi_{Prd} \\ 0 \\ 0 \end{bmatrix} \omega_e \right\} \tag{5.8}$$

Matrix branch induced voltage equation

$$\begin{bmatrix} I_a \\ I_b \\ I_c \\ I_d \\ I_q \\ I_s \end{bmatrix} = \begin{bmatrix} L_{aa} & L_{ab} & L_{ac} & L_{ad} & L_{aq} & 0 \\ L_{ba} & L_{bb} & L_{bc} & L_{bd} & L_{bq} & 0 \\ L_{ca} & L_{cb} & L_{cc} & L_{cd} & L_{cq} & 0 \\ L_{da} & L_{db} & L_{dc} & L_{dd} & 0 & 0 \\ L_{qa} & L_{qb} & L_{qc} & 0 & L_{qq} & 0 \\ 0 & 0 & 0 & 0 & 0 & L_{ss} \end{bmatrix}^{-1} \left\{ \begin{bmatrix} \psi_a \\ \psi_b \\ \psi_c \\ \psi_d \\ \psi_q \\ \psi_s \end{bmatrix} - \begin{bmatrix} \psi_{Pra} \\ \psi_{Prb} \\ \psi_{Prc} \\ \psi_{Prd} \\ 0 \\ 0 \end{bmatrix} \right\} \tag{5.10}$$

Matrix branch current equation

$$\begin{bmatrix} V_a \\ V_b \\ V_c \\ V_d \\ V_q \\ V_s \end{bmatrix} = \begin{bmatrix} R_a & 0 & 0 & 0 & 0 & 0 \\ 0 & R_b & 0 & 0 & 0 & 0 \\ 0 & 0 & R_c & 0 & 0 & 0 \\ 0 & 0 & 0 & R_d & 0 & 0 \\ 0 & 0 & 0 & 0 & R_q & 0 \\ 0 & 0 & 0 & 0 & 0 & R_s \end{bmatrix} \begin{bmatrix} L_{aa} & L_{ab} & L_{ac} & L_{ad} & L_{aq} & 0 \\ L_{ba} & L_{bb} & L_{bc} & L_{bd} & L_{bq} & 0 \\ L_{ca} & L_{cb} & L_{cc} & L_{cd} & L_{cq} & 0 \\ L_{da} & L_{db} & L_{dc} & L_{dd} & 0 & 0 \\ L_{qa} & L_{qb} & L_{qc} & 0 & L_{qq} & 0 \\ 0 & 0 & 0 & 0 & 0 & L_{ss} \end{bmatrix}^{-1} \left\{ \begin{bmatrix} \psi_a \\ \psi_b \\ \psi_c \\ \psi_d \\ \psi_q \\ \psi_s \end{bmatrix} - \begin{bmatrix} \psi_{Pra} \\ \psi_{Prb} \\ \psi_{Prc} \\ \psi_{Prd} \\ 0 \\ 0 \end{bmatrix} \right\} + p \begin{bmatrix} \psi_a \\ \psi_b \\ \psi_c \\ \psi_d \\ \psi_q \\ \psi_s \end{bmatrix} \qquad (5.12)$$

Matrix branch voltage equation

MESH NUMBER		1	2	3	4	5	6
CONDUCTING SWITCH NUMBERS	TOP	S3	S1	S1	S5	S5	S3
	BOTTOM	S2	S2	S6	S6	S4	S4

Table 5.1 Mesh definitions

$$\mathbf{V_m} = \mathbf{R_m}\,\mathbf{I_m} + p\Psi_m \tag{5.13}$$

where

$$\Psi_m = \mathbf{L_m}\,\mathbf{I_m} + \Psi_{Pm} \tag{5.14}$$

From equation 5.14, the mesh current vector is

$$\mathbf{I_m} = \mathbf{L_m^{-1}}\,(\Psi_m - \Psi_{Pm}) \tag{5.15}$$

and substituting this into equation 5.13 gives

$$\mathbf{V_m} = \mathbf{R_m}\,\mathbf{L_m^{-1}}\,(\Psi_m - \Psi_{Pm}) + p\Psi_m \tag{5.16}$$

where

$\mathbf{V_m}$ is the impressed mesh voltage vector,

$\mathbf{I_m}$ the mesh current vector,

Ψ_m the mesh total flux linkage vector,

Ψ_{Pm} the mesh flux linkage vector due to the permanent-magnet rotor, and

$\mathbf{R_m}$ and $\mathbf{L_m}$ are respectively the mesh resistance and inductance matrices.

Equation 5.16 may be re-arranged in the state-variable form

$$p\Psi_m = \mathbf{V_m} - \mathbf{R_m}\,\mathbf{L_m^{-1}}\,(\Psi_m - \Psi_{Pm}) \tag{5.17}$$

and integrated numerically, using the technique described in Appendix A2, to obtain a new machine flux linkage vector Ψ_m. A step-by-step solution for the mesh flux linkages may thus be obtained.

5.3 BRANCH-MESH TRANSFORMATION

The mathematical model has to generate automatically the relevant mesh equations as the switch and diode conduction pattern changes, and this is achieved by defining a transformation between the branch and mesh reference frames.

The branch/mesh current transformation $\mathbf{C}$ defines branch currents in terms of mesh currents. The relationship between the mesh currents shown in Figure 5.3 and the branch currents of Figure 5.4 may be obtained as

$$\begin{bmatrix} I_a \\ I_b \\ I_c \\ I_d \\ I_q \\ I_s \end{bmatrix} = \begin{matrix} \\ \\ \\ \text{BRANCH} \\ \\ \\ \\ \end{matrix} \overset{\text{MESH}}{\begin{bmatrix} -1 & 0 & 0 \\ 0 & 0 & 0 \\ +1 & 0 & 0 \\ 0 & +1 & 0 \\ 0 & 0 & +1 \\ +1 & 0 & 0 \end{bmatrix}} \begin{bmatrix} I_{m1} \\ I_{m2} \\ I_{m3} \end{bmatrix} \tag{5.18}$$

where a ± 1 denotes whether the mesh current has the same or the reversed sense as the branch current, and a 0 denotes that there is no mesh current in that branch. This equation may be written in abbreviated form as

$$\mathbf{I_b} = \mathbf{C}\,\mathbf{I_m} \tag{5.19}$$

where $\mathbf{C}$ is the branch/mesh current transformation matrix. An important constraint for tensor transformations is that of power invariance between reference frames[45,46], which may be expressed mathematically as

$$(\mathbf{V_b} - p\Psi_b)^t\,\mathbf{I_b} = (\mathbf{V_m} - p\Psi_m)^t\,\mathbf{I_m} \tag{5.20}$$

where the superscript t denotes a transpose. Substituting equation 5.19 in equation 5.20 and re-arranging yields

$$[\mathbf{C}(\mathbf{V_b} - p\Psi_b)^t - (\mathbf{V_m} - p\Psi_m)^t]\,\mathbf{I_m} = 0 \tag{5.21}$$

If equation 5.21 holds for any arbitrary current vector $\mathbf{I_m}$ then, by matrix transposition

$$(V_m - p\Psi_m) = C^t (V_b - p\Psi_b) \tag{5.22}$$

where C^t is the transpose of C, and is termed the branch/mesh voltage transformation matrix. Combining equations 5.2, 5.19 and 5.22, and re-arranging, gives

$$V_m - p\Psi_m = C^t R_b C I_m \tag{5.23}$$

and by comparison with equation 5.13

$$R_m = C^t R_b C \tag{5.24}$$

From equation 5.22, the branch/mesh flux linkages are related by

$$\Psi_m = C^t \Psi_b \tag{5.25}$$

The analysis above may be extended to show that the matrices for the mesh inductances and their rates-of-change are given respectively by

$$L_m = C^t L_b C \tag{5.26}$$

and

$$\frac{dL_m}{d\theta_e} = C^t \frac{dL_b}{d\theta_e} C \tag{5.27}$$

5.4 SYSTEM MECHANICAL EQUATION

The equation relating the various system torques is

$$T_e = J\frac{d\omega_r}{dt} + D\omega_r + T_F + T_L \tag{5.28}$$

where

T_e is the electromagnetic torque,

J the combined motor and load inertia,

$d\omega_r/dt$ the rotor angular acceleration,

D the viscous damping coefficient,

T_F the frictional torque, and

T_L the load torque.

The total power in the mesh reference frame is

$$P_m = I_m^t R_m I_m + I_m^t L_m \frac{dI_m}{dt} + I_m^t \left(\frac{dL_m}{d\theta_e} \cdot \frac{d\theta_e}{dt} \right) I_m + I_m^t \left(\frac{d\Psi_{Pm}}{d\theta_e} \cdot \frac{d\theta_e}{dt} \right) \qquad (5.29)$$

where the first term represents the copper losses and the second the rate of change of stored inductive energy. The final two terms of the equation are the instantaneous electromagnetic power, which is the power associated with the energy conversion process[20]. The instantaneous electromagnetic torque is obtained by dividing the instantaneous electromagnetic power by the mechanical speed ω_r. With $\omega_r = d\theta_r/dt$ and $\theta_r = \theta_e/P$, the result is

$$T_e = P \left\{ \left(I_m^t \cdot \frac{dL_m}{d\theta_e} \cdot I_m \right) + \left(I_m^t \cdot \frac{d\Psi_{Pm}}{d\theta_e} \right) \right\} \qquad (5.30)$$

Equation 5.28 may be rewritten as

$$\frac{d\omega_r}{dt} = \frac{(T_e - D\omega_r - T_F - T_L)}{J} \qquad (5.31)$$

which may be integrated numerically, to give the step-by-step variation of the rotor speed ω_r.

5.5 INDUCTANCE VARIATIONS

The variation of the unsaturated self and mutual inductances of the experimental machine were measured as functions of the electrical angle θ_e between the *a*-phase axis and the rotor axis using the methods described in chapter 6. The measurements provide the minimum and maximum of the

inductances variations, from which the average value of the self and mutual inductances L_o and M_o and the coefficient of the second harmonic component of the self and mutual inductances L_2 and M_2 may be calculated. Investigations have established that the stator current waveforms are influenced more by the induced voltage waveshape and by inverter switching, than by high-order harmonic components in the inductance variations[12].

A model which represents accurately the trapezoidal induced voltages and inverter switching instants, while approximating the inductance variations as cosinusoidal functions, is therefore reasonably accurate. On this basis the inductances of the experimental machine are[12,13]:

$$\begin{aligned} L_{aa} &= L_o - L_2 \cos 2\theta_e \\ L_{bb} &= L_o - L_2 \cos 2(\theta_e + 2\pi/3) \\ L_{cc} &= L_o - L_2 \cos 2(\theta_e - 2\pi/3) \end{aligned} \tag{5.32}$$

and

$$\begin{aligned} L_{ab} &= -M_o - M_2 \cos 2(\theta_e - 2\pi/3) \\ L_{ac} &= -M_o - M_2 \cos 2(\theta_e + 2\pi/3) \\ L_{bc} &= -M_o - M_2 \cos 2\theta_e \end{aligned} \tag{5.33}$$

5.6 COMPUTER IMPLEMENTATION

Figure 5.5 is a flowchart for the computer program written to predict the motor performance, based on solving numerically the differential equations expressed in the mesh reference frame. The solution process is described by the following algorithm

a. The branch resistance matrix is formed. This fixed matrix is assembled once only, at the beginning of the simulation.

b. The mesh resistance matrix is determined from

$$\mathbf{R}_m = \mathbf{C}^t \mathbf{R}_b \mathbf{C}$$

This matrix is dynamic and changes with the switch conduction pattern.

c. The time varying branch inductance matrix $\mathbf{L}_b$ is determined using equations 5.32 and 5.33. This matrix is formed at every integration step, since it contains elements which vary with the angular position of the rotor.

d. The mesh inductance matrix $\mathbf{L}_m$ is determined using equation 5.26, and its inverse is obtained.

e. The impressed mesh voltage vector is determined from

$$\mathbf{V}_m = \mathbf{C}^t \mathbf{V}_b$$

f. The branch flux linkage vector due to the permanent-magnet rotor is obtained using equation 5.3.

g. The mesh flux linkage vector due to the permanent-magnet rotor is obtained from

$$\Psi_{Pm} = \mathbf{C}^t \Psi_{Pb}$$

h. Equation 5.17 is integrated numerically, using the technique described in Appendix 2, to obtain the flux linkage vector Ψ_m.

i. The mesh current vector $\mathbf{I}_m$ is obtained from

$$\mathbf{I}_m = \mathbf{L}_m^{-1} (\Psi_m - \Psi_{Pm})$$

j. The branch current vector $\mathbf{I_b}$ is determined from

$$\mathbf{I_b} = \mathbf{C}\,\mathbf{I_m}$$

k. The branch rate-of-change of inductance matrix is obtained from the derivatives of the branch inductances with respect to θ_e.

l. The mesh rate-of-change of inductance matrix is obtained from

$$\frac{d\mathbf{L_m}}{d\theta_e} = \mathbf{C}^t \frac{d\mathbf{L_b}}{d\theta_e}\,\mathbf{C}$$

m. The mesh current derivative vector $\mathbf{pI_m}$ is determined from

$$\mathbf{pI_m} = \mathbf{L_m^{-1}}\,(\mathbf{V_m} - \mathbf{R_m}\,\mathbf{I_m} - \frac{d\mathbf{L_m}}{d\theta_e}\,\omega_e\,\mathbf{I_m} - \mathbf{p}\Psi_{Pm})$$

n. The branch current derivative vector $\mathbf{pI_b}$ is determined from

$$\mathbf{p}\,\mathbf{I_b} = \mathbf{C}\,\mathbf{pI_m}$$

o. The branch voltage vector is determined from

$$\mathbf{V_b} = \mathbf{R_b}\,\mathbf{I_b} + \mathbf{L_b}\,\mathbf{p}\,\mathbf{I_b} + \frac{d\mathbf{L_b}}{d\theta_e}\,\omega_e\,\mathbf{I_b} + \mathbf{p}\Psi_{Pb}$$

p. The new electromagnetic torque and angular velocity are obtained using equations 5.30 and 5.31 respectively.

The solution advances by one integration step, the initial conditions are up-dated, and procedures (c) to (p) repeated until the end of the simulation. At the end of each step, the system is tested for any changes which may have occurred in the bridge topology. If a change is detected, the solution proceeds as follows:

1. Determine the time between the start of the step and the point of discontinuity.
2. Re-integrate the mesh equations from the start of the step to the point of discontinuity.
3. Re-assemble the branch/mesh current transformation matrix $\mathbf{C}$ corresponding to the new circuit topology, and form its transpose $\mathbf{C}^t$.
4. Form the new mesh matrices $\mathbf{R}_m$, $\mathbf{L}_m$ and $\mathbf{L}_m^{-1}$ according to the new circuit topology.
5. Form the new mesh equations and integrate these from the point of discontinuity.
6. Test the system for changes in the switch condition pattern. If any occur, repeat operations (1) to (6). If not, the solution proceeds with operations (c) to (p) over the next integration step.

5.7 SYSTEM DISCONTINUITIES

When a switch commences or ceases conduction, the conduction pattern and consequently the transformation matrix also change. For the purpose of accurately simulating the system operation, it is necessary to determine when the discontinuity occurs.

Two kinds of discontinuity are possible:

a. Turn-on discontinuity.

b. Turn-off discontinuity.

and both are explained below.

5.7.1 TURN-ON DISCONTINUITY

A turn-on discontinuity occurs when a non-conducting switch has a gate signal applied and it commences conduction. To minimize the program complexity, changes in the conduction pattern are assumed to occur only at the end of a step. Thus, if a device is switched on during an integration step, it commences conduction at the end of the step and the system equations are changed at this instant. This approximation is valid, due to the very small integration step-length.

5.7.2 TURN-OFF DISCONTINUITY

A turn off discontinuity occurs during the commutation period when one switch turns off and another turns on. It is characterised by three separate circuit topologies, as shown typically in Figure 5.6. Figure 5.6(a) shows switches 4 and 5 conducting, and these produce three meshes as shown. The second period occurs when switch 5 turns off and 3 turns on as shown in Figure 5.6(b). For this condition four meshes are required, one of which I_{m2} passes through D2 and S4, to maintain the current flow through phase *c* during the commutation period. Thus at the commencement of commutation, the system equations are changed from three to four meshes.

During commutation, the incoming mesh current I_{m1} builds up while the outgoing mesh current I_{m2} decreases. At the end of each integration step, the polarity of the outgoing mesh current is tested. When it becomes negative (an unpermitted situation), the point at which it occurs is determined by linear interpolation as shown by Figure 5.7. If the mesh currents at the beginning and the end of the step

are respectively I_1 and I_2, then the time to the point of discontinuity is

$$T_c = \frac{I_1}{I_1 - I_2} \times h \qquad (5.34)$$

where h is the integration step length. After commutation switches 3 and 4 are conducting, and the system is represented by the three meshes defined in Figure 5.6(c).

5.8 MASTER MATRIX

Six distinct meshes are possible during normal operating conditions, with a further six to account for commutation. These are all defined in Table 5.2.

The current transformation matrix **C** for the case shown in Figure 5.6(a)is

Branch \ Mesh	1	2	3
a	-1	0	0
b	0	0	0
c	+1	0	0
d	0	+1	0
q	0	0	+1
s	+1	0	0

MESH		1	2	3	4	5	6	7	8	9	10	11	12
CONDUCTING SWITCHES	TOP	S3	S1	S1	S1	S1	S5	S5	S5	S5	S3	S3	S3
	BOTTOM	S2	S2	S2	S6	S6	S6	S6	S4	S4	S4	S4	S2
CONDUCTING DIODES	TOP				D5				D3				D1
	BOTTOM		D6				D4				D2		

Table 5.2 Mesh definitions (with commutation periods)

and for that shown in Figure 5.6(b) is

Branch \ Mesh	1	2	3	4
a	-1	-1	0	0
b	+1	0	0	0
c	0	+1	0	0
d	0	0	+1	0
q	0	0	0	+1
s	+1	0	0	0

The method by which changes in **C** are produced automatically as the switch and diode conduction pattern changes makes use of a master matrix[45,46] relating the system branches to all possible meshes that can be formed by switch and diode conduction. The matrix is given in Figure 5.8, with the relevant column being loaded into **C** whenever the corresponding switch-pair or diode turn-on and retained in **C** until a commutation occurs.

5.9 DISCUSSION OF RESULTS

The computer model described above was used to investigate the steady-state and transient performance of the drive using the motor parameters given in Appendix 1. Figure

5.9 shows the predicted phase current, torque and speed waveforms with a 24V supply voltage, a 0.7Nm load torque with a moment of inertia of 0.003kg.m^2, when the motor is started from rest and run up to a steady-state speed of 222rpm. As the motor speed rises the electromagnetic torque continues to accelerate the rotor, until the increasing generated emf produced by the rotating magnetic field decreases the winding currents, and consequently the electromagnetic torque, to a level at which it is balanced by the load and friction torques. As expected, the electromagnetic torque is pulsating and the starting torque is higher than the running torque. The predicted phase current, torque and speed waveforms on no-load, with a 24V supply voltage and when the motor is started from rest, are shown in Figure 5.10. The speed increases linearly during the initial start-up period and the increasing generated emf decreases the winding currents almost to zero, since the generated emf and the phase voltage are almost equal on no-load. The electromagnetic torque decreases to a level at which its average value balances the friction torque. As expected, the rise-time of the speed to its steady-state no-load value is less than that with load. This is because the total moment of inertia on no-load is simply the moment of inertia of the motor rotor. The system response to a typical load change is shown in Figure 5.11. The motor is running initially at a steady-state speed of 222rpm with a load torque of 0.7Nm, and when this is suddenly removed the motor torque decreases to satisfy the new condition as the rotor accelerates to its new speed (260rpm). When the new steady-state condition has been

reached, the load torque is re-applied and the motor decelerates. Figure 5.12 shows the increase in the motor phase emf with speed and the effect of this on the phase current. In Figures 5.13 and 5.14 the predicted motor speed and phase current waveforms when the motor is started from rest and for the same load conditions described previously are compared with the measured waveforms. It is clear from Figure 5.13, that the predicted speed response during the start-up period is in good agreement with the experimental result. The predicted speed response time from start to its steady-state value is 120ms and the measured response time is 110ms. The predicted steady-state speed (218rpm) is also in good agreement with the measured result (222rpm). Close agreement between the predicted and measured current waveforms during the start-up period is evident in Figure 5.14, with the simulated currents being slightly greater than the measured values, since the simulation does not account for voltage drops in the switching devices. The simulation of the transient period is of great importance, since one can predict the nature and value of the starting current waveform which can be very harmful if its value exceed the rating of the semiconductor switching devices. In Figure 5.15 the predicted steady-state current waveform on load and without PWM control is compared with the measured waveform. The 60°e non-conducting and 120°e conducting periods are clearly seen in both waveforms. The phase current waveform has a dip at the instant of commutation, due both to the phase winding inductance which prevents the phase current from changing instantaneously during the commutation

period and the generated emfs in the motor phases. The generated voltage of the outgoing phase assists the current decay, whereas that of the incoming phase opposes the current build-up, and consequently there is a dip in the phase current which is not undergoing commutation. Good agreement between predicted and measured waveforms is evident. Figure 5.16 shows both predicted and measured phase current waveforms with a 70V supply voltage, 1Nm load torque, a steady state speed of 300rpm and with the PWM control set at a 70% duty cycle with a 20kHz switching frequency. The high frequency current ripple due to the PWM switching of the inverter is evident in both waveforms of Figure 5.16. Predicted and measured phase current waveforms on no-load are shown in Figure 5.17, and Figures 5.18 and 5.19 show respectively predicted and measured phase and line voltage waveforms without PWM control. As expected, without PWM control during the 60°e period when the phase is not conducting, the phase voltage is equal to the generated emf, as is evident in both waveforms of Figure 5.18. The sudden change in the phase current at the commutation instants results in voltage spikes on the phase and line voltage waveforms, as seen in both sets of results. Figures 5.20 and 5.21 show respectively predicted and measured phase and line voltage waveforms with PWM control. The effect of the chopping action of the PWM controller on these waveforms is evident. With PWM control, oscillations occur in the phase voltage waveform during the non-conducting period, due to induced voltages caused by rapidly changing currents in the other windings. The voltage spikes due to the sudden change

in the phase current at the commutation instants are also evident in both sets of results. The difference between the shapes of the predicted and measured phase current and phase voltage waveforms is due to the fact that the effects of the reverse recovery in the free-wheeling diodes are not included in the model. Predicted and measured no-load phase voltage waveforms are both trapezoidal as shown in Figure 5.22. Predicted and measured supply current waveforms are shown in Figure 5.23 and good agreement between them is evident.

In conclusion, the close agreement between the predicted and experimental results presented demonstrates the ability of the mathematical model to predict accurately the steady-state and transient performance of the drive. This capability will be utilized in chapter 7 to investigate the factors which effect torque ripple and the ways by which this might be minimized.

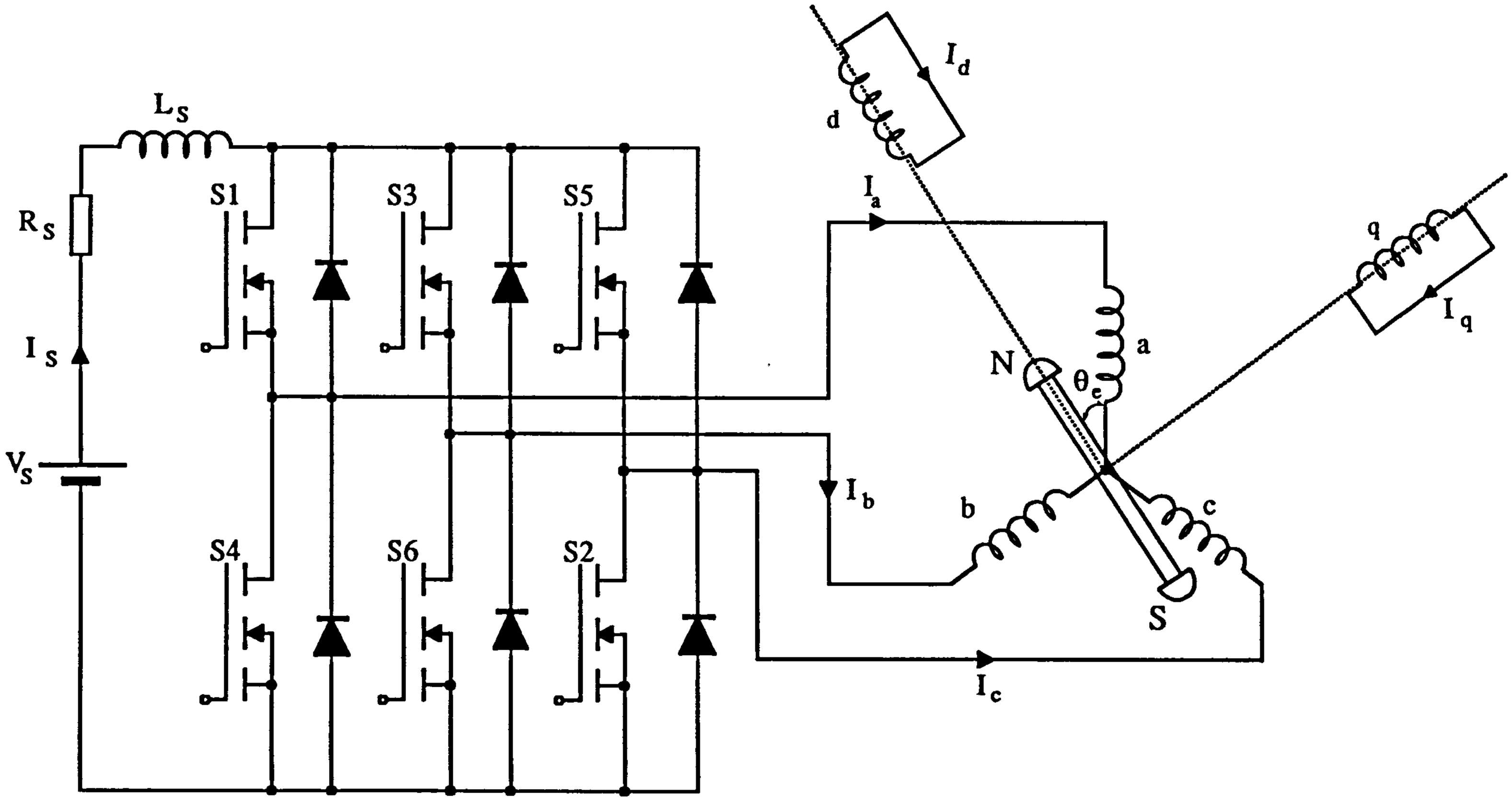

Figure 5.1 Phase model of a 3-phase brushless dc motor drive with permanent-magnet rotor

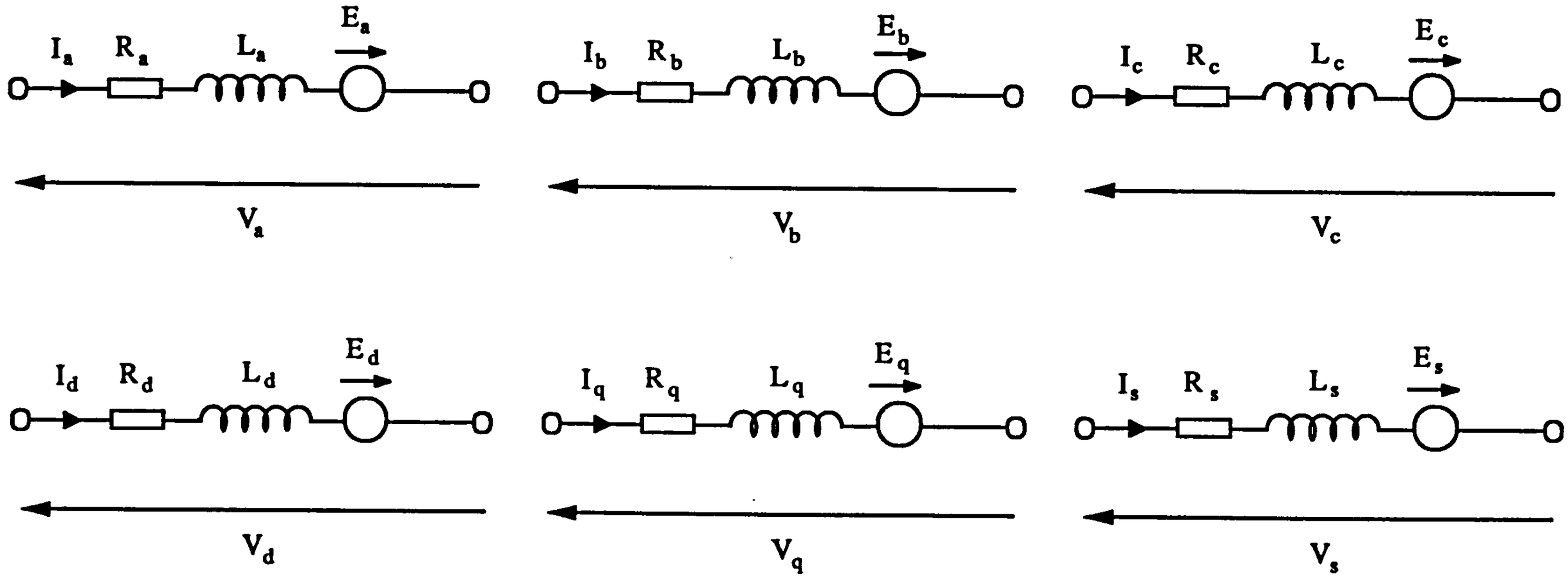

Figure 5.2 System branch reference frame

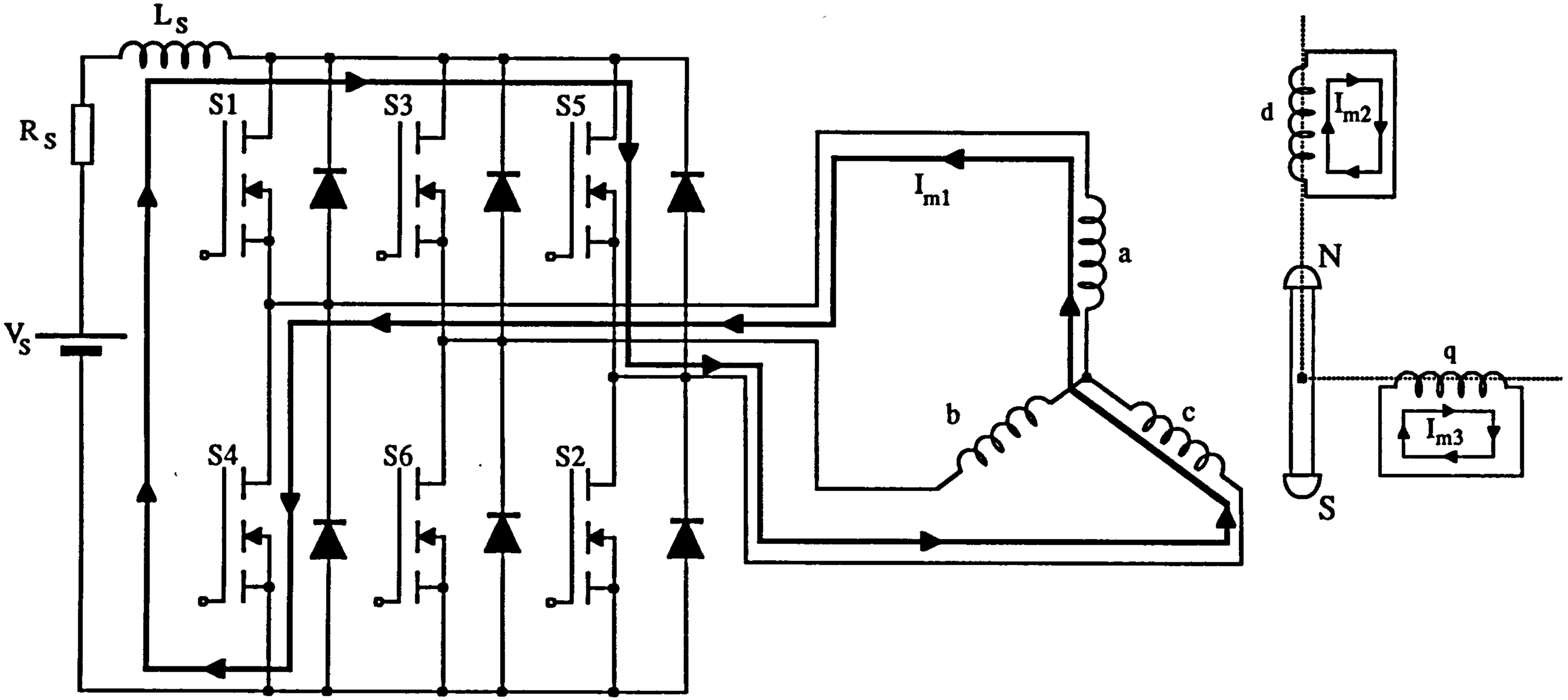

Figure 5.3 Brushless dc motor system with S5 and S4 on (showing mesh currents)

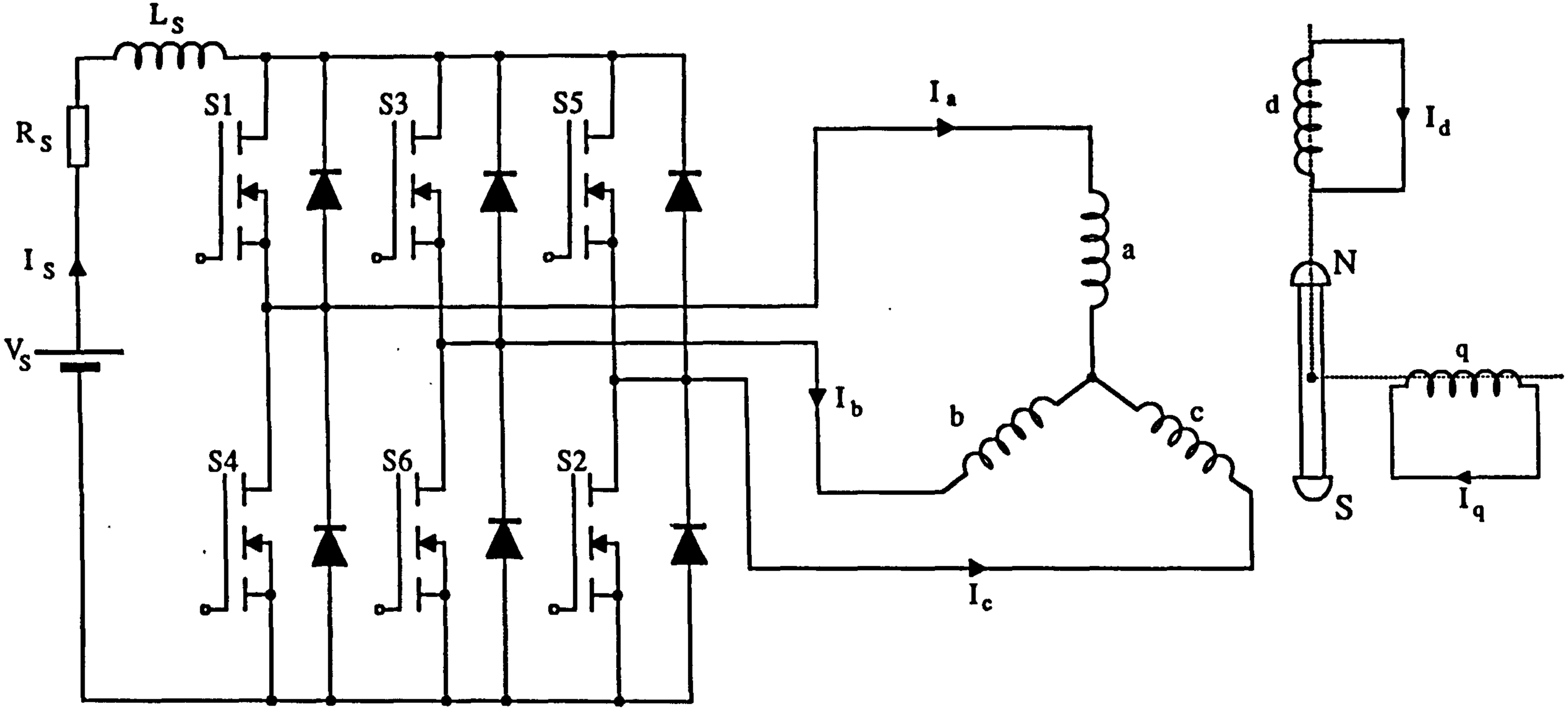

Figure 5.4 Brushless dc motor system (showing branch currents)

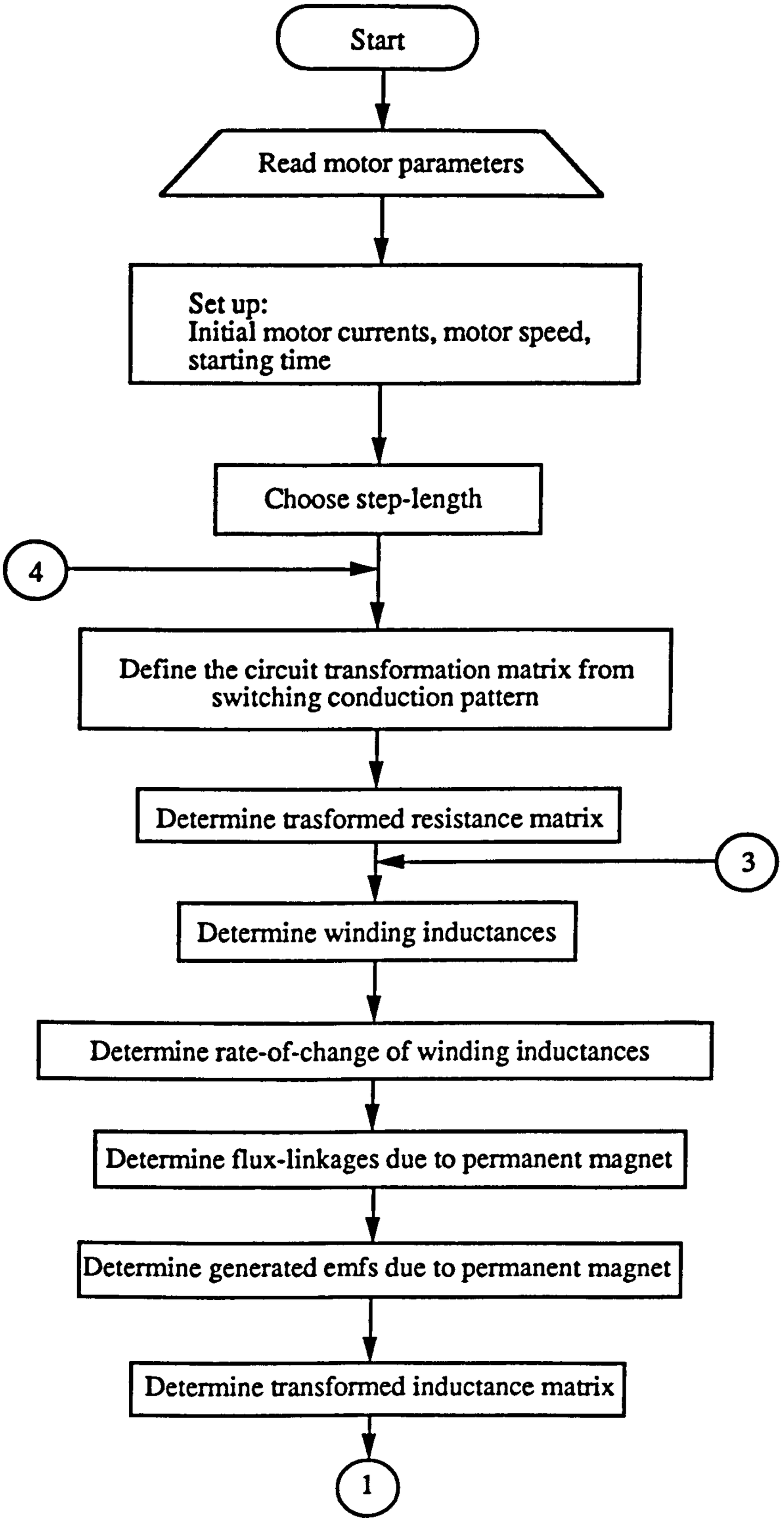

Figure 5.5 Flow chart for motor model

...continued

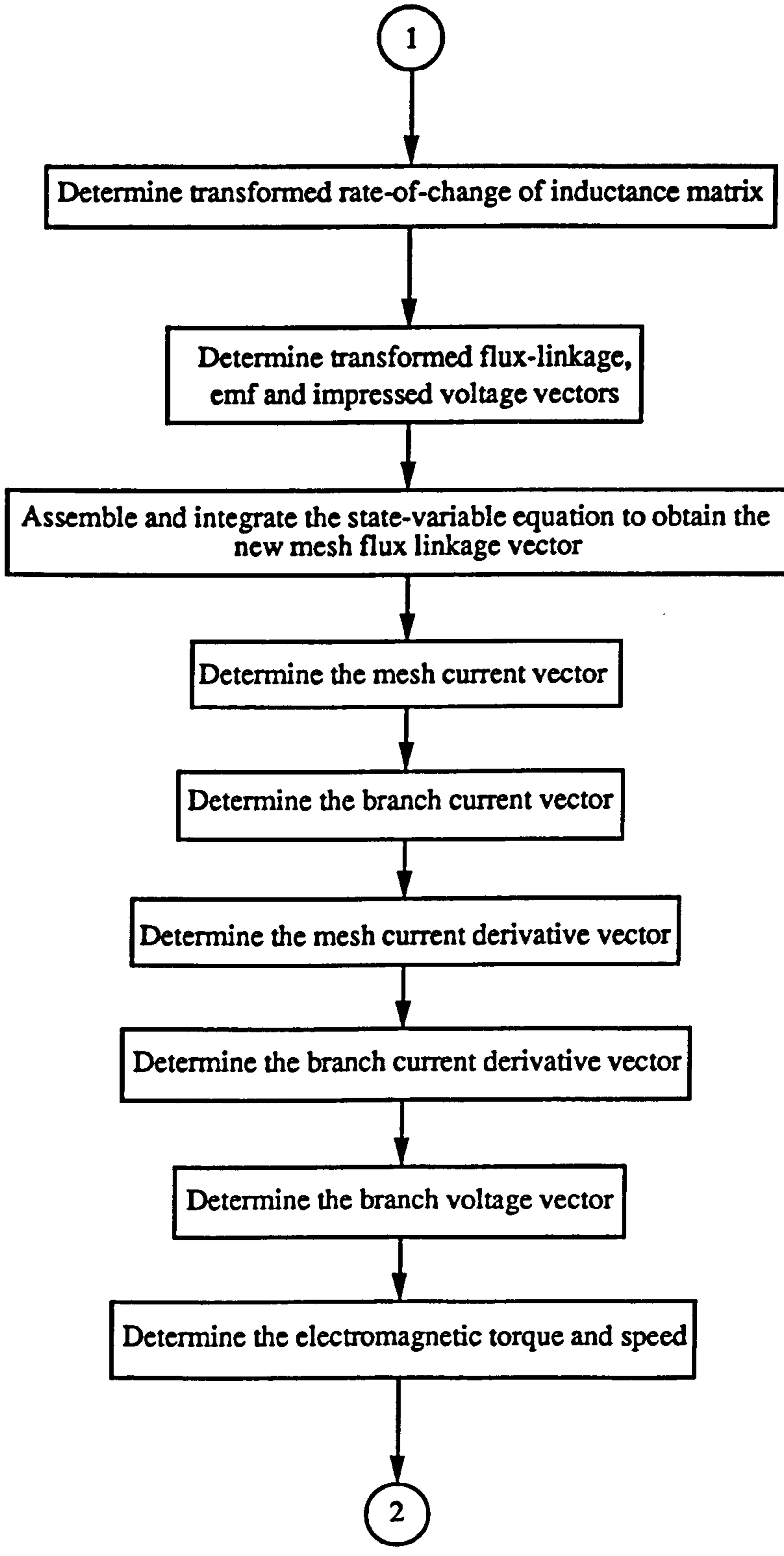

Figure 5.5 Flow chart for motor model

...continued

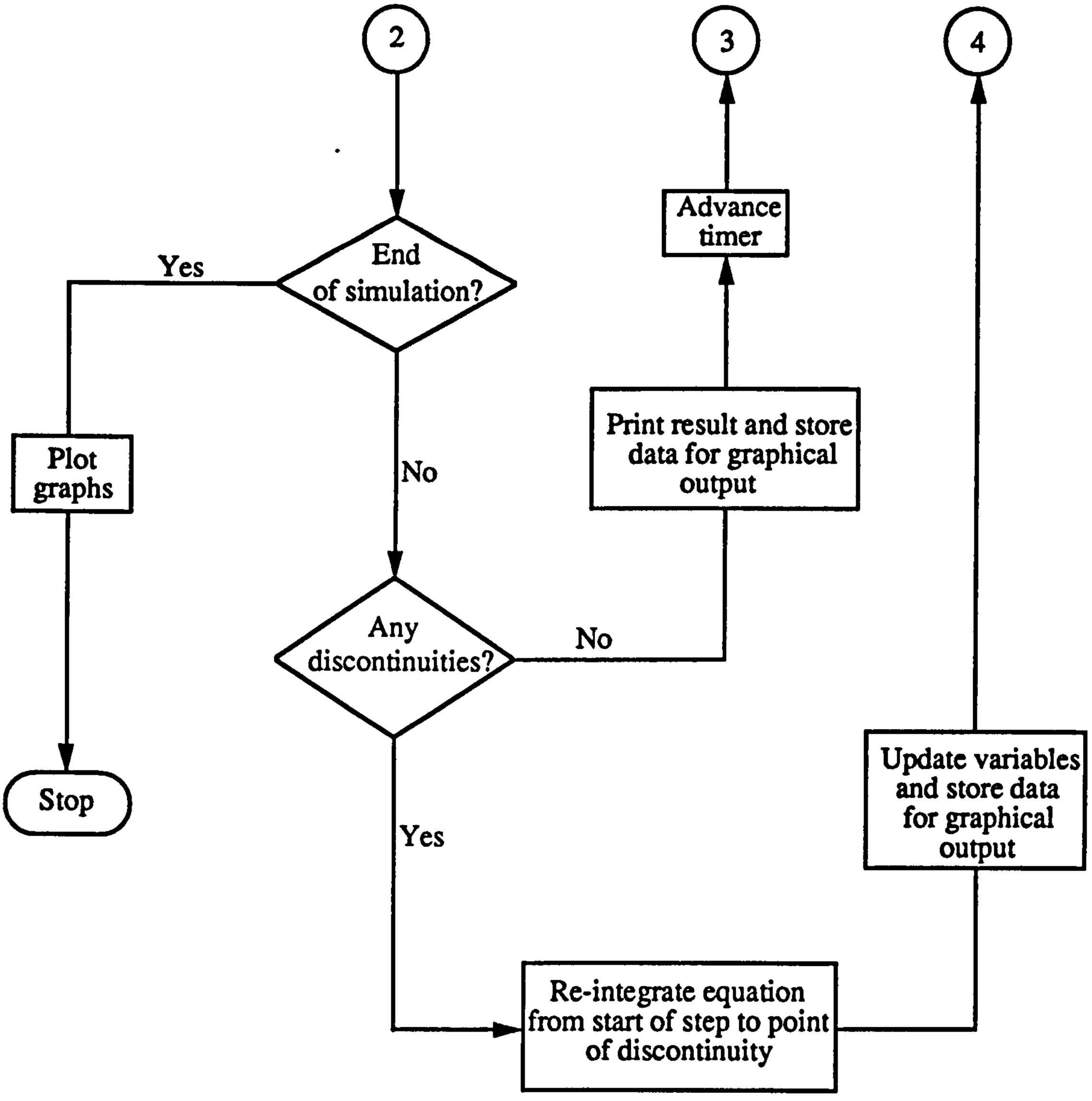

Figure 5.5 Flow chart for motor model

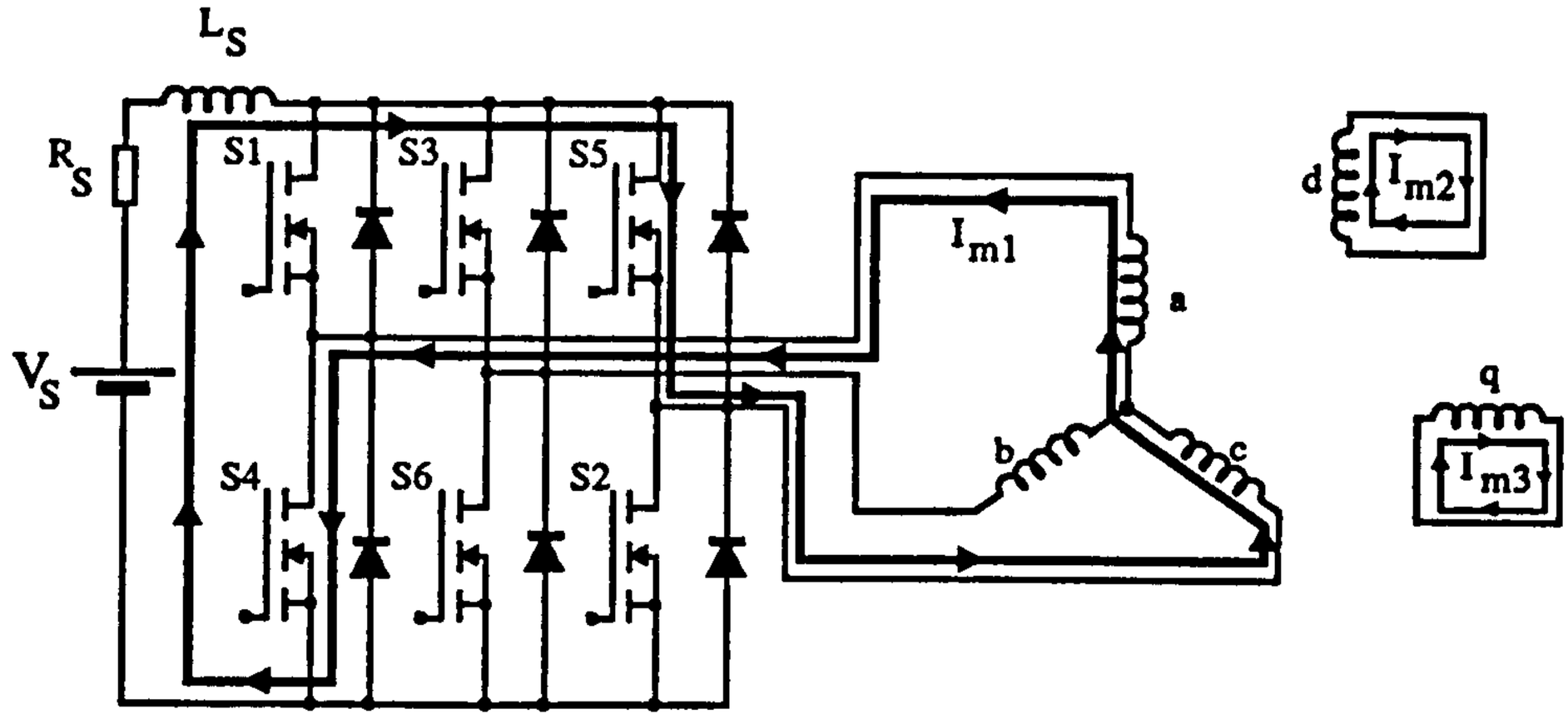

(a) State 1 : S5 and S4 ON

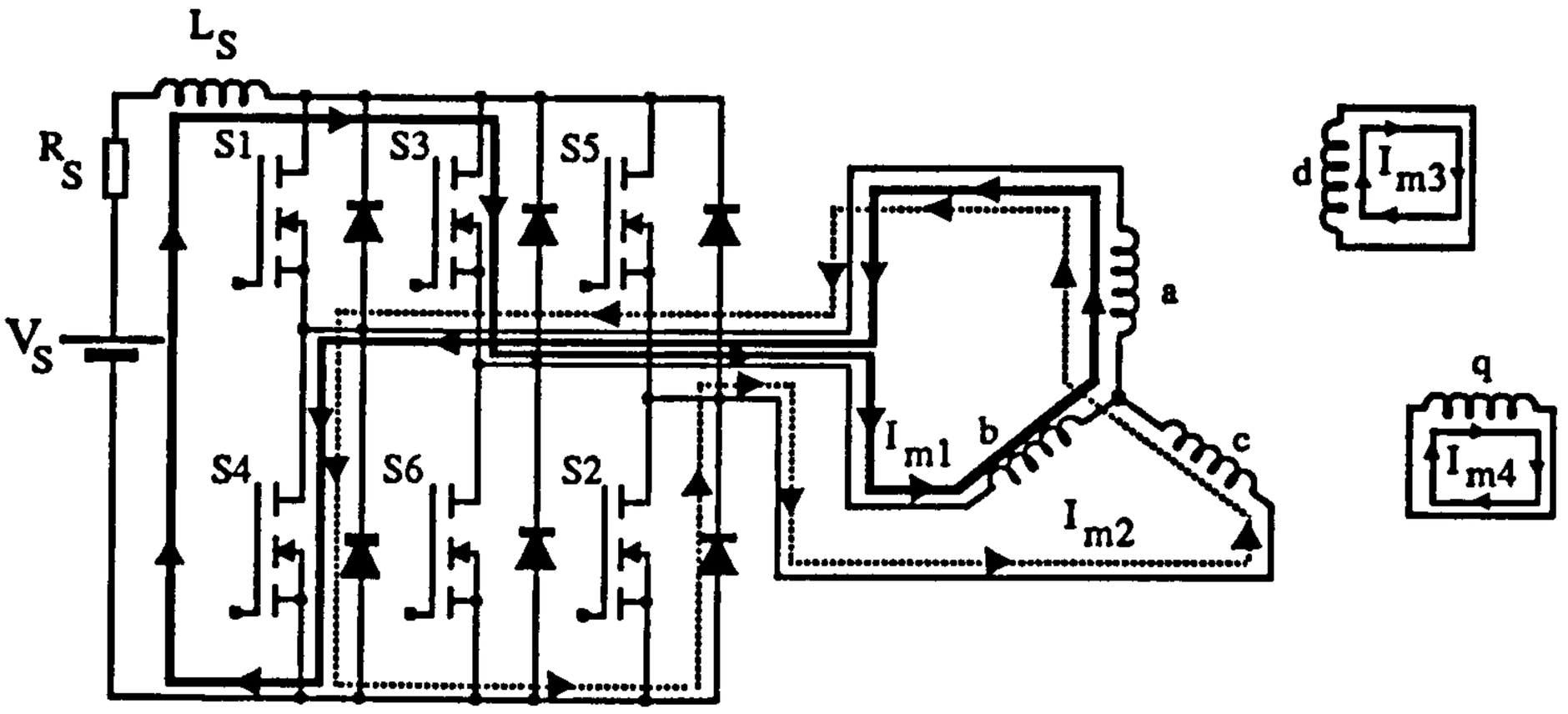

(b) During commutation S3, S4 and D2 ON

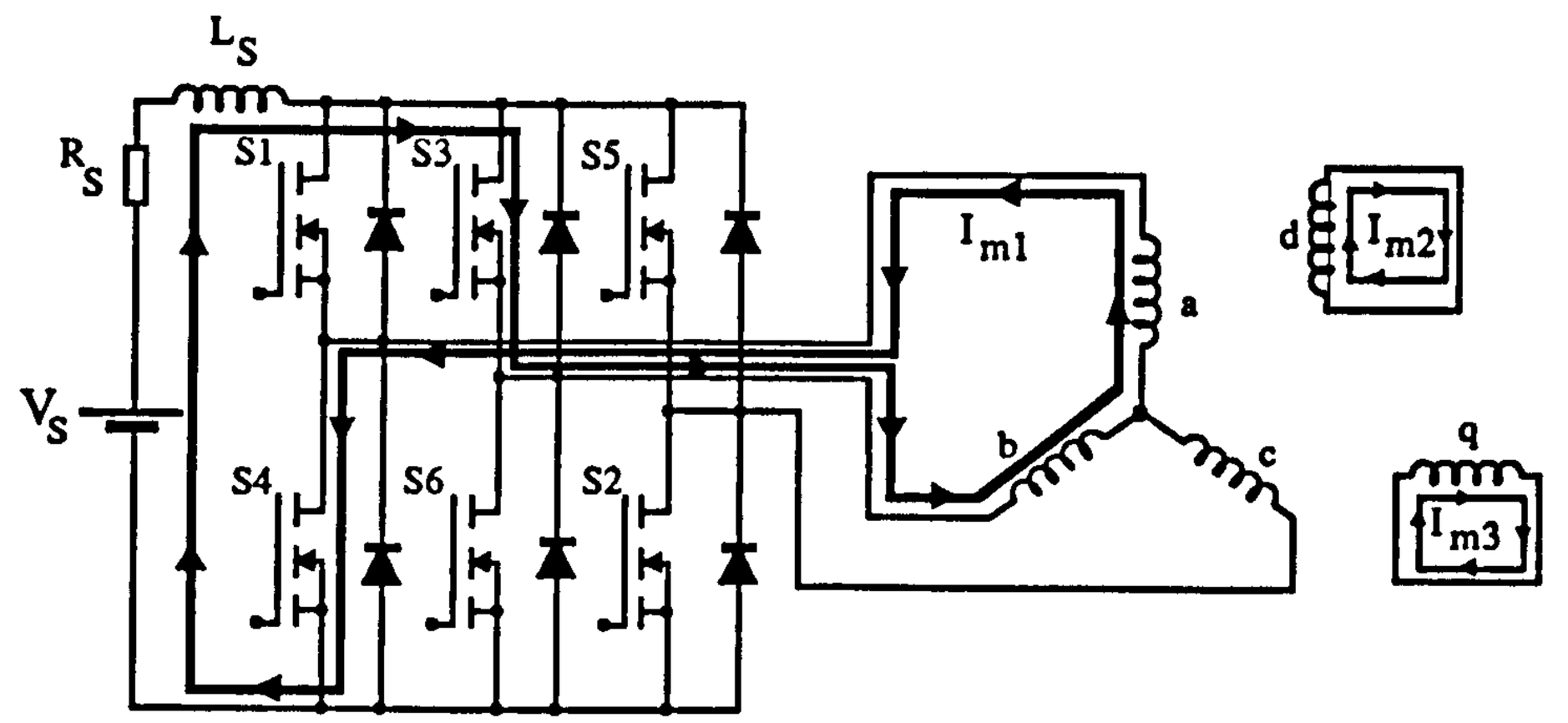

(c) State 2 : S3 and S4 ON

Figure 5.6 Typical system meshes

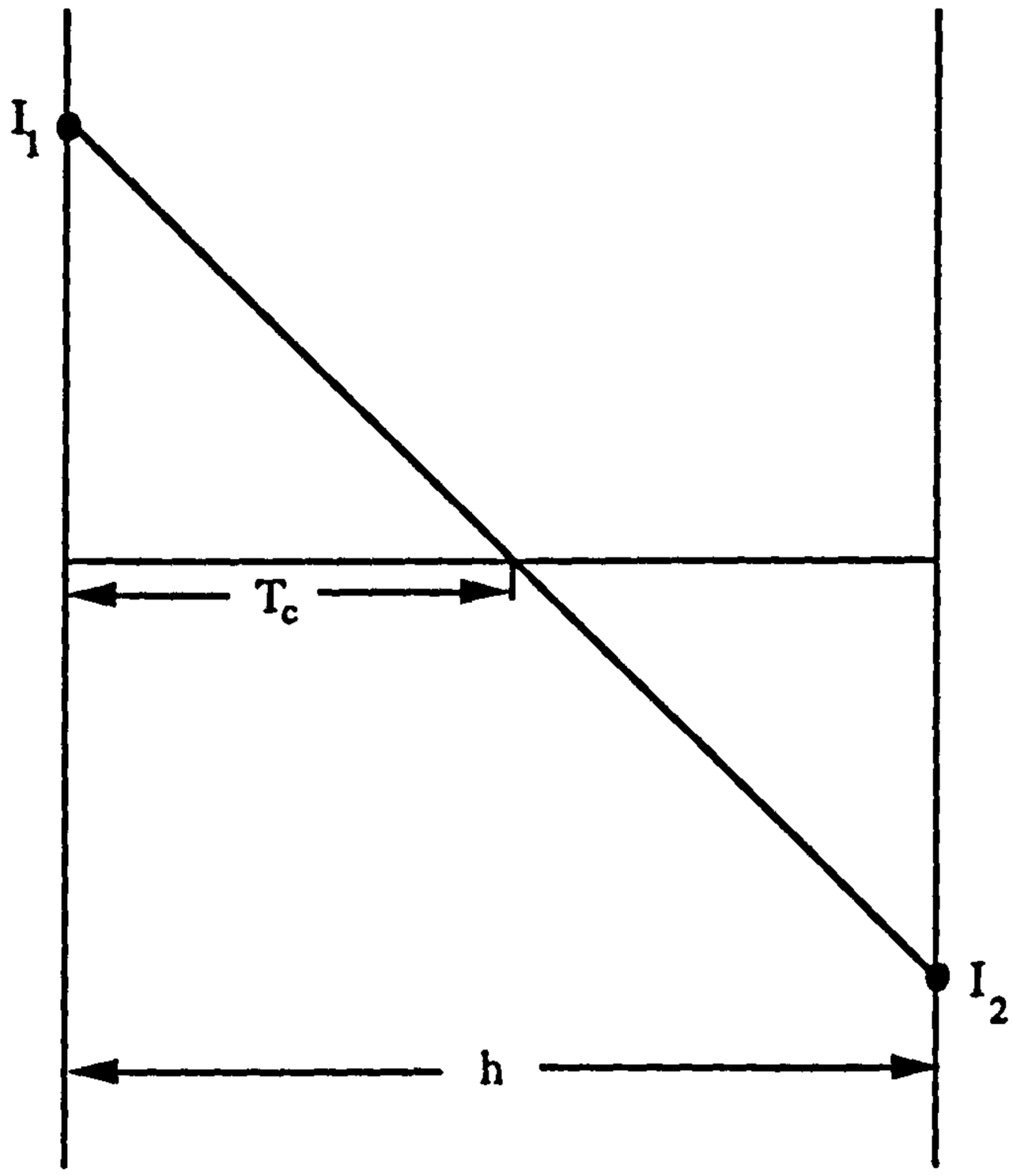

Figure 5.7 Turn-off discontinuity

		MESH													
		1	2	3	4	5	6	7	8	9	10	11	12	13	14
BRANCH	a	0	0	1	1	1	1	0	0	-1	-1	-1	-1	0	0
	b	1	1	0	0	-1	-1	-1	-1	0	0	1	1	0	0
	c	-1	-1	-1	-1	0	0	1	1	1	1	0	0	0	0
	d	0	0	0	0	0	0	0	0	0	0	0	0	1	0
	q	0	0	0	0	0	0	0	0	0	0	0	0	0	1
	s	1	0	1	0	1	0	1	0	1	0	1	0	0	0

1 = the branch current has the same sense as the mesh current.
-1 = the branch current has the reversed sense to the mesh current.
0 = no mesh current in that branch.

Figure 5.8 Master matrix

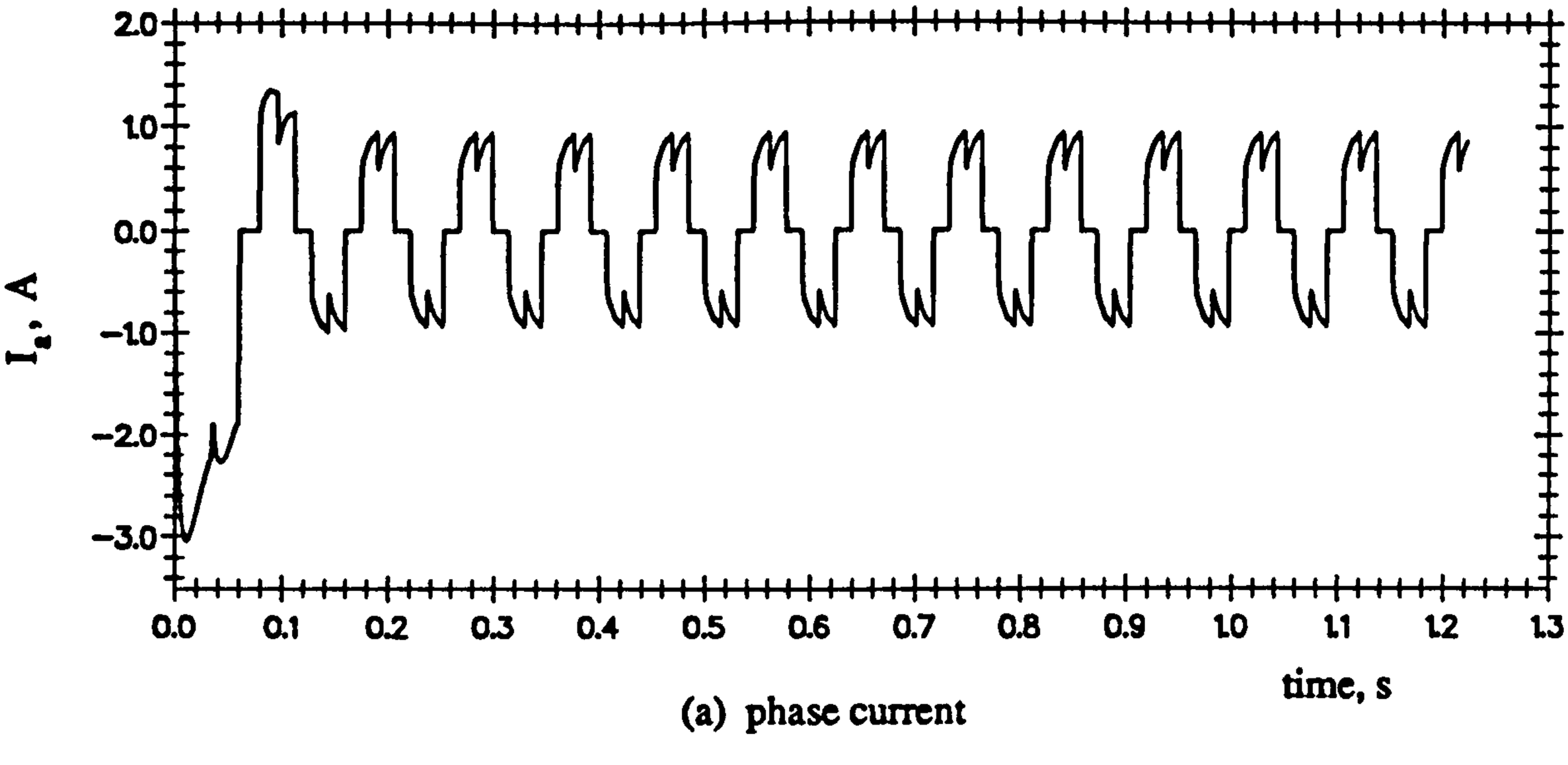

(a) phase current

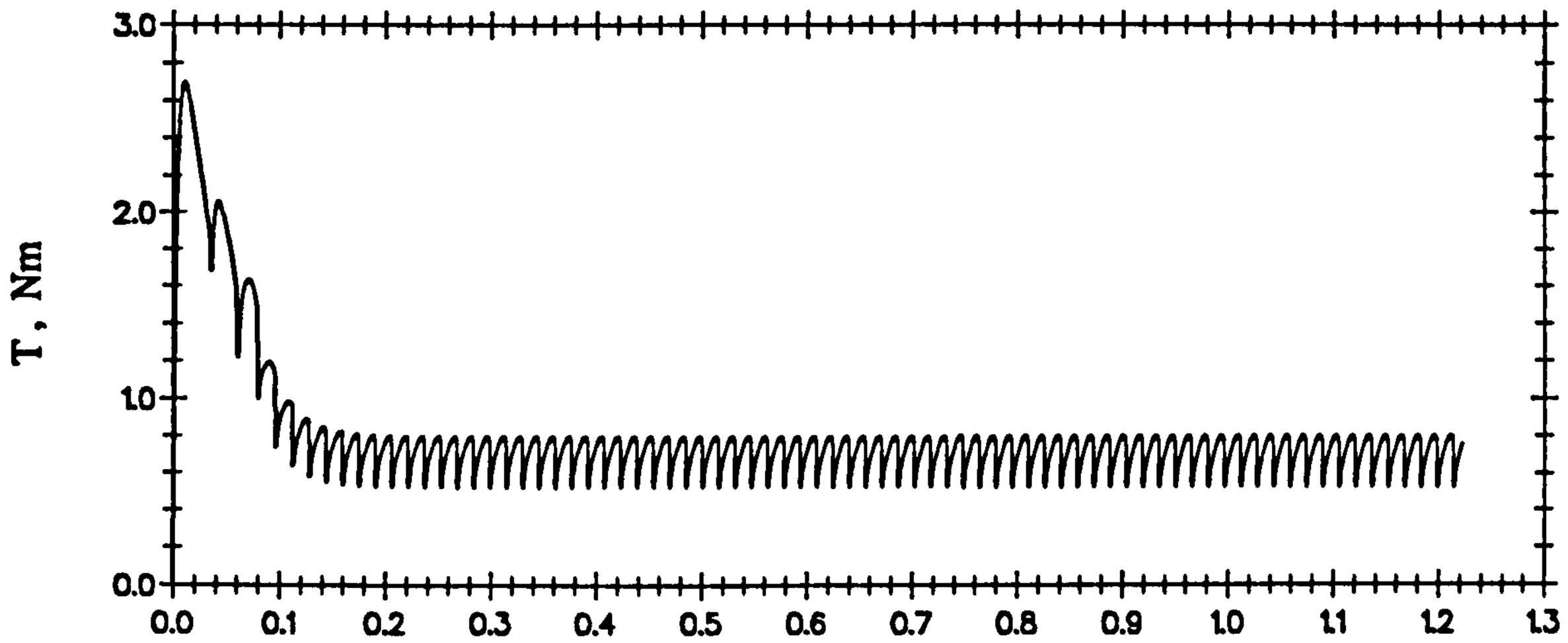

(b) motor torque

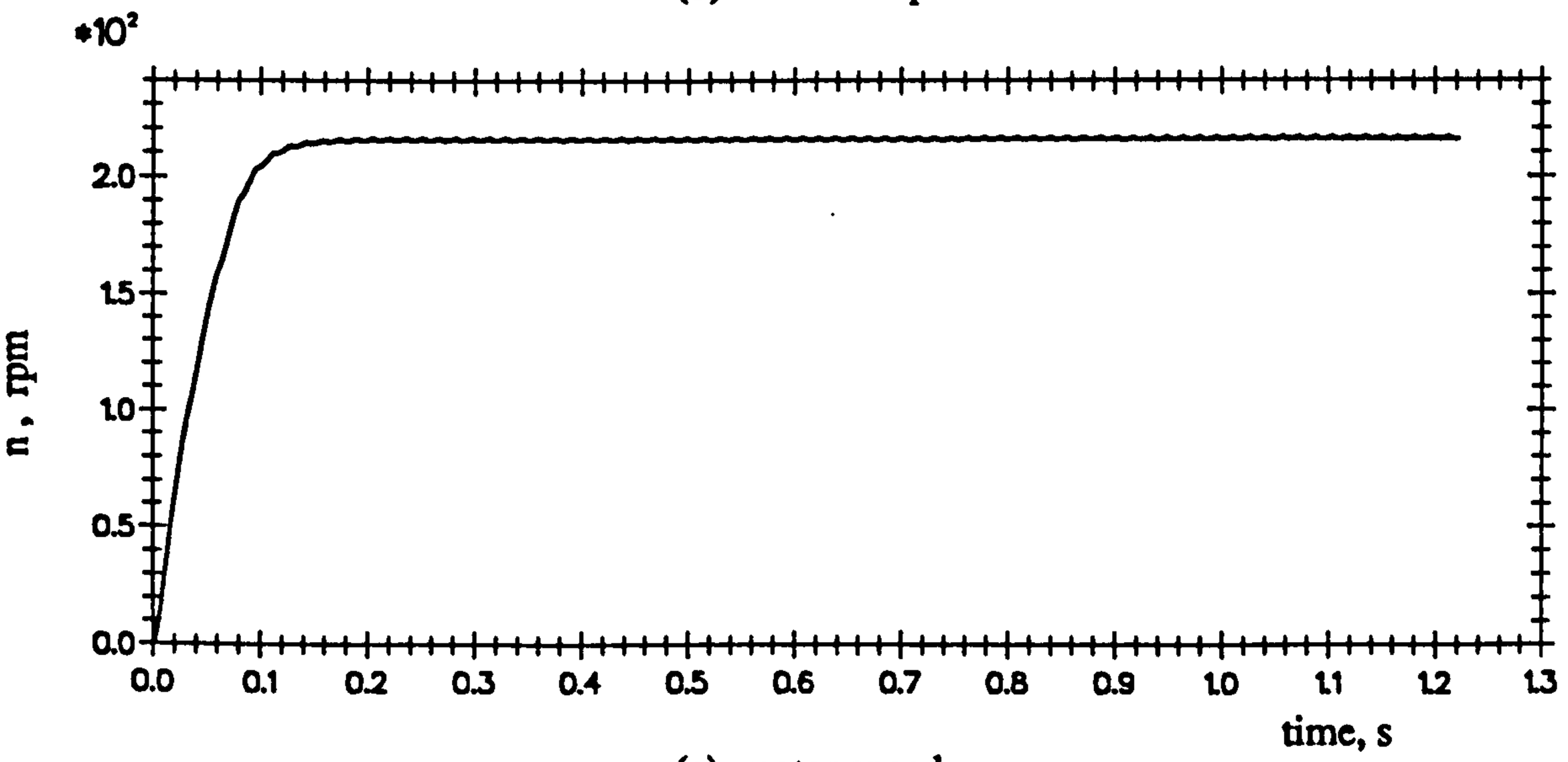

(c) motor speed

Figure 5.9 Simulated waveforms (Load condition : 0.7Nm at 222rpm)

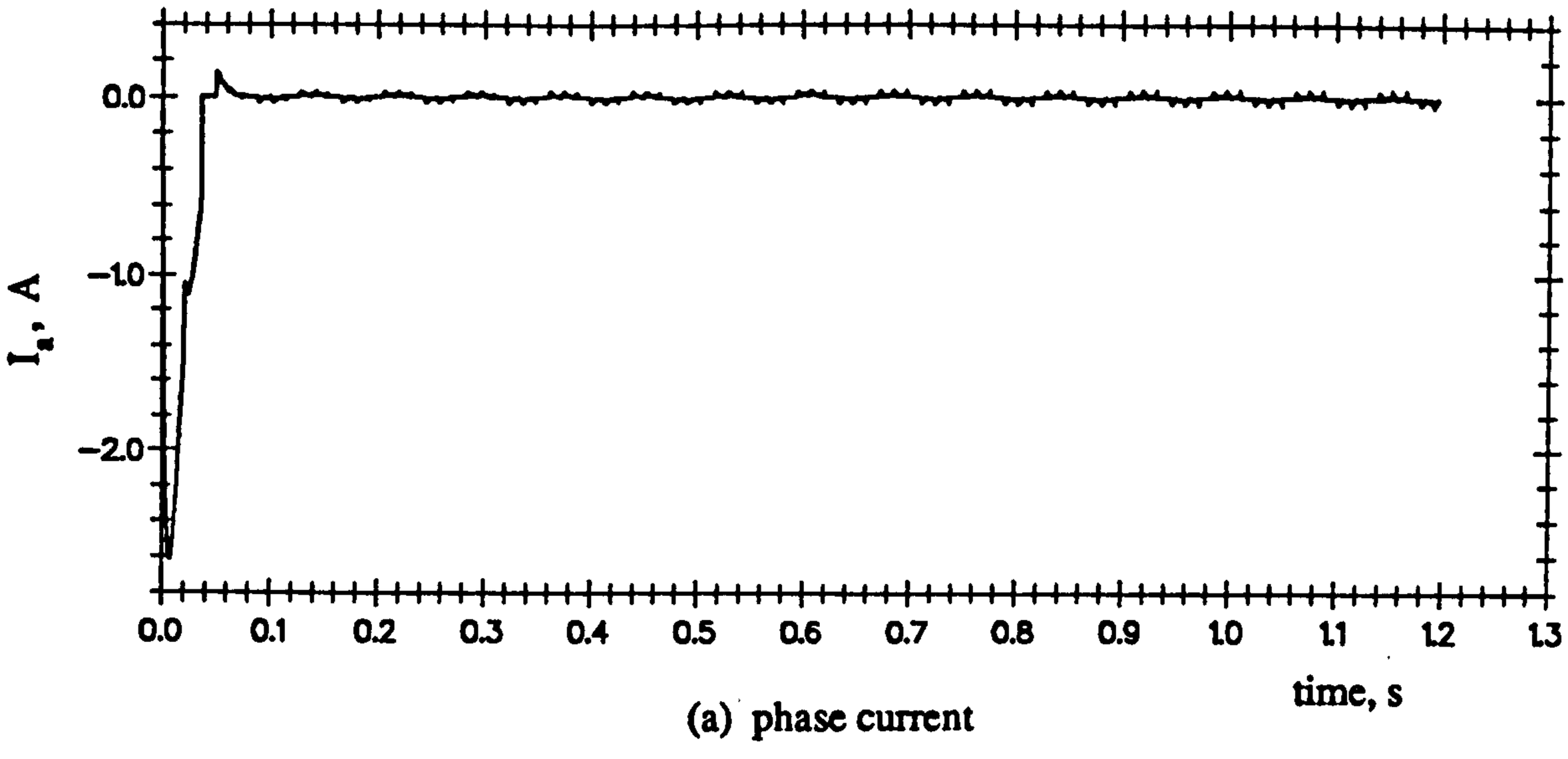

(a) phase current

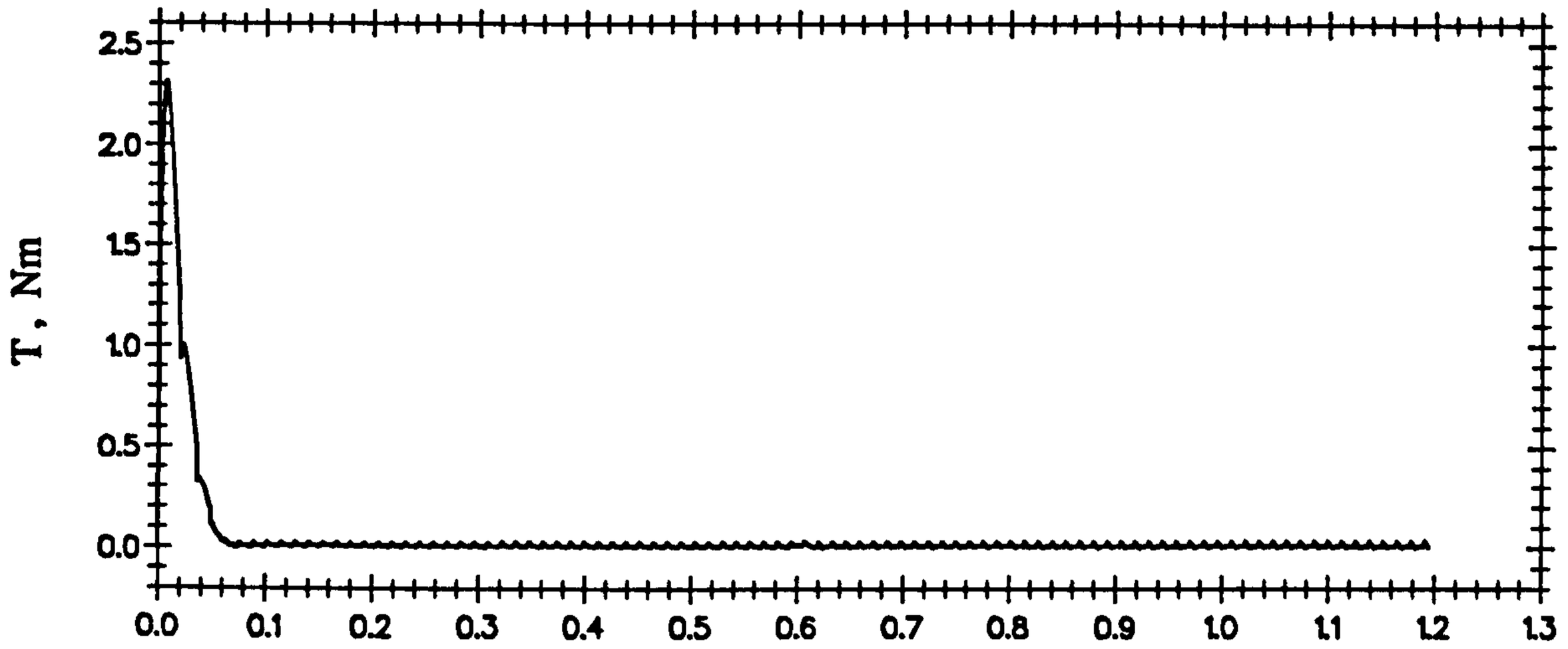

(b) motor torque

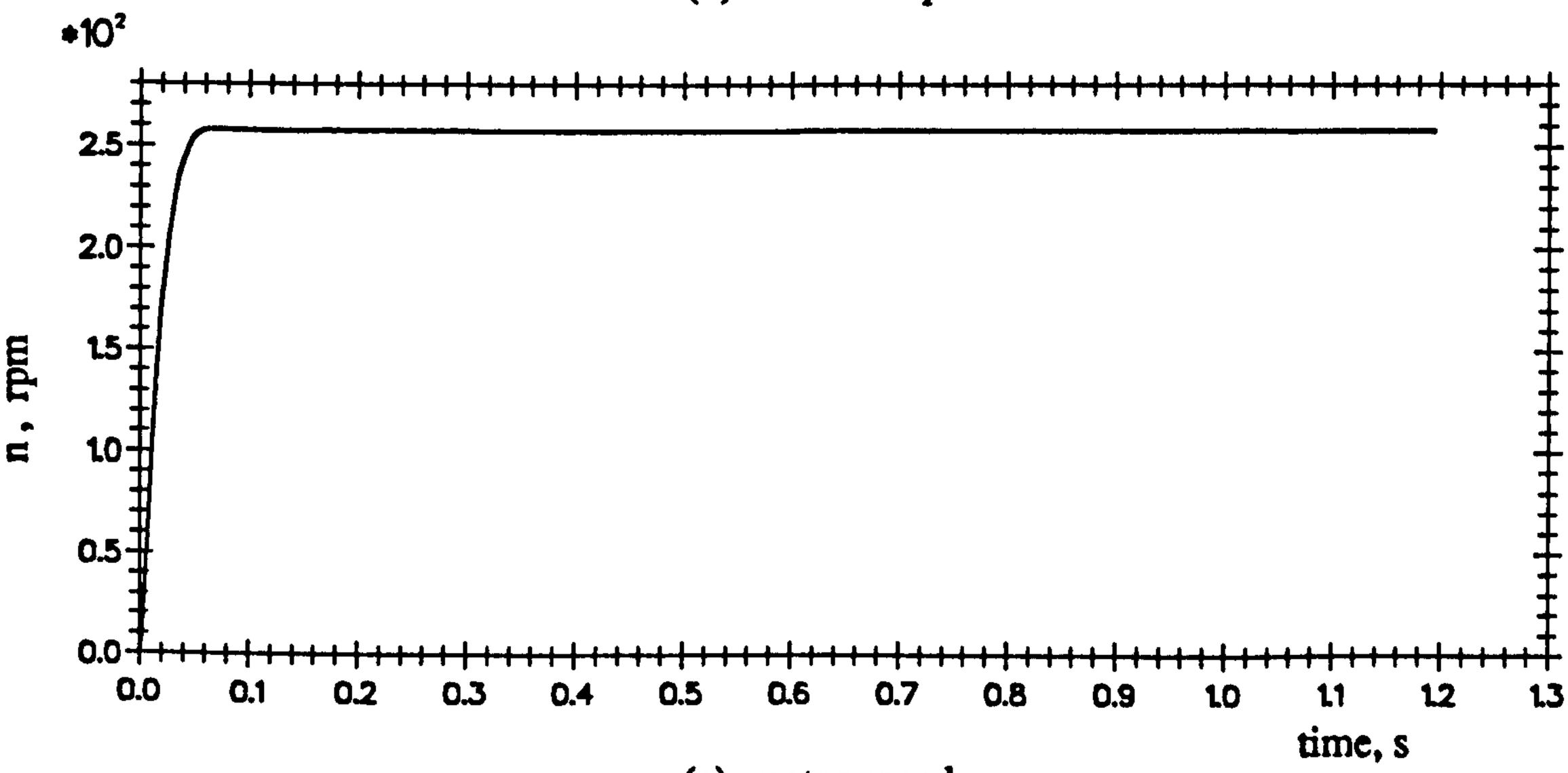

(c) motor speed

Figure 5.10 Simulated waveforms (No-load condition)

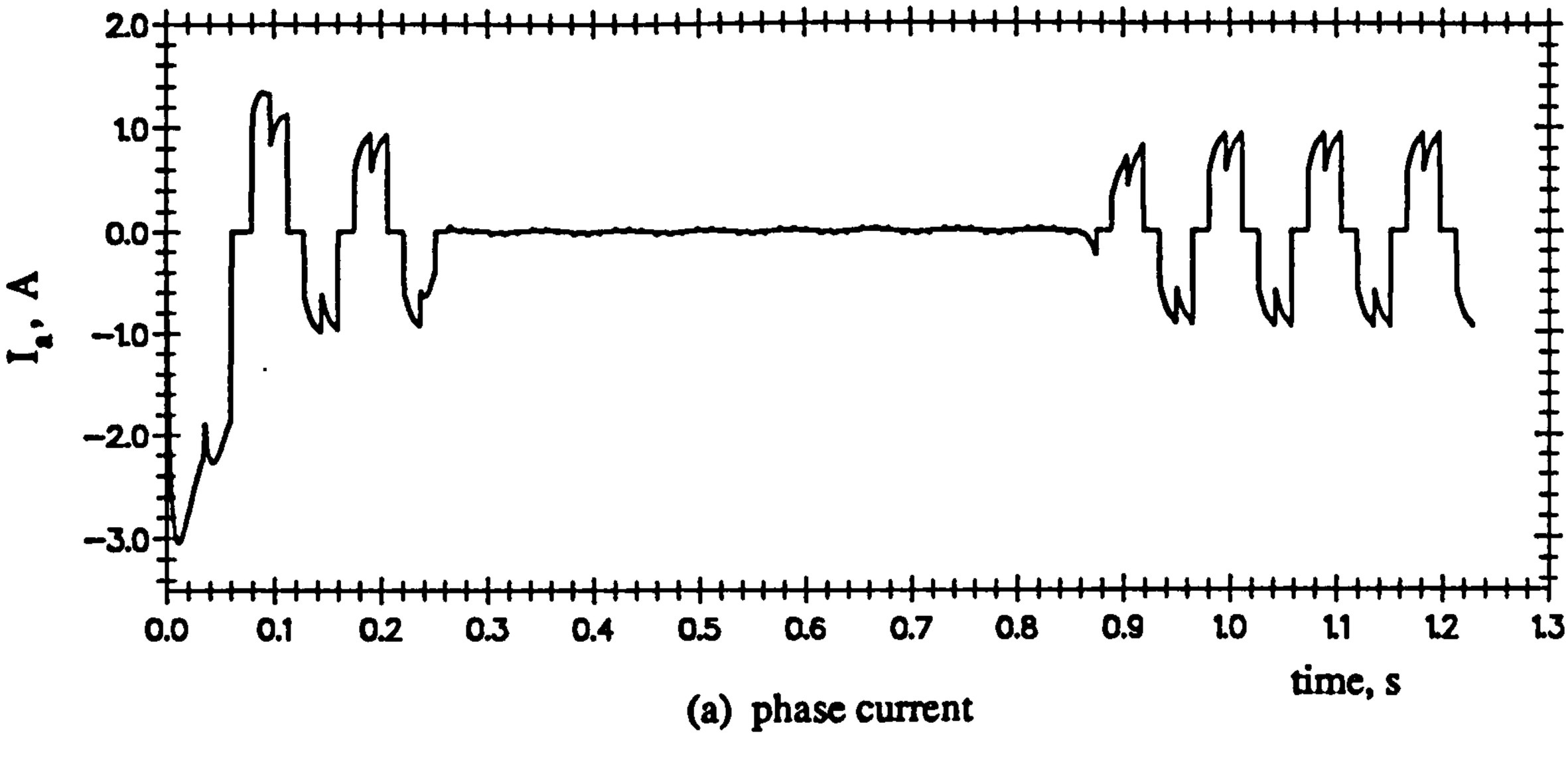

(a) phase current

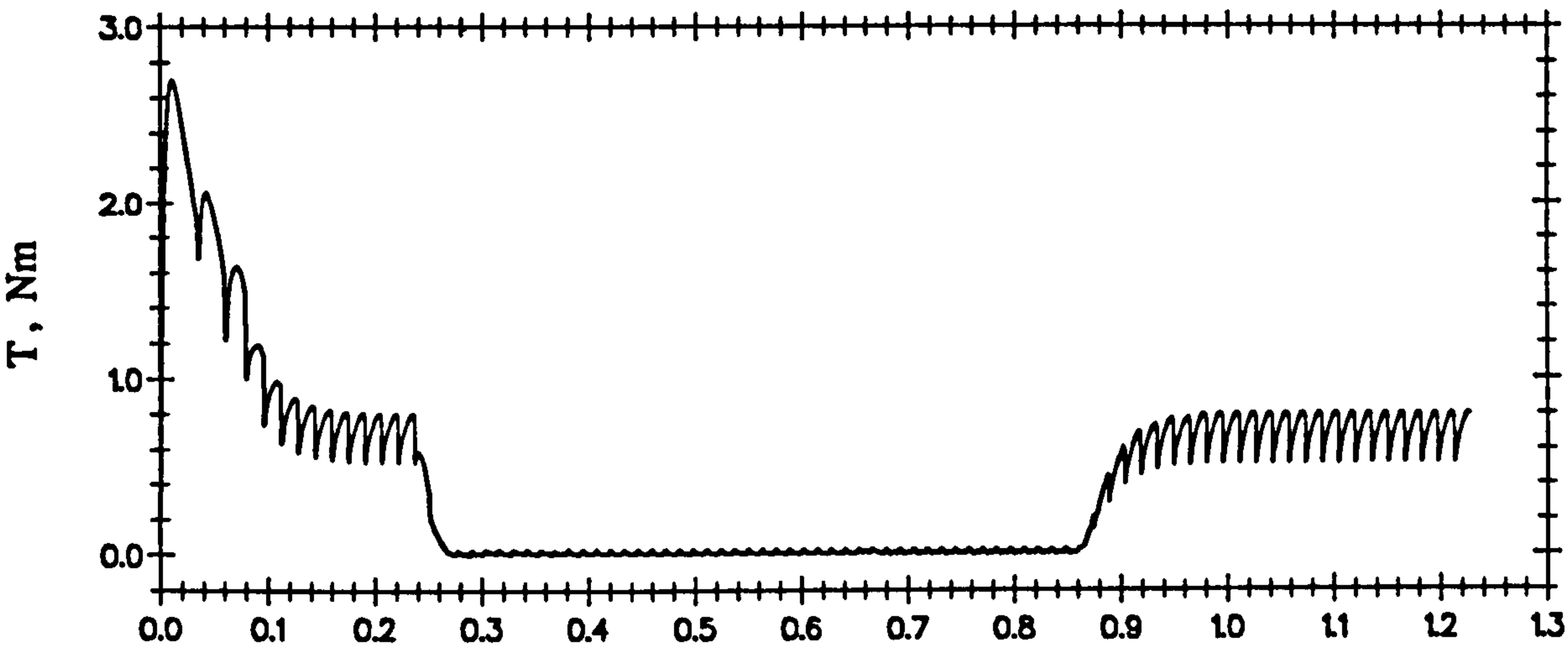

(b) motor torque

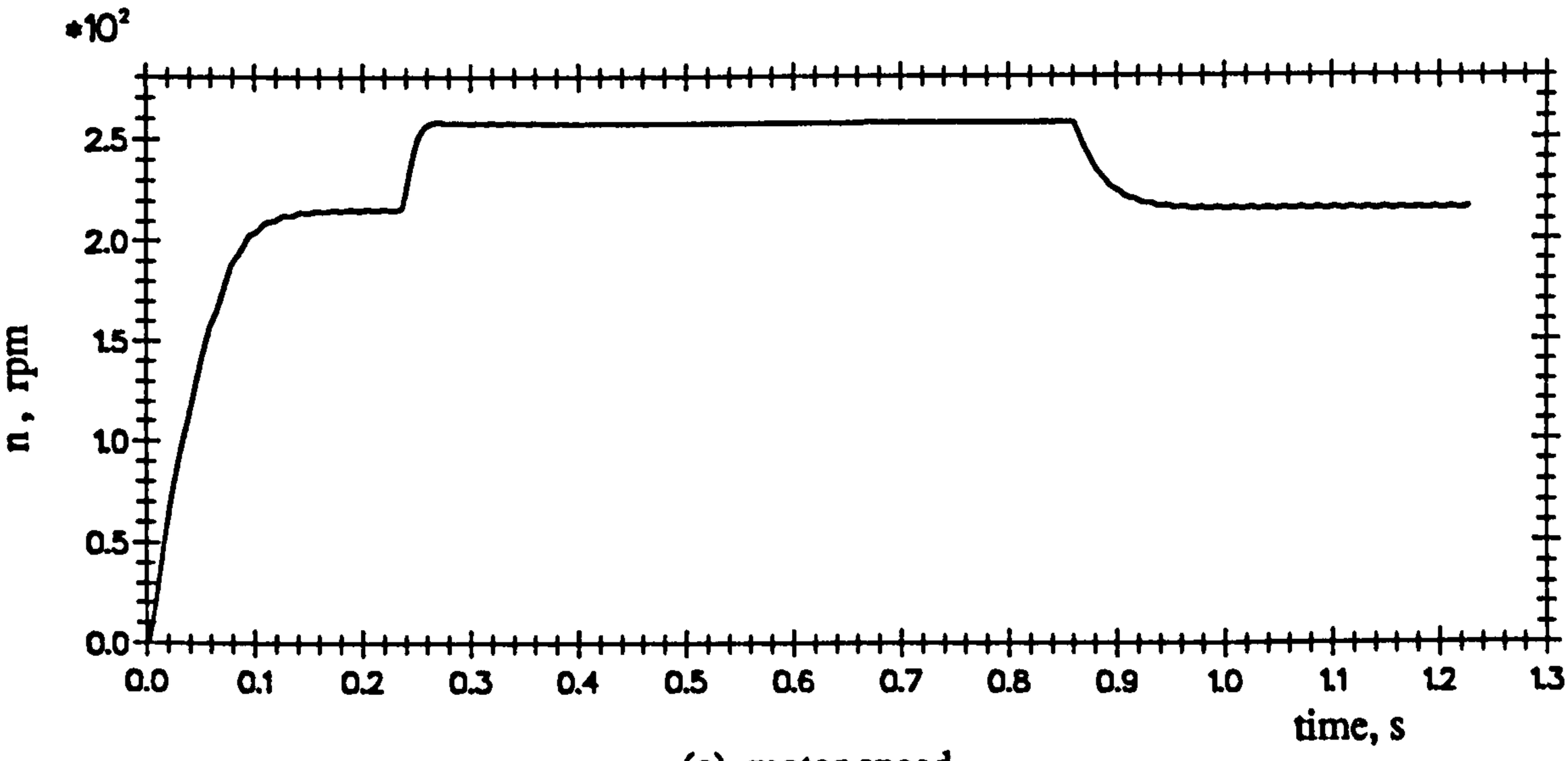

(c) motor speed

Figure 5.11 Simulated waveforms during load change

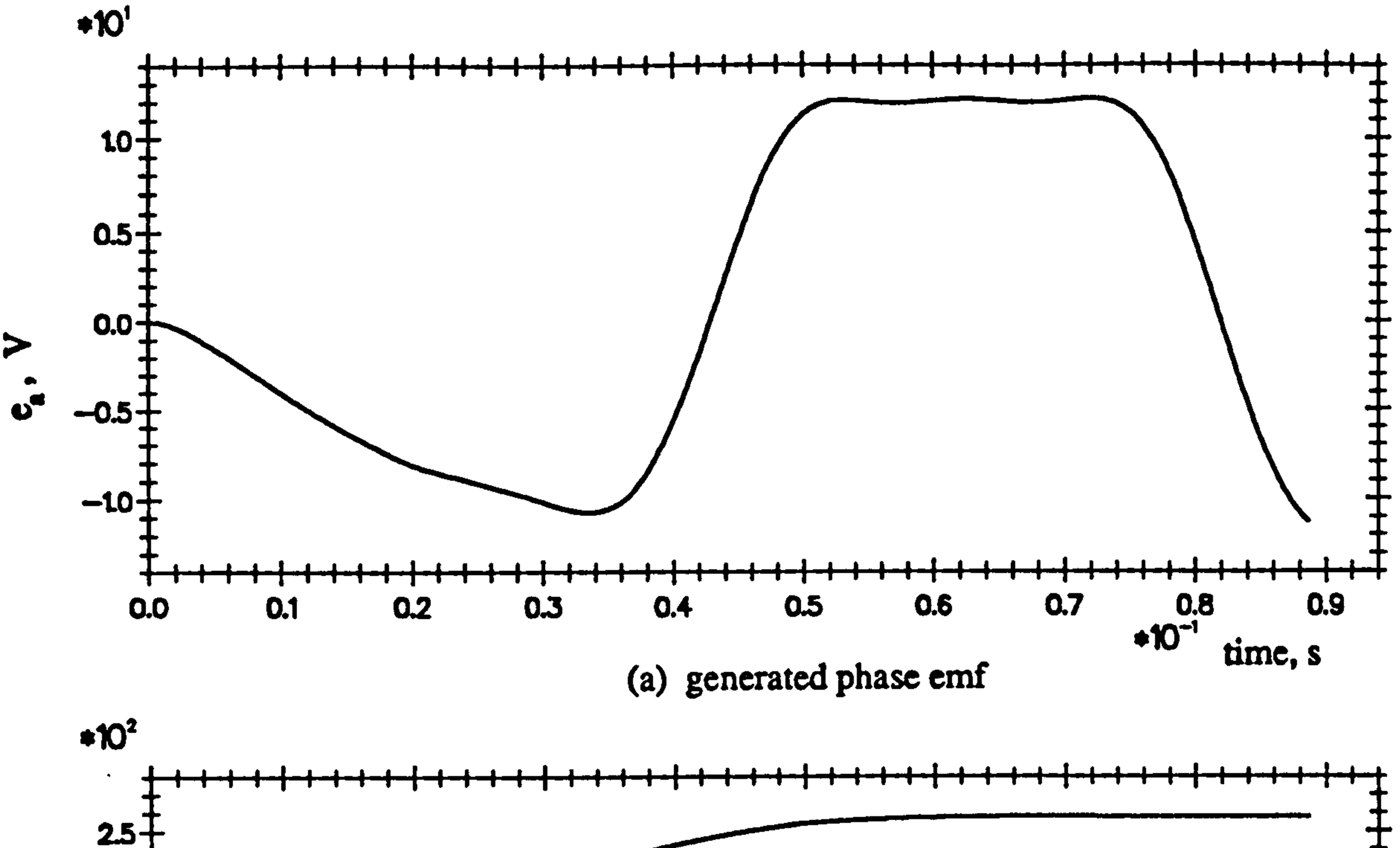

(a) generated phase emf

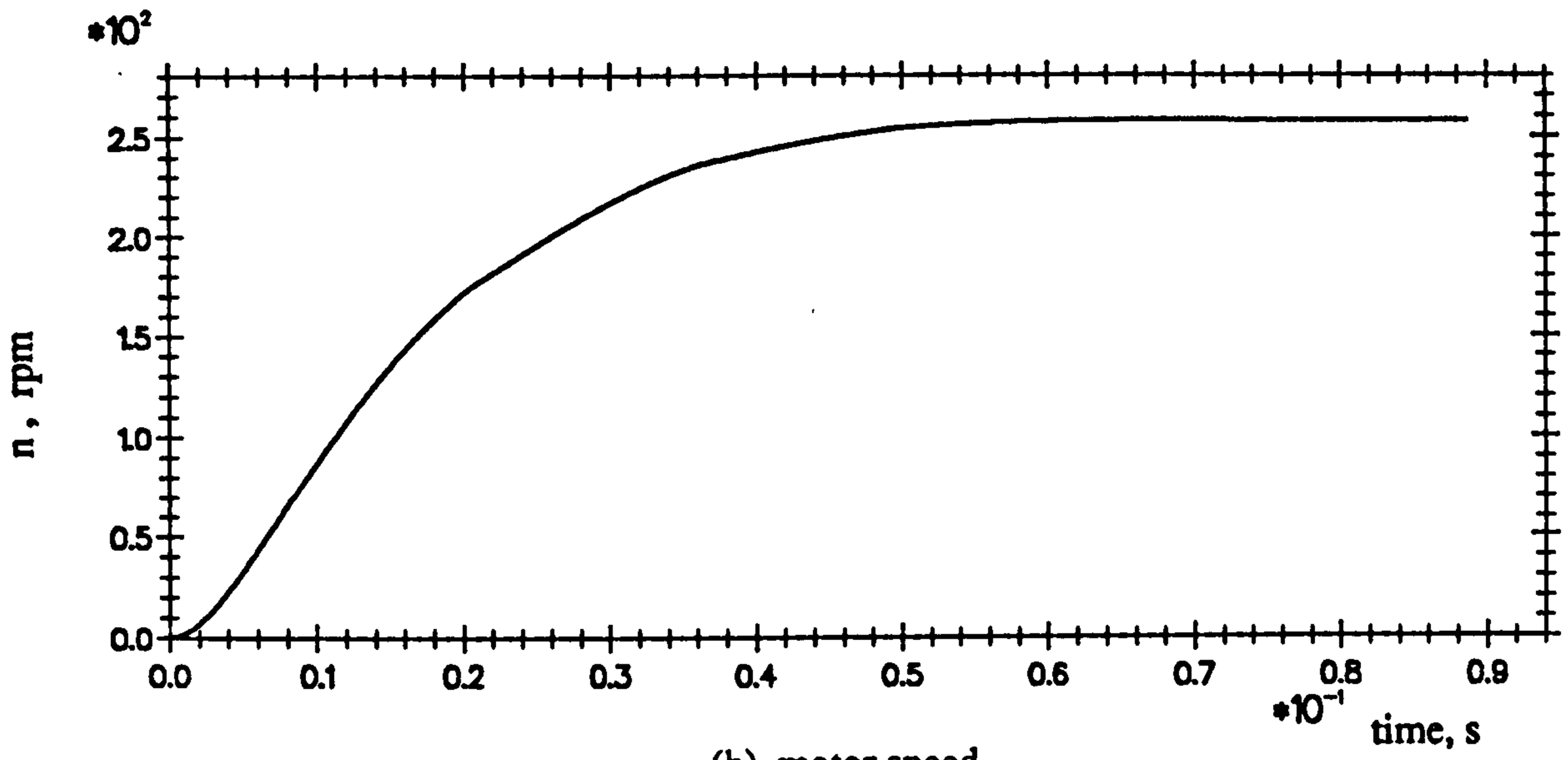

(b) motor speed

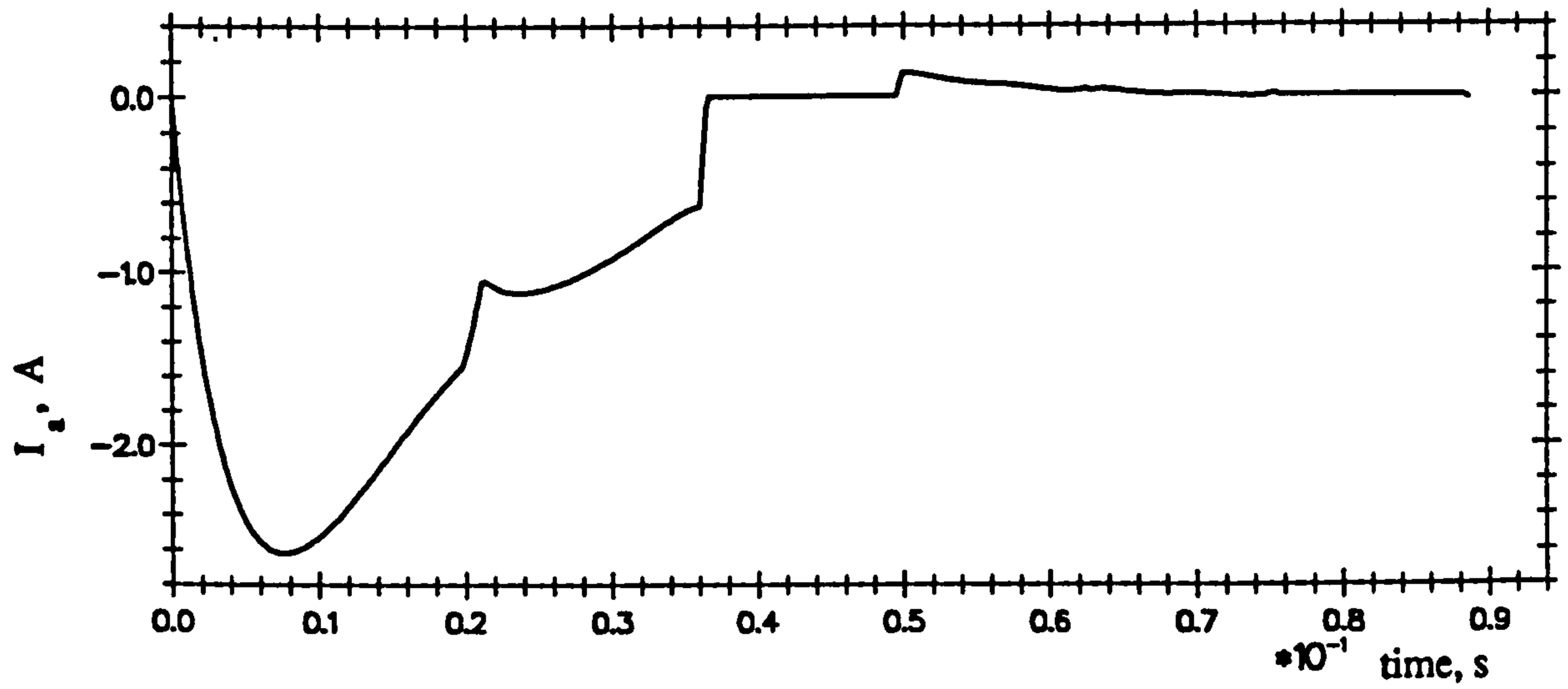

(c) phase current

Figure 5.12 Current inrush phenomenon during starting

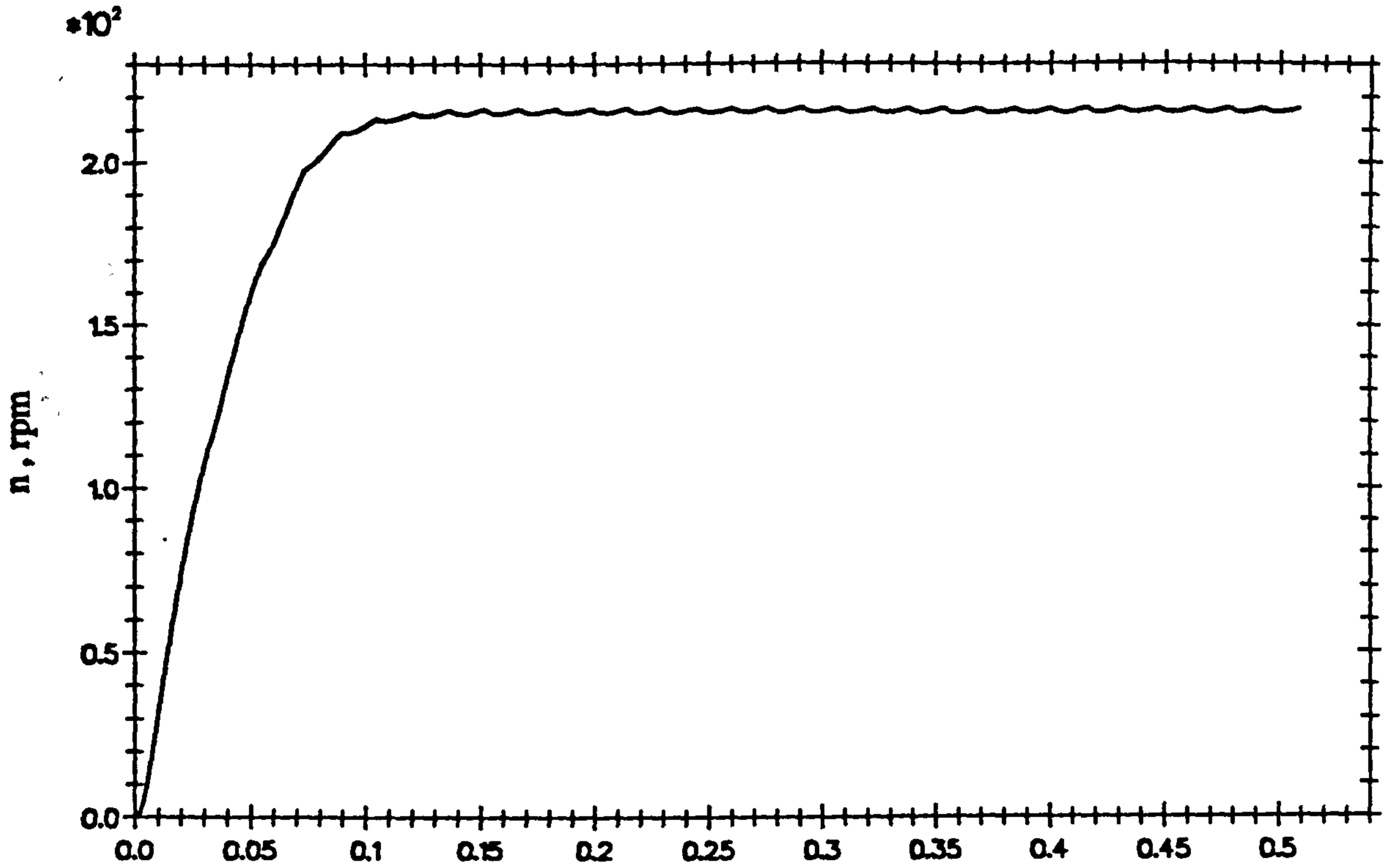

(a) simulated waveform

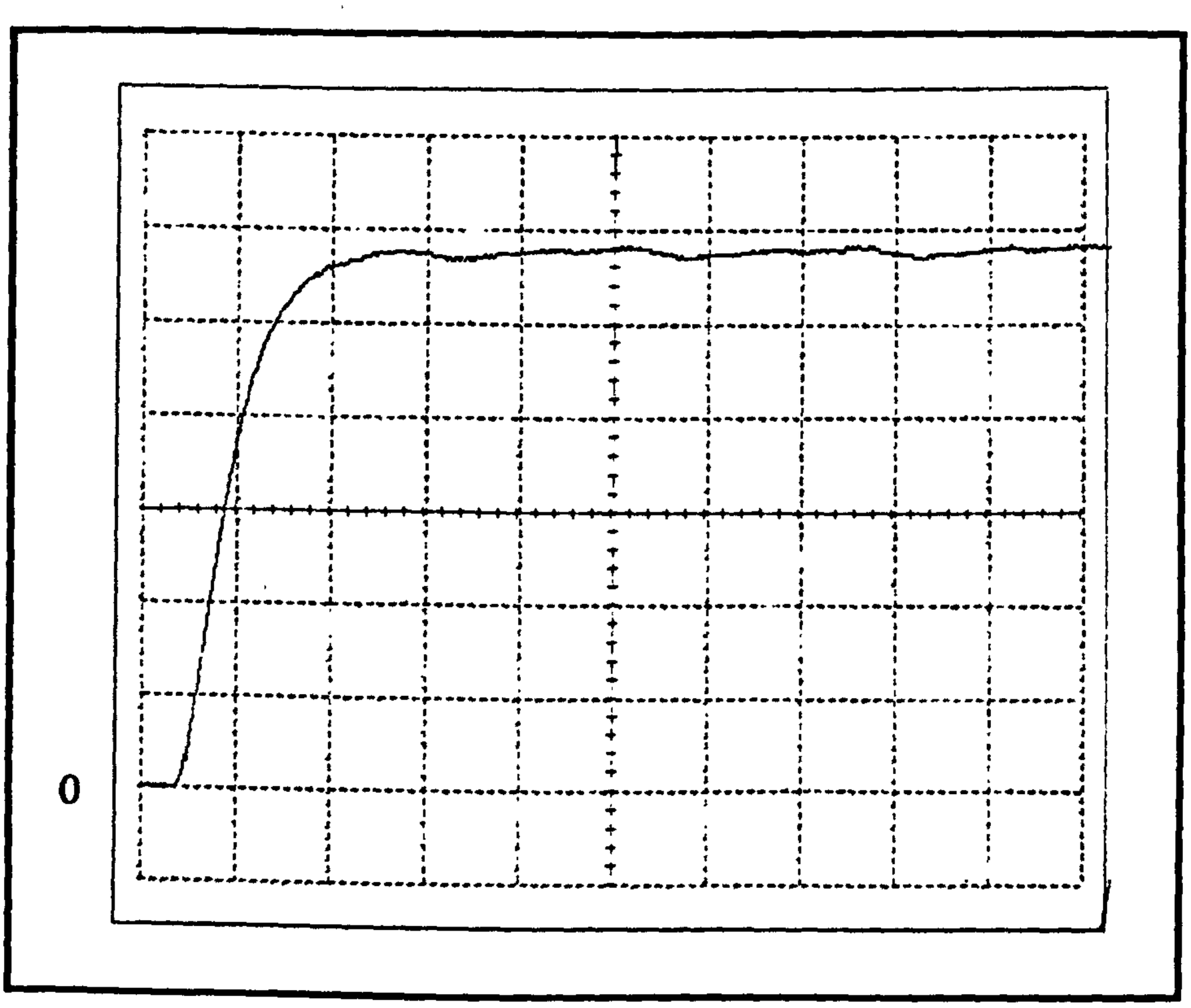

(b) measured waveform

Figure 5.13 Motor speed waveforms during starting
(Load condition : 0.7Nm at 222 rpm)

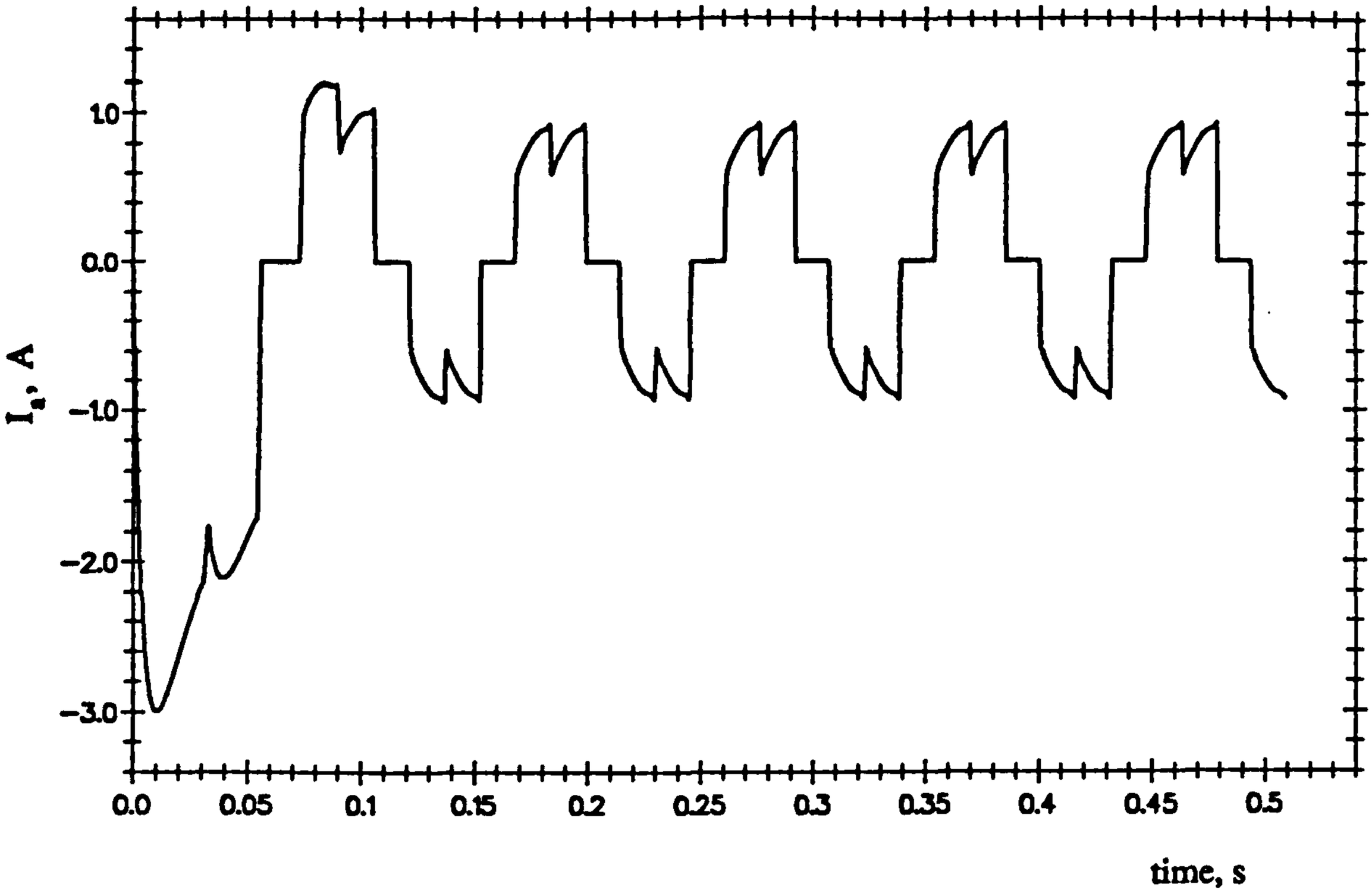

(a) simulated waveform

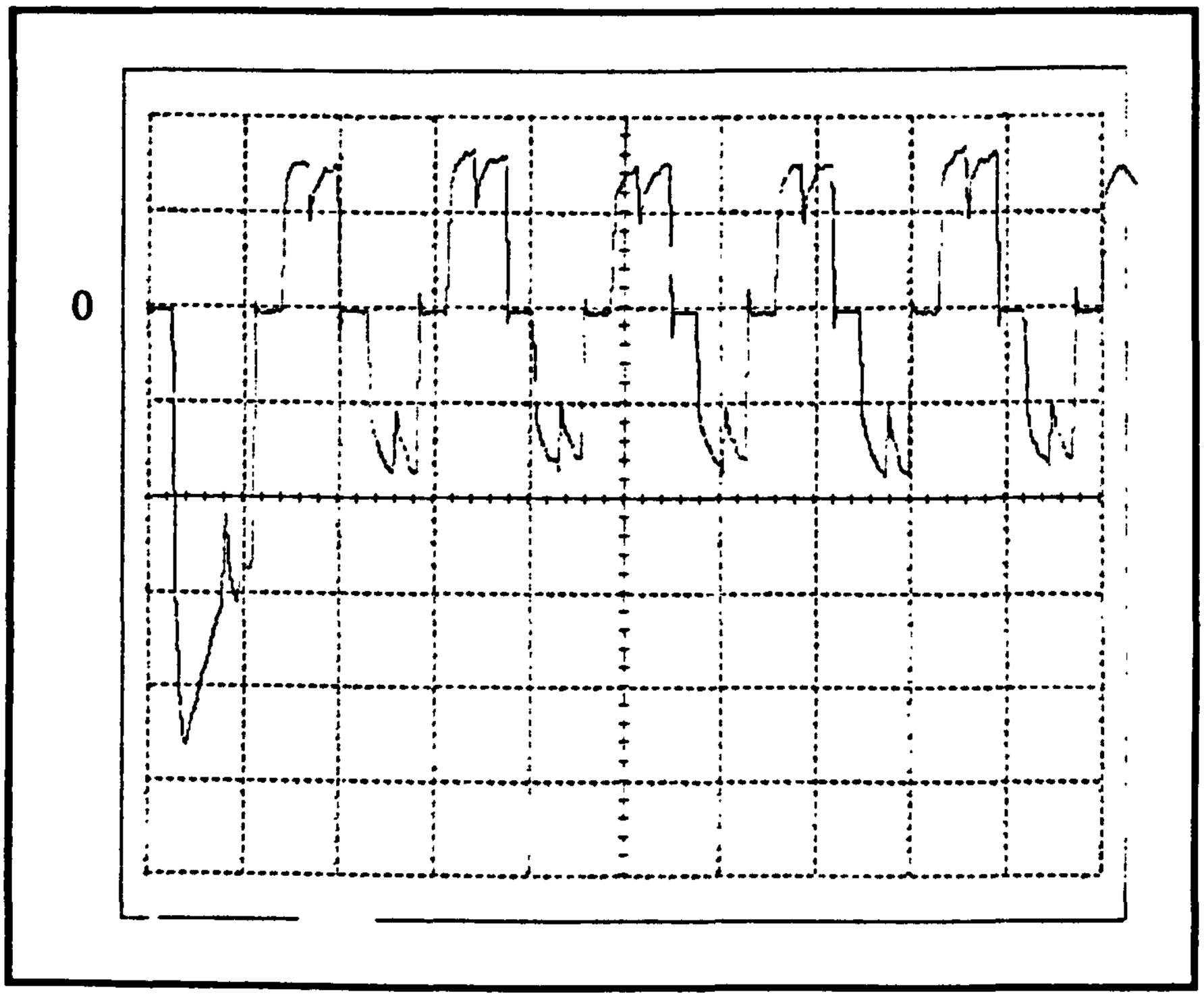

(b) measured waveform

Figure 5.14 Phase current waveforms during starting
(Load condition : 0.7Nm at 222 rpm)

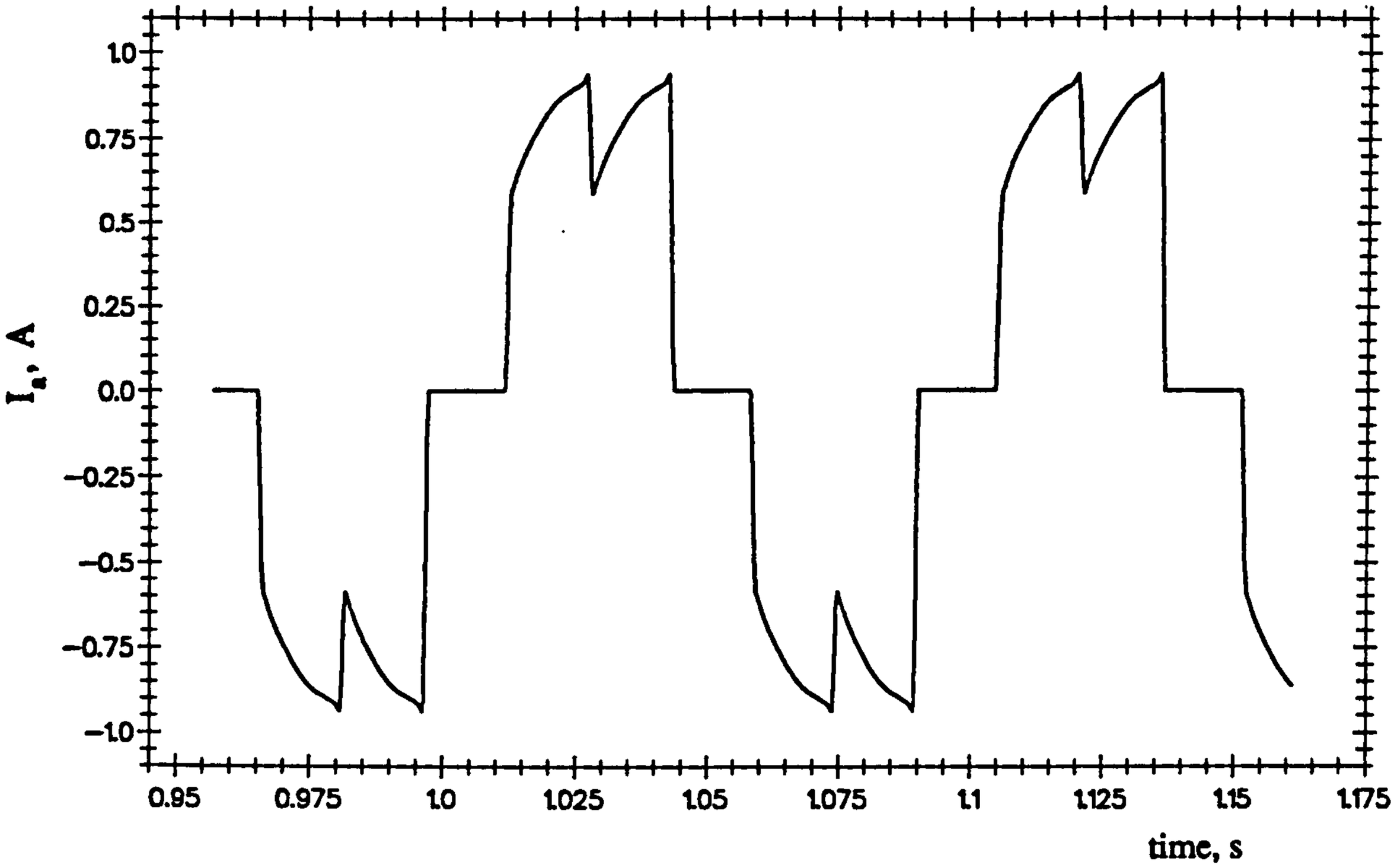

(a) simulated waveform

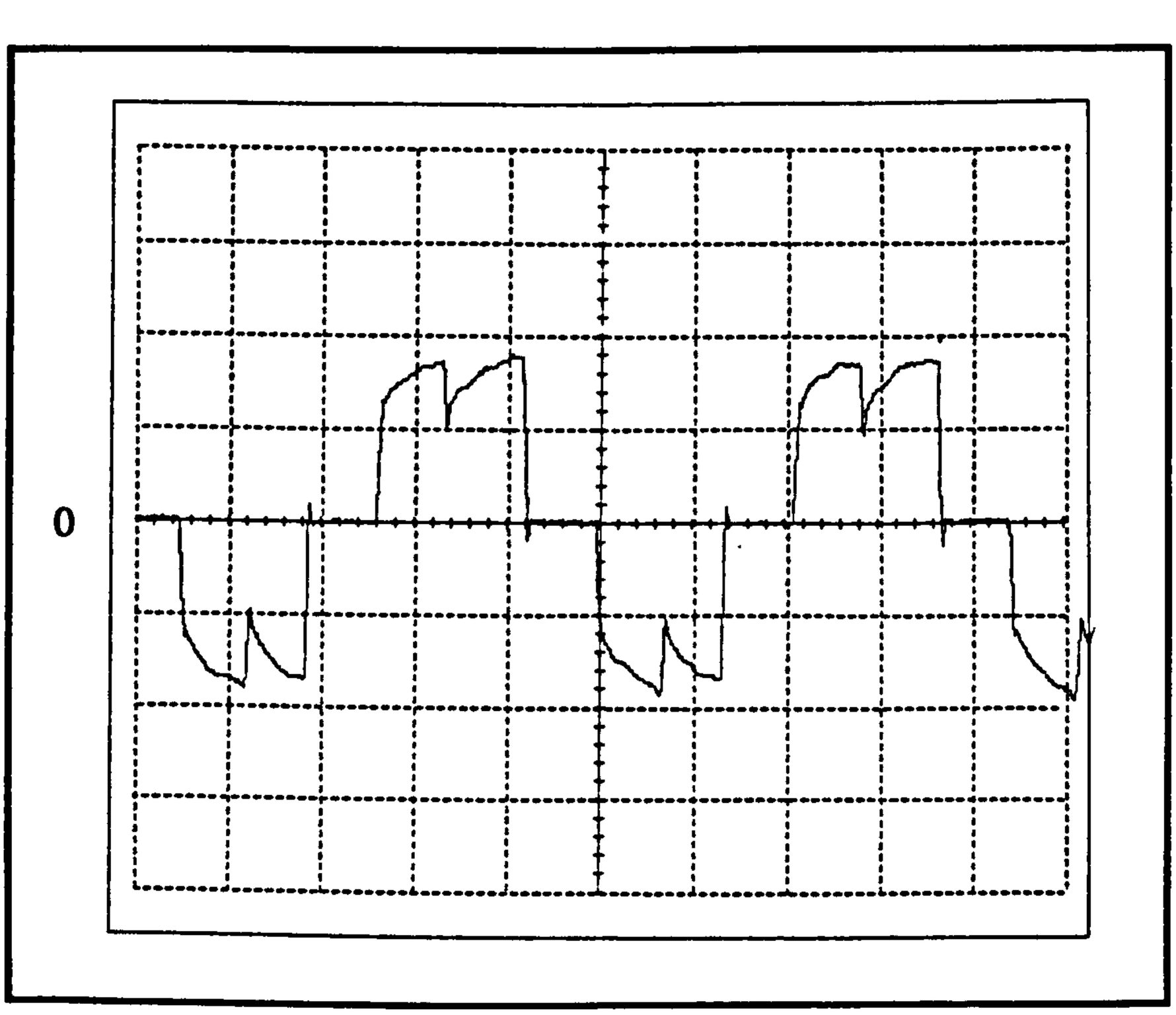

(b) measured waveform

Figure 5.15 Phase current waveforms without PWM control
(Load condition : 0.7Nm at 222 rpm)

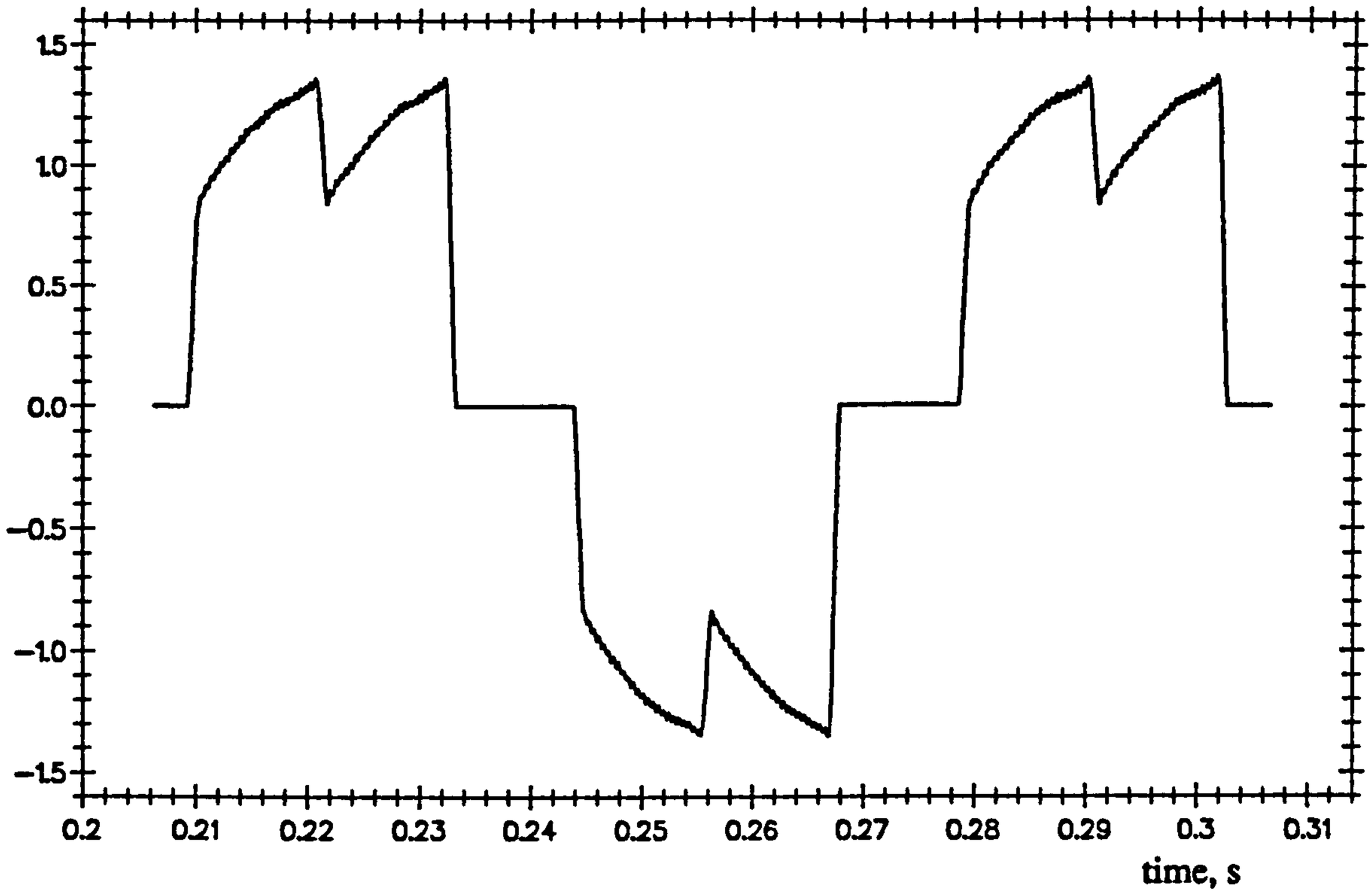

(a) simulated waveform

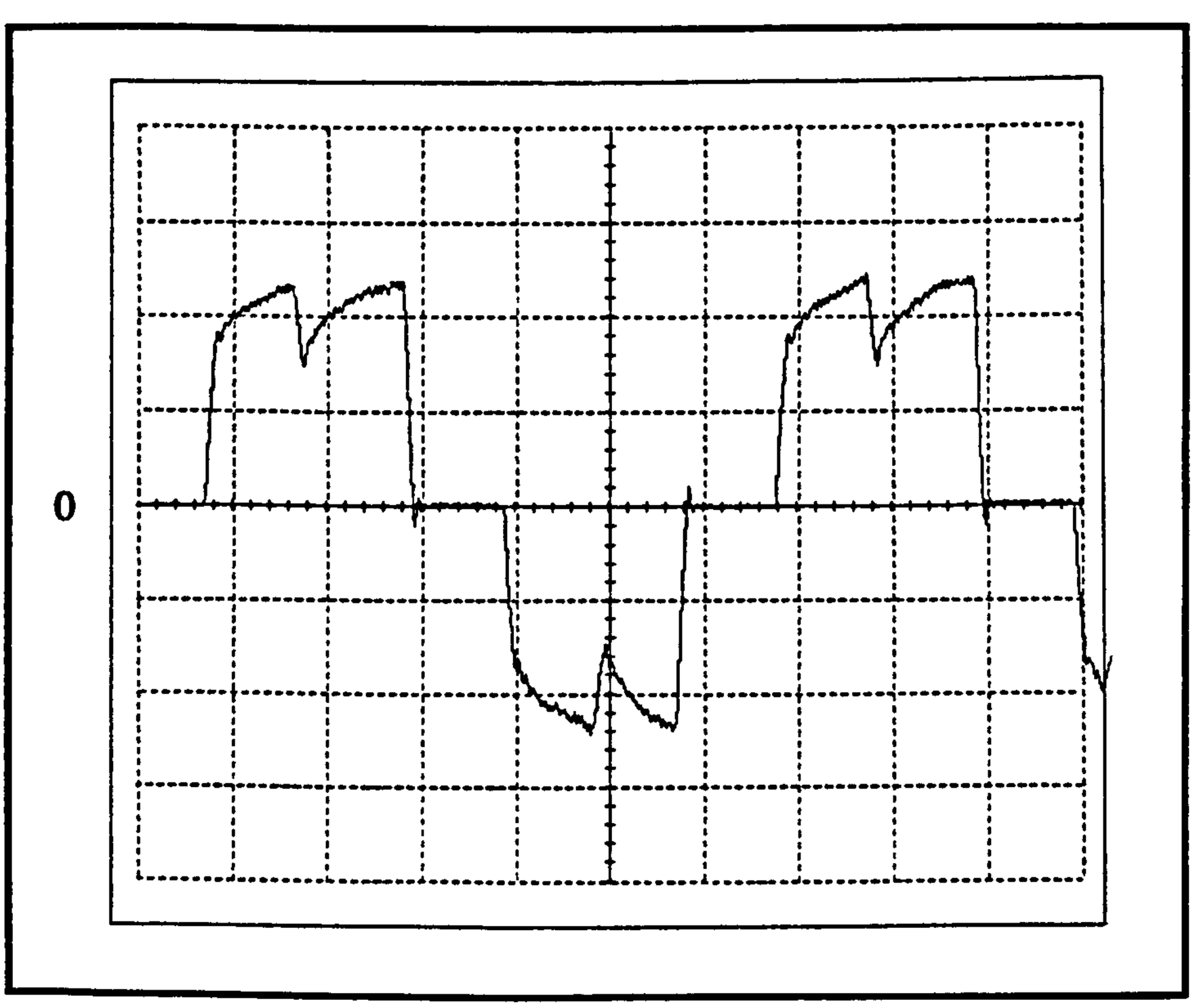

(b) measured waveform

Figure 5.16 Phase current waveforms with PWM control
(Load condition : 1Nm at 300 rpm)

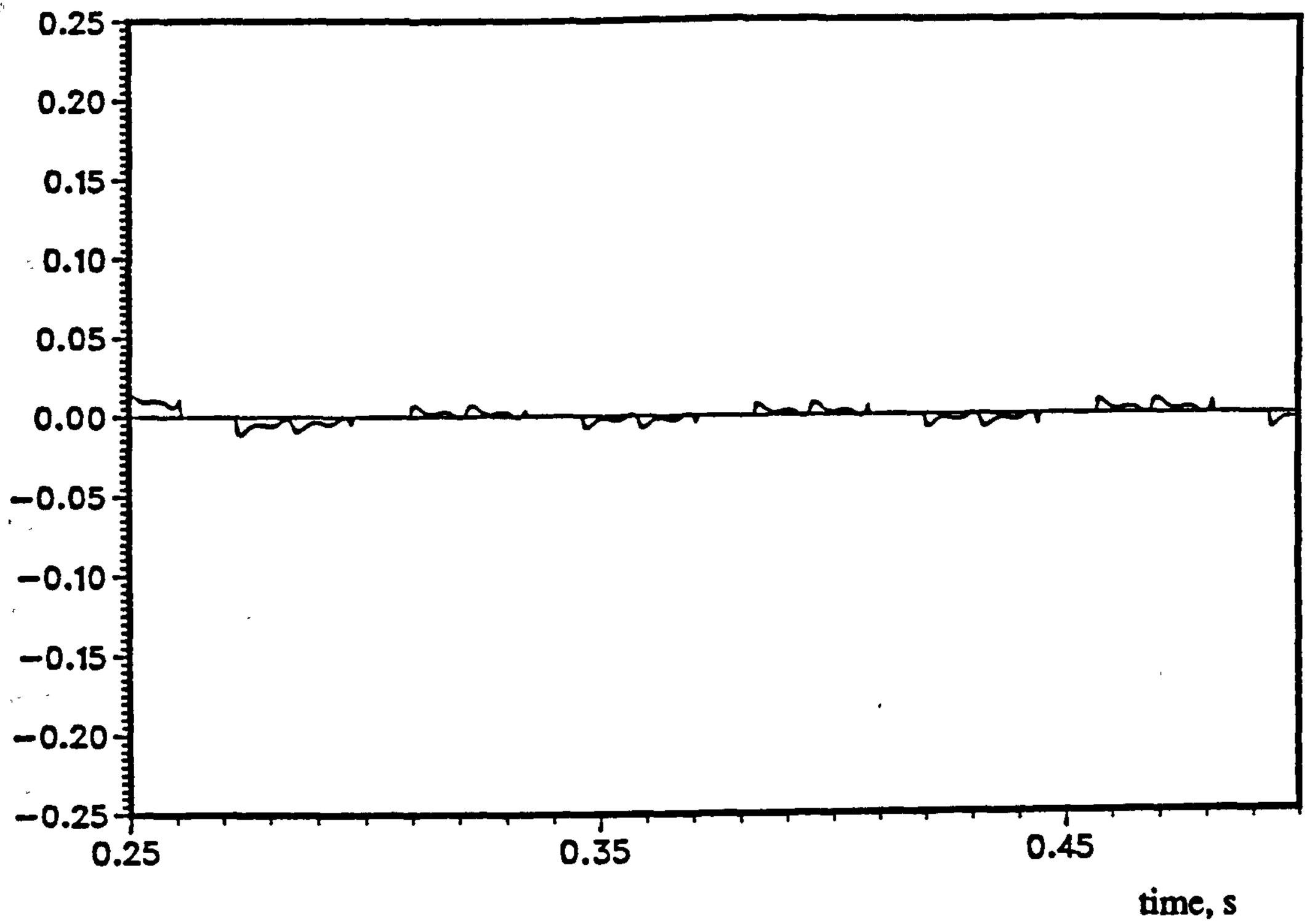

(a) simulated waveform

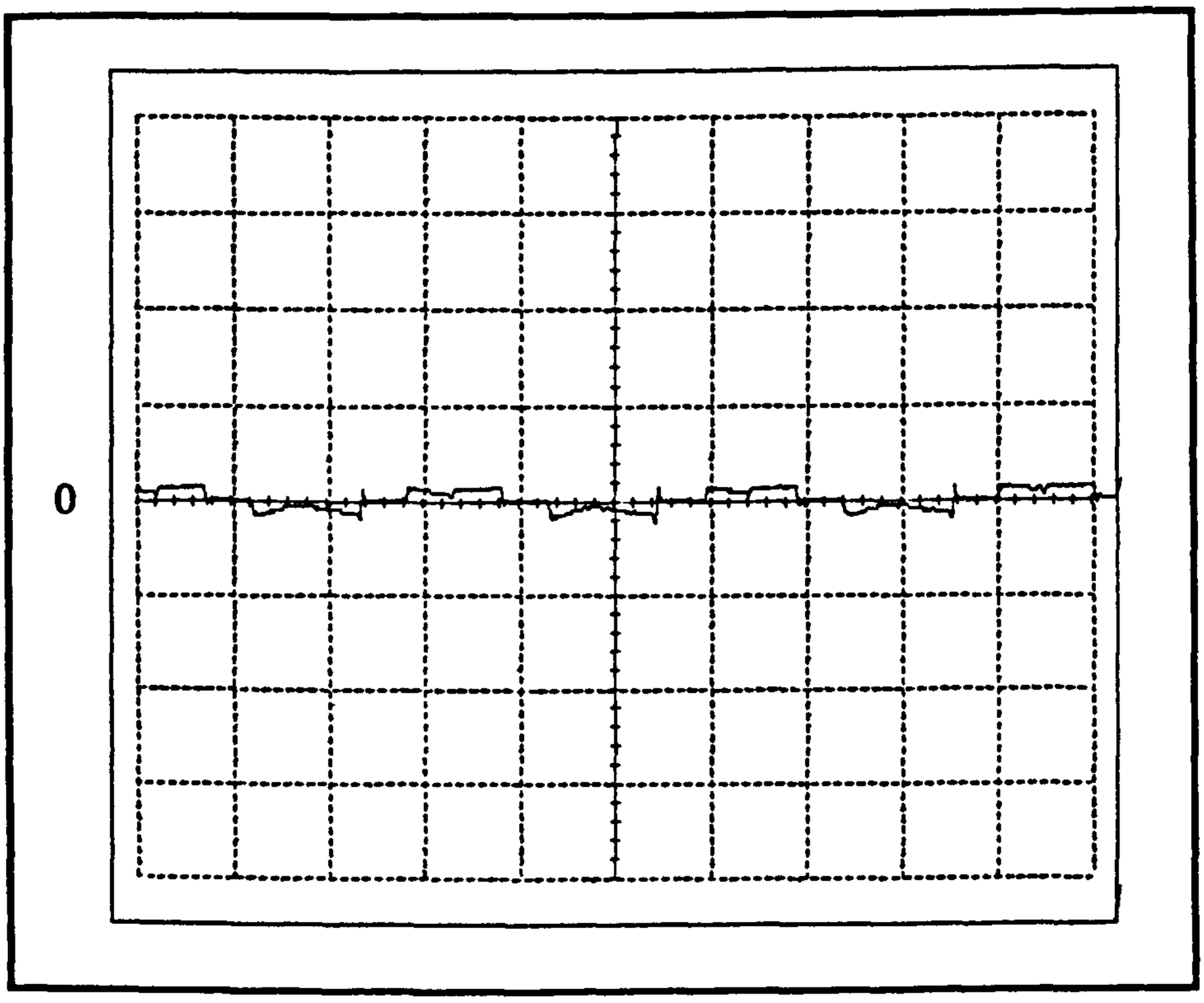

(b) measured waveform

Figure 5.17 Phase current waveforms (No-load condition)

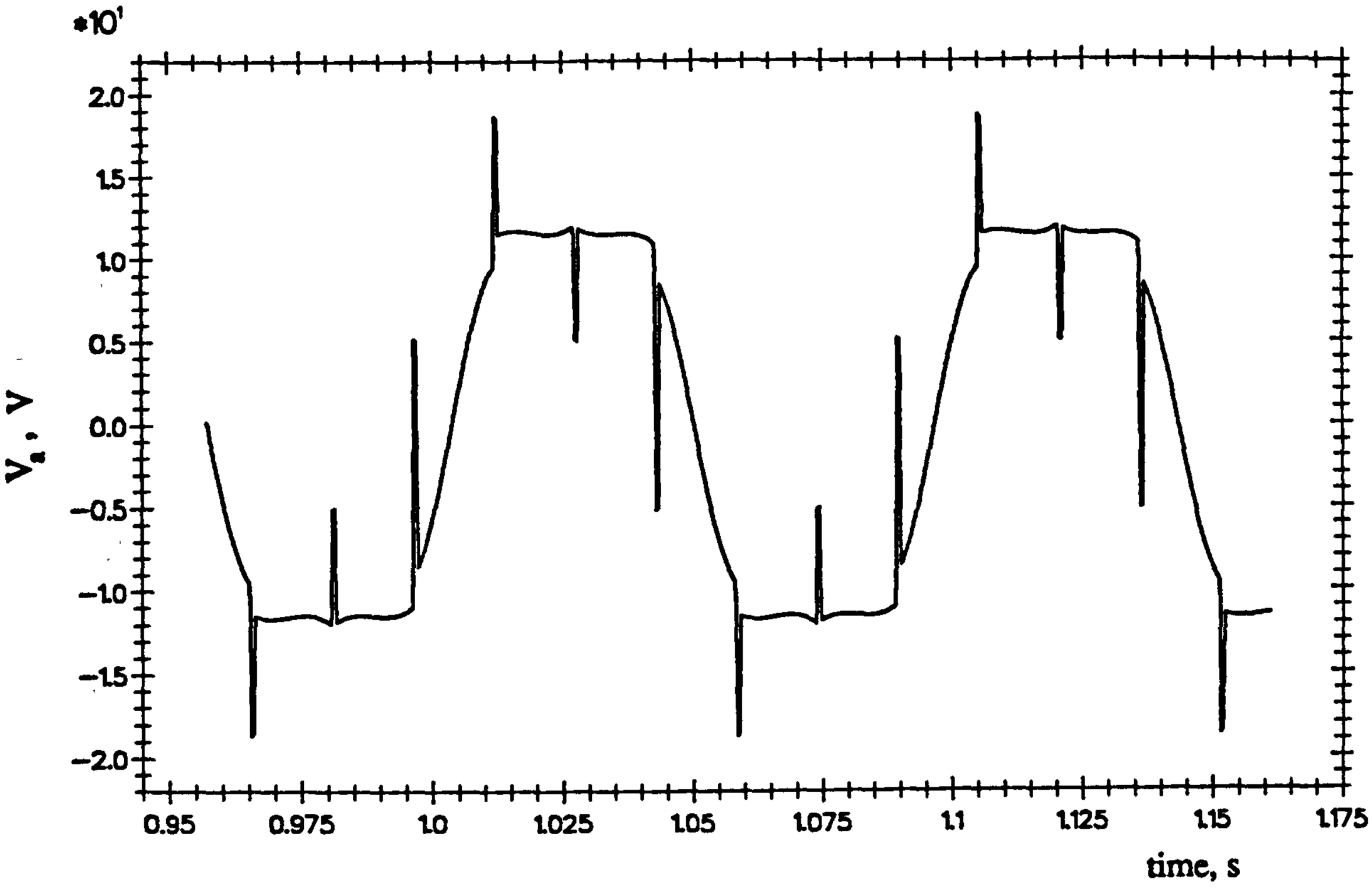

(a) simulated waveform

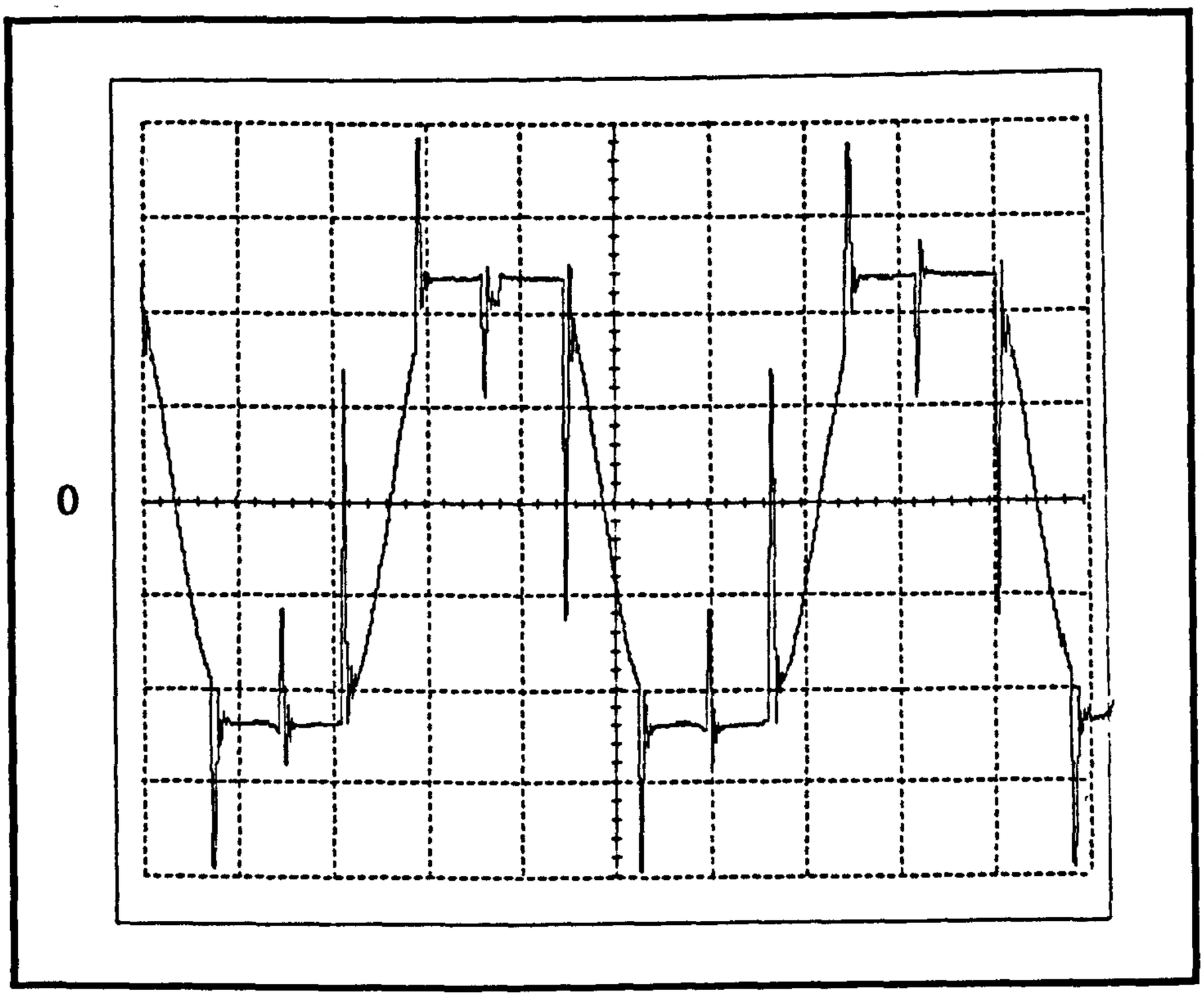

(b) measured waveform

Figure 5.18 Phase voltage waveforms without PWM control
(Load condition : 0.7Nm at 222rpm)

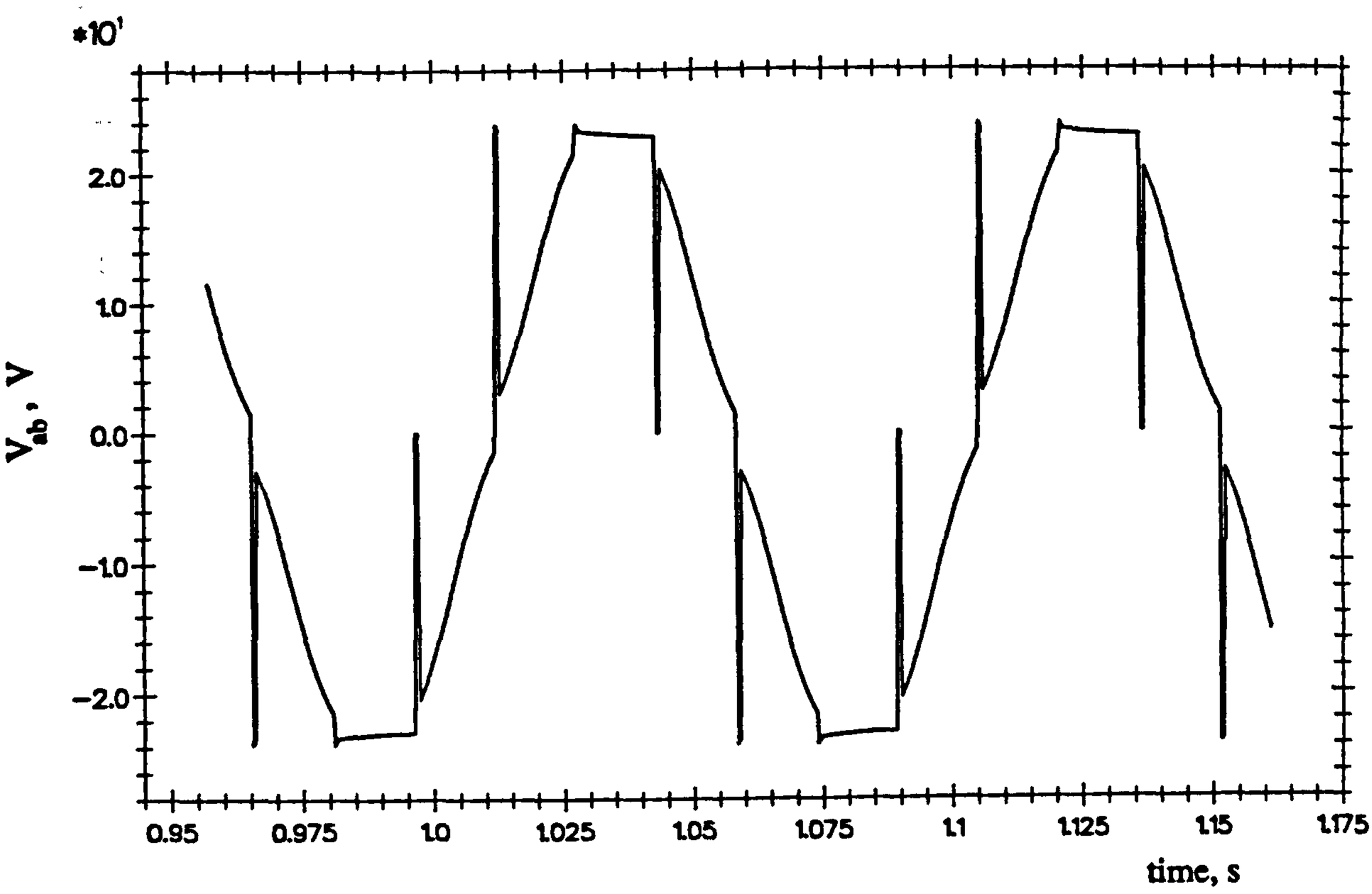

(a) simulated waveform

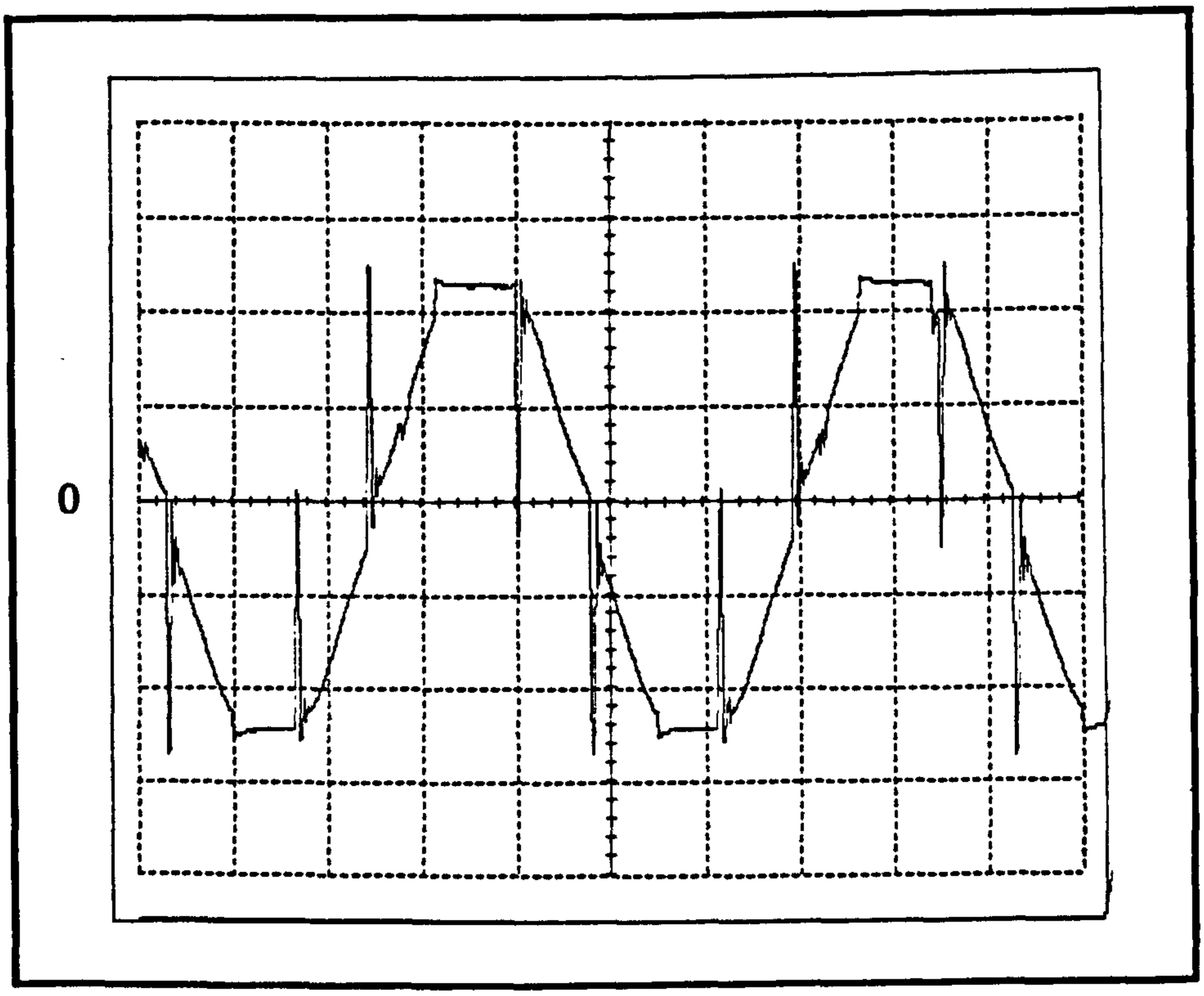

(b) measured waveform

Figure 5.19 Line voltage waveforms without PWM control
(Load condition : 0.7Nm at 222rpm)

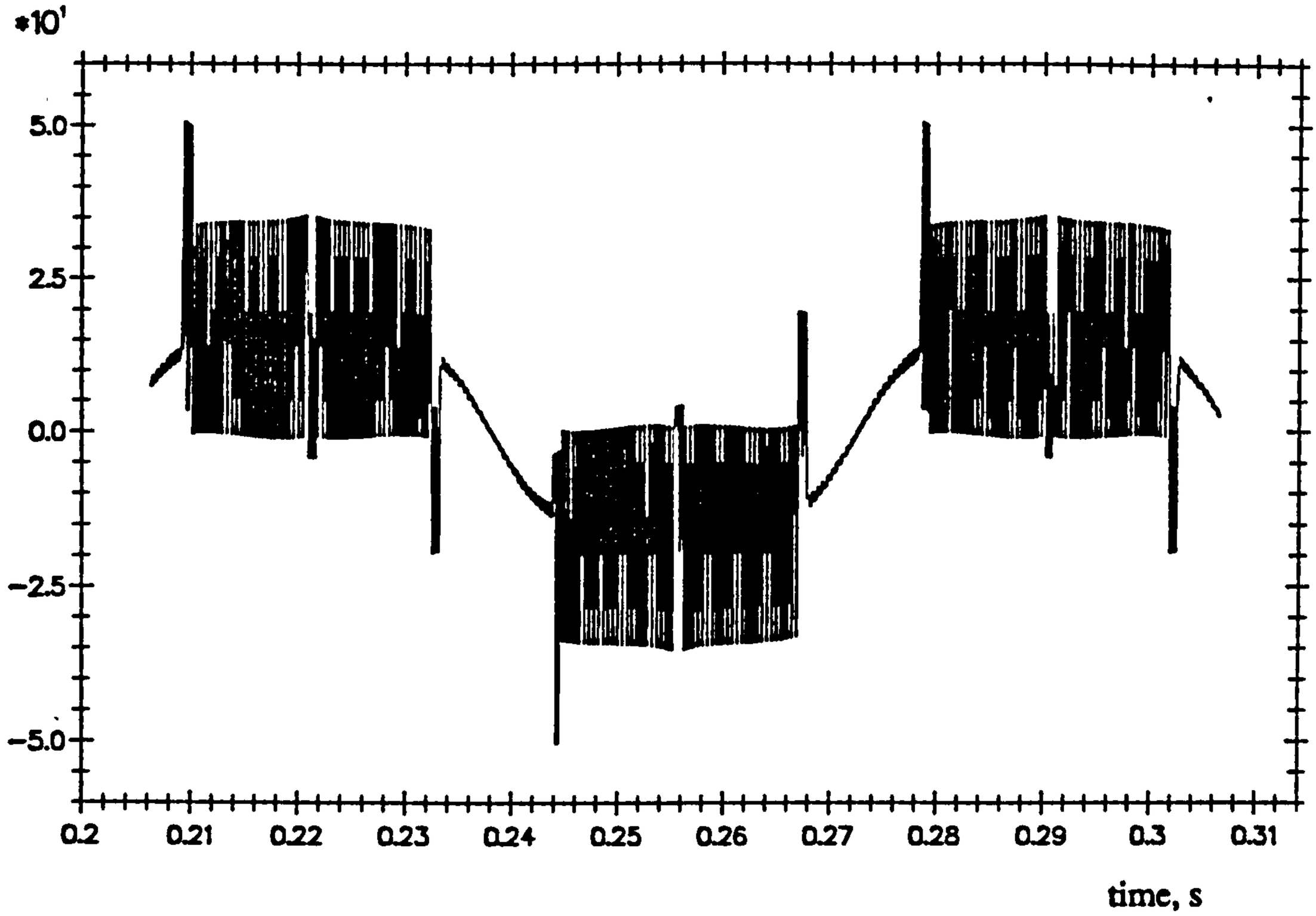

(a) simulated waveform

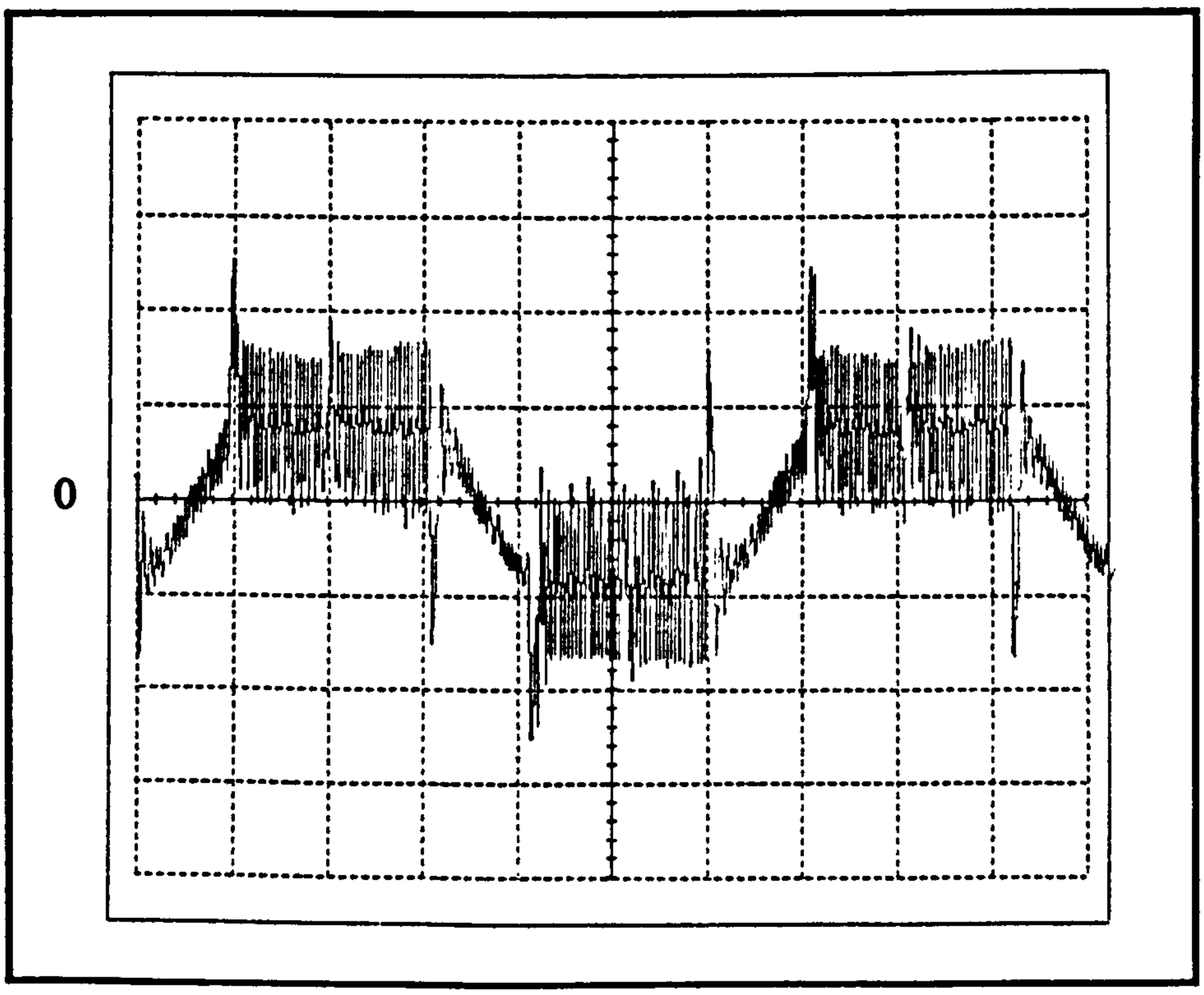

(b) measured waveform

Figure 5.20 Phase voltage waveforms with PWM control
(Load condition : 1Nm at 300rpm)

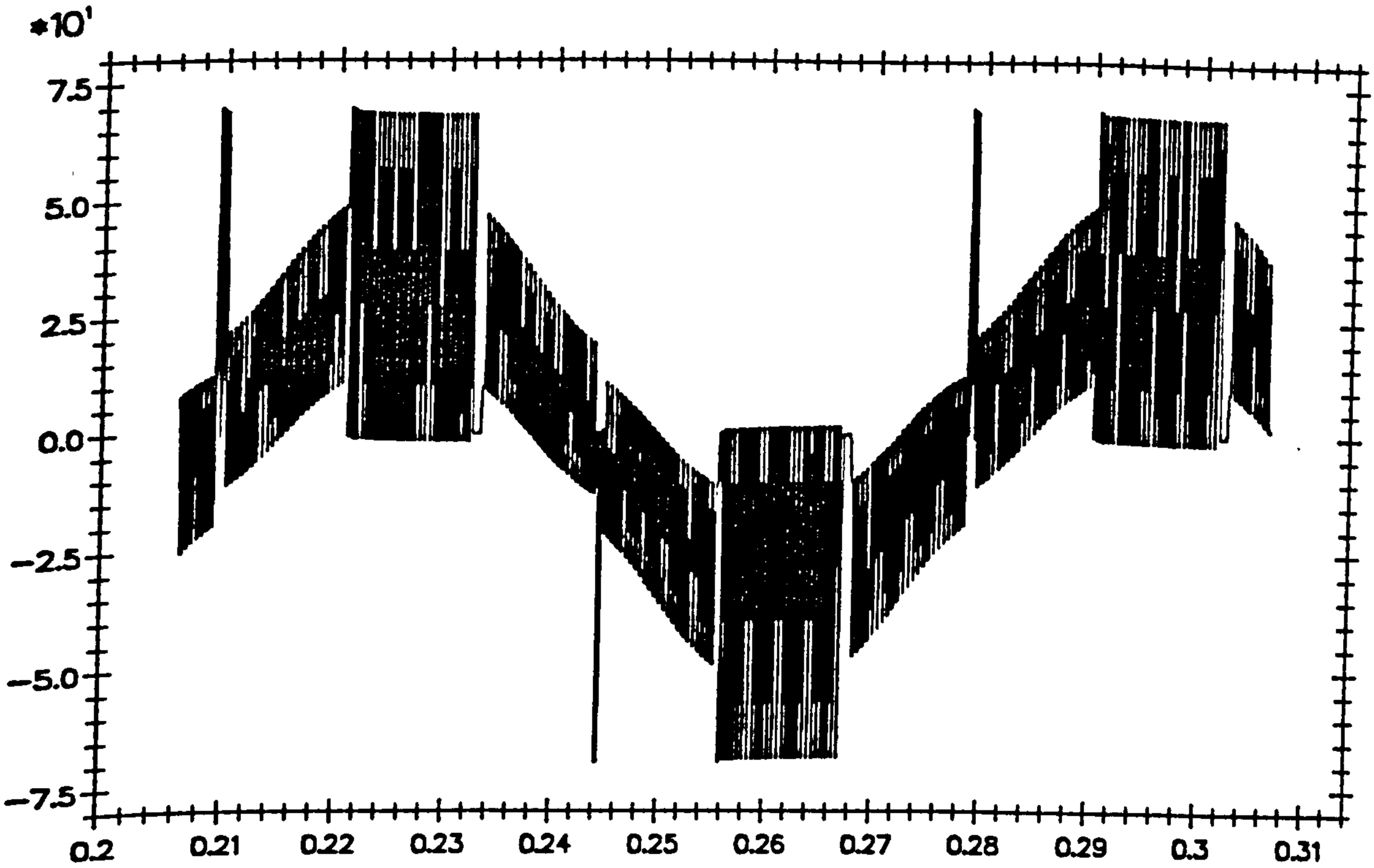

(a) simulated waveform

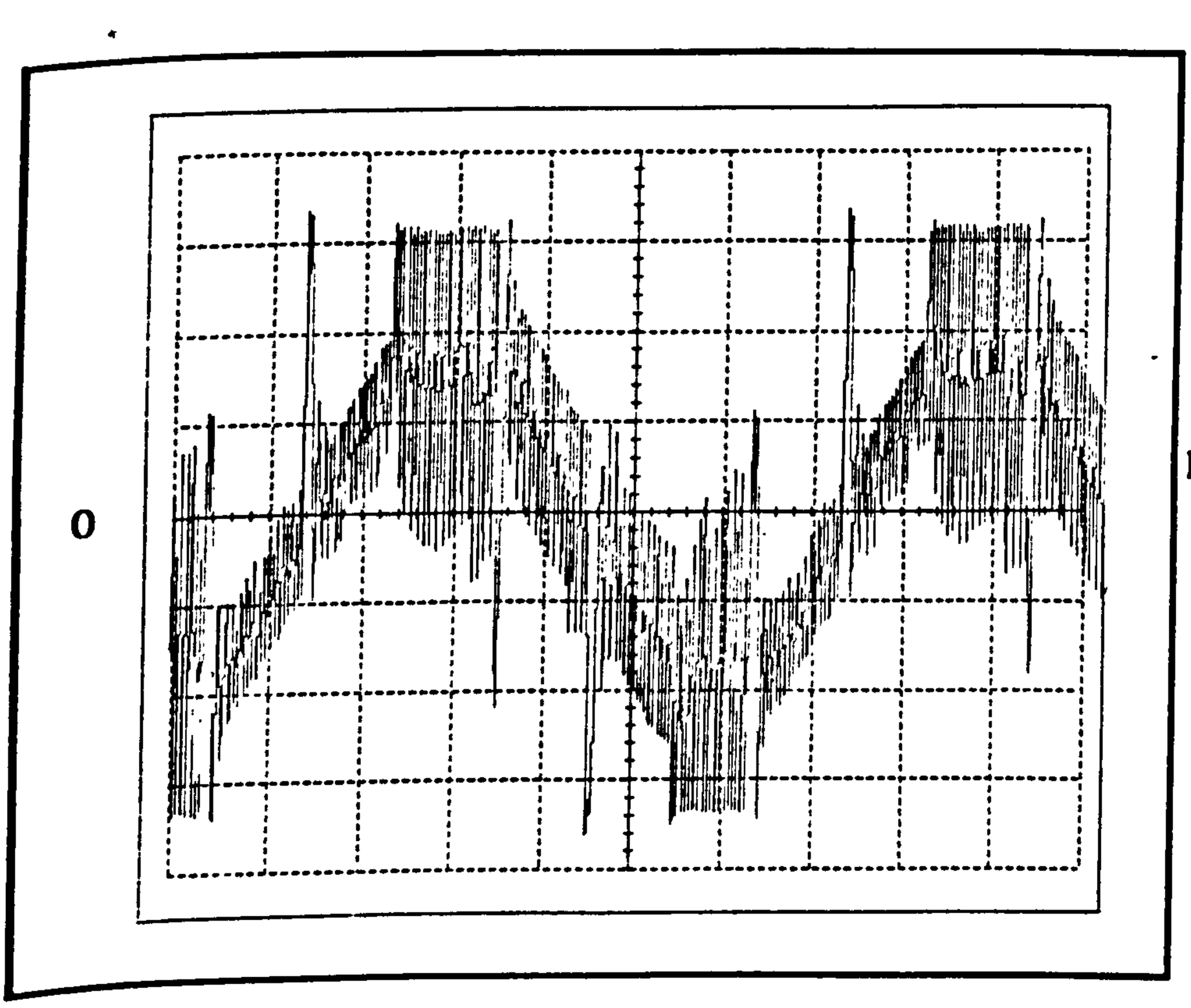

(b) measured waveform

Figure 5.21 Line voltage waveforms with PWM control
(Load condition : 1Nm at 300rpm)

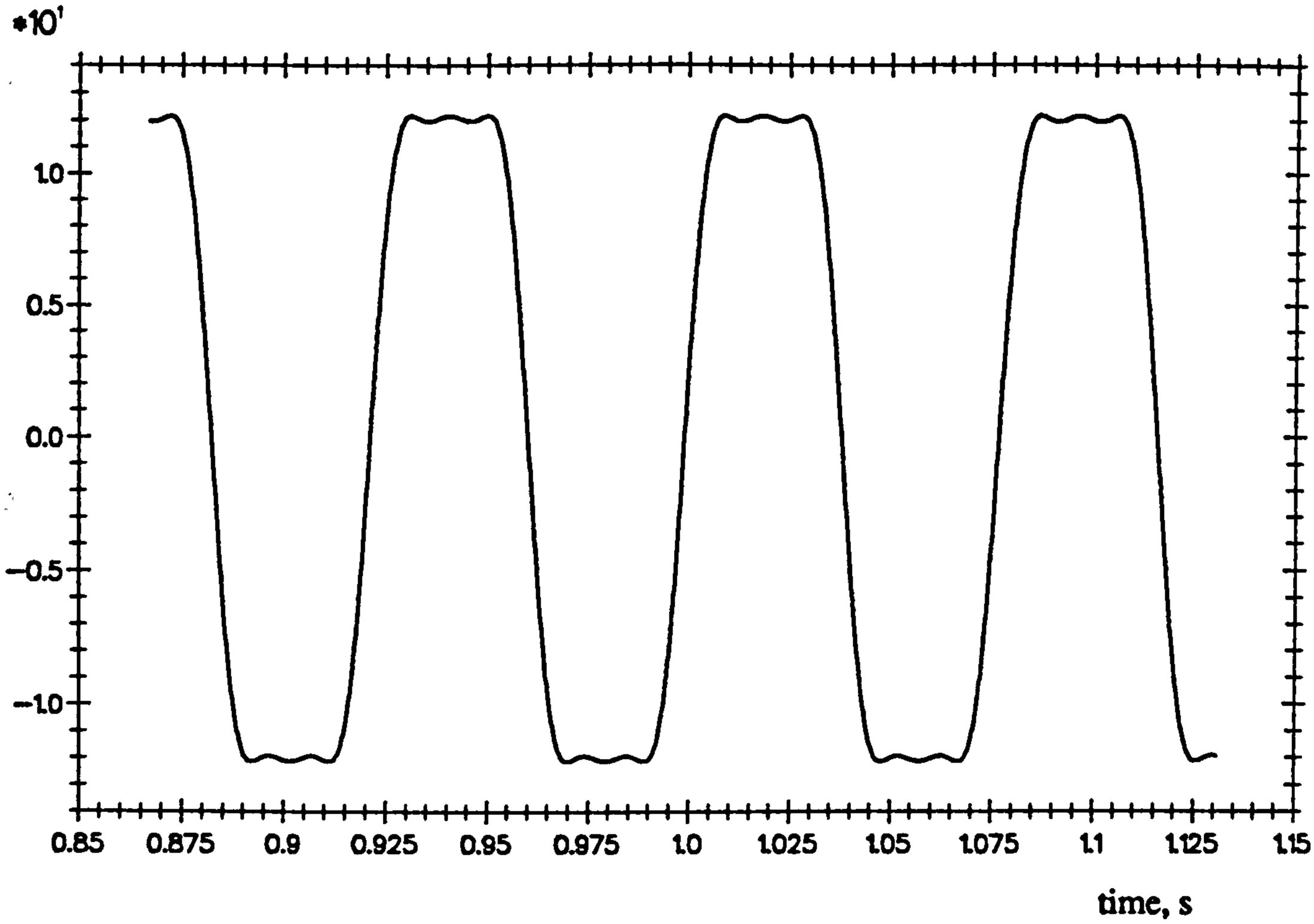

(a) simulated waveform

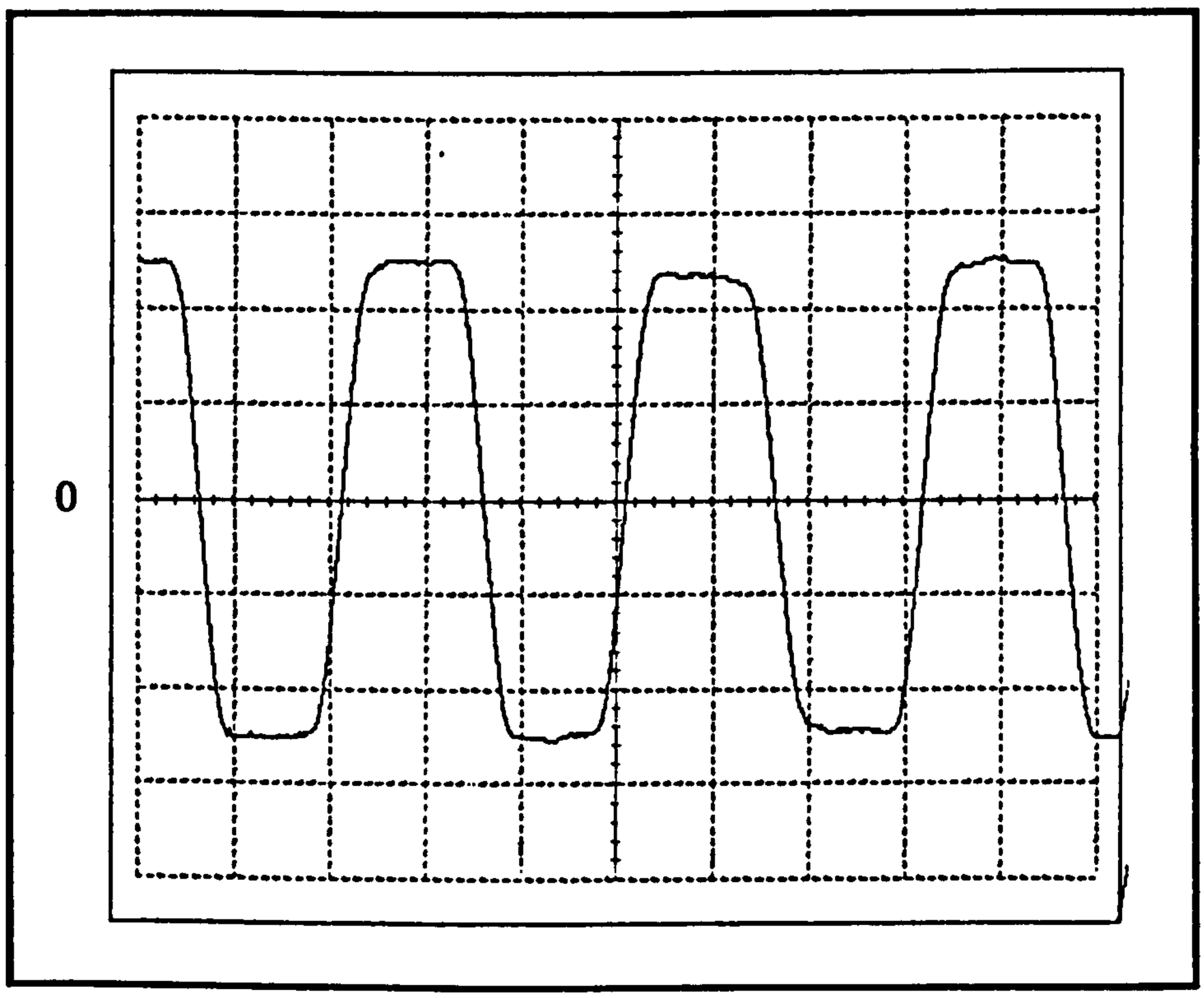

(b) measured waveform

Figure 5.22 Generated phase emf waveforms (No-load condition)

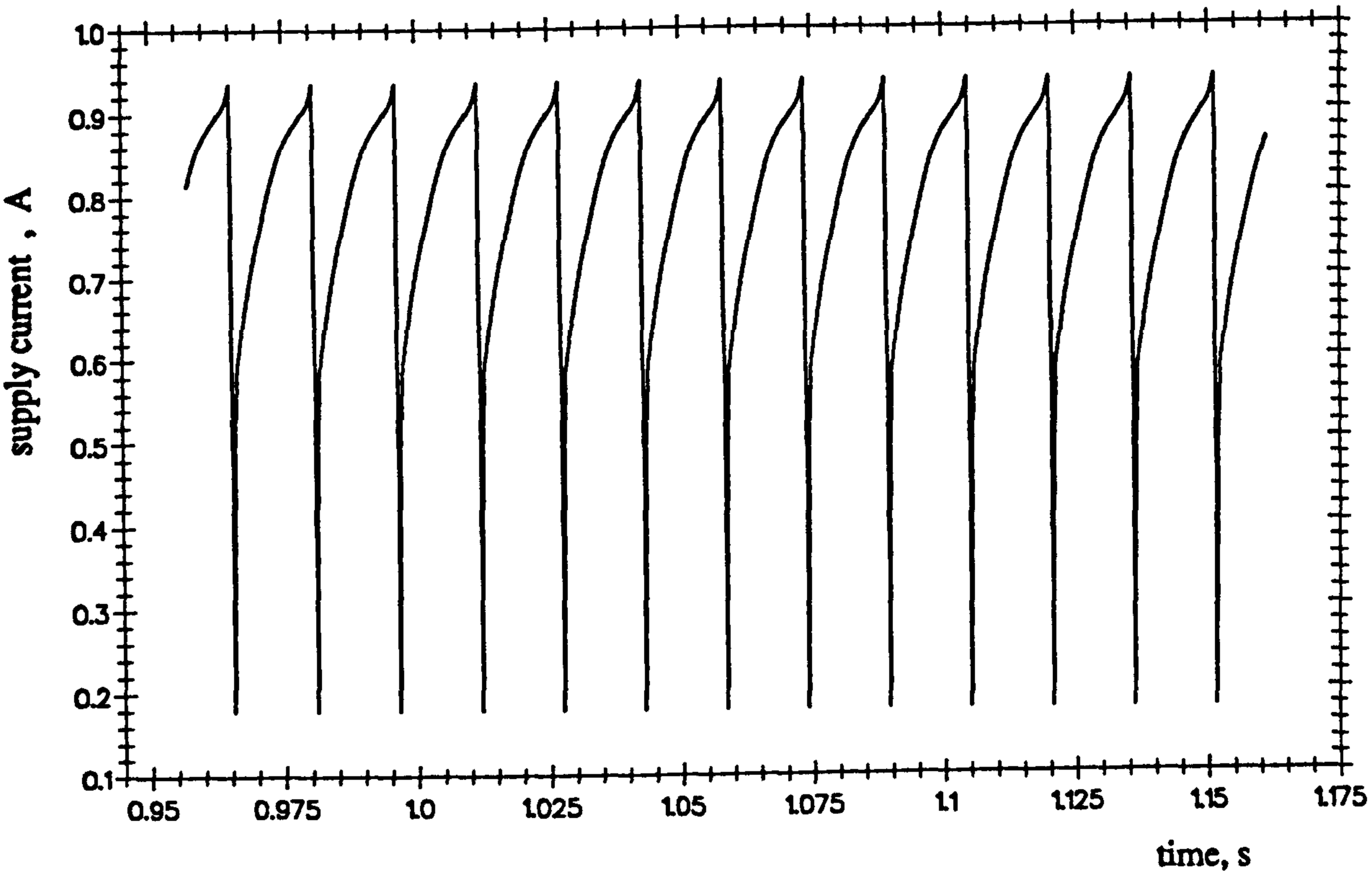

(a) simulated waveform

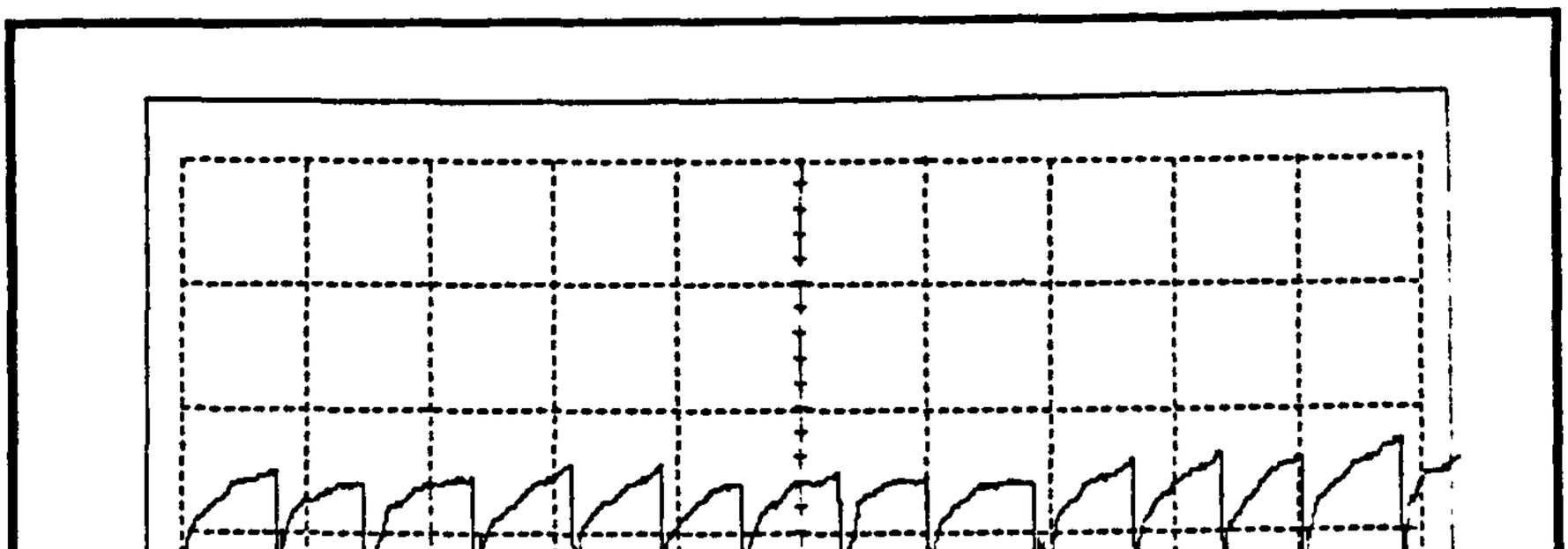

(b) measured waveform

Figure 5.23 Supply current waveforms (Load condition : 0.7Nm at 222rpm)

CHAPTER 6

DETERMINATION OF MOTOR PARAMETERS

The machine parameters required for the brushless dc motor model are the stator phase resistance and self-inductance, the mutual-inductance between stator phases and the no-load stator phase flux linkages due to the permanent-magnet rotor.

This chapter describes how the parameters of the 1.3kW experimental machine were obtained.

6.1 STATOR PHASE RESISTANCE

The resistances of the three stator phases were measured at an ambient temperature of 25°C using a Kelvin double-bridge[47]. The average of the three results was 1.278Ω.

6.2 STATOR PHASE SELF-INDUCTANCE

The unsaturated stator phase self-inductance was measured at different rotor angles using the bridge circuit of Figure 6.1. Three legs of the bridge are non-inductive resistances R_2, R_3, R_4, while the fourth is the stator phase whose inductance is to be measured. The bridge was balanced by adjustment of the ratio arms R_3 and R_4, until the voltage across the fluxmeter was zero and the steady-state current through the test winding was I_a. The supply connections were then reversed using the change-over switch and as a consequence the test winding current I_a also reverses. At the

end of the current reversal, the steady-state condition is again achieved, but there is a transient period due to the inductance L_a. The emf induced by the changing flux in the inductance L_a during this period produces a voltage which is integrated by the fluxmeter. If v is the instantaneous voltage across the bridge during this period, the current through the lower branches is $v/(R_3+R_4)$ and the instantaneous voltage across R_3 is $[R_3/(R_3+R_4)]v$. The voltage equation for the upper branches is $v=(R+R_2)i_a+L_a(di_a/dt)$ and the current in the phase winding is therefore

$$i_a = \frac{v}{R + R_2} - \frac{1}{R + R_2} L_a \frac{di_a}{dt}$$

while the instantaneous voltage across resistor R_2 is

$$v_{R2} = \frac{R_2}{R+R_2} v - \frac{R_2}{R+R_2} L_a \frac{di_a}{dt}$$

Since the bridge is balanced $R_3/R_4=R_2/R$ and the instantaneous voltage v_g across the fluxmeter, being the difference of the voltages across R_2 and R_3, is given by [48]

$$v_g = - \frac{R_2}{R + R_2} L_a \frac{di_a}{dt}$$

The deflection of the fluxmeter ψ is proportional to the time integral of this voltage[48,49], so that

$$\psi = \int_0^{\infty} v_g \, dt$$

$$= - \frac{R_2}{R + R_2} L_a \int_{+I_a}^{-I_a} di_a$$

$$= 2 L_a I_a \frac{R_2}{R + R_2}$$

and the stator phase self-inductance is

$$L_a = \frac{\psi}{2I_a} \frac{R + R_2}{R_2}$$

$$= \frac{\psi}{2I_a} \frac{R_3 + R_4}{R_3}$$

The variation of the phase self-inductances L_{aa}, L_{bb}, L_{cc} with rotor angle displacement θ_e for a fixed stator current of 3A is given in Figure 6.2, and the variation of these inductances with dc current in the stator phase for a fixed rotor angle $\theta_e = 0$ is given in Figure 6.3. The machine clearly remains unsaturated up to its rated current and the inductances consequently remain unchanged.

If L_{max} and L_{min} are respectively the maximum and minimum values of the phase winding self-inductances, the terms L_o and L_2 of equation 5.32 are:

$$L_o = \frac{L_{max} + L_{min}}{2} \tag{6.1}$$

and

$$L_2 = \frac{L_{max} - L_{min}}{2} \tag{6.2}$$

and it follows from Figure 6.2 that , approximately,

$$L_o = 9.85 \text{ mH}$$

and

$$L_2 = 0.45 \text{ mH}$$

6.3 STATOR PHASE MUTUAL-INDUCTANCE

Figure 6.4 shows the circuit used to measure the mutual-inductance between any two stator phases[48,50]. The resistance R_v provides the source resistance required by the fluxmeter. A reversal of the voltage applied to phase *a* causes a reversal of the current from I_a to $-I_a$. During this reversal, the instantaneous voltage induced in phase *b* is

$$V_b = L_{ba} \frac{di_a}{dt}$$

and the corresponding voltage-time integral is

$$\int_0^{\infty} V_b \, dt = L_{ba} \int_{+I_a}^{-I_a} di_a$$

If the fluxmeter deflection is ψ for a current reversal of $2I_a$, the mutual-inductance between phases *a* and *b* is

$$L_{ba} = - \frac{\psi}{2I_a}$$

Figures 6.5 and 6.6 show respectively the angular variation of the mutual-inductances L_{ab}, L_{bc}, L_{ca} for a stator current of 3A, and their variations with stator current for a fixed rotor angle ($\theta_e = 0$).

If M_{max} and M_{min} are respectively the maximum and the minimum values of phase-to-phase mutual-inductance, the terms M_o and M_2 of equation 5.33 are:

$$M_o = \frac{M_{max} + M_{min}}{2} \tag{6.3}$$

and

$$M_2 = \frac{M_{max} - M_{min}}{2} \tag{6.4}$$

and it follows from Figure 6.5 that, approximately,

$$M_o = 1.95 \text{ mH}$$

and

$$M_2 = 0.45 \text{ mH}$$

6.4 NO-LOAD STATOR WINDING FLUX LINKAGE DUE TO THE PERMANENT-MAGNET ROTOR

A Hewlett Packard 3582A harmonic analyser was used to determine the frequency spectrum of the generated open-circuit phase voltage at a rotor speed of 800 rpm. If only the first three harmonic terms are considered, the generated open-circuit voltage of phase *a* is

$$e_{oa} = 45.537 (\sin\theta_e + 0.229 \sin 3\theta_e + 0.0574 \sin 5\theta_e) \tag{6.5}$$

where θ_e is the electrical angle between the rotor axis and the *a* phase axis. With the instantaneous voltage given by

$$e_{oa} = -\omega_e \frac{d\psi_{Pra}}{d\theta_e}$$

where $d\psi_{Pra}/d\theta_e$ is the rate-of-change of flux linkage due to the permanent-magnet with rotor position and ω_e the rotor angular velocity in electrical radians per second. It follows that

$$\frac{d\psi_{Pra}}{d\theta_e} = 0.181 (\sin \theta_e + 0.229 \sin 3\theta_e + 0.0574 \sin 5\theta_e) \tag{6.6}$$

Integrating equation 6.6 with respect to θ_e gives the flux linkage of the permanent-magnet rotor with phase *a*, ψ_{Pra}, as

$$\psi_{Pra} = 0.181\,(\cos\theta_e + 0.0763\cos 3\theta_e + 0.0114\cos 5\theta_e)$$

Similar calculations were made for the other phases and the spatial variations of the various flux linkages due to the permanent-magnet rotor are given in equation 5.3.

6.5 DISCUSSION OF RESULTS

It is evident from Figures 6.2 and 6.5 that the stator phase self-inductances and the mutual-inductance between any two phases are functions of the rotor position θ_e. This arises from the variation in the airgap length and consequently the reluctance of the flux path as the rotor turns. As a result of the reluctance variation, the winding inductances also vary with rotor position, being a maximum when the rotor and phase axes are aligned and a minimum when they are in quadrature. It is also evident that the variations with rotor position of the stator phase self-inductances and the mutual-inductance between phases repeat twice every 360°e, and that the reluctance variation has a frequency six times the frequency of the rotor rotation.

Figures 6.3 and 6.6 show that, probably due to the high reluctance of the rare-earth permanent-magnet, there is negligible magnetic saturation evident in both the self-inductance and the mutual-inductance. Even above the rated figure of 5.5A, the stator current has an insignificant demagnetizing effect on the permanent-magnet. The values of

the stator phase self-inductances L_{bb} and L_{cc} shown in Figure 6.3 are larger than those of L_{aa} and the values of the mutual-inductances L_{ab} and L_{ca} shown in Figure 6.6 are smaller than those of L_{bc}. This is due to the stator phase windings being mutually displaced by 120° and all these inductances being measured at the same rotor angle (θ_e=0).

The experimental parameters obtained in this chapter were used in the mathematical model developed in chapter 5 to simulate the performance of the brushless drive.

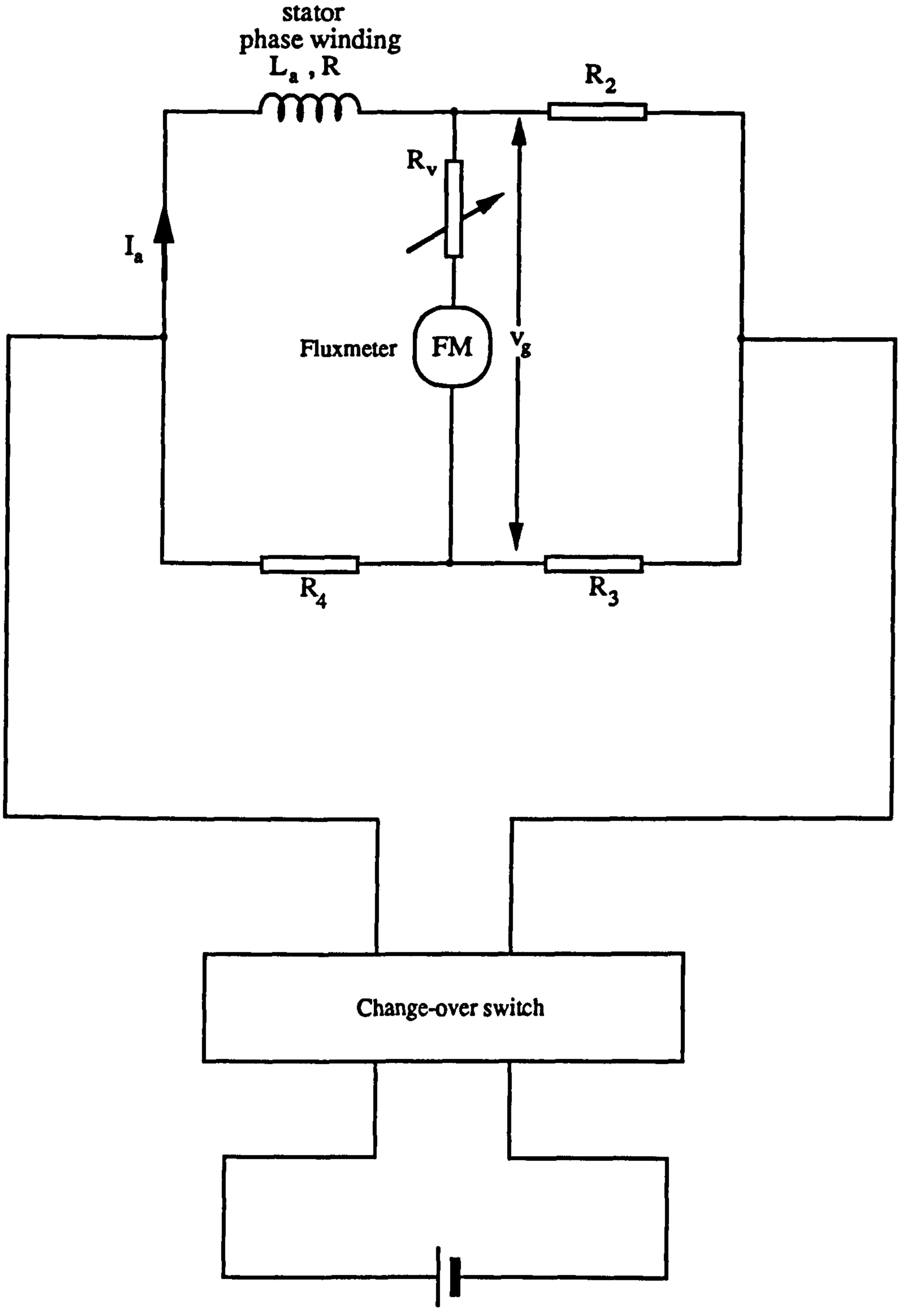

Figure 6.1 Circuit for measurement of phase self-inductance

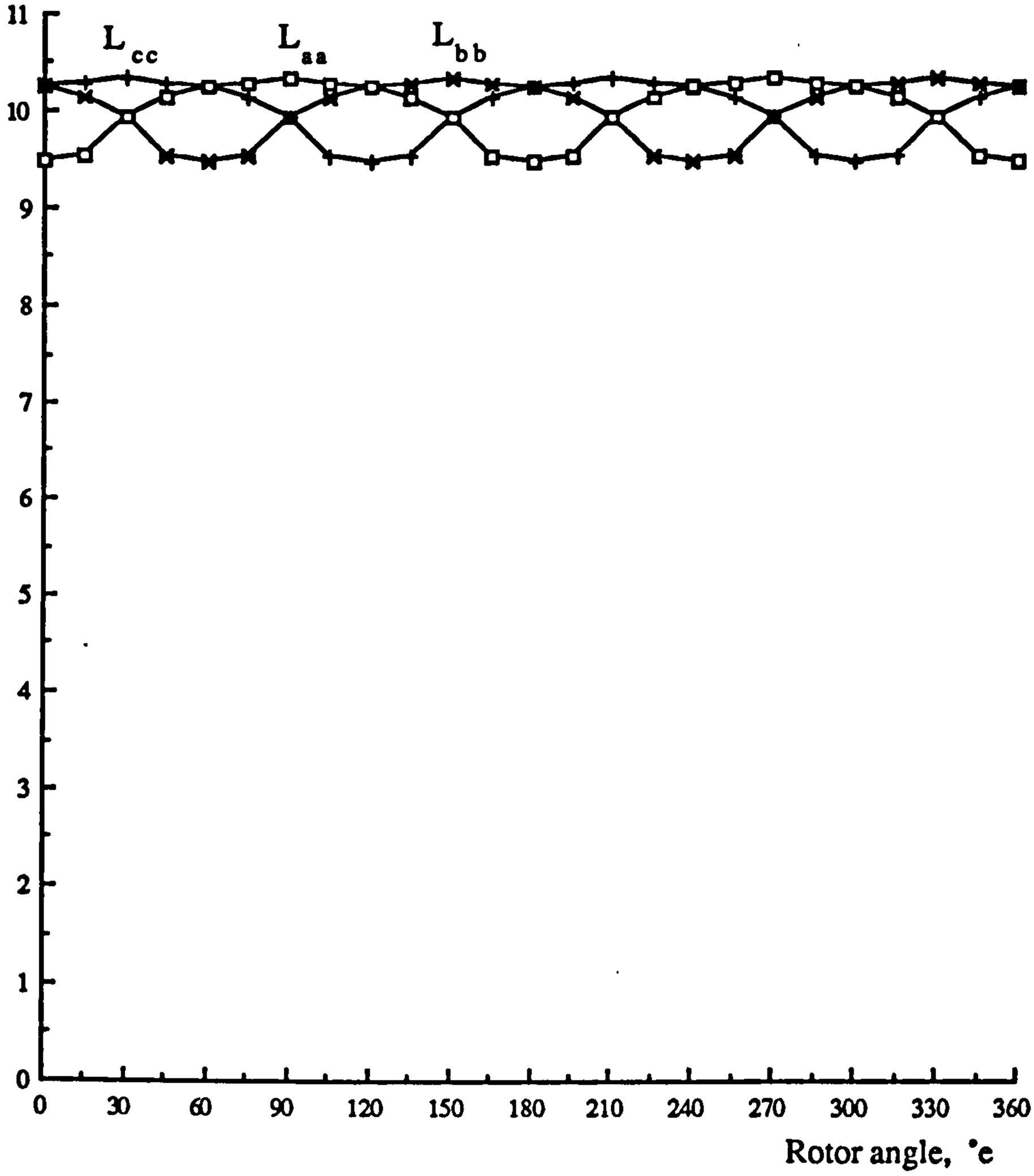

Figure 6.2 Angular variation of stator phase self-inductances

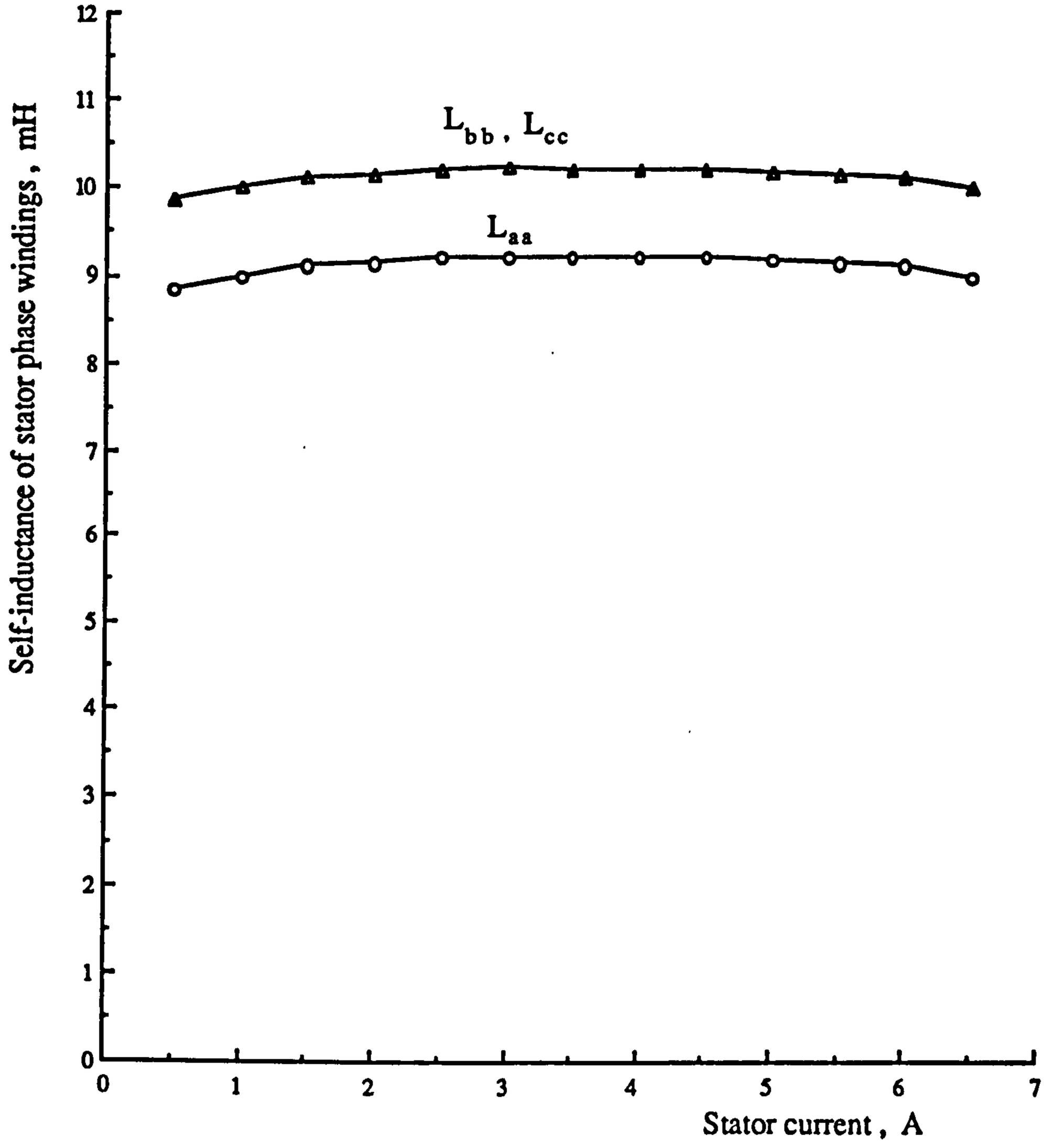

Figure 6.3 Variation of stator self-inductances L_{aa} , L_{bb}, L_{cc} with stator current for rotor displacement $\theta_e = 0°$

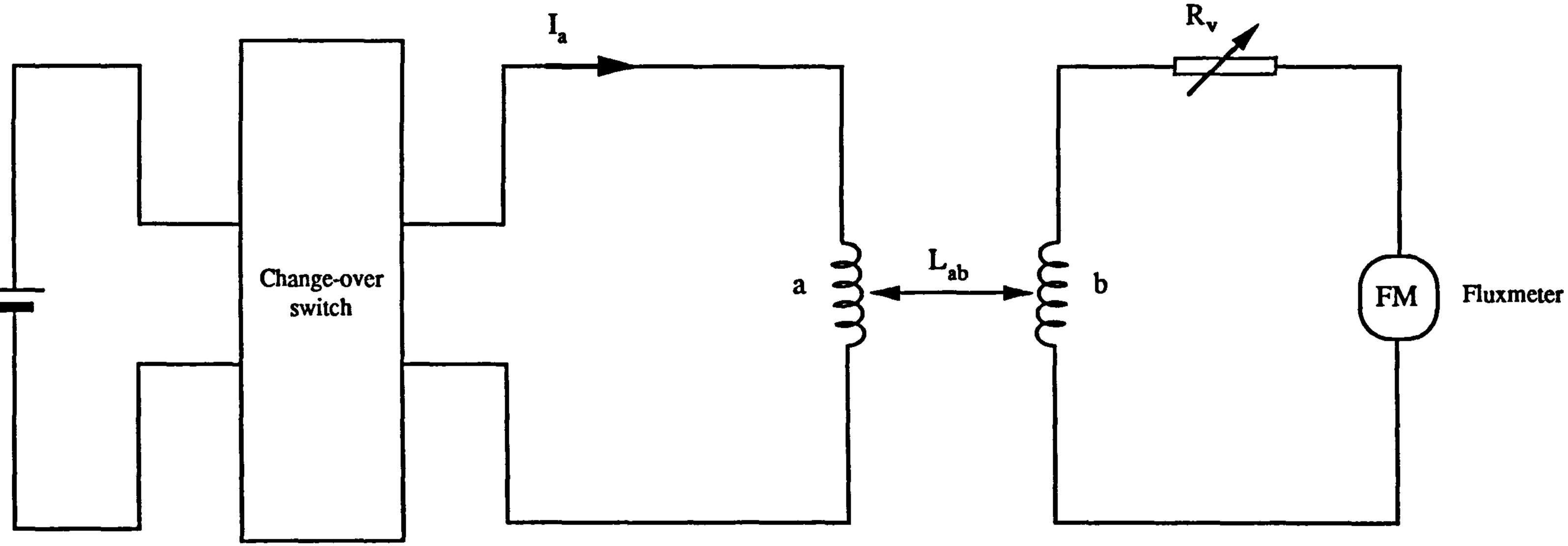

Figure 6.4 Circuit for measurement of phase-to-phase mutual-inductance

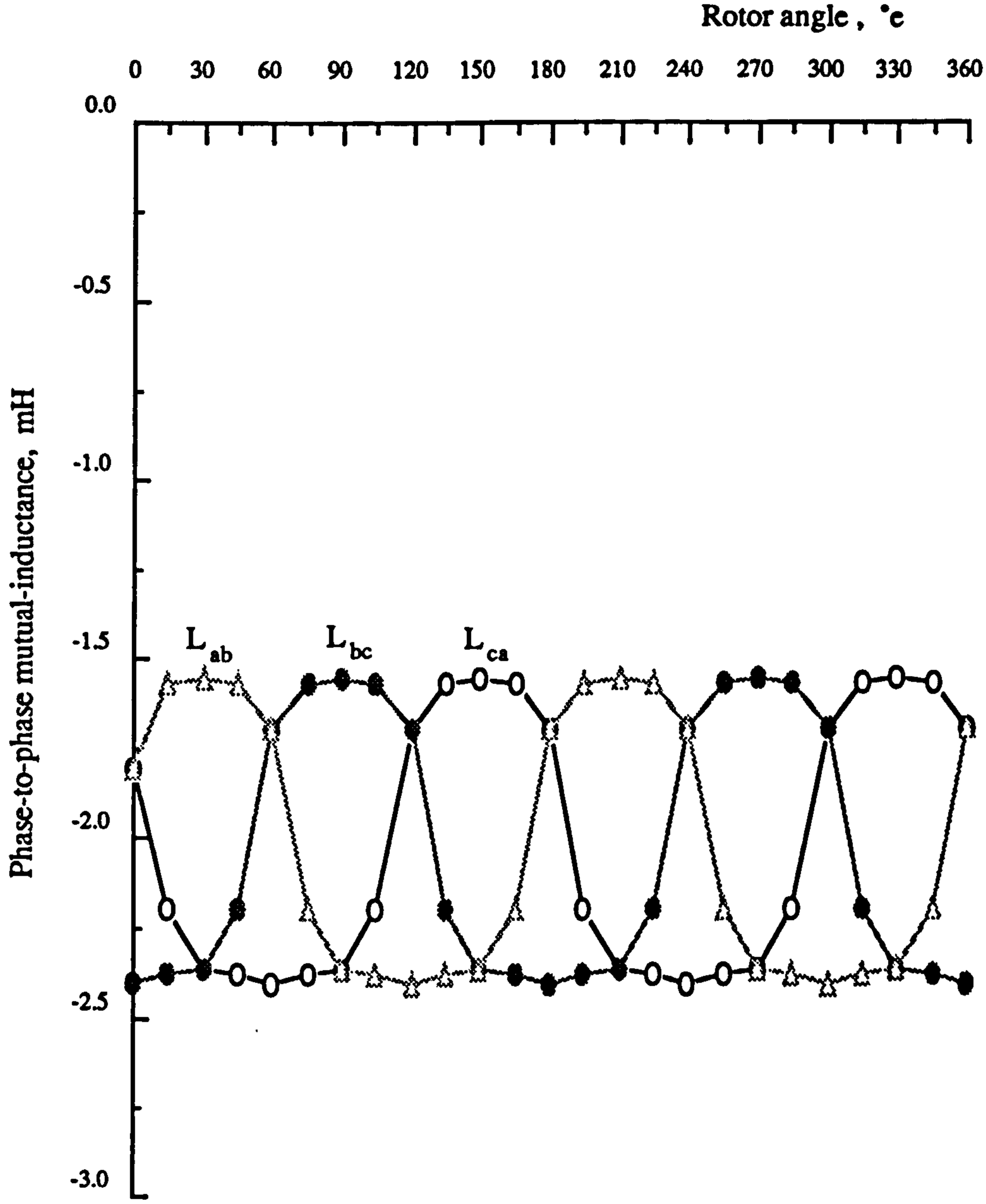

Figure 6.5 Angular variation of mutual-inductance between stator phases

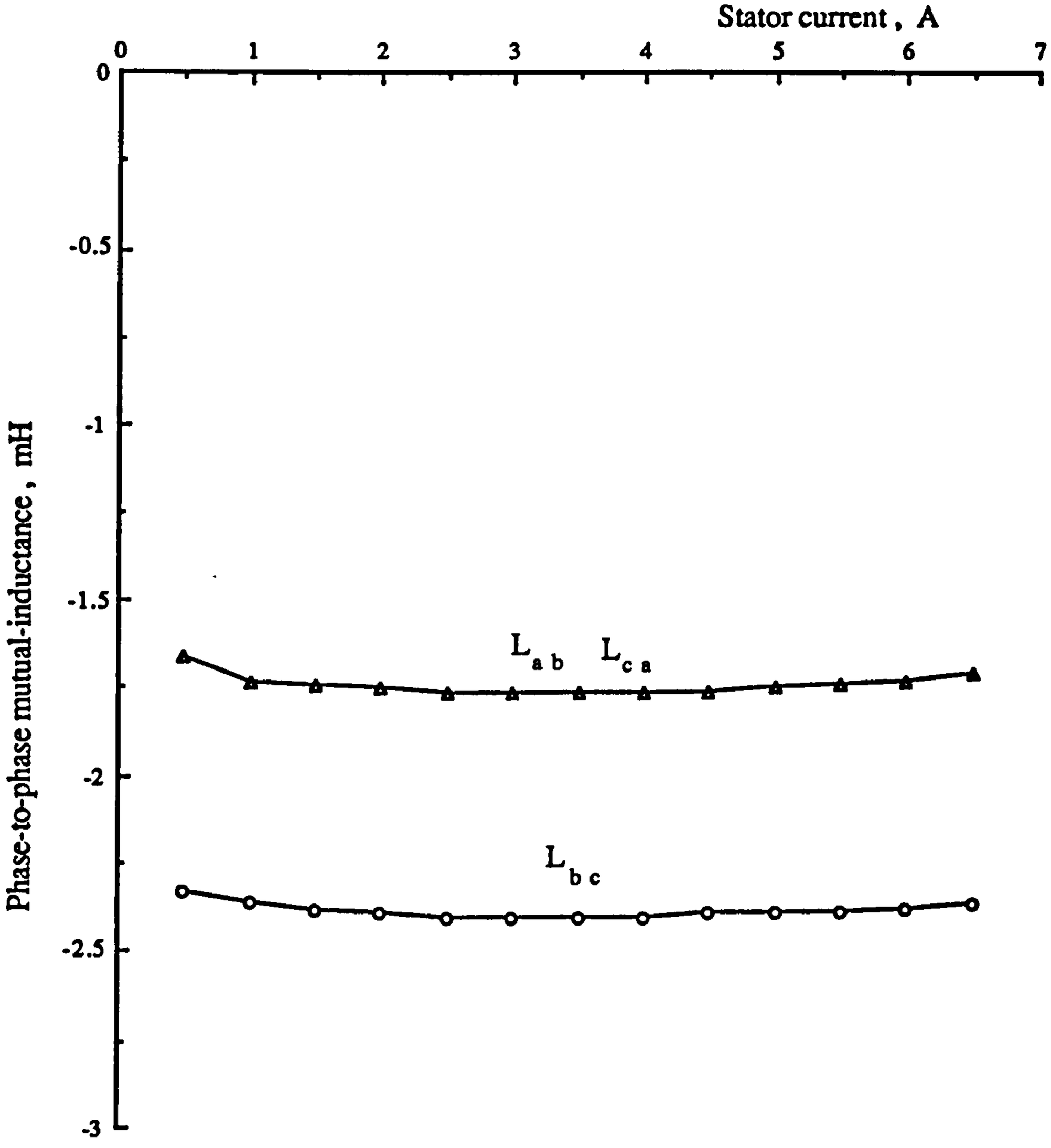

Figure 6.6 Variation of mutual-inductance between stator phases with stator current at rotor displacement $\theta_e = 0°$

CHAPTER 7

ANALYSIS AND MINIMIZATION OF TORQUE RIPPLE IN BRUSHLESS DC MOTORS

A major drawback with brushless dc motors, especially at low speed, is the presence of torque and speed ripples which can give rise to serious problems in applications such as precise positioning or robotics. The recent introduction of rare-earth permanent-magnet rotors has resulted in a reduced inertia and a faster response, but this is at the expense of an increased speed ripple as shown in the predicted result of Figure 7.1.

The emf generated in a brushless motor is trapezoidal with a flat-top spanning 120°e and, since the electromagnetic torque is proportional to the product of this emf and the stator current[51], a rectangular motor phase current waveform is needed to produce constant torque. In practice however, the waveforms of both generated emf and stator current differ from the ideal, and the torque exhibits a ripple which is periodic and dependent on the rotor position and the commutation events. Other factors, such as the switching frequency of the current controller, the stator magnetic field and the firing angle of the inverter, also affect the magnitude of the torque ripple. At high speed, these effects are masked by the drive inertia, but at low speed they may severely affect the performance of the drive.

The computer program described in chapter 5 was written to simulate the drive, and to study the factors which affect

torque ripple and the ways by which this might be reduced. In particular, the optimum phase current waveforms which produce a smooth torque were determined.

The following sections present an analytical study of low-speed torque ripple, with rectangular phase current waveforms, and discuss various methods by which it might be reduced. A torque ripple factor[7,18] may be defined for use in the study as

$$T_r = \frac{\Delta T}{T_{av}} \tag{7.1}$$

where

ΔT is the peak-to-peak torque ripple, and

T_{av} the average torque

7.1 FACTORS AFFECTING TORQUE RIPPLE

7.1.1 EFFECT OF COMMUTATION EVENTS

The ideal rectangular phase-current waveforms of Figure 7.2(a), required to produce a constant torque is difficult to achieve in practice, since the current commutates regularly from one phase to another. In particular, during the commutation period the winding inductance prevents the phase current from changing instantaneously. Consequently, the motor phase current waveform has the rounded edges shown in Figure 7.2(b), rather than the theoretical rectangular waveshape, and a torque ripple accompanies every stator current commutation[51,52]. The torque profile for these phase current waveforms and with ideal trapezoidal generated phase emf waveforms is shown in Figure 7.3. The frequency of the torque ripple is six times that of the stator supply

frequency and its magnitude is approximately proportional to the operating current level. Figure 7.4 shows the predicted relationship between the torque ripple amplitude and the stator current value for the experimental machine. It is evident that the torque ripple is larger with a higher current value.

7.1.2 EFFECT OF PHASE EMF WAVEFORMS

Ideally, the airgap flux-density distribution of the brushless motor should be rectangular and a trapezoidal phase emf waveform should be generated. For a 3-phase brushless motor, the flat-top of this waveform ideally spans 120°e, as shown in Figure 7.5(a). In practice however, because of fringing, the airgap flux-density distribution is not rectangular, and the corners are rounded as shown in Figure 7.6[53]. Consequently, the flat-top of the generated emf spans less than 120°e, as shown in Figure 7.5(b). This has a direct effect on both the rate of build up and the magnitude of the phase current and in turn leads to an increased torque ripple[38,54]. The generated emf waveform also contains fluctuations, which have a direct effect on the fluctuations in the output torque. The torque profile for these generated phase emf waveforms and with ideal rectangular phase current waveforms is shown in Figure 7.7.

7.1.3 EFFECT OF INCORRECT ADJUSTMENT OF POSITION SENSORS ON COMMUTATION

Inaccurate timing of the phase switching devices is a further factor which can significantly effect the magnitude

of the torque ripple. The three position sensors should be arranged accurately to ensure that an optimum commutation angle can be obtained as will be explained in section 7.2.3. Also they should be equally spaced, by careful assembly, so that the transition from one energizing state of the stator windings to another will occur at the correct time.

7.1.4 EFFECT OF ROTOR AND STATOR TEETH

In a permanent-magnet machine, the interaction between the stator teeth and the magnetic saliency of the rotor can produce a reluctance torque which is a function of the rotor position[55].

7.1.5 EFFECT OF STATOR FIELD

The magnetic field created by the stator winding currents interacts with the main field of the permanent-magnet, to cause distortion of the flux-density distribution in the airgap. The magnitude of the consequent distortion in the torque waveform depends on the type of permanent-magnet material, the magnitude of the winding currents, and whether or not saturation occurs. If it does, there will be a net reduction of flux, by a process similar to the armature reaction effect in a brushed dc machine. The increase in flux on one side of the stator pole is always less than the reduction on the other side, as the maximum flux is limited by saturation of the magnetic path[56].

The use of a strong permanent-magnet material, such as samarium-cobalt, has a direct effect on minimizing the main magnetic field distortion caused by the stator magnetic

field. Samarium-cobalt has a high coercivity, high energy density and a linear demagnetization characteristic. A given stator MMF therefore causes less disturbance to the flux-density distribution in the airgap than would be the case with most other magnetic materials[54].

7.1.6 EFFECT OF INHOMOGENEOUS MAGNETIZATION

Inhomogeneous magnetization of the permanent-magnets can be another reason for additional irregularity in the magnetic field distribution and increased torque ripple. This sometimes occurs when the rotor poles have been fixed to the rotor surface and subsequently magnetized using a special magnetization yoke[27].

7.2 TORQUE RIPPLE MINIMIZATION METHODS

This section discusses the methods available for minimizing the speed and torque ripples which occur in a practical drive.

7.2.1 ADJUSTING ROTOR MAGNET POLE ARCS

It is possible to minimize the torque ripple by adjusting the rotor magnet pole arcs. When a 3-phase star-connected 2-pole brushless dc motor is fed by a 120° voltage source inverter, a 120°e rectangular current waveform is set up. To minimize the torque dips at the commutation events, the rotor magnetic pole arcs should be 180°e. The magnet is thus able to rotate 60°e with no change in the flux-density under either of the conducting phases[53], as shown in Figure 7.8.

7.2.2 INCREASING THE NUMBER OF PHASES

Since each phase produces torque for 120°e, considerable attention must be paid to the wave-shape of the generated phase emf required to produce constant torque for constant current over this range. The emf waveform depends on the winding distribution and the profile of the permanent-magnet[27,51], and with a sinusoidal emf waveform and two phases energized simultaneously for 60°e the corresponding torque profile for a rectangular phase current is shown in Figure 7.9. The same motor, with a trapezoidal emf waveform having a 120°e flat-top, has the constant torque profile of Figure 7.10. In practice however the generated emf is not constant for the full 120°e, as explained in section 7.1.2, and the torque profile is more as shown in Figure 7.7. The effect of such a waveform on the torque profile may be reduced by increasing the number of phases[57], as shown in Figures 7.11 and 7.12, which represent the torque profiles for 6-phase and 9-phase motors respectively. This solution however increases both the complexity of the electronic circuitry and the number of positional sensors which are required.

7.2.3 ADJUSTMENT OF THE COMMUTATION ANGLE

The rate-of-change of winding current during commutation depends on many factors, such as the winding inductance and the shape of the generated emf waveform. Another important factor is the commutation angle, defined as the angle between the injected phase current and the generated emf. A commutation angle of zero is defined in Figure 7.13, with the

phase current applied 30°e after the generated emf passes through zero. When closure of the switches applying the phase current is advanced by 30°e, to the point where the generated emf is zero as shown in Figure 7.14, the situation is defined as 30° commutation advance[38,58]. From these two figures, it is evident that the instantaneous difference between the supply voltage V and the commutated winding emf E may be controlled by changing the commutation angle, and this has a direct effect on the profile of the current in that winding and hence on the torque waveform. The effect of changing the commutation angle on the torque ripple was investigated using the computer model described in chapter 5. Figures 7.15, 7.16 and 7.17 show the predicted motor phase current, torque and speed waveforms with a 1Nm load torque and a steady-state speed of 160rpm for commutation angles of 0°,15° and 30°e respectively. For these conditions, the smallest torque ripple is achieved with a 30°e advance, since the instantaneous potential difference between the supply voltage V and the commutated winding emf E is larger and consequently the winding current rises quicker to its desired steady state.

7.2.4 REDUCING THE STATOR WINDING INDUCTANCE

The actual phase current waveform shown in Figure 7.2(b) does not have the ideal rectangular shape, but has rounded edges and a dip at every commutation instant due to the stator winding inductance and the generated emf. The effect of commutation on the torque profile may be minimized by designing the machine with a low stator inductance, such that

the electrical time constant is small and the current rapidly attains its final value. Figure 7.18 shows the predicted relationship between the torque ripple and the stator winding inductance value, for a load torque of 1Nm and a speed of 160rpm. It is evident that the torque ripple is less with a smaller inductance value. The phase inductance is directly proportional to the square of the number of turns per phase and the magnetic circuit cross-sectional area, and inversely proportional to the length of the magnetic circuit[38]. Thus a reduction in the stator winding inductance necessitates modifications to the motor design.

7.2.5 SKEWING OF THE STATOR SLOTS

It is well known that skewing the stator slots or rotor magnets by one slot pitch reduces reluctance torque effect[55].

7.2.6 IMPROVEMENT TO THE CURRENT CONTROLLER

The current ripple produced by the current controller causes a high-frequency torque ripple, which depends on the switching frequency of the PWM current controller as shown in the simulated results given in Figures 7.19 and 7.20. It is evident that the high-frequency torque ripple at 25kHz switching frequency is less than that at 5kHz. The high frequency torque ripple magnitudes are much less than those produced by current commutation and they produce only a small speed ripple, which is expected to be filtered out by the rotor inertia[55]. However, the PWM controller designed in the course of this research is capable of operating at 50kHz,

and this relatively high-frequency considerably reduces the current ripple magnitude and consequently the high-frequency torque ripple. Figures 7.21 and 7.22 show the predicted and measured phase *a* current waveforms at 5 and 25kHz switching frequency, which confirm that an increased switching frequency reduces the current ripple.

7.2.7 ADJUSTMENT OF THE PHASE CURRENT WAVEFORMS

The methods described above for minimizing torque ripple necessitate modifications to the motor design, and when this is not practicable adjustment of the phase current waveforms provides an attractive and novel alternative. Both adjustment of the phase current waveforms to minimize the torque ripple and the practical implementation of this concept are explained in detail below.

7.3 CURRENT PROFILING

Since instantaneous torque is proportional to the instantaneous product of generated emf and phase current, it should be possible to produce a smooth torque by adjusting the current profile in a way which eliminates the torque ripple. The instantaneous electromagnetic torque developed in a brushless dc motor may be expressed as

$$T_e = \frac{1}{\omega_r}\left(e_a i_a + e_b i_b + e_c i_c\right) \qquad (7.2)$$

where

e_a, e_b, e_c are respectively the instantaneous emfs generated in phases *a*, *b* and *c*,

i_a, i_b, i_c are respectively the instantaneous currents

in phases *a*, *b* and *c* , and

ω_r is the rotor angular velocity.

At any given time, only two of the three phases are conducting, and commutation from one pair of stator windings to the next occurs every 60°e of rotor position. The phase currents defined in Figure 7.23 for a typical 60°e of rotation are $i_a = -I_s$, $i_b = 0$ and $i_c = I_s$, where I_s is the dc supply current. The total instantaneous torque during this period becomes

$$T_e = \frac{I_s}{\omega_r}(e_c - e_a) \tag{7.3}$$

With a constant dc supply current, the torque is constant if the term $(e_c - e_a)$ is constant over the 60°e of rotation, and this is possible with a trapezoidal emf having a 120°e flat-top. However, as explained previously, this is not the case in practice. The generated phase emf has a flat-top of less than 120°e, contains fluctuations and the phase current does not have the ideal rectangular shape and has a dip every 60°e of rotor position due to commutation. The combination of these two factors result in the torque ripple shown in Figure 7.24. The resultant torque ripple may be minimized by adjusting the phase current waveforms to compensate for any deviation and fluctuations in the generated emf waveforms and to minimize the effect of the commutation. The phase current waveforms thus have to be adjusted in proportion to the term $1/(e_c - e_a)$ over the 60°e period considered and at the commutation instant, to achieve the optimum minimization of the torque ripple. This is achieved in the program (and in

practice) by introducing a current control loop with PWM control of the inverter switches to force the motor phase current to follow the above proportionality. Figure 7.25 shows the simulated phase current without any such modification, together with the corresponding torque and speed waveforms for a load torque of 0.6Nm and an average speed of 102rpm. It is evident that the motor torque is not constant and this has resulted in a fluctuation in the speed waveform. Figure 7.26 shows the adjusted profile of current waveform required to compensate for the deviation and fluctuations in the generated emf and the corresponding torque and speed waveforms for the same conditions of Figure 7.25. It is evident from Figure 7.26 that the torque and speed ripples are considerably reduced. There are still torque and speed ripples evident in Figure 7.26 and these clearly occur at commutation instants. To minimize these ripples, the current waveform has to be further modified. A current boost during commutation was therefore introduced into the control loop, together with the current profiling, and Figure 7.27 shows the effect of this on the waveforms. The slight increase in phase current at commutation has virtually eliminated the torque and speed ripples. A practical circuit to implement current profiling is described in the following section.

7.4 PRACTICAL IMPLEMENTATION OF CURRENT PROFILING

A block diagram for the current profiling circuit is shown in Figure 7.28. Accurate information on the rotor position is necessary, to enable the correct profile of the

current waveform to be obtained, since the torque ripple is synchronized both to the commutation events and the rotor position. The encoder detailed in Appendix 3 produces 1080 pulses per revolution, corresponding to 60 pulses per 60°e, so that the rotor position and the commutation instants can be defined to an accuracy of 1°e. The encoder pulses are supplied to the counter shown in Figure 7.29, which counts from 0 to 59 and is reset by a pulse applied to the counter reset pin every 60°e. The reset pulse is obtained by applying the counter binary output to an AND gate, such that the gate output is high every 60°e. The encoder zero mark pulse is also used to reset the counter every 360°m, ensuring that counting always starts from the same shaft reference position. The output of the counter addresses an EPROM which contains a numerical representation of the required current profile. The digital signal output from the EPROM is applied to a D/A converter which converts the data to an appropriate analogue voltage. The voltage amplitude may be varied by potentiometer Pt1 of Figure 7.29, before being subtracted from the average speed-demand voltage. The resultant voltage is compared with a sawtooth waveform to generate a PWM signal, whose mark-to-space ratio controls the on/off state of the switching device and subsequently the voltage applied to the stator winding. The motor current is thereby shaped according to the data in the EPROM and, by changing the values at the appropriate addresses in the EPROM, the mark-to-space ratio of the generated PWM signal can be adjusted in relation to the rotor position and commutation instants and the required current shape may be achieved.

In order to store several output waveforms in the same EPROM, switches S1 and S2 are used to provide several blocks of memory, each comprising 60 bytes, to store the individual current waveforms.

Several experimental D/A converter output waveforms and the corresponding motor phase current waveforms are given in Figure 7.30. Figure 7.30(a) shows the waveform with current boost during the commutation instants to minimize the effect of the commutation on the output torque, and Figure 7.30(b) the waveform required to compensate for the deviation and fluctuations in the generated emf waveform and consequently to minimize the effect of such deviation and fluctuations on the output torque. To achieve the best overall performance, both forms of compensation are necessary, as shown in Figure 7.30(c). Close similarity can be seen between the predicted and measured phase current waveforms of Figures 7.26, 7.27 and 7.30. Accurate measurement of torque and speed ripples is not easy to achieve. Many attempts were made to measure the torque ripple using a strain gauge and the speed ripple using frequency to voltage converter circuit and the output voltage of the tachometer, but unfortunately it was difficult to obtain accurate results due to mechanical problems arising from slight misalignment of the motor corrupting the torque and speed readings which were, in any case, of small magnitude.

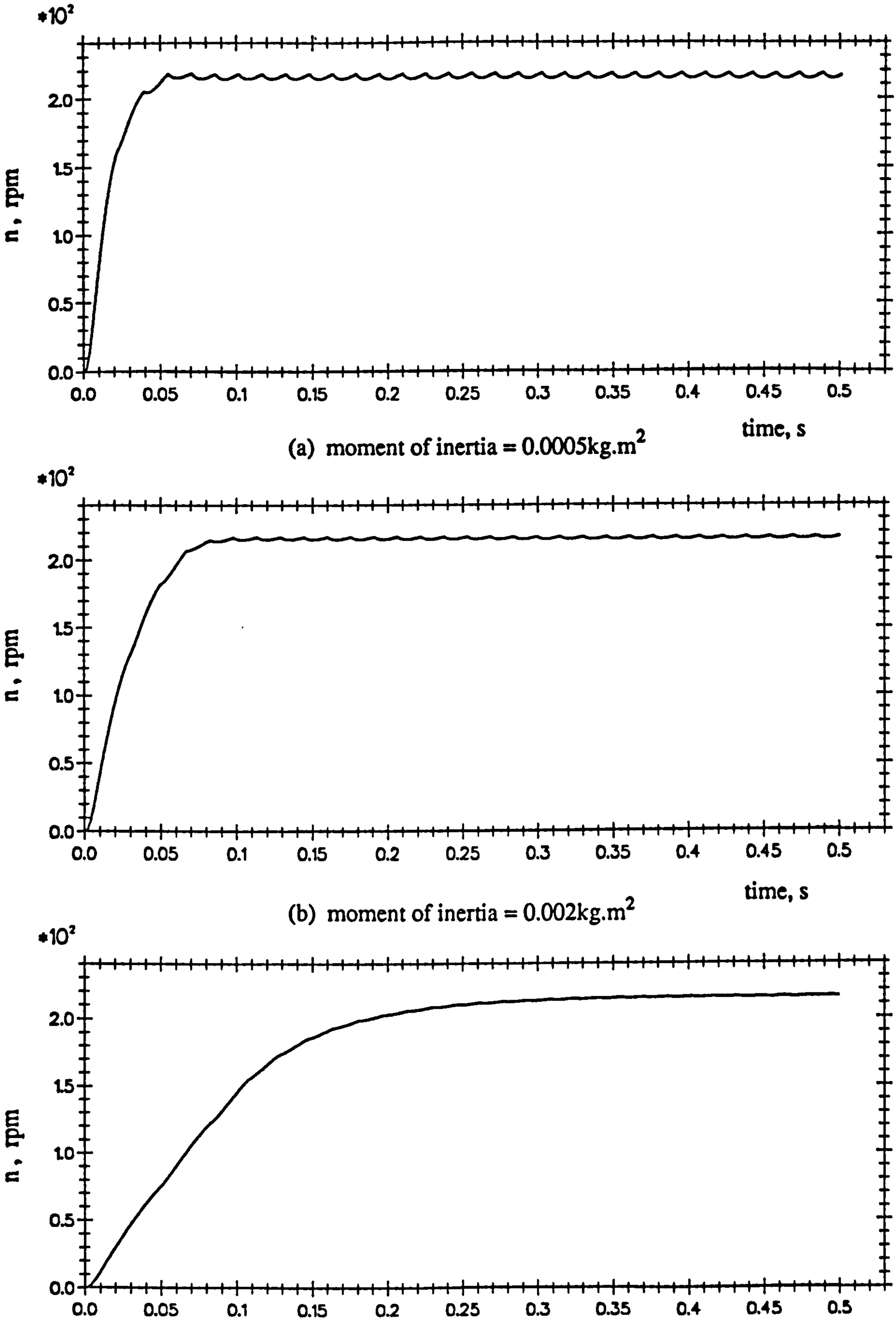

(a) moment of inertia = 0.0005kg.m^2

(b) moment of inertia = 0.002kg.m^2

(c) moment of inertia = 0.008kg.m^2

Figure 7.1 Simulated motor speed waveforms for various moments of inertia

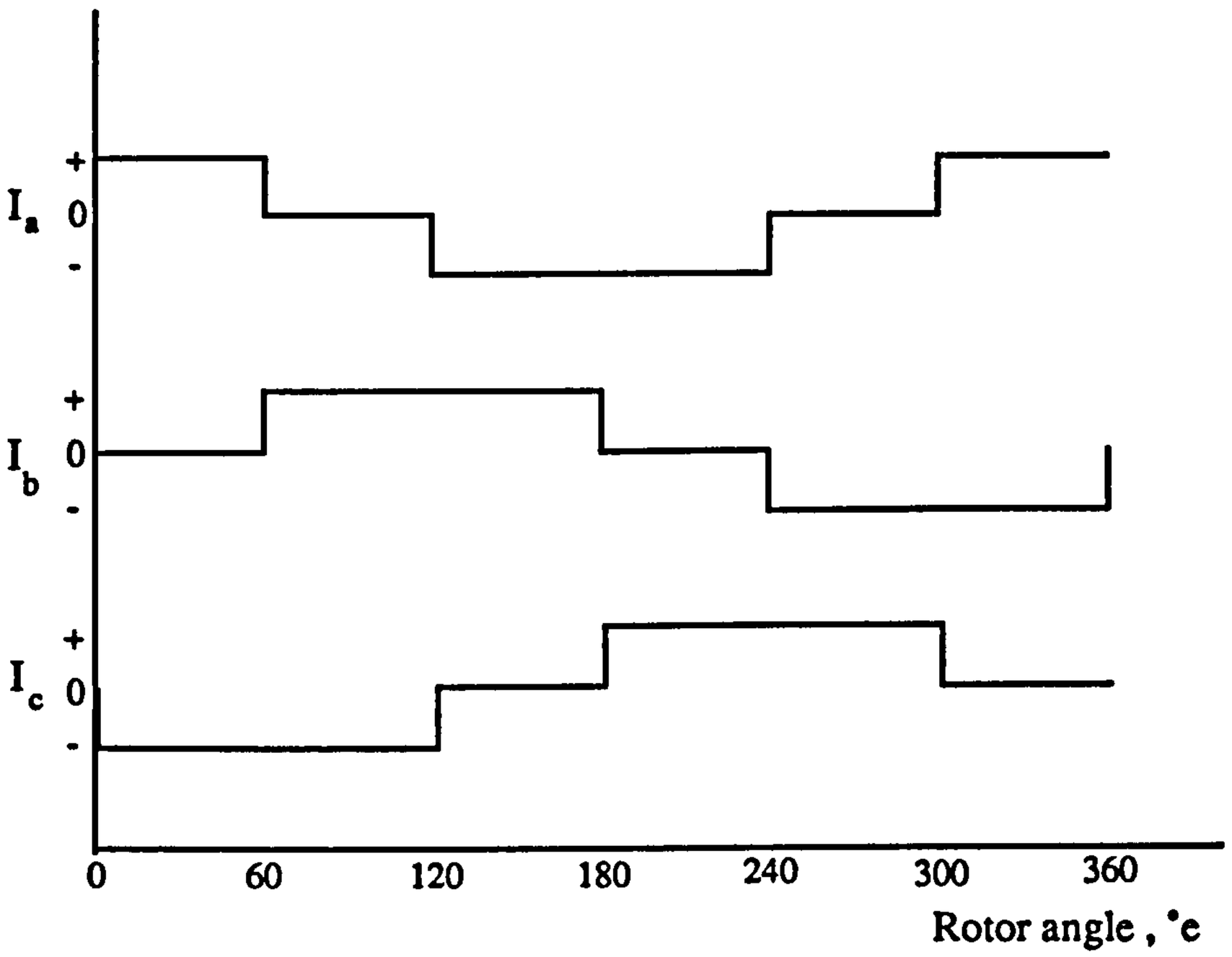

(a) Idealized phase currents

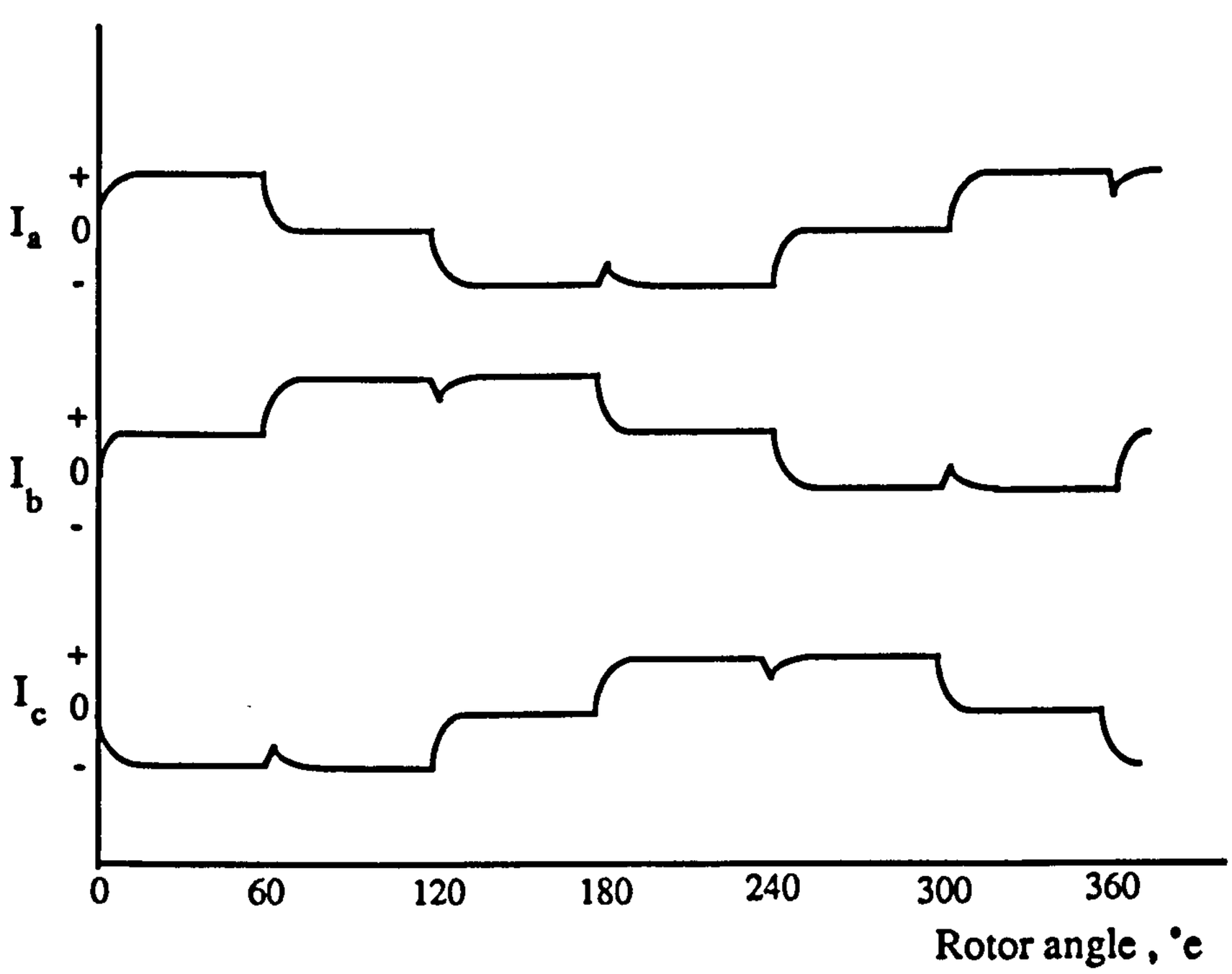

(b) Actual phase currents

Figure 7.2 Comparison between idealized and actual phase current waveforms

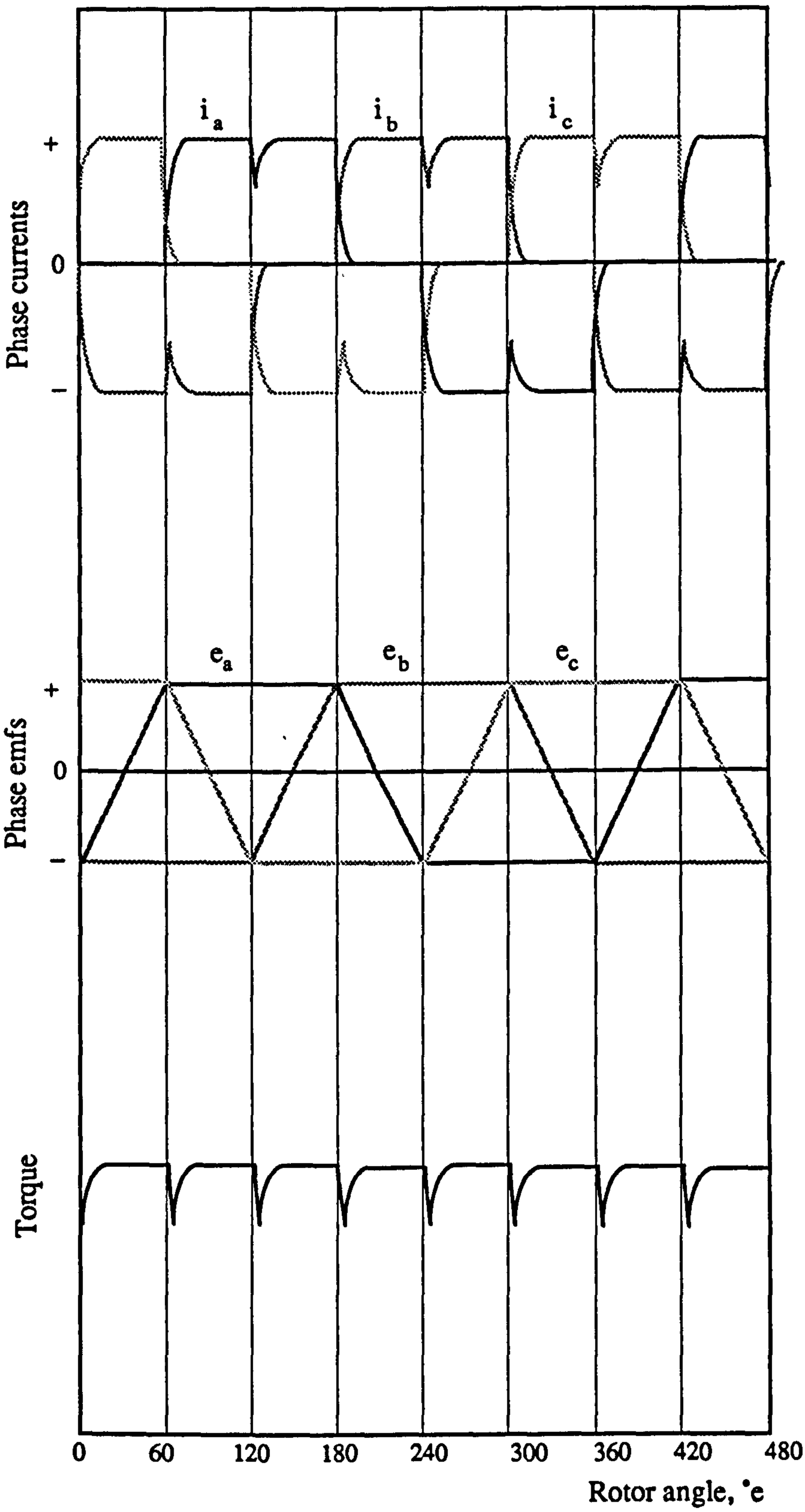

Figure 7.3 Effect of phase current waveforms on torque profile

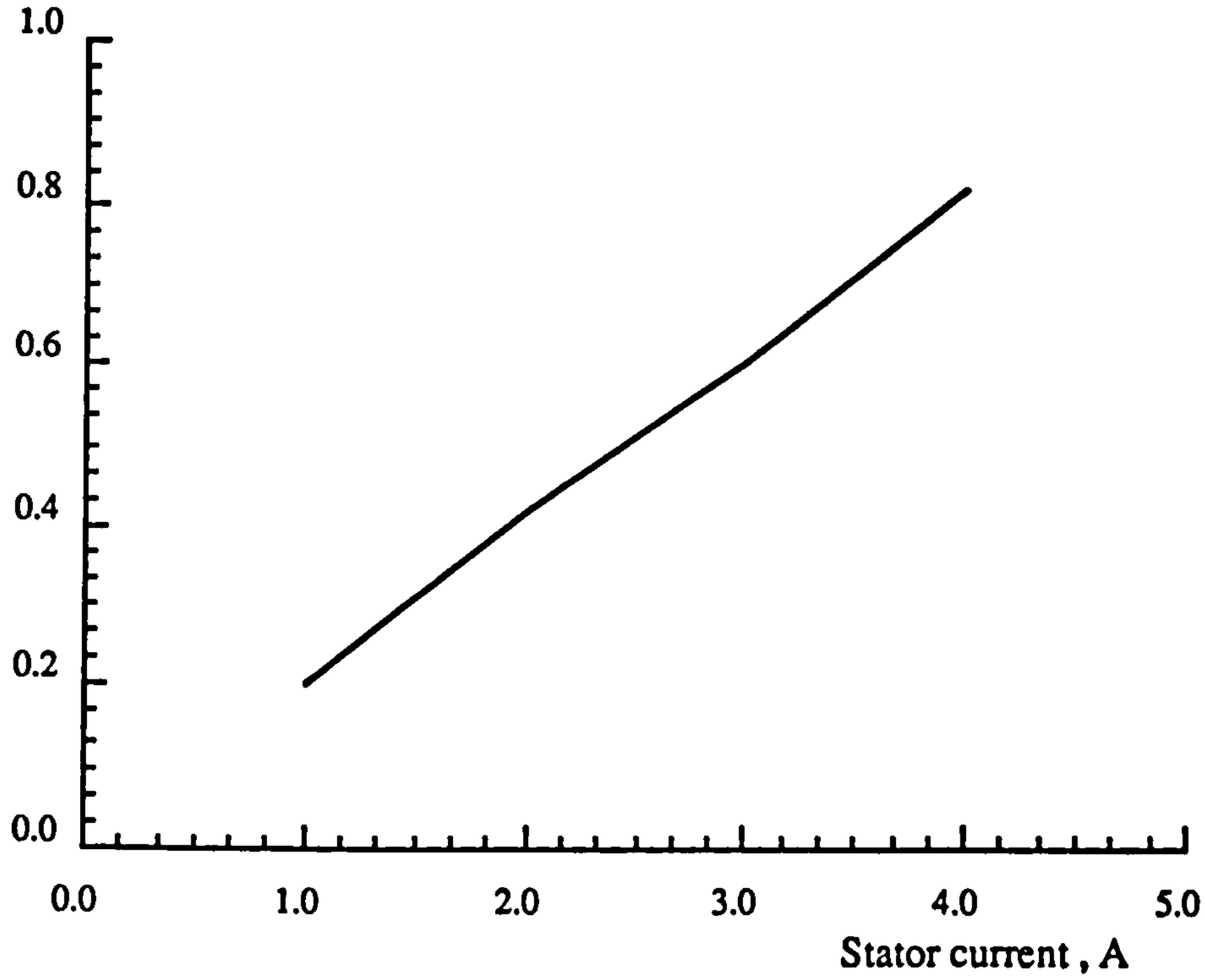

Figure 7.4 Variation of torque ripple with stator current

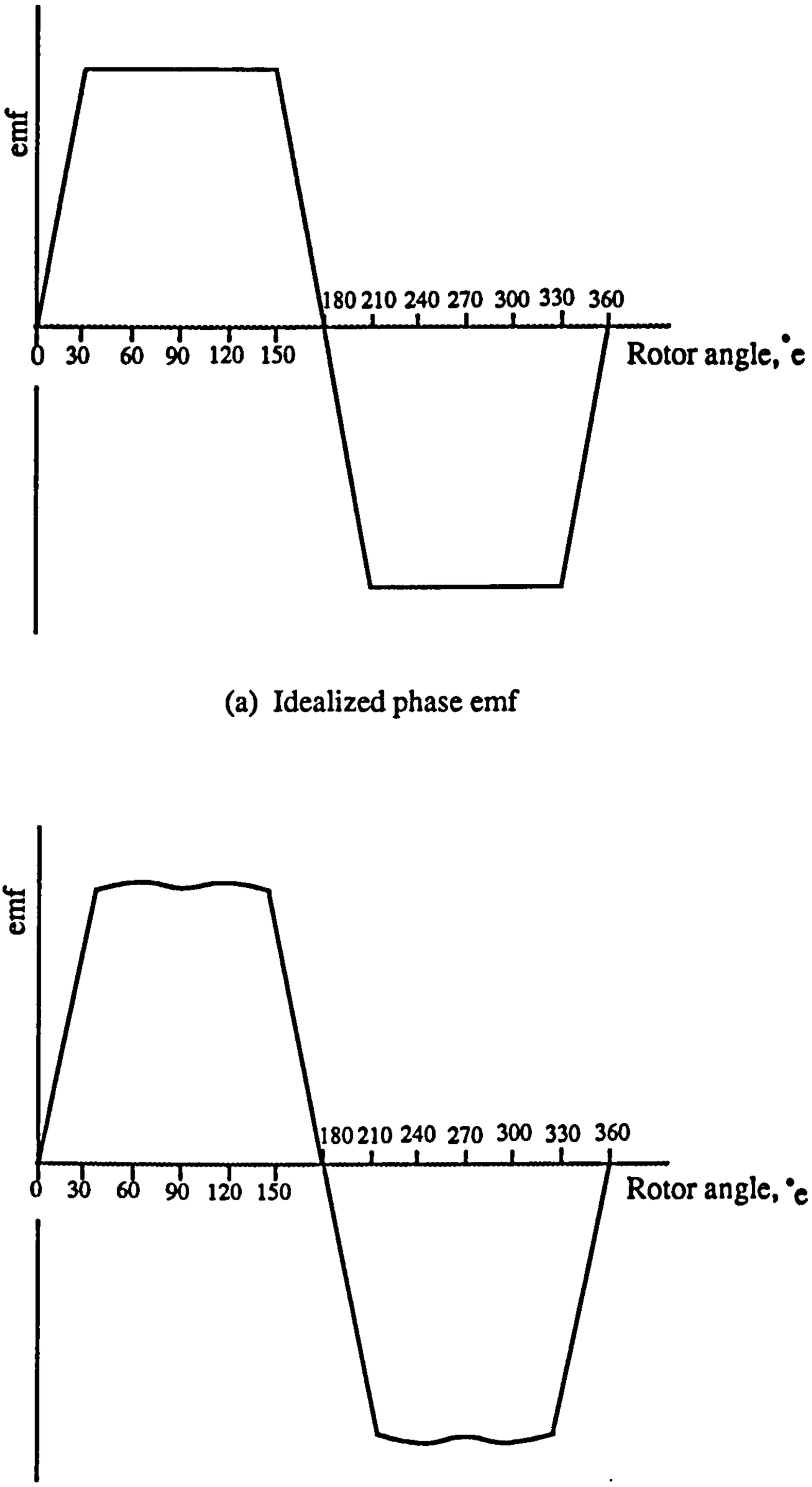

(a) Idealized phase emf

(b) Actual phase emf

Figure 7.5 Comparison between idealized and actual phase emf waveforms

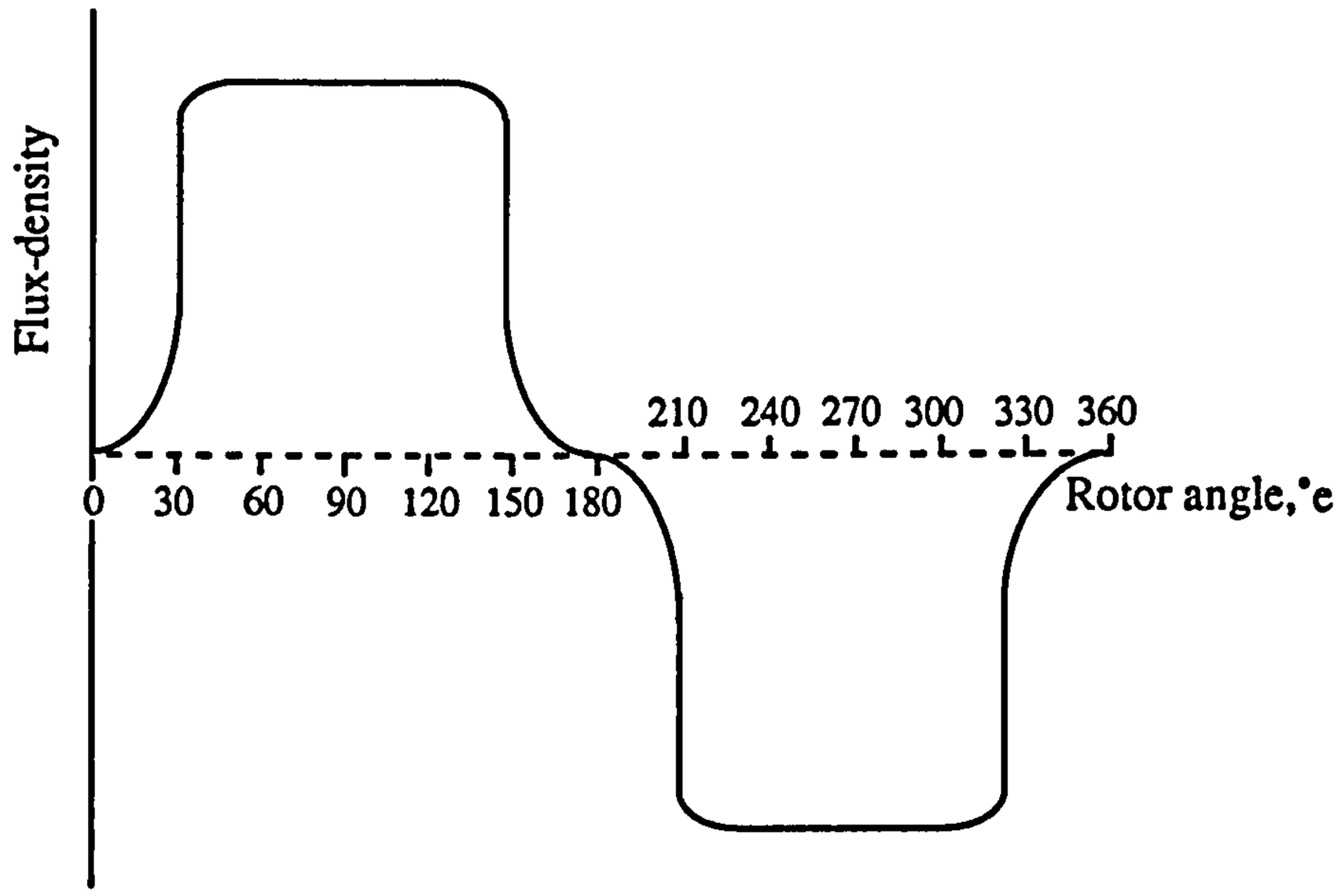

Figure 7.6 Typical practical airgap flux-density distribution

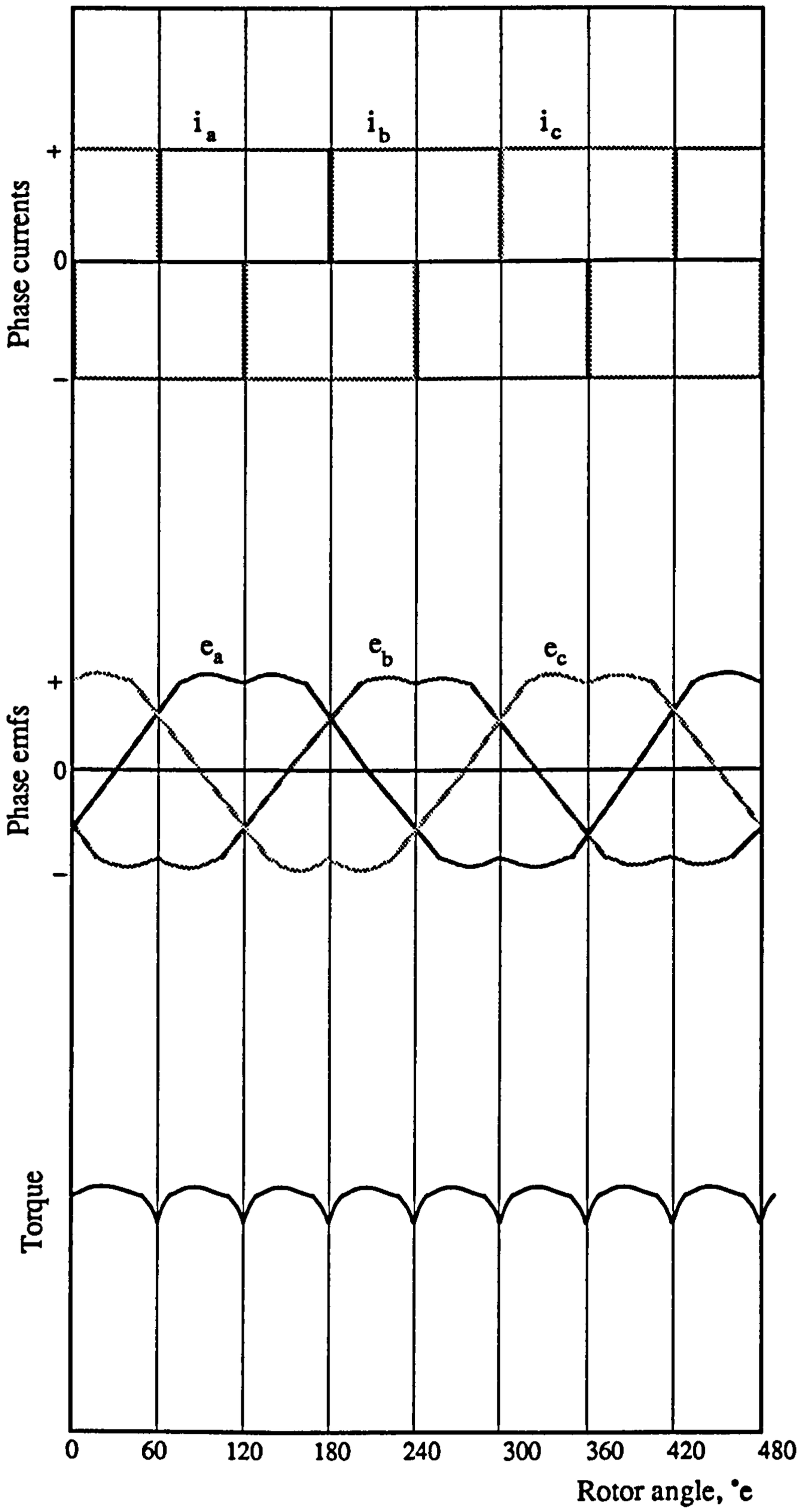

Figure 7.7 Effect of phase emf waveforms on torque profile

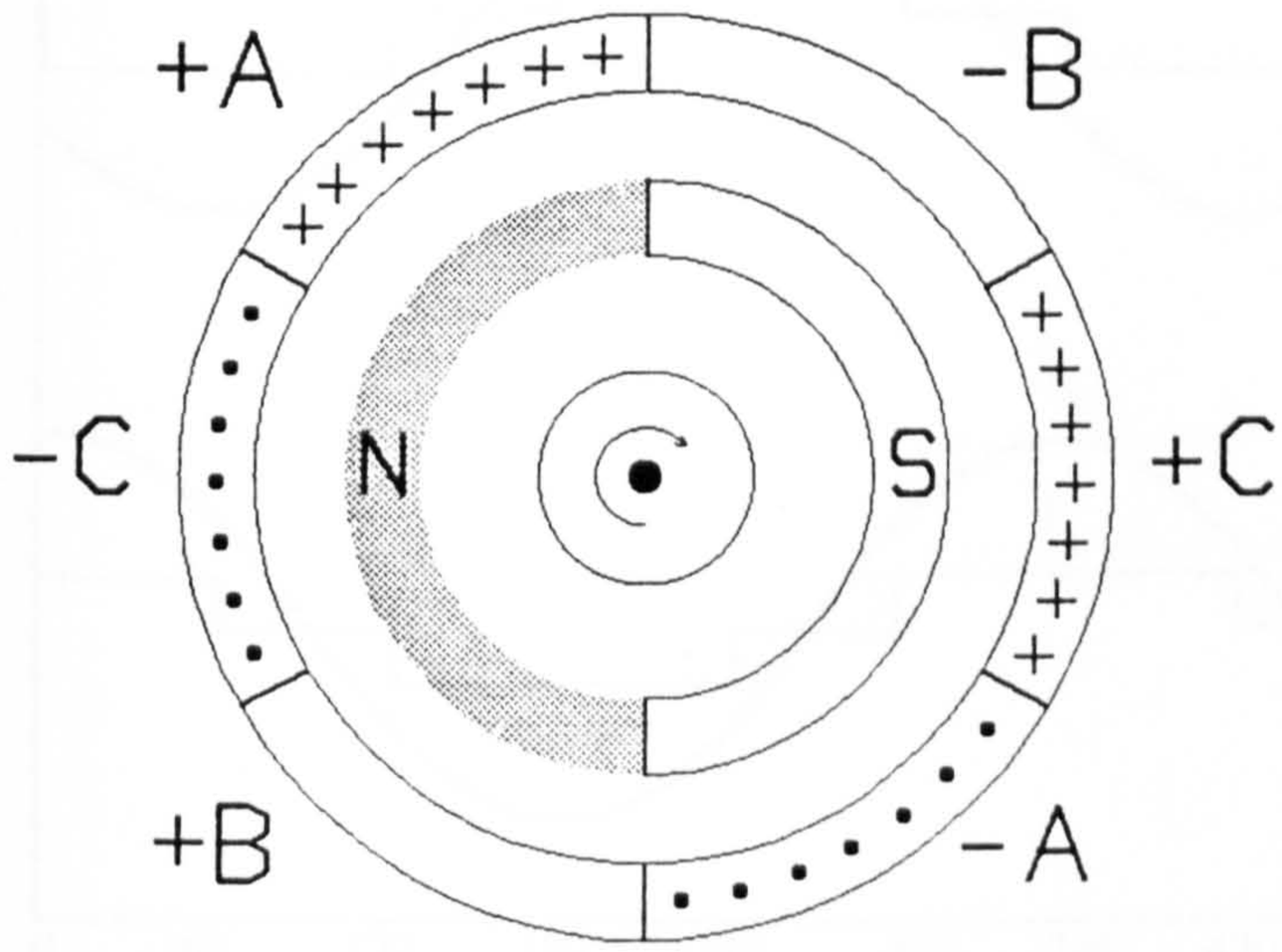

Figure 7.8 Brushless dc motor with 120°e rectangular phase current excitation and rotor magnet with 180°e arc

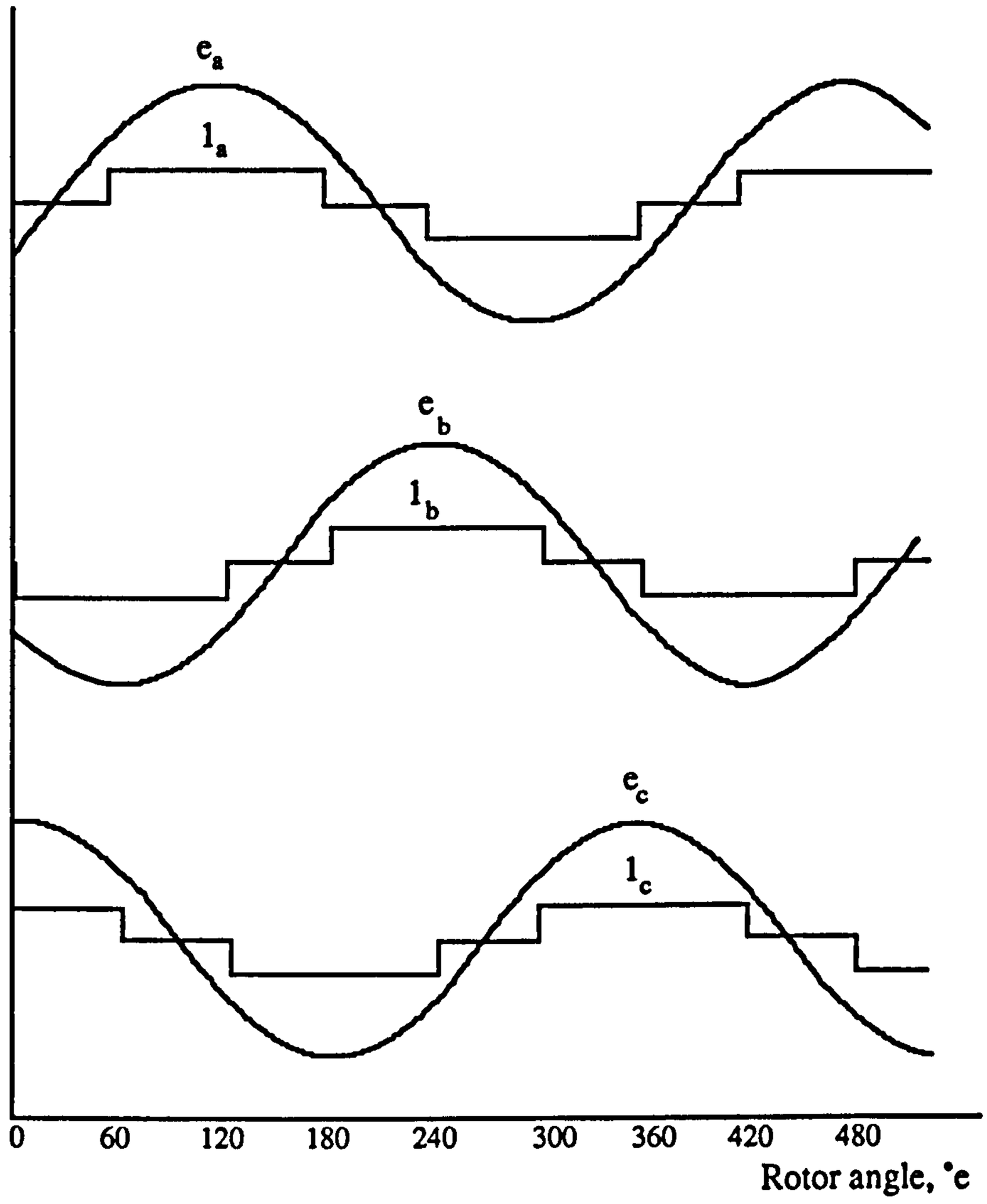

(a) Sinusoidal generated emf and rectangular current waveforms

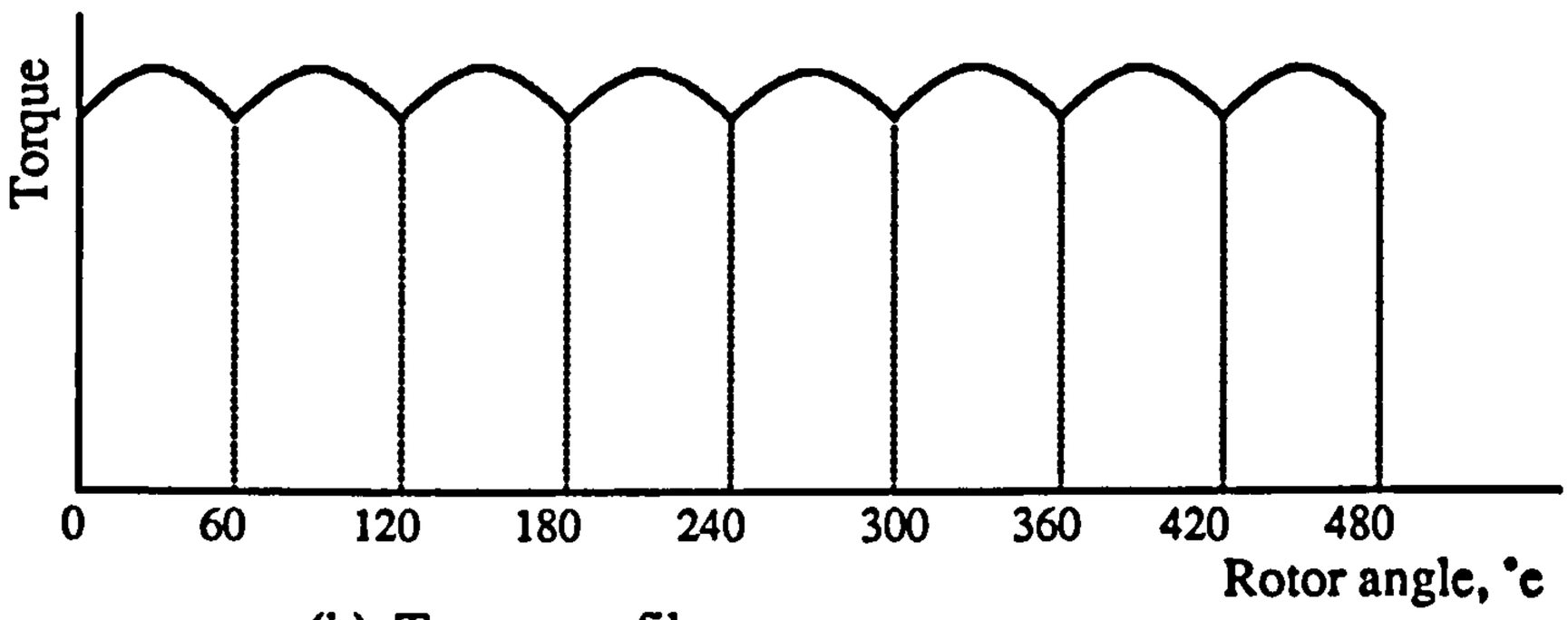

(b) Torque profile

Figure 7.9 Torque profile resulting from sinusoidal generated emf and rectangular current waveforms

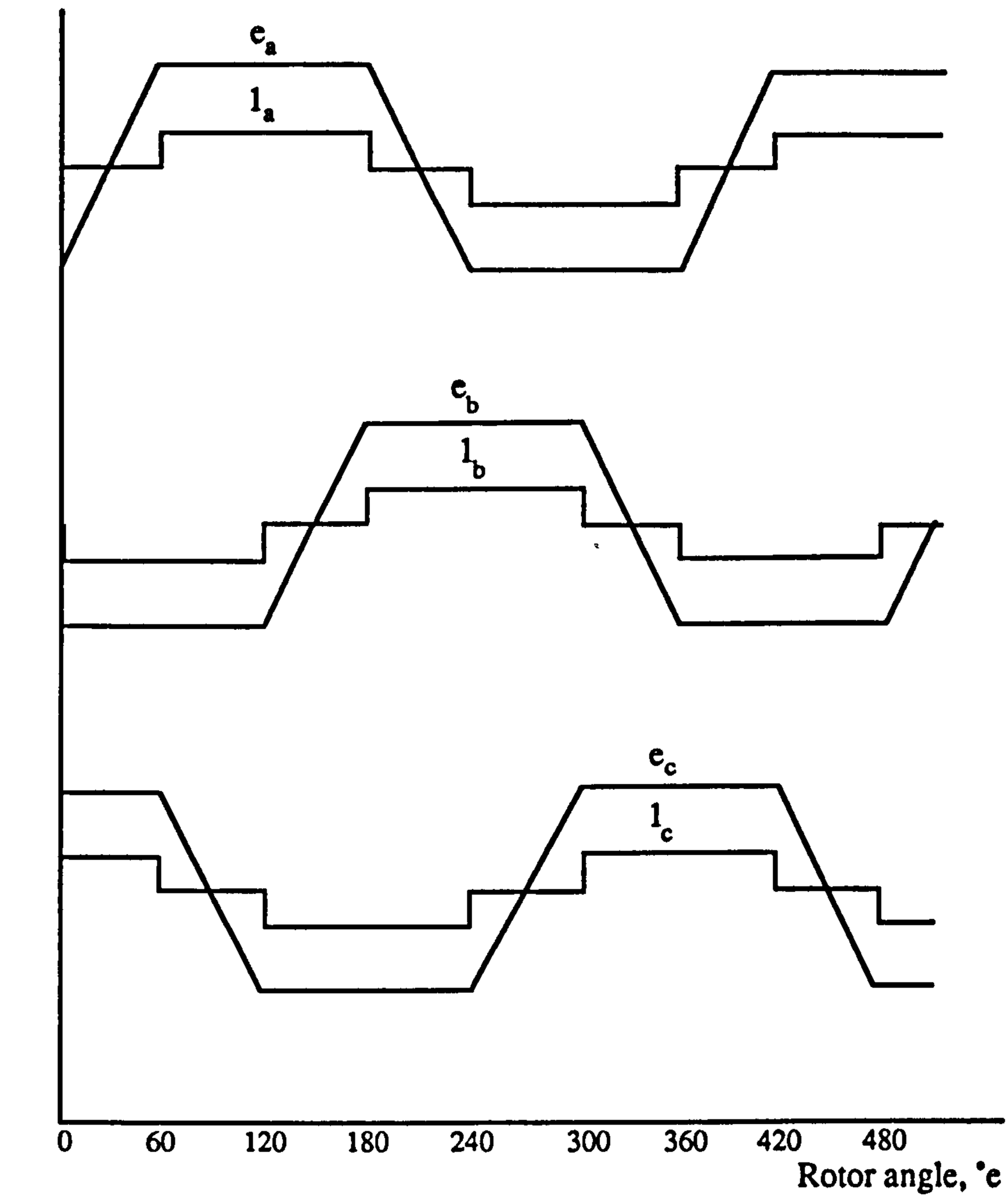

(a) Ideal trapeziodal generated emf and rectangular current waveforms

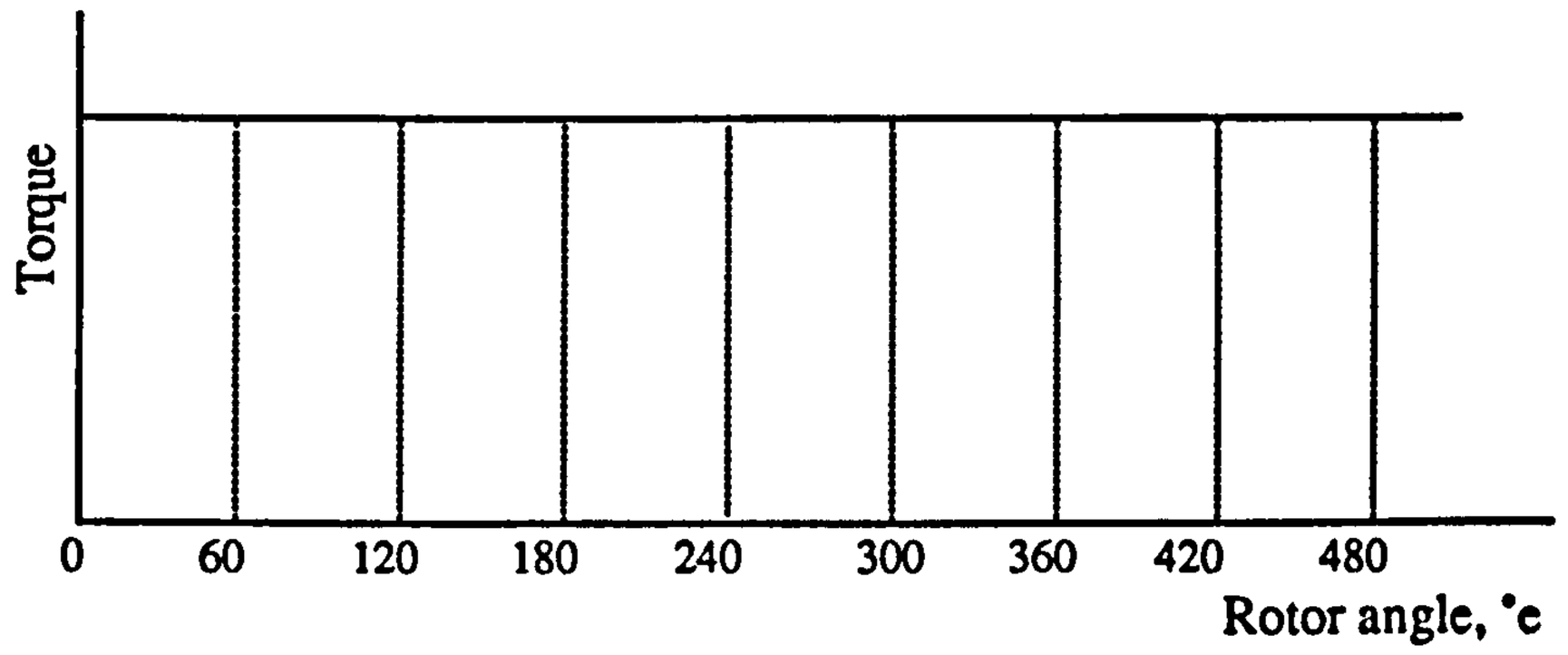

(b) Torque profile

Figure 7.10 Torque profile resulting from ideal trapeziodal generated emf and rectangular current waveforms

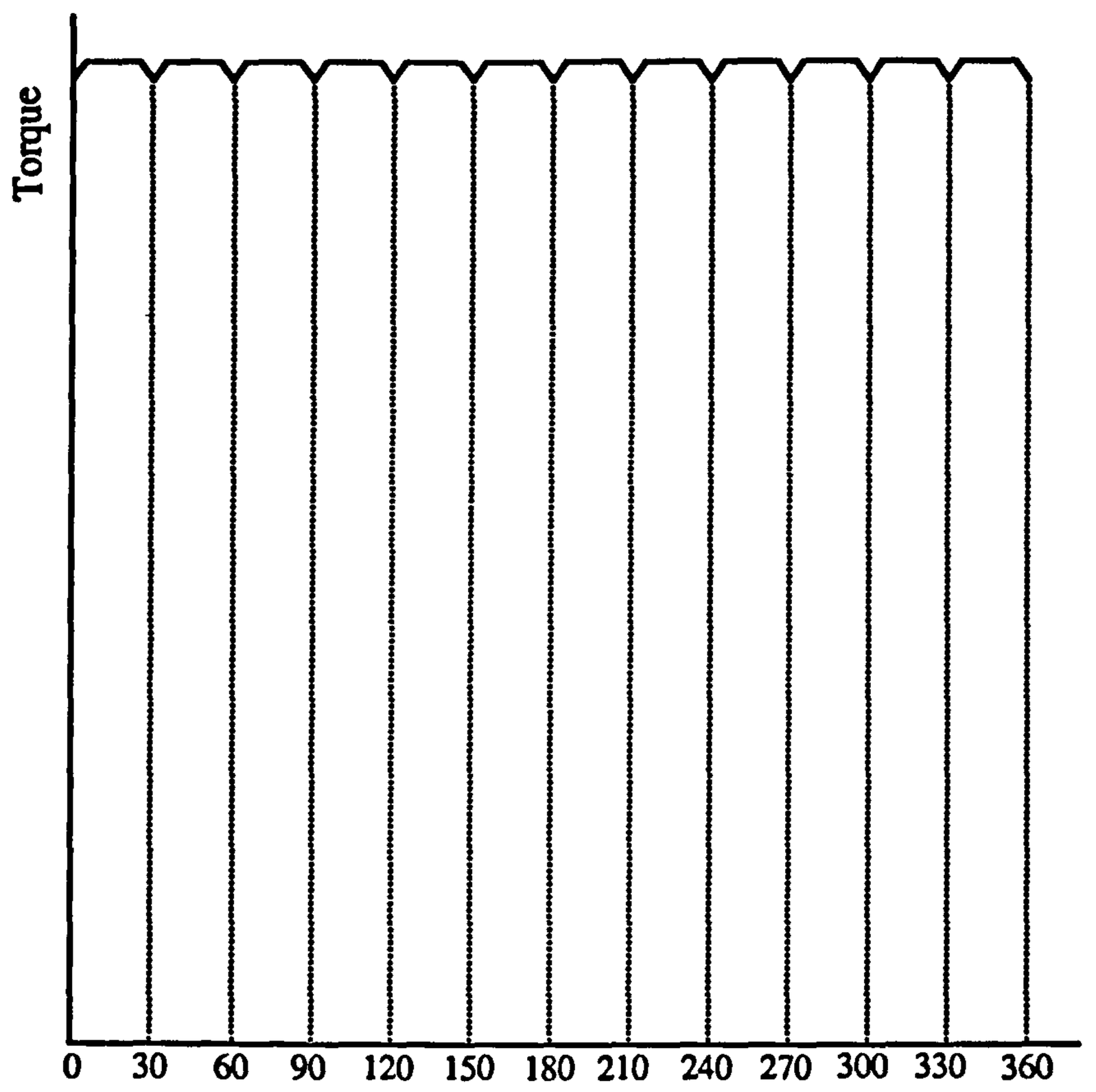

Figure 7.11 Torque profile for a 6-phase brushless dc motor

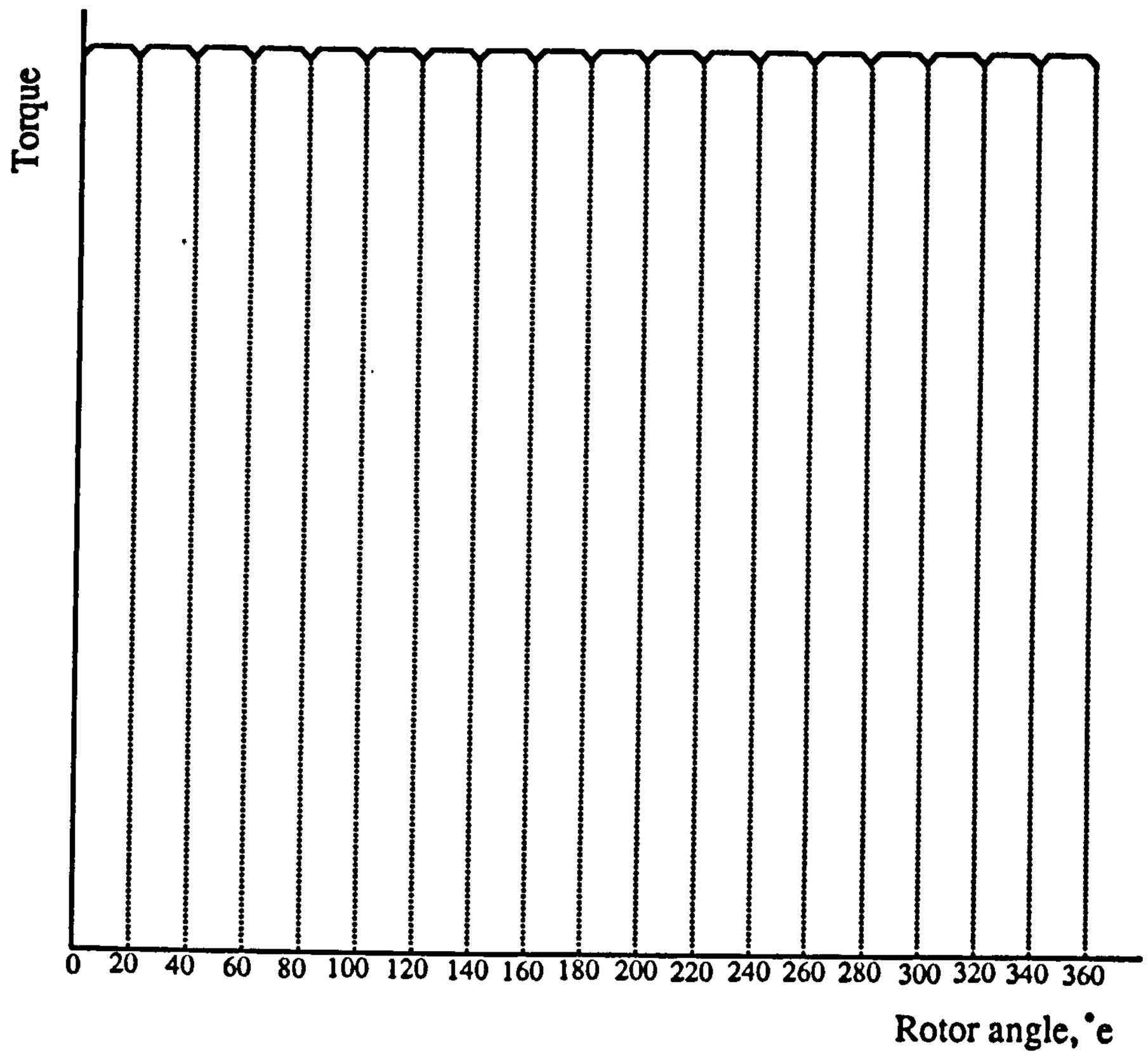

Figure 7.12 Torque profile for a 9-phase brushless dc motor

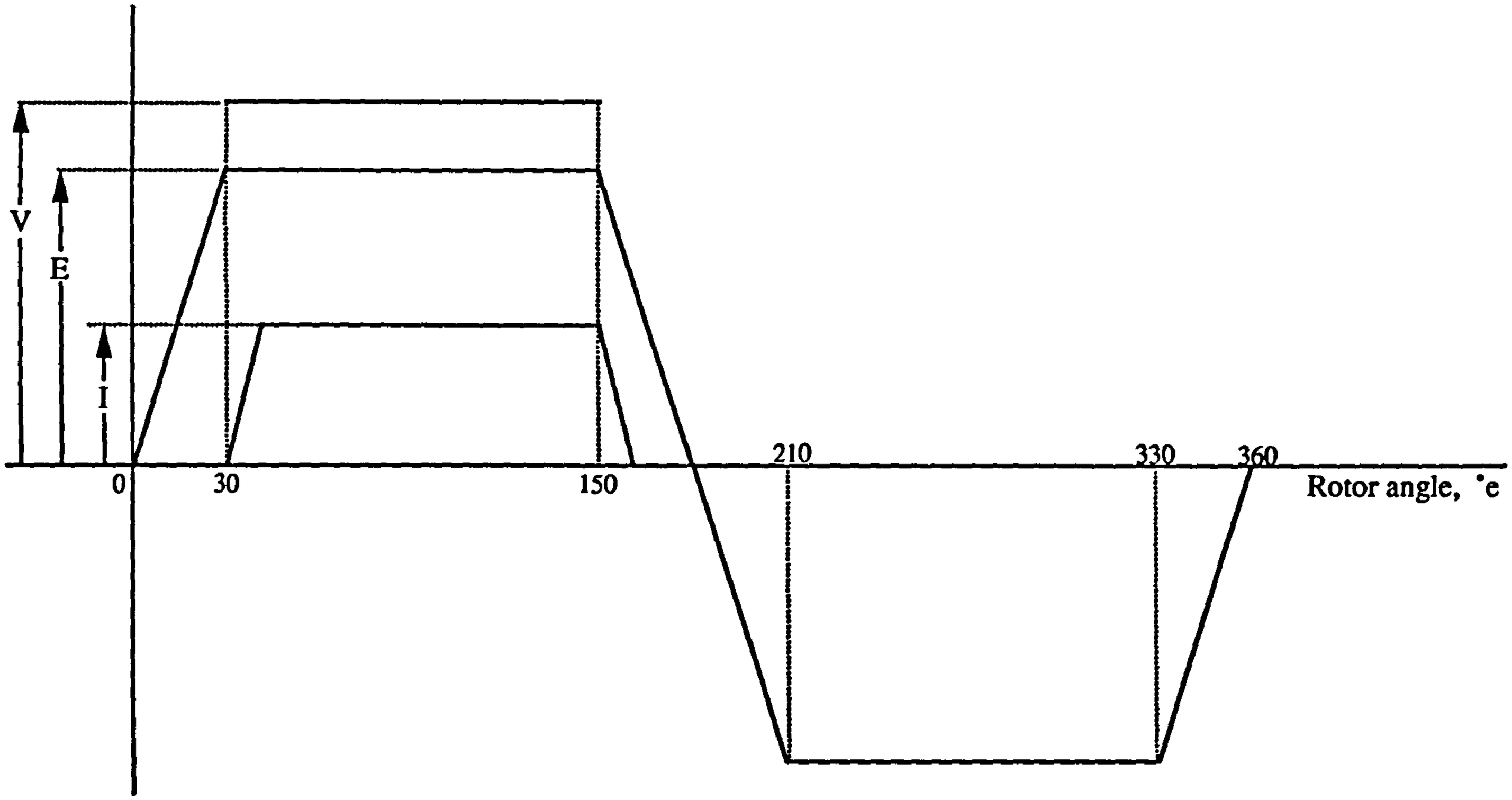

Figure 7.13 Relationship between voltage, current and generated emf with zero commutation advance

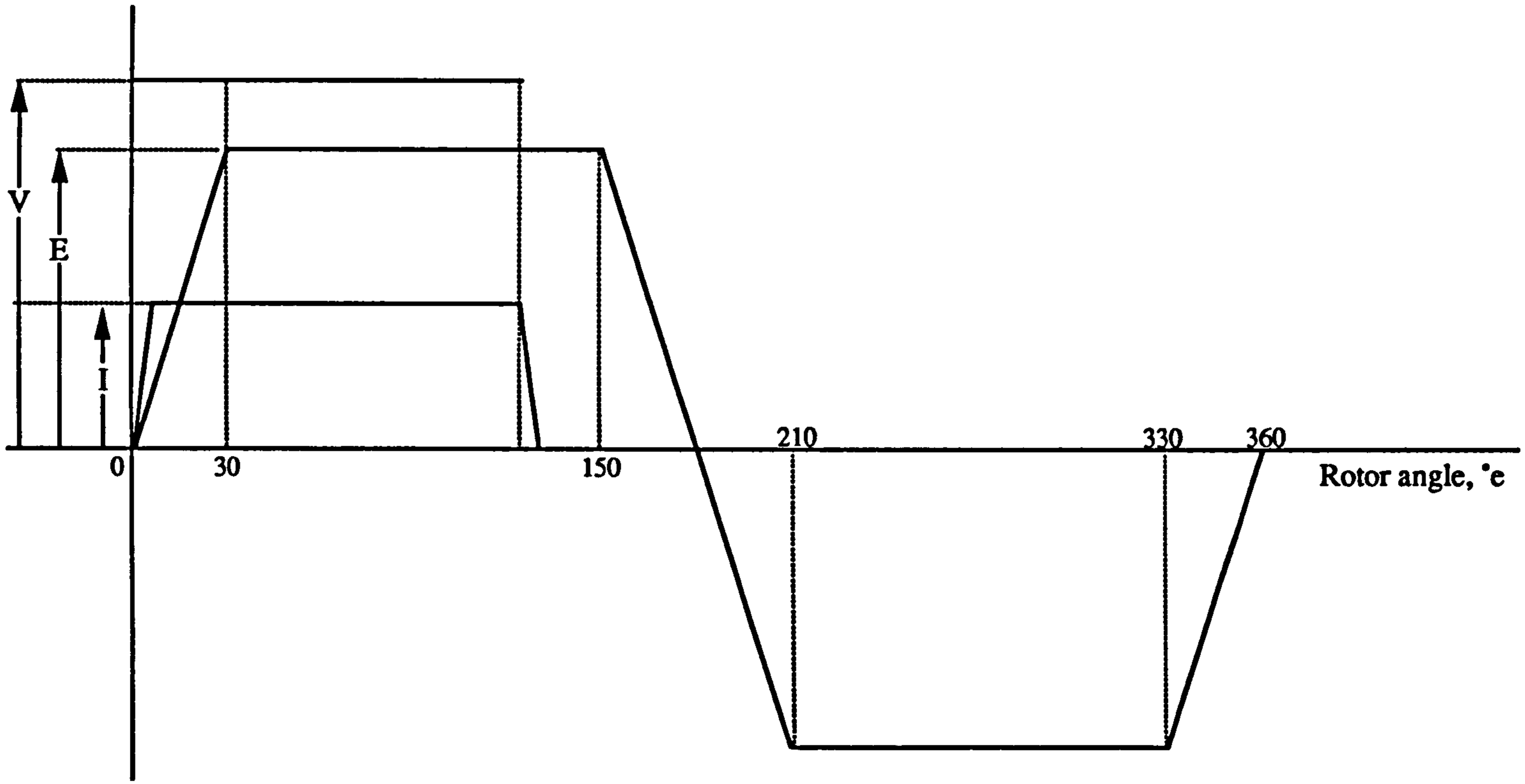

Figure 7.14 Relationship between voltage, current and generated emf with 30°e commutation advance

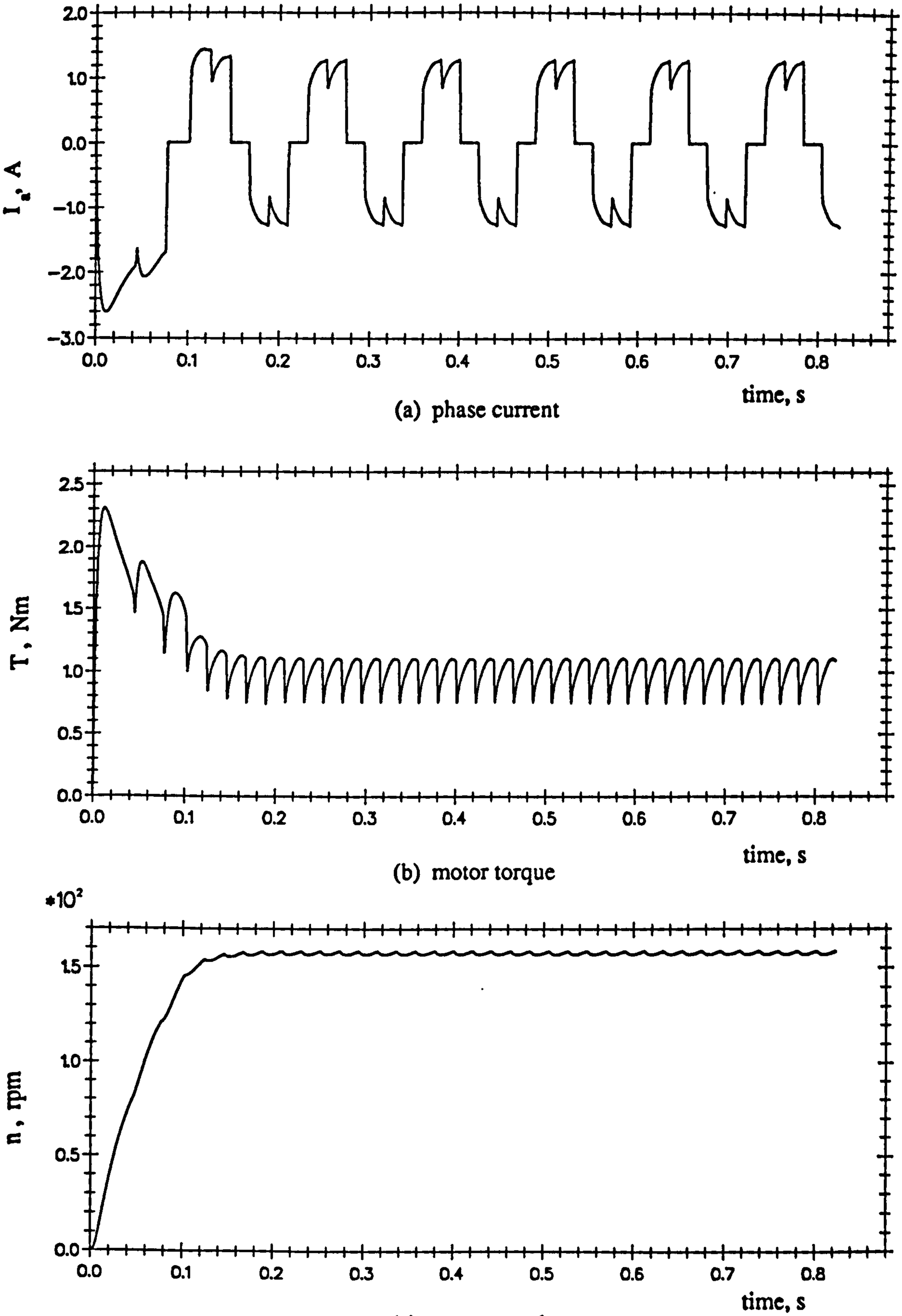

Figure 7.15 Simulated waveforms with 0°e commutation advance (Load condition : 1Nm at 160rpm)

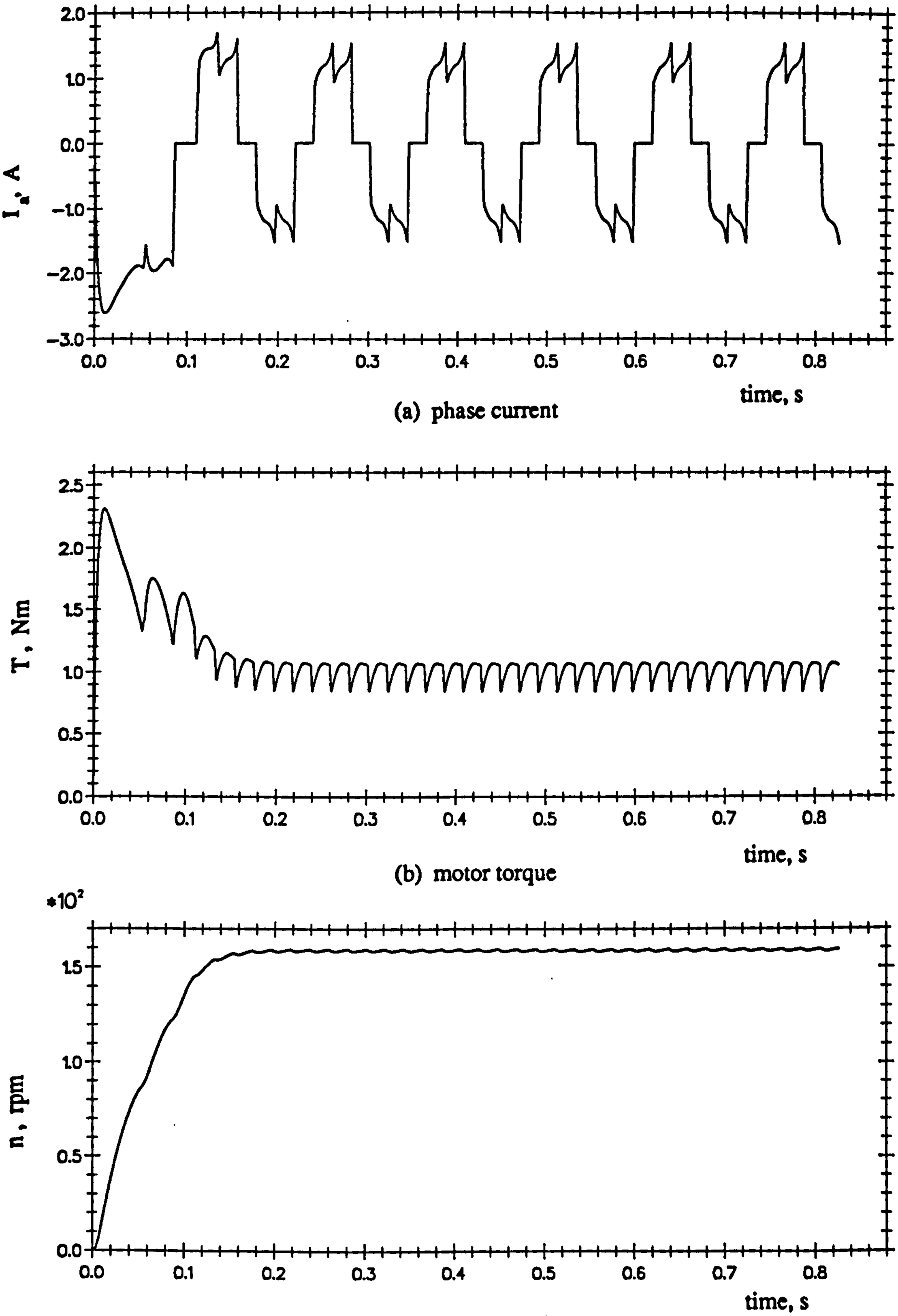

Figure 7.16 Simulated waveforms with 15°e commutation advance (Load condition : 1Nm at 160rpm)

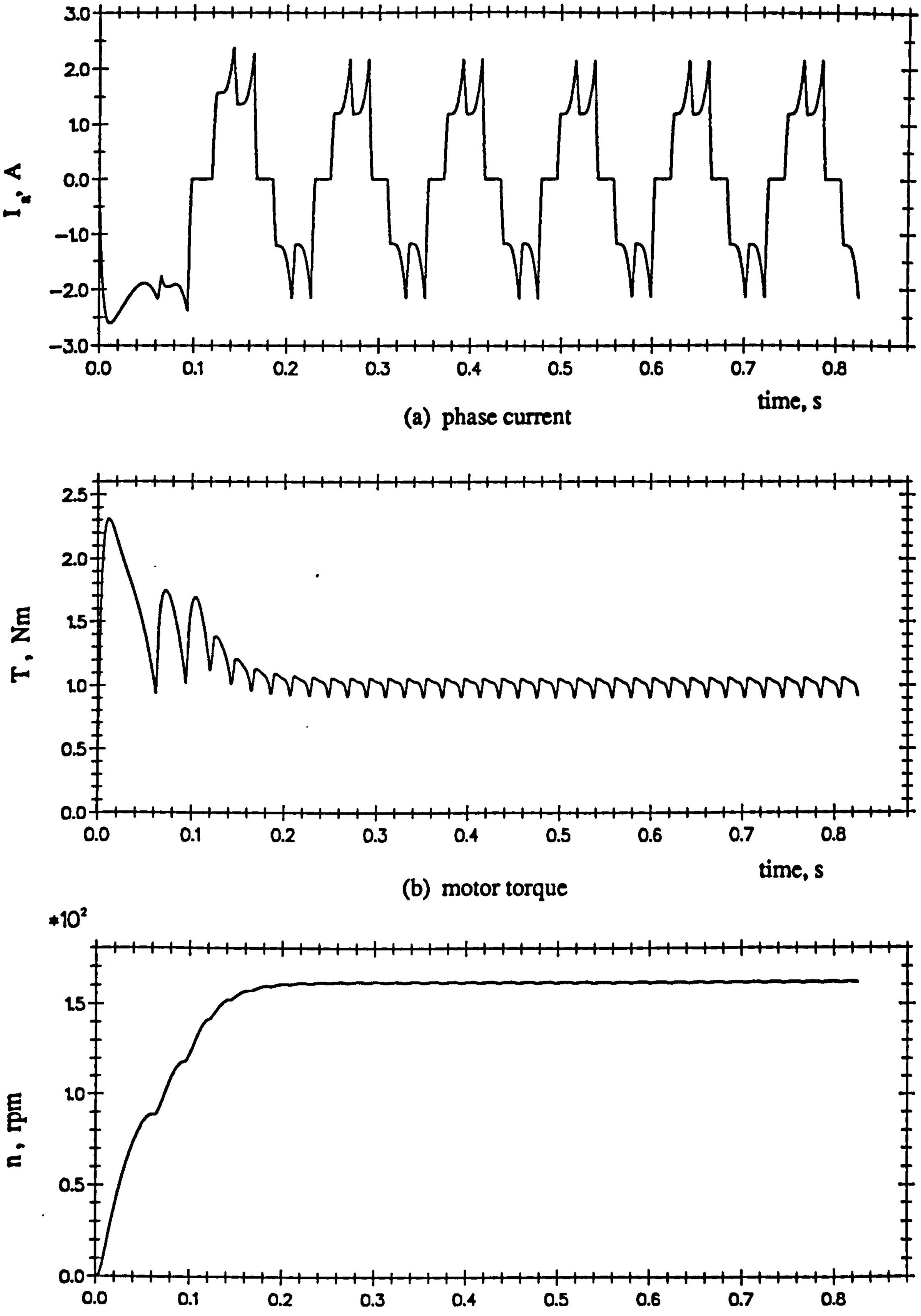

Figure 7.17 Simulated waveforms with 30°e commutation advance (Load condition : 1Nm at 160rpm)

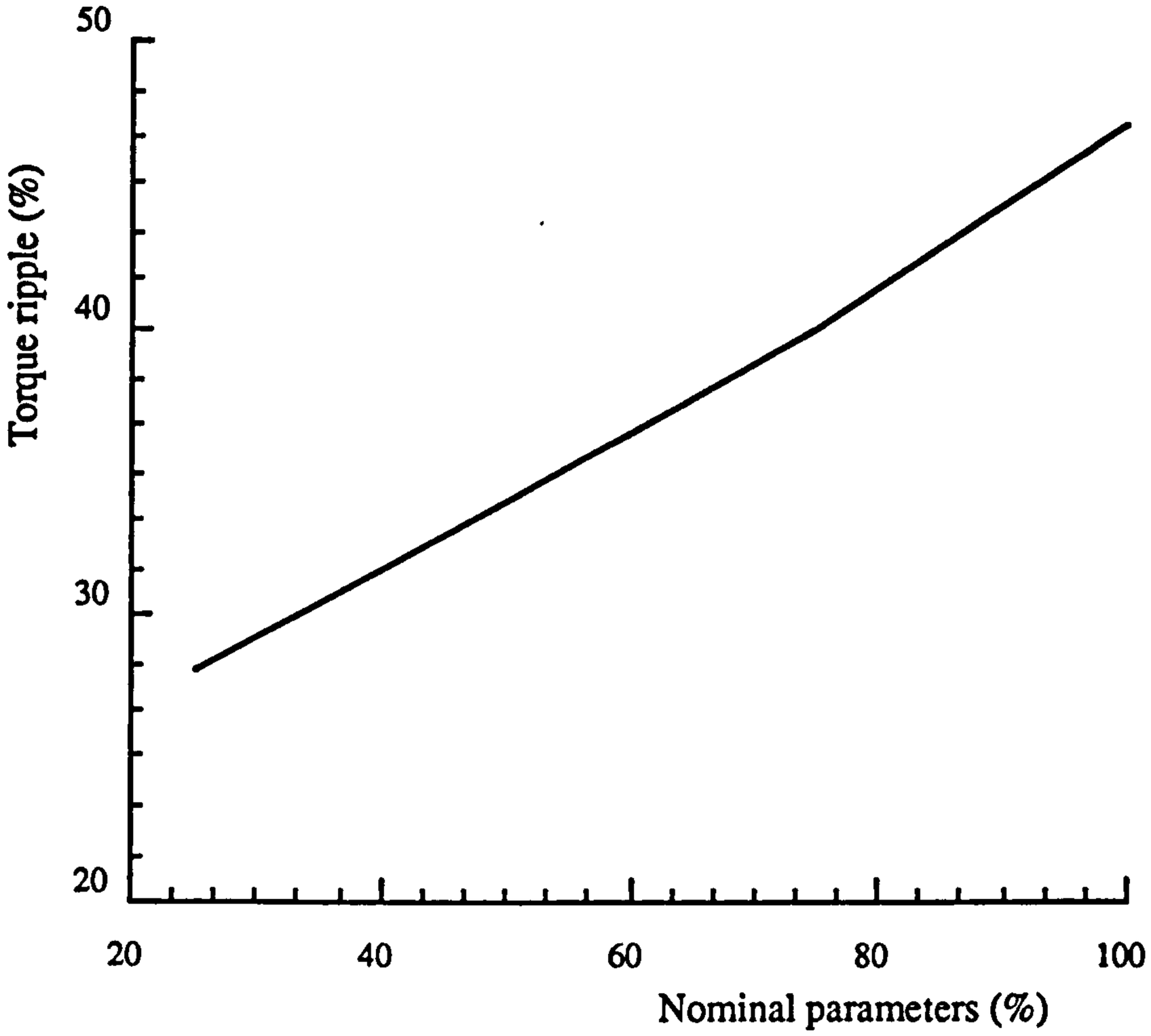

Figure 7.18 Variation of torque ripple with stator winding inductance

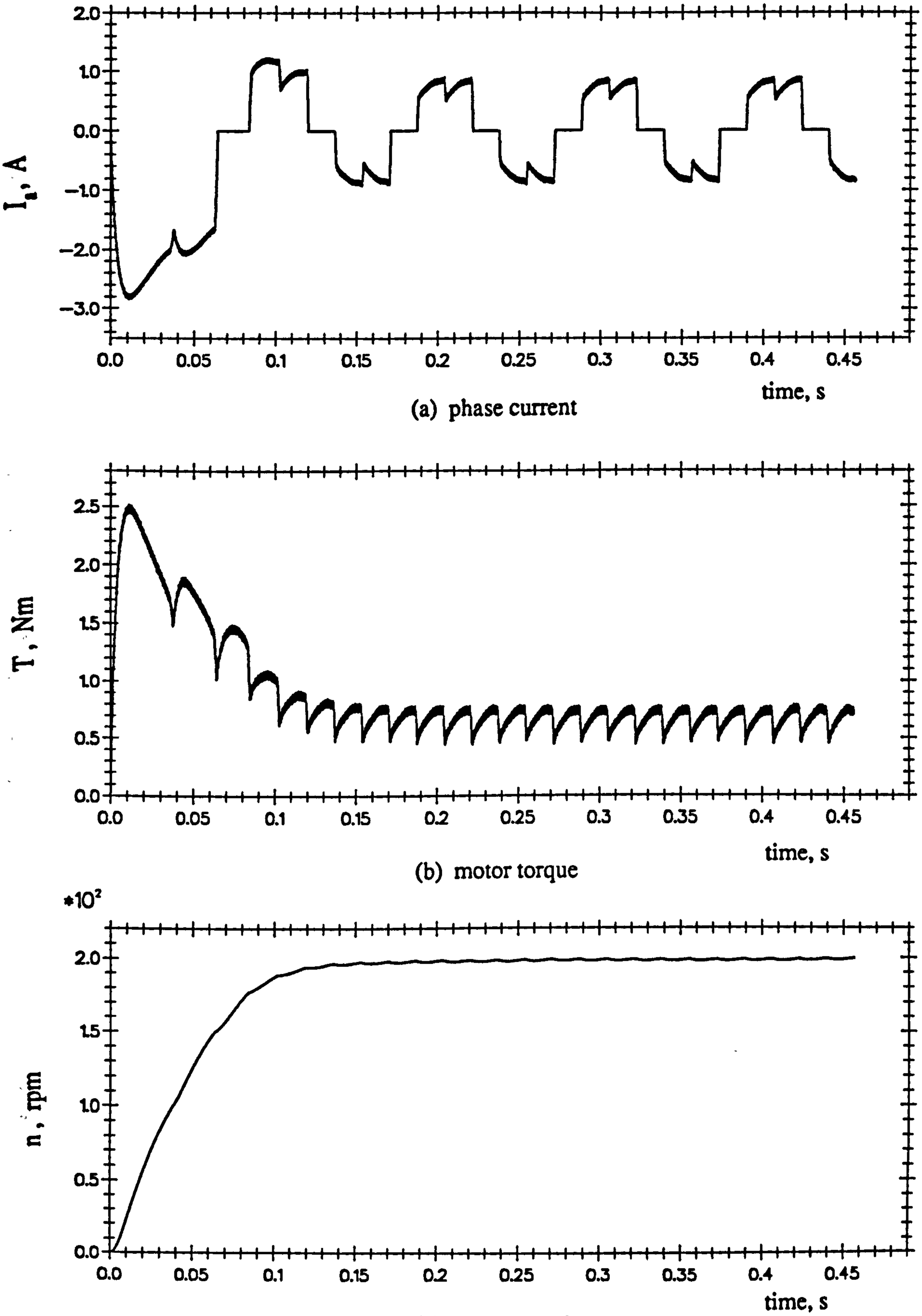

Figure 7.19 Simulated waveforms (Load condition : 0.7Nm at 200rpm, switching frequency = 5kHz)

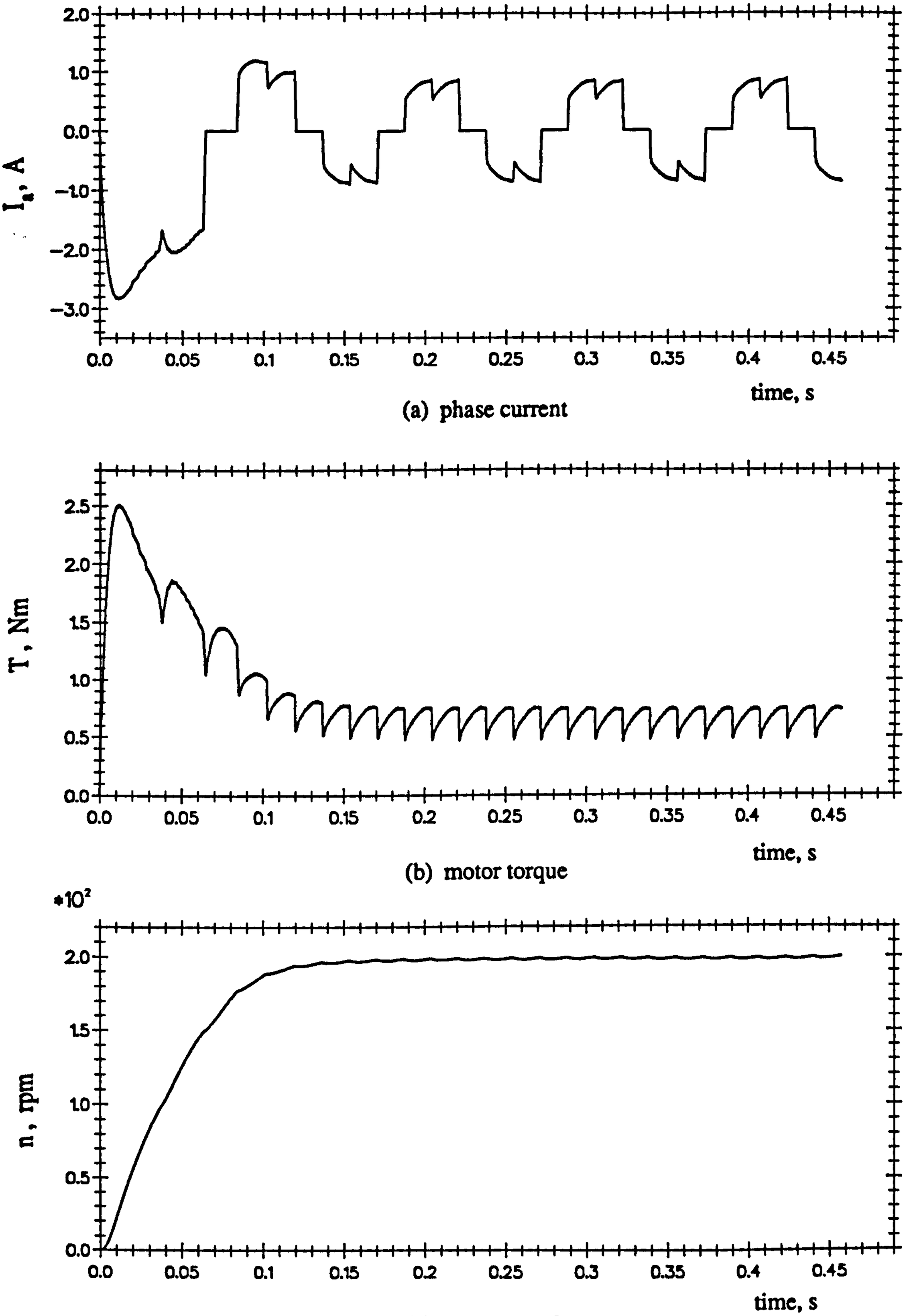

Figure 7.20 Simulated waveforms (Load condition : 0.7Nm at 200rpm, switching frequency = 25kHz)

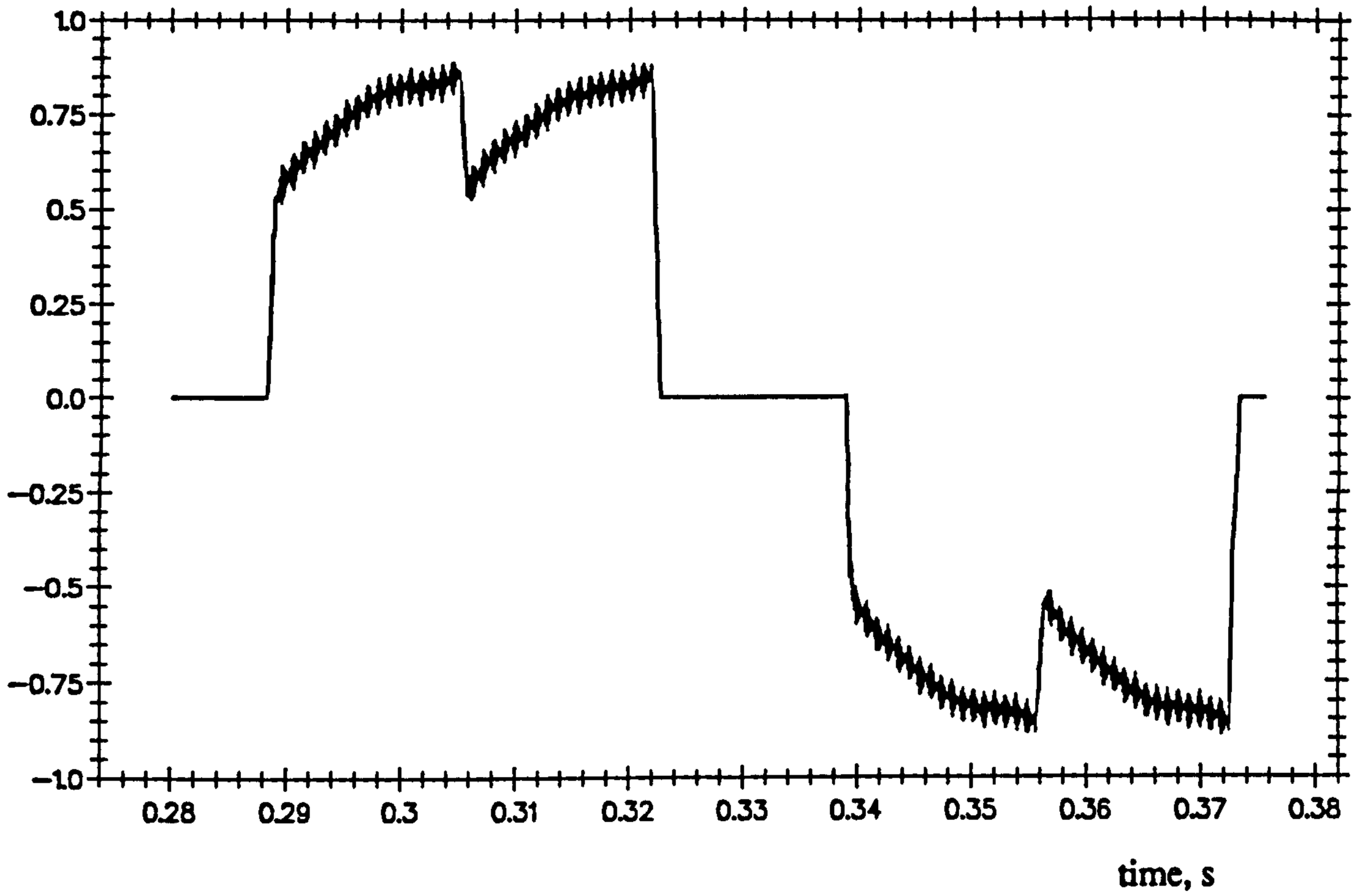

(a) simulated waveform

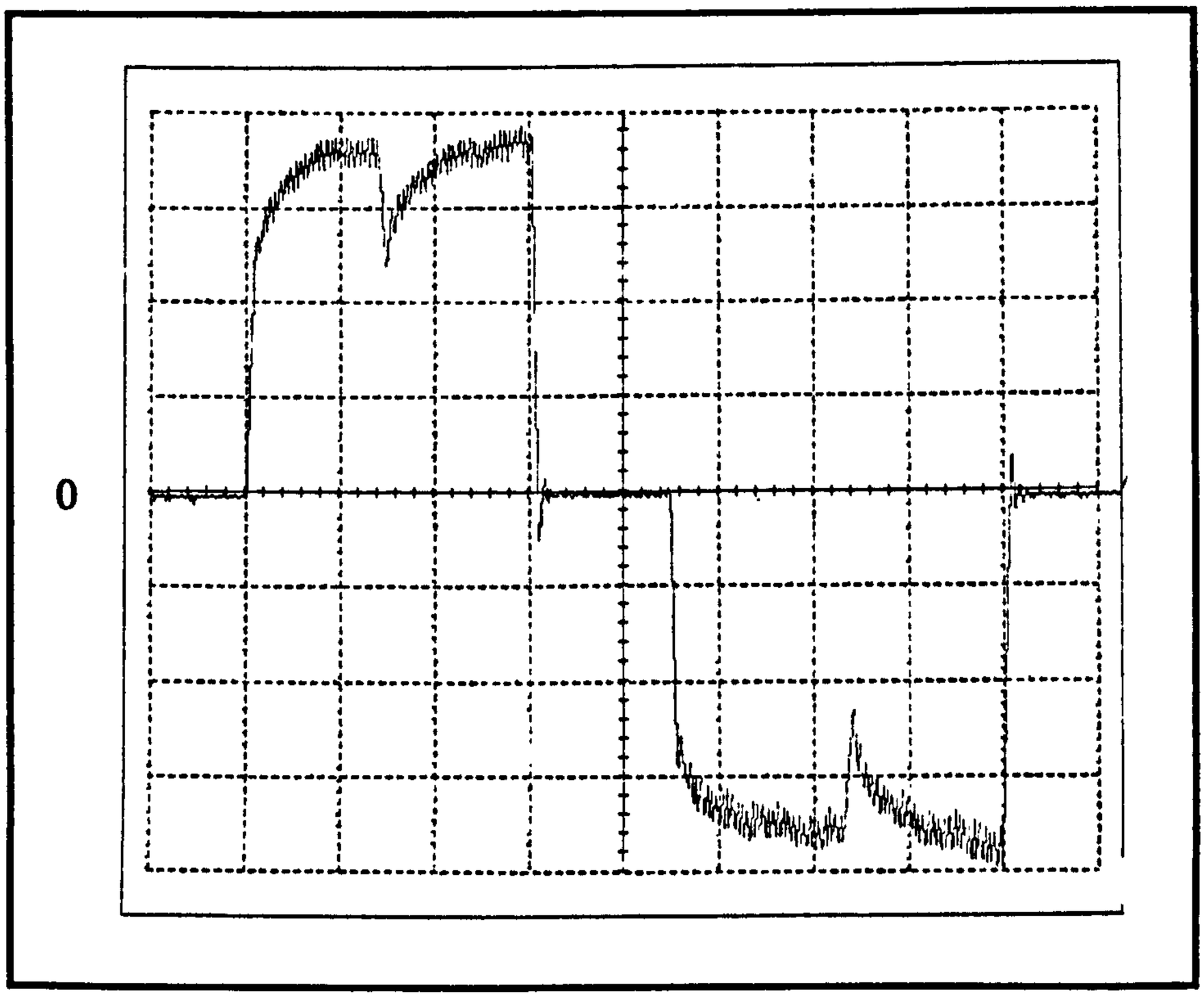

(b) measured waveform

Figure 7.21 Phase current waveforms (Load condition : 0.7Nm at 200rpm, switching frequency = 5kHz)

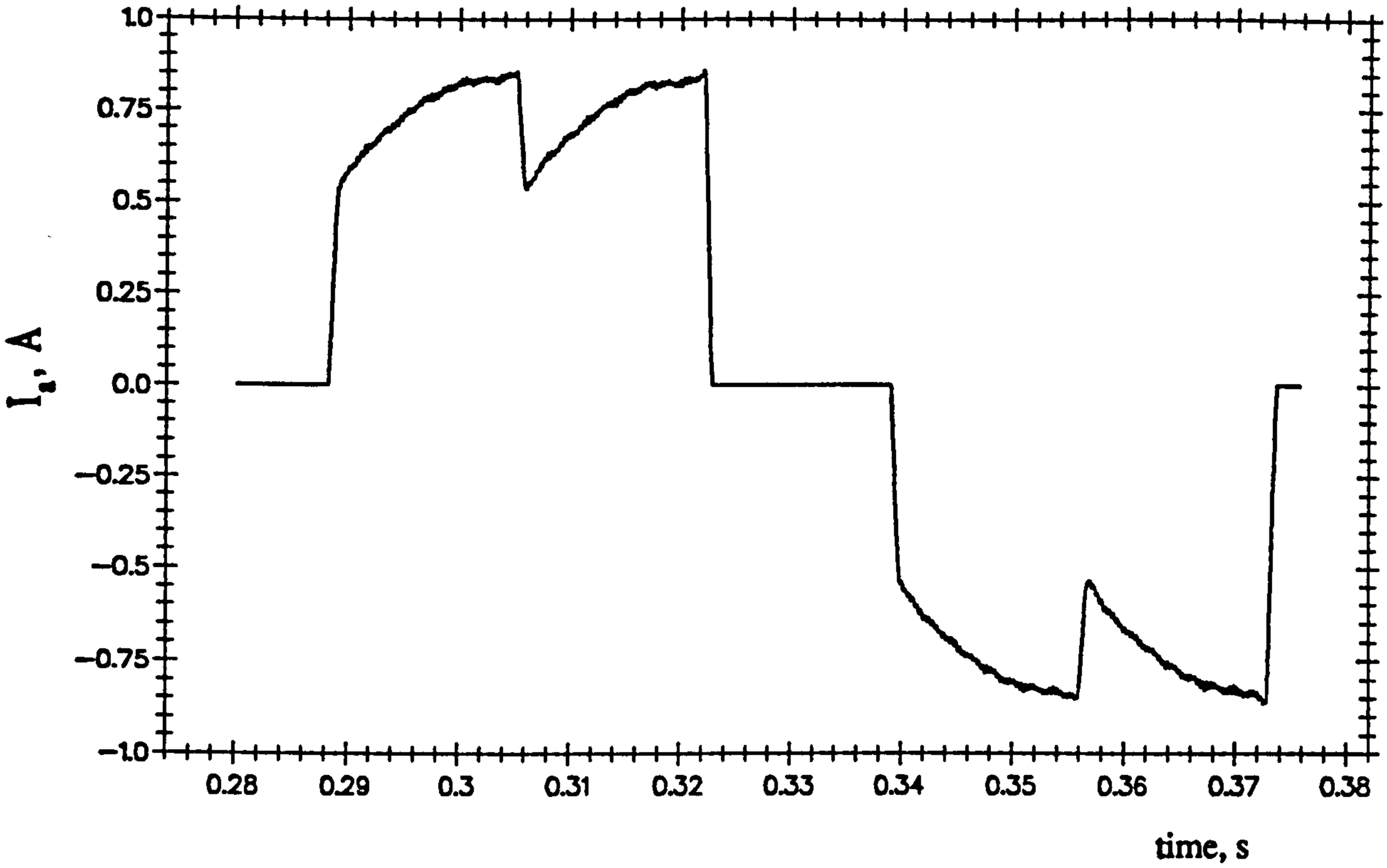

(a) simulated waveform

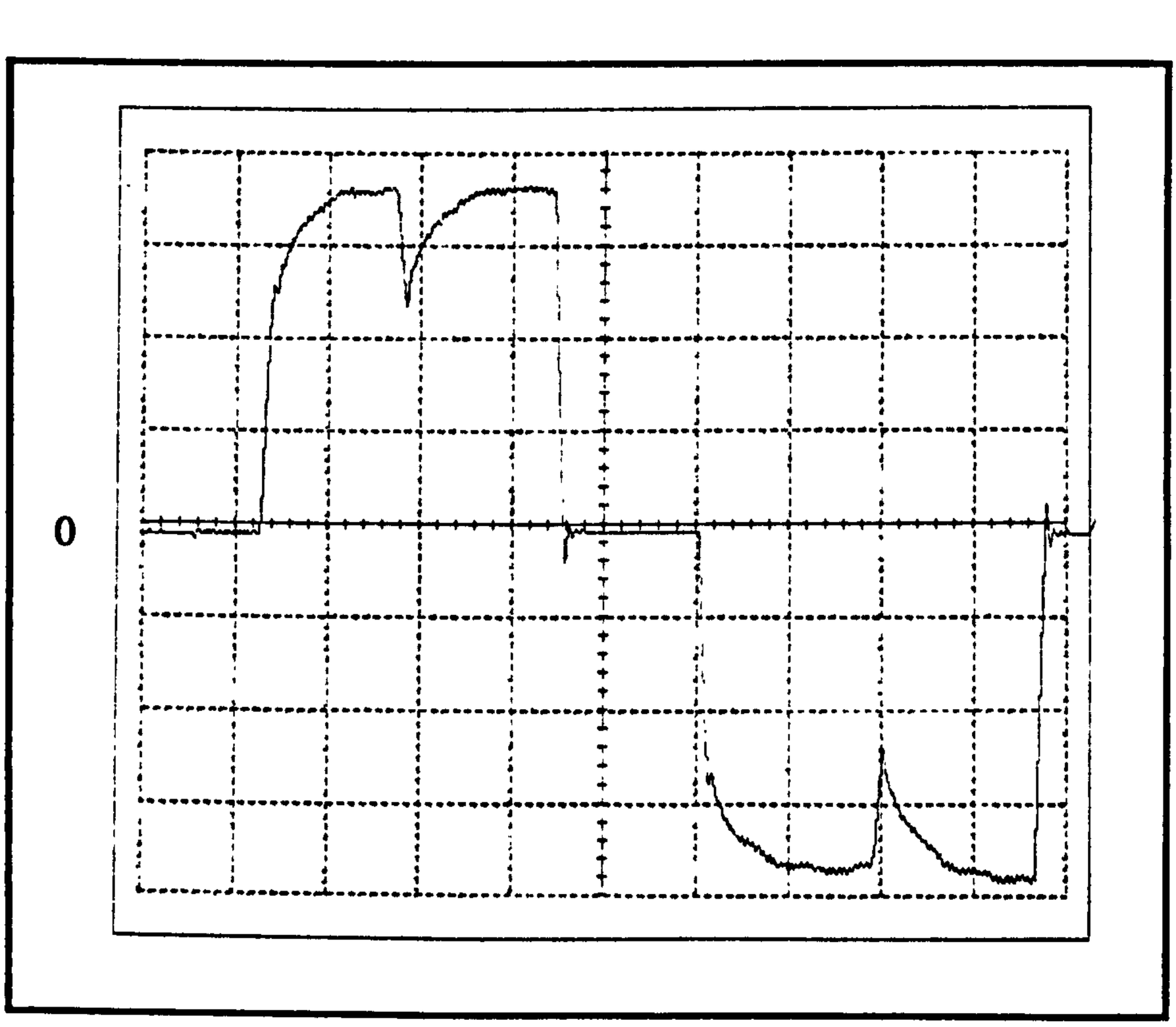

(b) measured waveform

Figure 7.22 Phase current waveforms (Load condition : 0.7Nm at 200rpm, switching frequency = 25kHz)

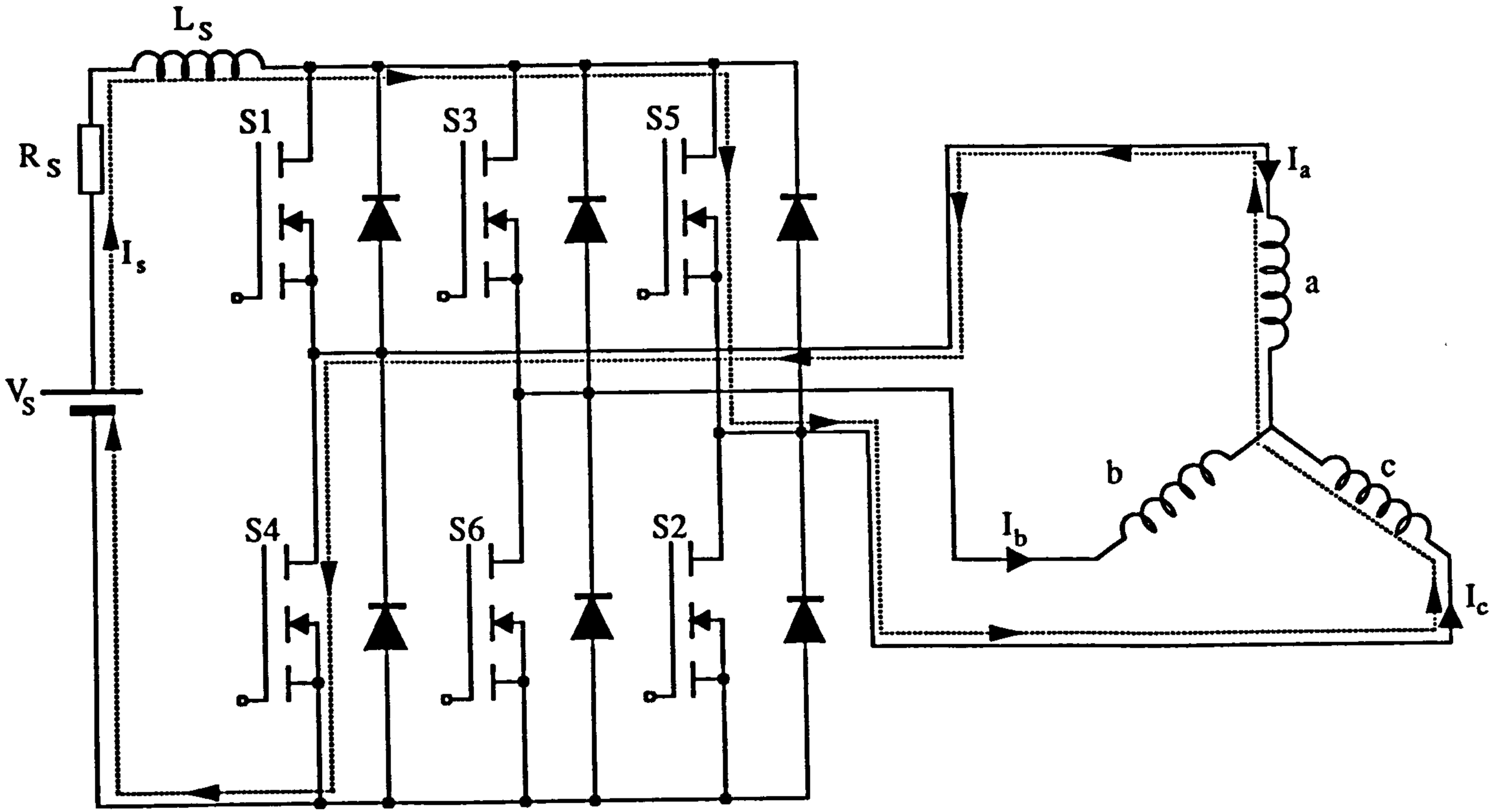

Figure 7.23 Current conduction during 60°e of rotation

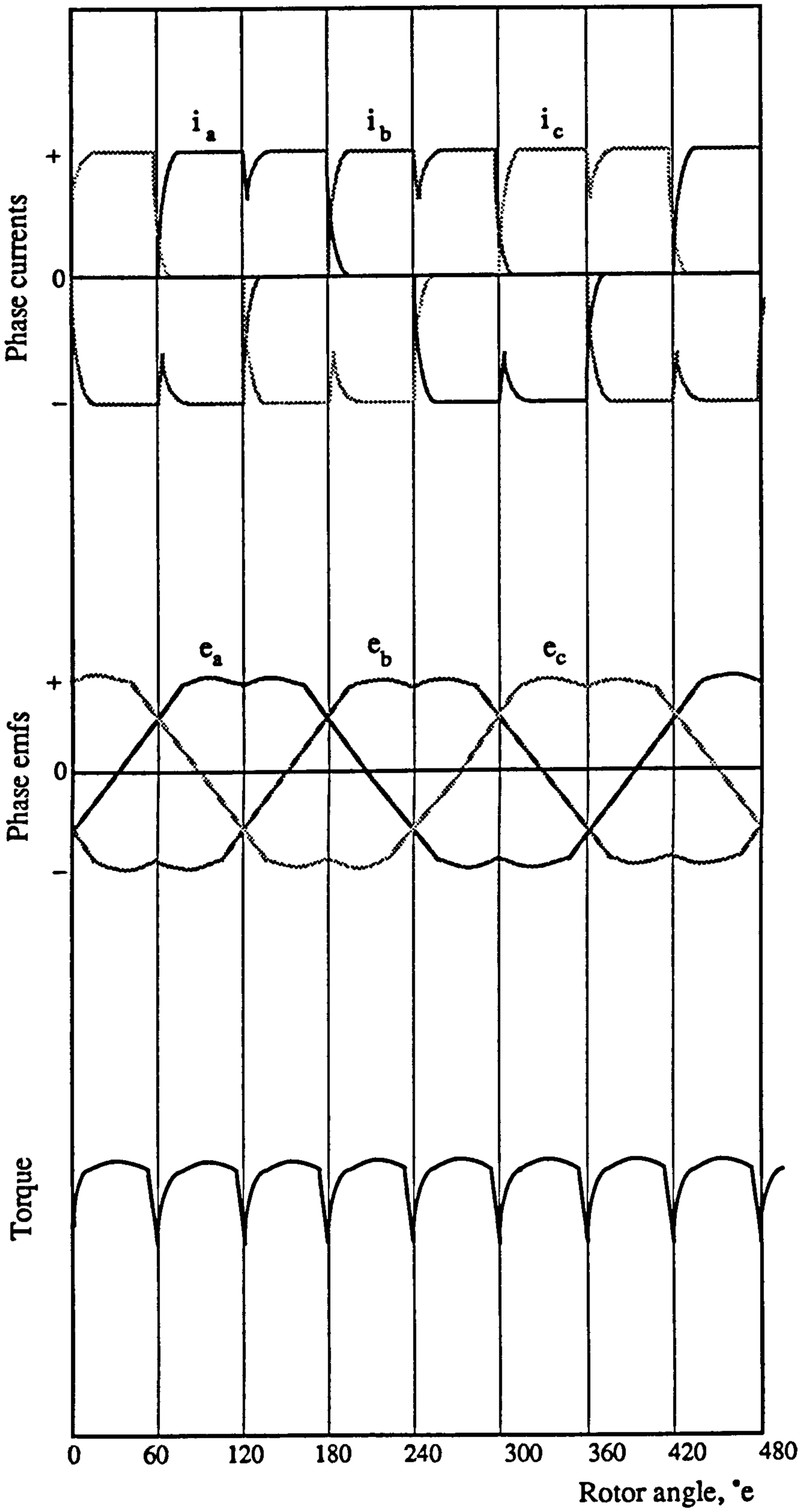

Figure 7.24 Effect of phase current and emf waveforms on torque profile

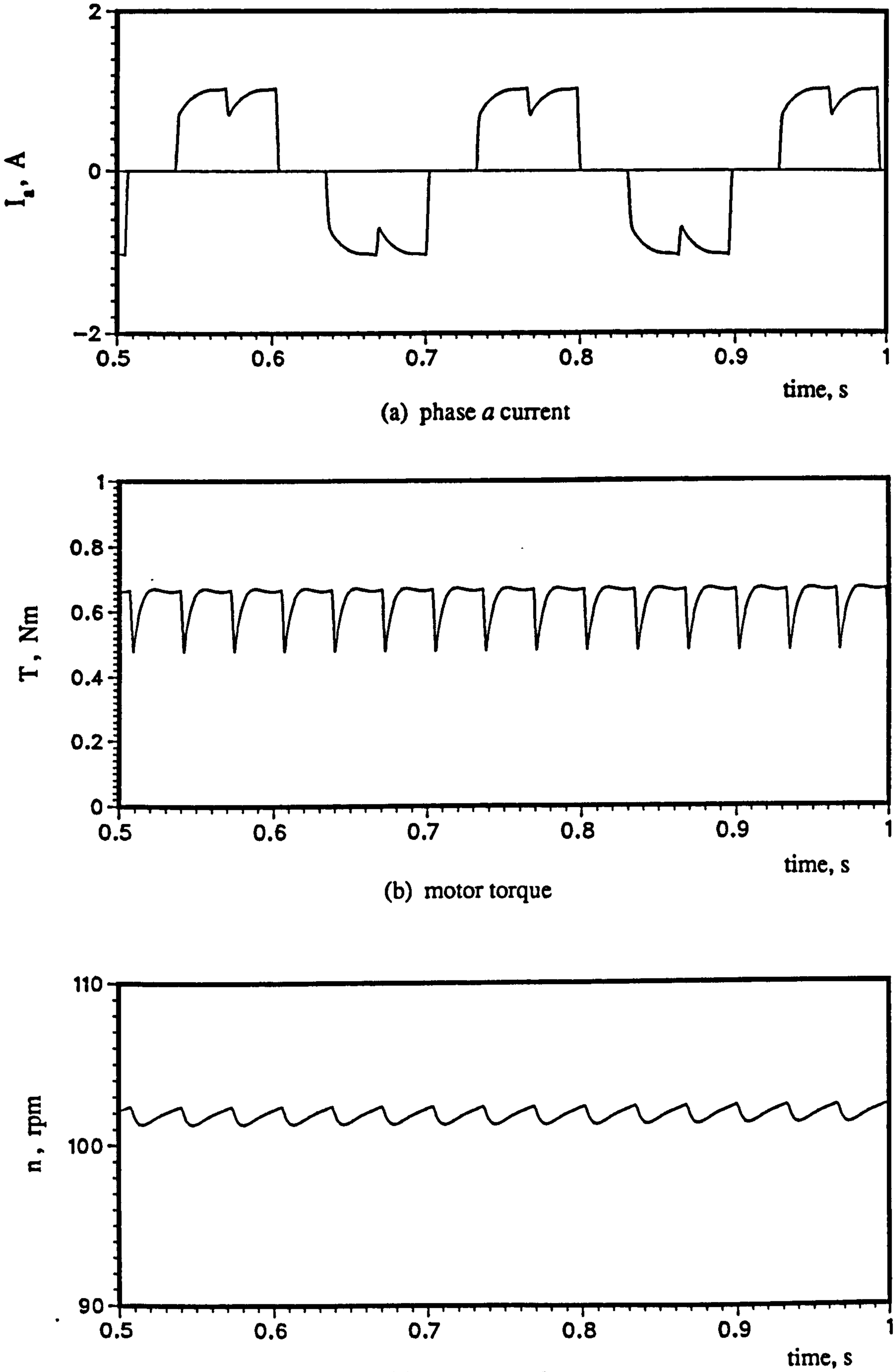

(a) phase *a* current

(b) motor torque

(c) motor speed

Figure 7.25 Simulated waveforms without compensation (Load condition : 0.6Nm at 102rpm)

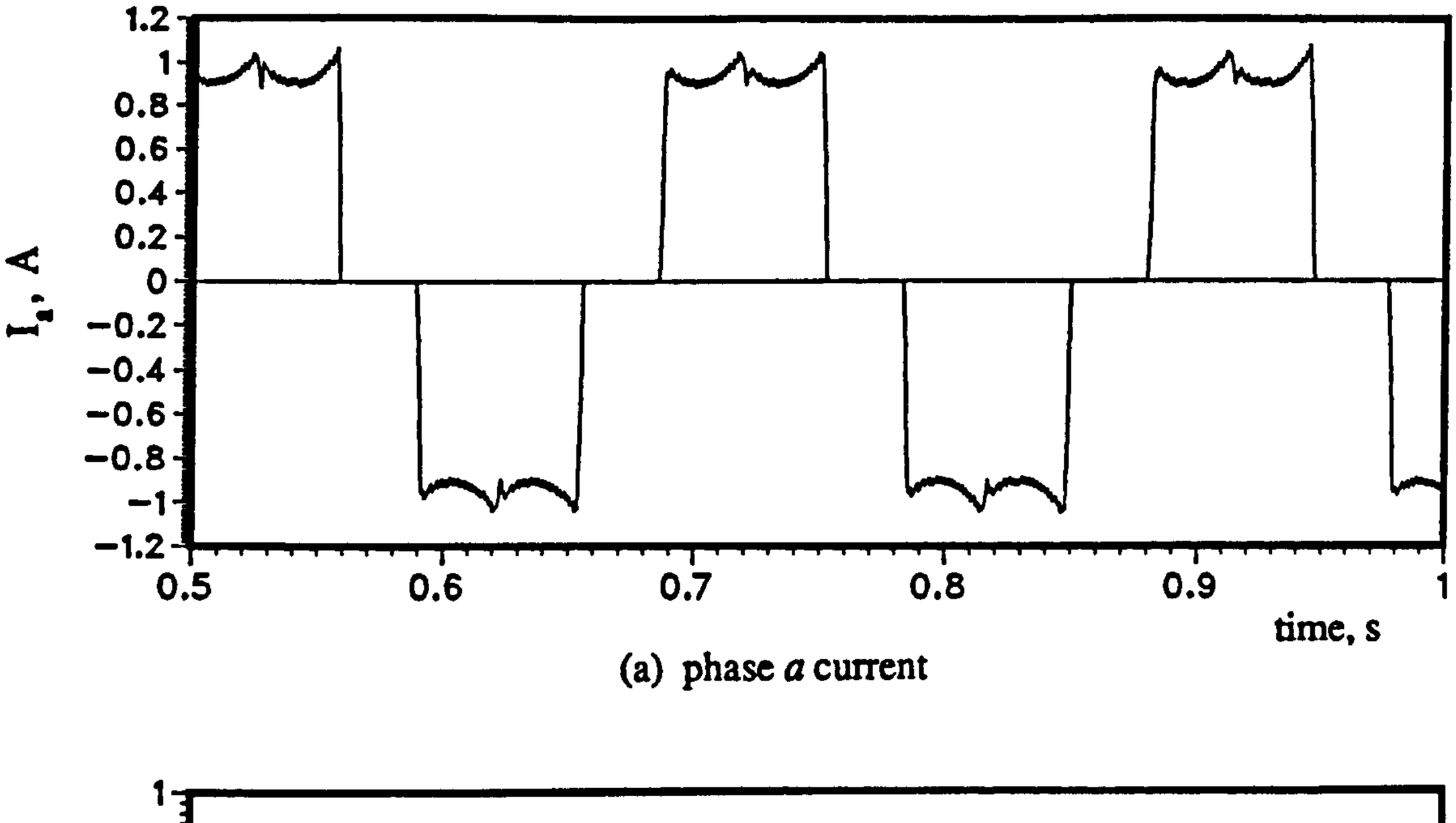

(a) phase *a* current

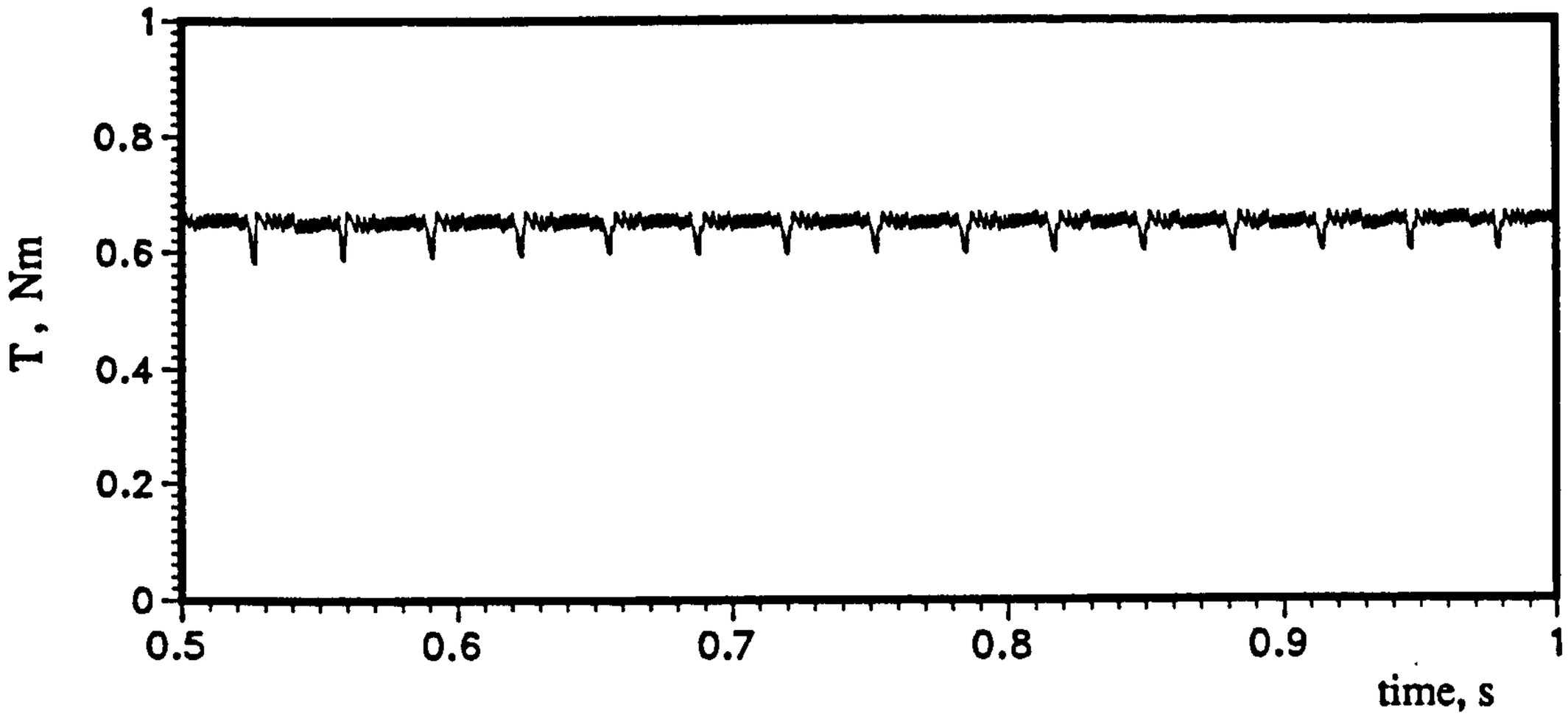

(b) motor torque

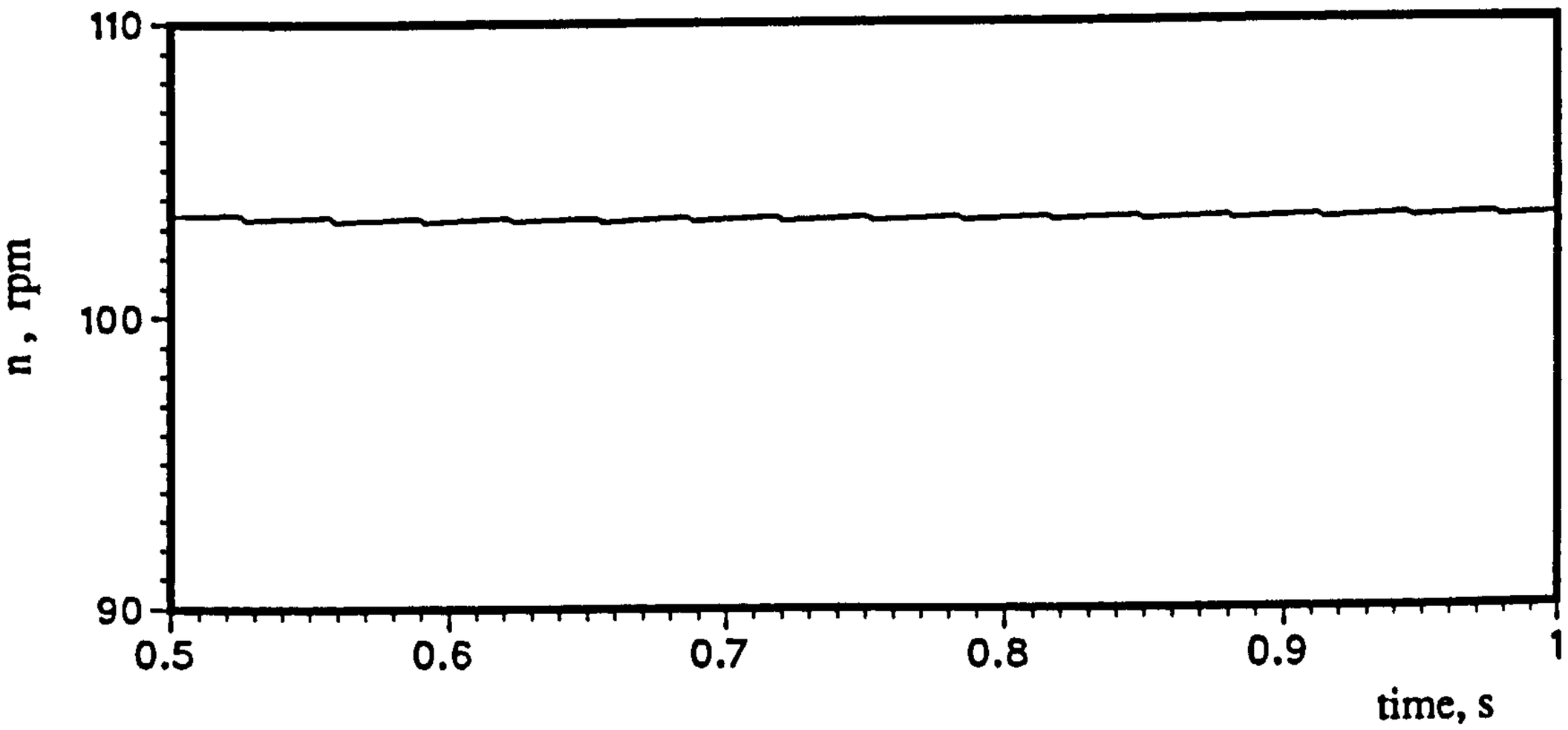

(c) motor speed

Figure 7.26 Simulated waveforms with generated emf compensation (Load condition : 0.6Nm at 102rpm)

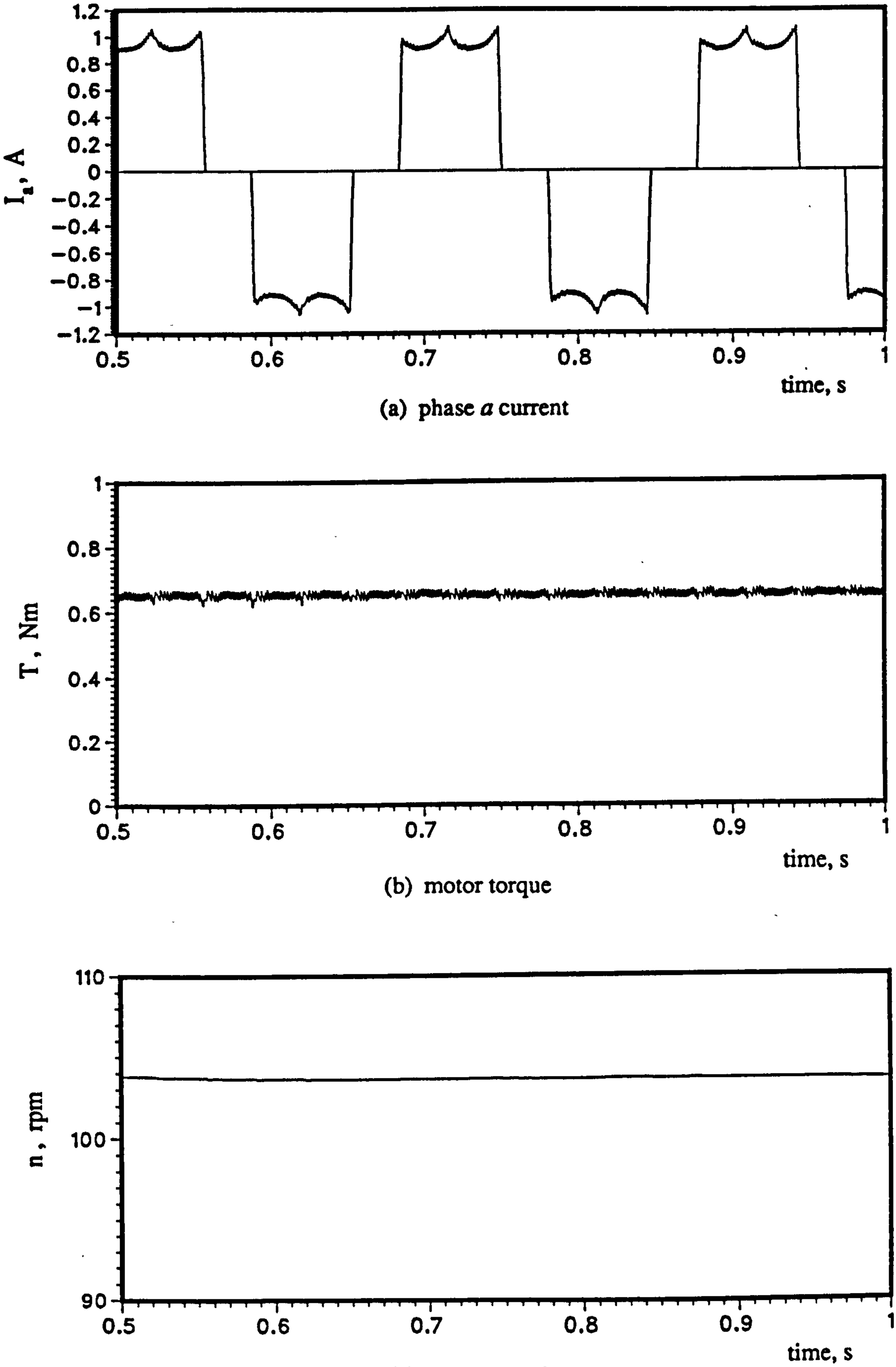

Figure 7.27 Simulated waveforms with combined generated emf and commutation compensation (Load condition : 0.6Nm at 102rpm)

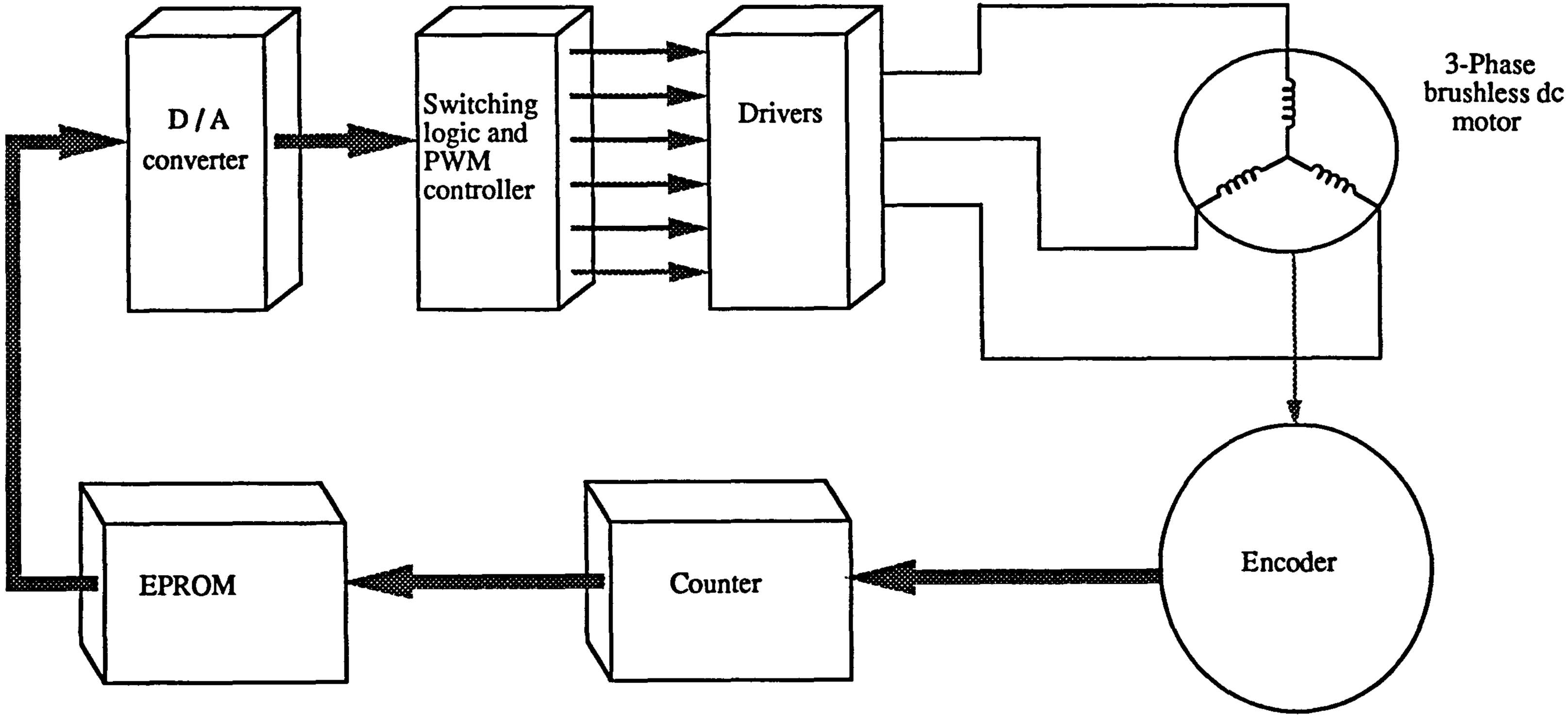

Figure 7.28 Current shaping circuit block diagram

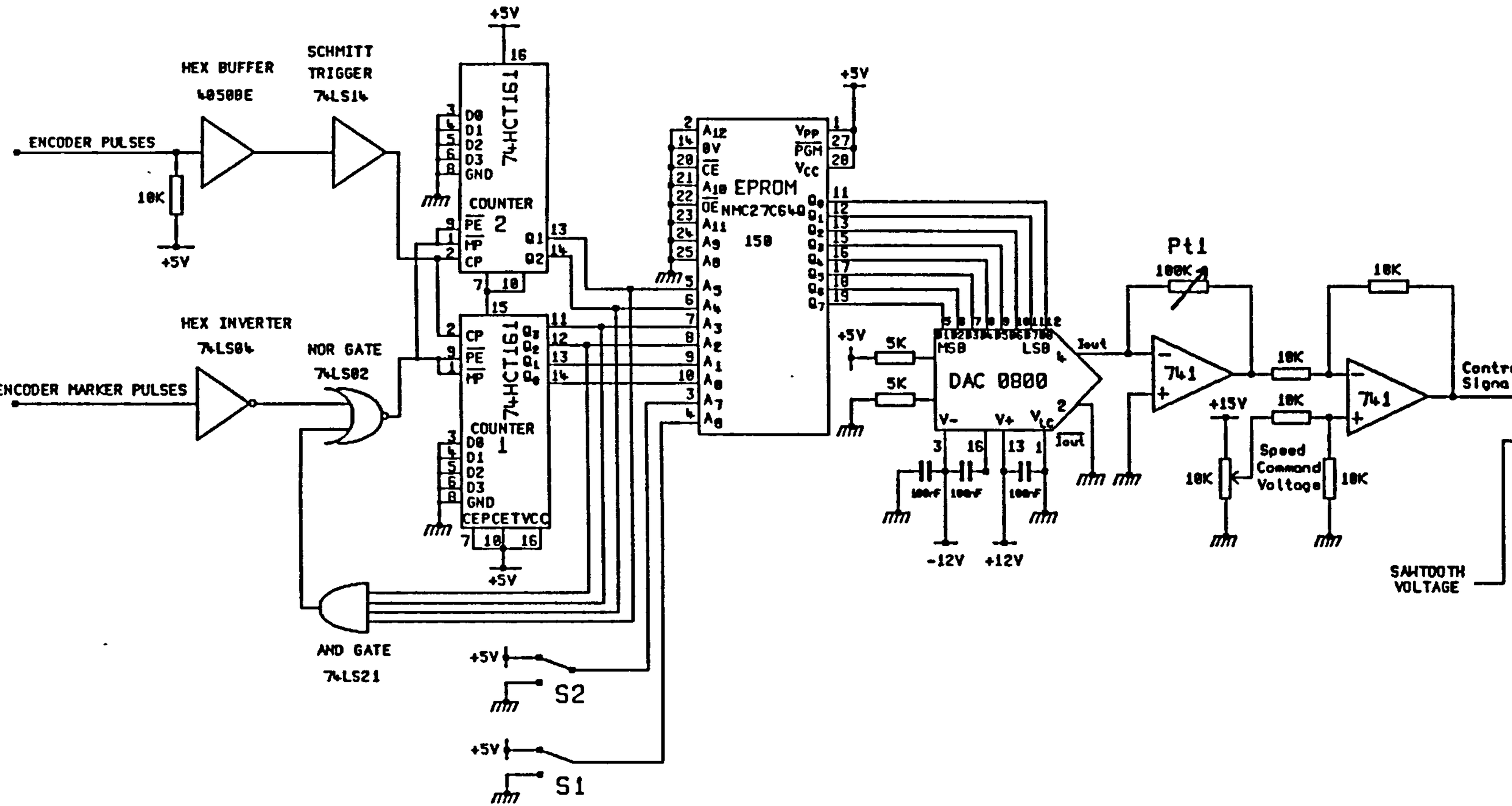

Figure 7.29 Current shaping circuit diagram

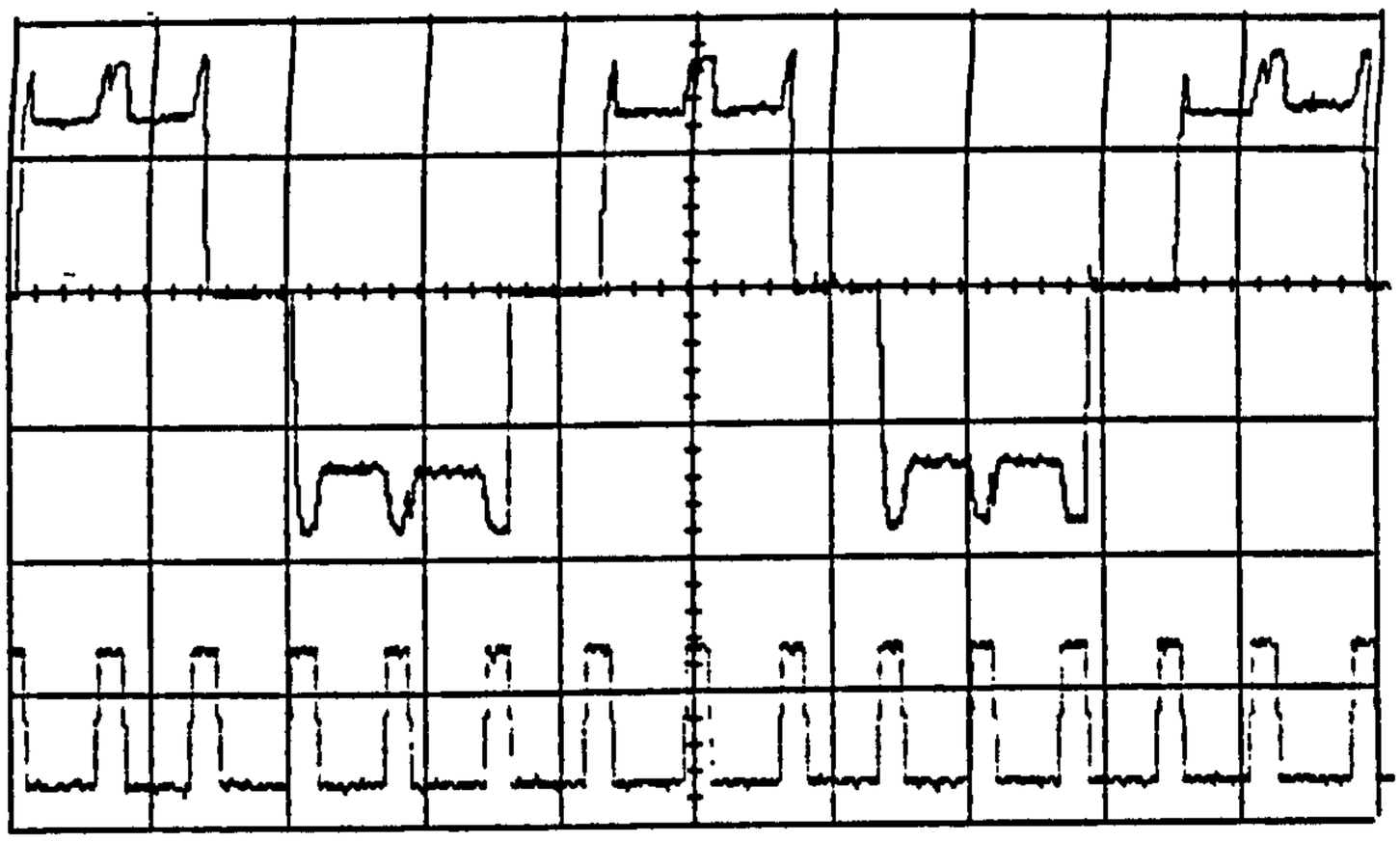

vertical scale
0.5A/div
horizontal scale
25ms/div

(a) phase current waveform with commutation compensation

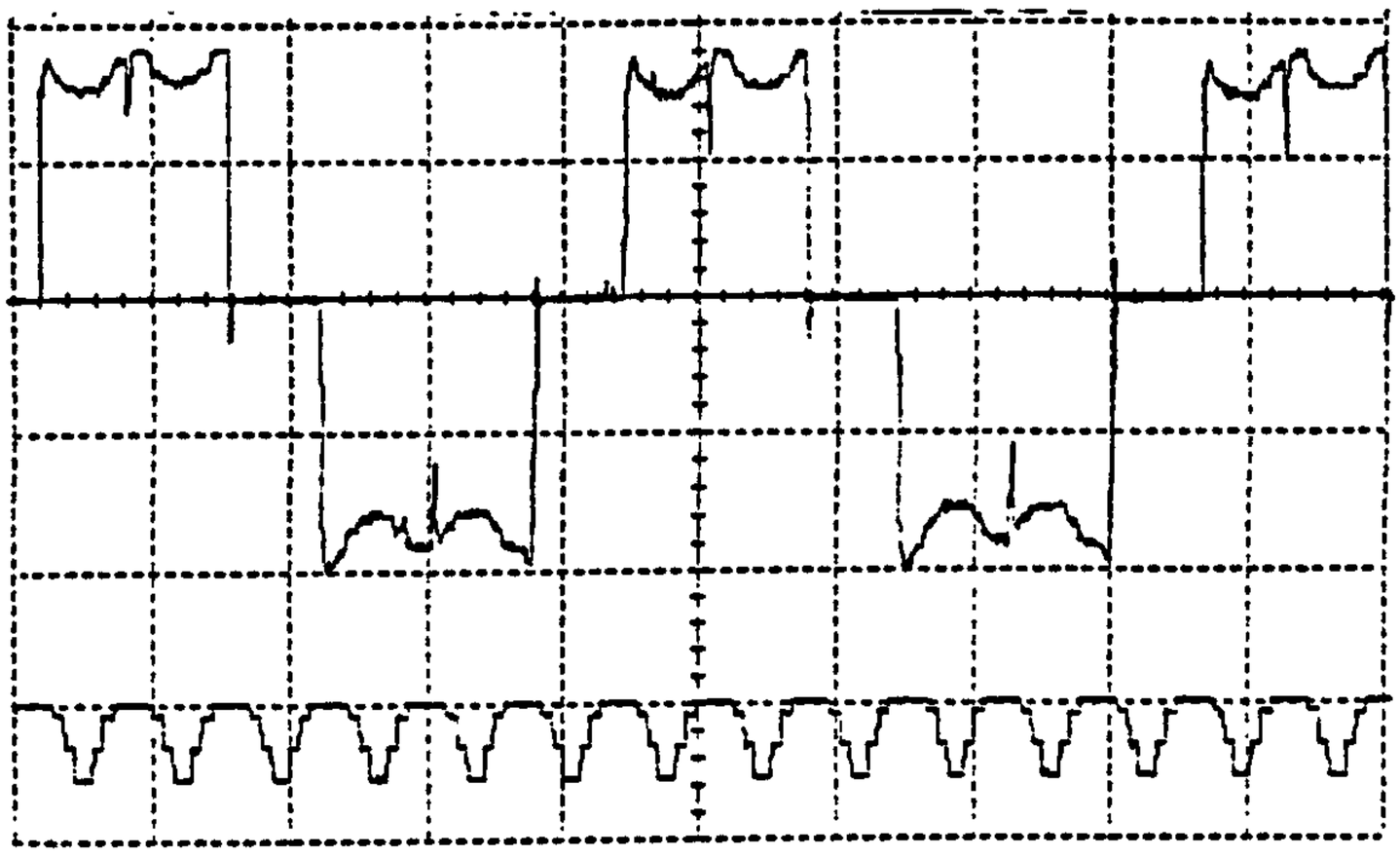

vertical scale
0.5A/div
horizontal scale
25ms/div

(b) phase current waveform with generated emf compensation

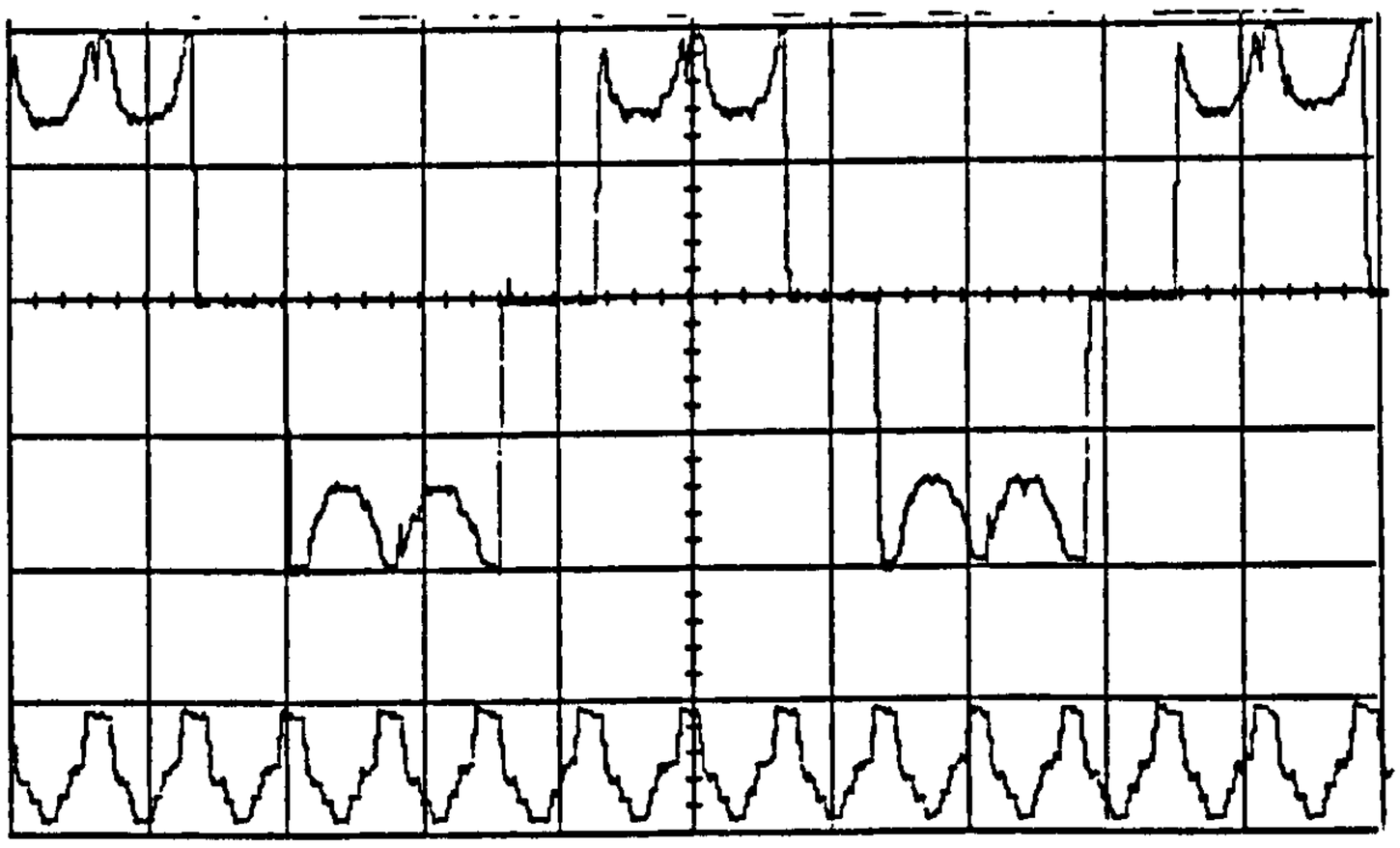

vertical scale
0.5A/div
horizontal scale
25ms/div

(c) phase current waveform with combined generated emf and commutation compensation

Figure 7.30 Measured phase current and current reference waveforms for various current shaping profiles (Load condition : 0.6Nm at 102rpm)

CHAPTER 8

CONCLUSIONS AND RECOMMENDATIONS

This chapter presents conclusions arising from the research described in the thesis, together with recommendations for further work.

8.1 CONCLUSIONS

A comprehensive mathematical model has been developed and used to investigate the steady-state and transient performance of a brushless dc motor drive under various operating conditions and for both square-wave and PWM modes of operation. The model is based on the numerical solution of the machine flux linkage differential equations formulated in the phase reference frame, together with the mechanical differential equation defining the various torques at the machine shaft. Tensor methods are used to account for the varying circuit topology arising from changes in the inverter switching pattern, and all practical topologies are included in the model. Central to this model is the accurate representation of the stator winding flux linkage due to the rotor permanent-magnet and this was determined experimentally and included in the model.

An experimental drive was designed and built for a 1.3kW brushless dc motor during the course of the research and the experimental motor parameters, required by the mathematical model, were measured as described in chapter 6. At all stages predicted results were substantiated by experimental

investigation, and the close correlation obtained in both shape and magnitude has confirmed the validity and accuracy of the mathematical model developed and the modelling technique described. In particular, the results presented in chapters 5 and 7 demonstrated the model's ability to predict accurately the trapezoidal waveform of generated emf and the effect of commutation on the stator currents and consequentially the undesirable torque ripple.

Having established confidence in the model, it was then used in an investigation of the factors affecting the torque and speed ripples produced by the drive and the ways by which they might be minimized. Practical investigations established that the actual phase current waveform has rounded edges due to winding inductance and a dip due to commutation at every 60°e of the rotor position, rather than the ideal rectangular wave-shape. Also, the trapezoidal emf has a flat-top region of less than 120°e, which contains fluctuations. The combination of these two factors result in a torque ripple which is periodic and dependent on both the rotor position and the commutation events. Based on these observations, a novel and effective method to eliminate the torque ripple was proposed in chapter 7. Profiling the phase current waveforms in relation to the rotor position and commutation instants, in a way which compensates for any deficiencies in the shape of the generated emf waveforms and minimizes the effect of the commutation, virtually eliminates torque and speed ripples from the drive output. This was achieved in practice by introducing a current control loop with the PWM controller and a current boost during commutation. The results presented

in section 7.3 show that the relatively modest increase in the stator current of 9% during the commutation instants eliminated a 30% torque ripple. Practical results obtained from the experimental rig verified that these modifications to the phase current waveforms provided significant improvements in the drive performance.

The effect of the commutation angle on the torque ripple was examined. It was shown that the magnitude could be reduced by advancing the instant of commutation and, for the machine under consideration, the smallest torque ripple was achieved with a 30°e advance. This indicates that accurate rotor position sensing is important in producing smooth shaft torque.

The experimental PWM current controller is capable of operating at a switching frequency of up to 50kHz, and the model was used to investigate the effect of the controller on the ripple in the machine output torque. The results presented in chapter 7 show that the current ripple produced by the controller causes a high-frequency torque ripple, which depends on the controller switching frequency. The magnitude of these pulsations is much smaller than those produced by current commutation and, due to their high frequency, they produce only a small speed ripple.

8.2 RECOMMENDATIONS

There are several areas in which further research could lead to significant benefits and some of these are discussed below.

(1) A valuable extension to the work described would be the development of a smart system, which would profile automatically the motor phase currents to minimize the torque ripple. This would enable the optimization of off-the-shelf controllers and motors.

(2) Since torque pulsations are extremely undesirable in position control applications, the technique developed to eliminate torque pulsations may be used in studies of position control schemes.

(3) The prediction of the voltage spikes on the phase voltage waveforms may be improved by considering:

   (a) The inclusion of reverse-recovery effects in the free-wheeling diodes.

   (b) The inclusion of the snubber circuits which prevent excessive voltage spikes during turn-off of the inverter switches.

(4) Since the generated phase emf waveforms seem to strongly effect the torque ripple, it would be useful to investigate the effect of different widths of the flat-top region of this emf on the output torque profile.

(5) Since the model is capable of including the effect of rotor damping, it would be useful to investigate the performance of the drive, in particular the output torque behaviour, when additional damping circuits, such as a damper cage, are added to the rotor.

REFERENCES

1. Murugesan, S.,"An overview of electric motors for space applications", IEEE Trans. on Industrial Electronics and Control Instrumentation, Vol. IECI-28, No. 4, November 1981, pp. 260-265.

2. Buschow, K. H. J., Luiten, W. and Westendorp, F. F., "High-energy product Permanent magnets", Journal of Applied Physics", Vol. 40, No. 3, March 1969, p. 1309.

3. Das, D. K., "Twenty million energy product samarium-cobalt magnet", IEEE Trans. on Magnetics, Vol. MAG-5, No. 3, September 1969, pp. 214-216.

4. Howlett, J. F., "Brushless dc motors", Proc. Second International Motorcon Conference, San Fransisco, CA, March 1982, pp. 594-604.

5. Williams, S., "Direct drive system for an industrial robot using a brushless dc motor", Proc. IEE, Vol. 132, Pt. B, No. 1, January 1985, pp. 53-56.

6. Sawyer, B. and Edge, J. T., "Design of a samarium cobalt brushless dc motor for electromechanical actuator applications", IEEE-National Aerospace Electronics Conference Record (NAECON'77), Dayton, Ohio, May 1977, pp. 1108-1112.

7. Engineering Handbook, "DC motors, speed controls, servo systems", Electro-Craft Corp., Fifth Edition, 1980.

8. Bolton, H. R., Liu, Y. D. and Mallinson, N. M., "Investigation into a class of brushless dc motor with quasisquare voltages and currents", Proc. IEE, Vol. 133, Pt. B, No. 2, March 1986, pp. 103-111.

9. Davat, B., Rezine, H. and Lajoie-Mazenc, M., "Modelling of a brushless dc motor with solid parts involving eddy currents", IEEE Trans. on Industry Applications, Vol. IA-21, No. 1, January/February 1985, pp.202-206.

10. Krause, P. C., Voyles, R. M. and Wasynczuk, O., "Analysis and simulation of a brushless dc servomotor", Proc. Sixth International Motorcon Conference, Atlantic City, NJ, April 1984, pp. 86-94.

11. Jahns, T. M., "Flux-weakening regime operation of an interior permanent magnet synchronous motor drive", IEEE-IAS Annual Meeting Conference Record, Vol. 1, Denver, CO, September/October 1986, pp. 814-823.

12. Spee, R., "Prediction of brushless dc drive performance considering non-sinusoidal parameter variations and asymmetrical operating conditions", PhD Thesis, Oregon State University, 1988.

13. Subramaniam, P. and Malik , O. P., "Digital simulation of a synchronous generator in direct-phase quantities", Proc. IEE, Vol. 118, No. 1, January 1971, pp. 153-160.

14. Smith, I. R. and Snider, L. A., "Prediction of transient performance of isolated saturated synchronous generator", Proc. IEE, Vol. 119, No. 9, September 1972, pp. 1309-1318.

15. Pillay, P. and Krishnan, R., "Modelling of permanent magnet motor drives", IEEE Trans. on Industrial Electronics, Vol. 35, No. 4, November 1988, pp. 537-541.

16. Kron, G., "Tensors for circuits", Dover Publications, Second Edition, 1959.

17. Gibbs, W. J., "Tensors in electrical machine theory",

Chapman and Hall Ltd., First Edition, 1952.

18. Piriou, F., Razek, A., Perret, R. and Le-Huy, H., "Torque characteristics of brushless dc motors with imposed current waveform", IEEE-IAS Annual Meeting Conference Record, Vol. 1, Denver, CO, September/October 1986, pp. 176-181.

19. Kenjo, T. and Nagamori, S., "Permanent-magnet and brushless dc motors", Oxford University Press, First Edition, 1985.

20. Hindmarsh, J., "Electrical machines and their applications", Pergamon Press, Fourth Edition, 1984.

21. Gould, J. E., "Permanent magnets", Proc. IEE., Vol. 125, No. 11R, November 1978, pp. 1137-1151.

22. Gray, C. B., "Electrical machines and drive systems", Longman Scientific and Technical, First Edition, 1989.

23. Mullard Ltd., "Magnadur magnets for dc motors", 1970.

24. Murphy, J. M. D. and Turnbull, F. G., "Power electronic control of ac motors" , Pergamon Press, First Edition, 1988.

25. Persson, E. K., "Brushless dc motors - a review of the state of the art", Proc. First International Motorcon Conference, Chicago, Ill, June 1981, pp. 1-16.

26. Kusko, A. and Peeran, S. M., "Brushless dc motors using unsymmetrical field magnetization", IEEE-IAS Annual Meeting Conference Record, Denver, CO, September/October 1986, pp. 774-780.

27. Weschta, A., "Design considerations and performance of brushless permanent magnet servo motors", IEEE-IAS

Annual Meeting Conference Record, Mexico, October 1983, pp. 469-475.

28. Persson, E. K., "Brushless motors using rare earth magnets", Proc. of the Third International Workshop of Rare-Earth-Cobalt Permanent Magnets and Their Applications", San Diego, CA, June 1978, pp. 27-43.

29. Demerdash, N. A., Miller, R. H., Nehl, T. W. and Nyamusa, T. A., "Improved transistor-controlled and commutated brushless dc motors for electric vehicle propulsion", Report No. NASA CR 168053, Final Report on NASA/DOE Contract No. DEN3-65, January 1983.

30. Mohan, N., Undeland, T. M. and Robbins, W. P., "Power electronics: converters, applications and design", John Wiley and Sons, First Edition, 1989.

31. Brosnan, M. and Barber, N. T., "Rare-earth high performance brushless drives and their application", Proc. Seventh International Motorcon Conference, Hannover, Germany, April 1985, pp. 75-85.

32. Weinmann, D., Nicoud, G. and Gallo, F., "Advantages of permanent magnet motors", Proc. Conference on Drives/ Motors/Controls, Brighton, England, October 1984, pp. 113-120.

33. Lander, C. W., "Power electronics", McGraw-Hill Publishing Company, Second Edition, 1987.

34. Williams, B. W., "Power electronics : devices, drivers and applications", Macmillan Education Ltd., First Edition, 1987.

35. Bradley, D. A., "Power electronics", Van Nostrand Reinhold Company Ltd., First Edition, 1987.

36. "Power MOSFET HEXFET designer's manual", International Rectifier Corp., Fourth Edition, 1987.

37. "Basic GTO drive circuits", Mullard Technical Publication, M81-0128.

38. Nehl, T. W., Demerdash, N. A. and Fouad, F. A., "Impact of winding inductances and other parameters on the design and performance of brushless dc motors", IEEE Trans. on Power Apparatus and Systems, Vol. PAS-104, No. 8, August 1985, pp. 2206-2213.

39. Kuo, B. C., "Theory and applications of step motors", West Publishing Company, First Edition, 1974.

40. Demerdash, N. A. and Nehl, T. W., "Dynamic modelling of brushless dc motors for Aerospace Actuation", IEEE Trans. on Aerospace and Electronic Systems, Vol. AES-16, No.6, November 1980, pp. 811-821.

41. Nehl, T. W., Demerdash, N. A., Hijazi, T. M. and McHale, T. L., "Automatic formulation of models for simulation of the dynamic performance of electronically commutated dc machines", IEEE Trans. on Power Apparatus and Systems, Vol. PAS-104, No. 8, August 1985, pp. 2214-2222.

42. Gerald, C. F., "Applied numerical analysis", Addison Wesley, Second Edition, 1978.

43. Wylie, C. R., "Advanced engineering mathematics", McGraw-Hill Publishing Company, Fifth Edition, 1982.

44. Vadher, V. V., Smith, I. R. and Fanthome, B. A., "Mathematical modelling of complex electromagnetic/ mechanical networks", Proc. International Conference on Modelling and Simulation, Sorrento (Italy), September/October 1986, pp. 93-104.

45. Happ, H. H., "Diakoptics and networks", Academic Press, First Edition, 1971.

46. Hancock, N. N.,"Matrix analysis of electrical machinery", Pergamon Press, Second Edition, 1974.

47. Golding, E. W. and Widdis, F. C., "Electrical measurements and measuring instruments", Pitman, Fifth Edition, 1963.

48. Jones, C. V., "The unified theory of electrical machines", Butterworths, First Edition, 1967.

49. Prescott, J. C. and EL-Kharashi, A. K., "A method of measuring self-inductances applicable to large electrical machines", Proc. IEE, Vol. 106A, April 1959, pp. 169-173.

50. Snider, L. A. and Smith, I. R., "Ballistic techniques for the measurement of self and mutual inductance of windings with a ferromagnetic core", Journal of Physics E:Scientific Instruments, Vol. 4, May 1971, pp. 733-736.

51. Jahns, T. M., "Torque production in permanent-magnet synchronous motor drives with rectangular current excitation", IEEE Trans. on Industry Applications, Vol. 1A-20, No. 4, July/August 1984, pp. 803-813.

52. Stone, A. C. and Buckley, M. G., "Novel design and control of a trapezoidal back emf motor - the smooth transition from brush to brushless dc", Proc. Seventh International Motorcon Conference, Hannover, Germany, April 1985, pp. 86-95.

53. Miller, T. J. E., "Brushless permanent-magnet and reluctance motor drives", Oxford University Press, First Edition, 1989.

54. Stone, A. C. and Buckley, M. G., "Ultra high performance brushless dc drive", Proc. Conference on Drives/Motors /Controls, Brighton, England, October 1984, pp. 86-91.

55. Pillay, P. and Krishnan, R., "Application characteristics of permanent magnet synchronous and brushless dc motors for servo drives", IEEE-IAS Annual Meeting Conference Record, Vol. 1, Atlanta, GA, October 1987, pp. 380-390.

56. Brentani, G., "Considerations on the locked rotor torque characteristics of brushless dc motors", Proc. Seventh International Motorcon Conference, Hannover, Germany, April 1985, pp. 107-114.

57. Bolton, H. R. and Ashen, R. A., "Influence of motor design and feed-current waveform on torque ripple in brushless dc drives", Proc. IEE, Vol. 131, Pt. B, No. 3, May 1984, pp. 82-90.

58. Nucera, R. R. and Krause, P. C., "Computation of steady state performance of an electronically commutated motor", IEEE-IAS Annual Meeting Conference Record, Vol. 1, Denver, CO, September/October 1986, pp. 902-908.

APPENDIX A1

A1.1 PHYSICAL DETAILS OF THE BRUSHLESS DC MOTOR

A connection diagram and outline drawing for the motor are shown in Figures A1.1 and A1.2 respectively. Figure A1.3 shows the motor connected to the inverter and coupled to the dc generator which acts as a load.

A1.2 MAIN MOTOR AND TACHOMETER PARAMETERS

Parameters	Value	
R_k	1.278	Ω at 20°C
L_o	9.85	mH
L_2	0.45	mH
M_o	1.95	mH
M_2	0.45	mH
K_T	0.966	Nm/A
K_B	$1.68*10^{-3}$	V/rps
K_G	$3.3*10^{-5}$	V/rps
J_m	0.002	$kg.m^2$
T_F	0.15	Nm
D	0.03	Nm/krpm

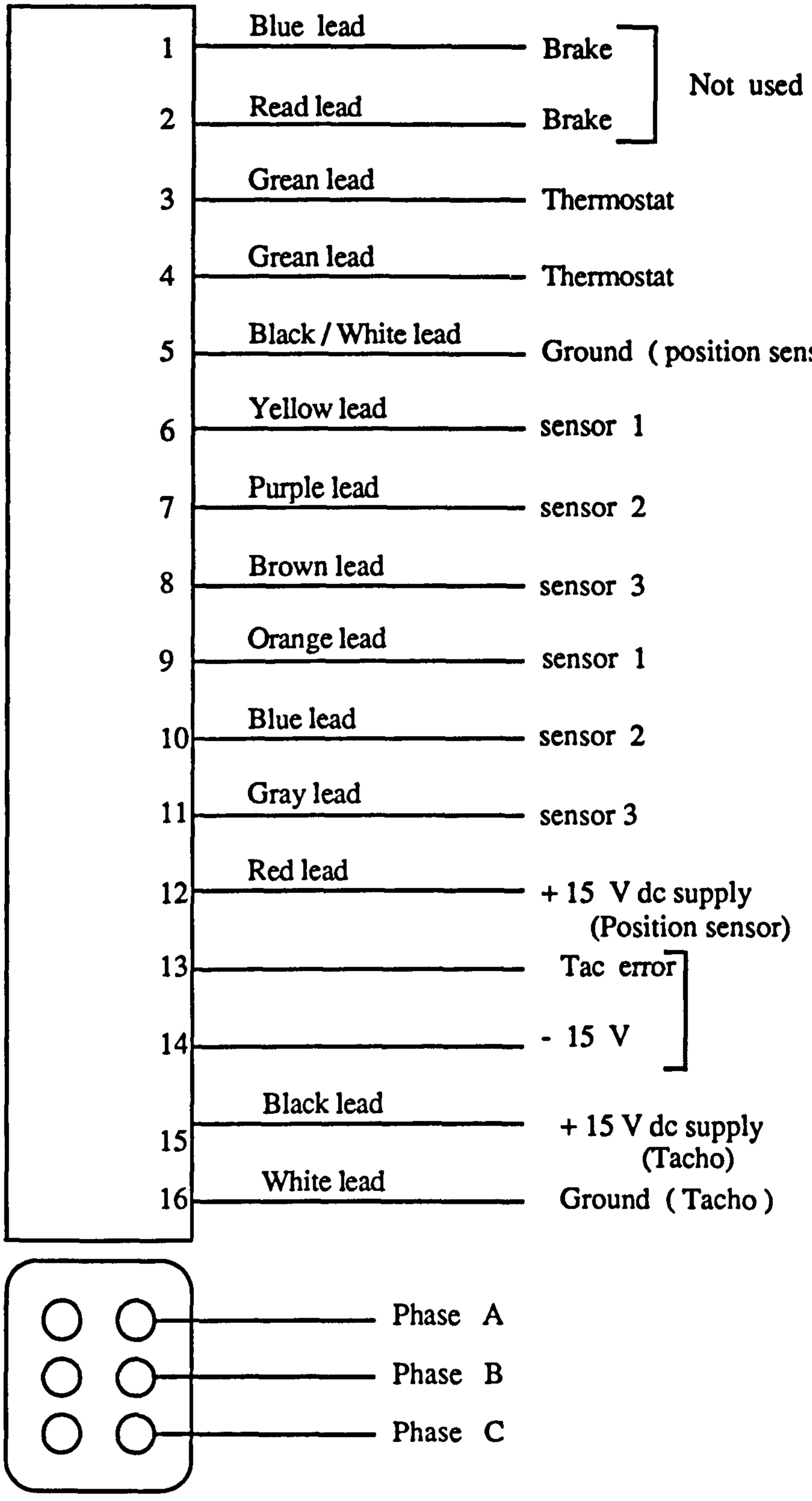

Figure A1.1 Motor connection diagram

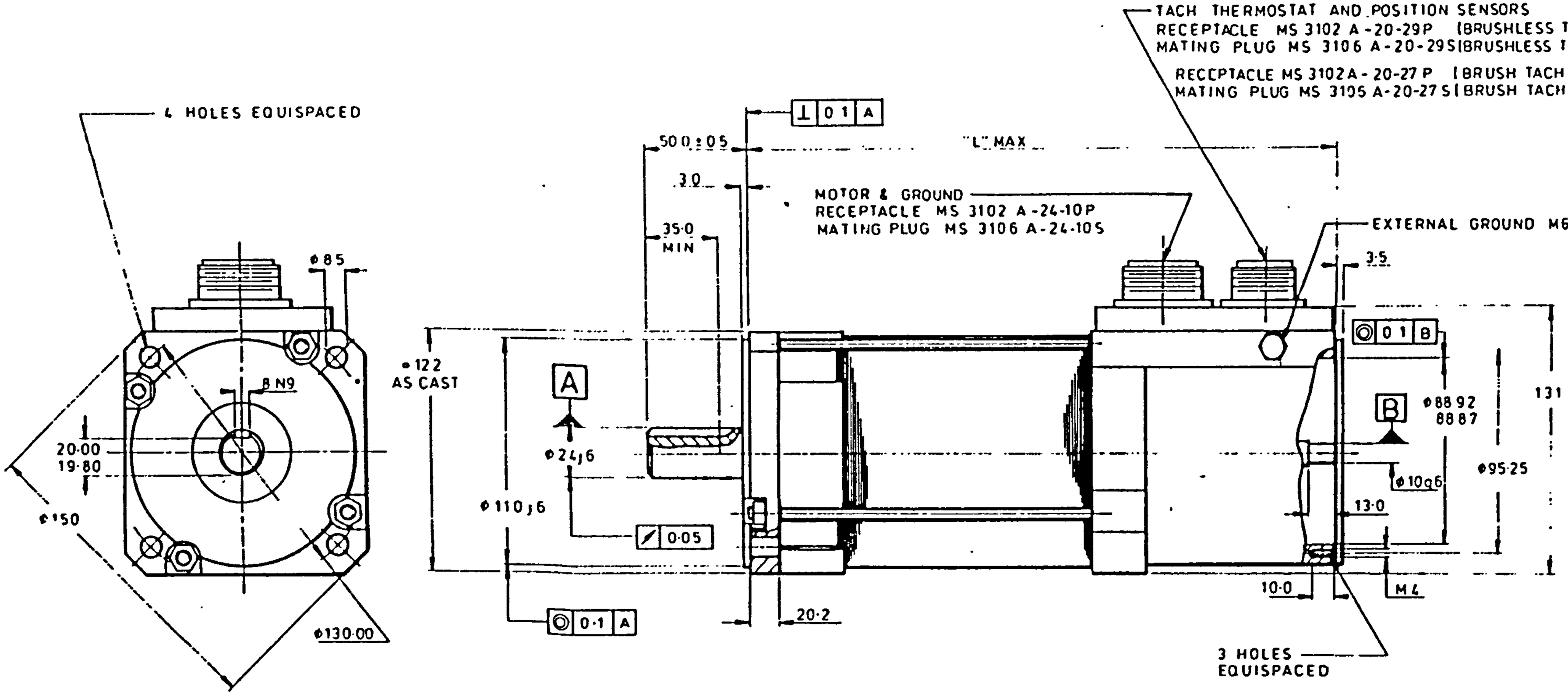

Figure A1.2 Motor outline drawing

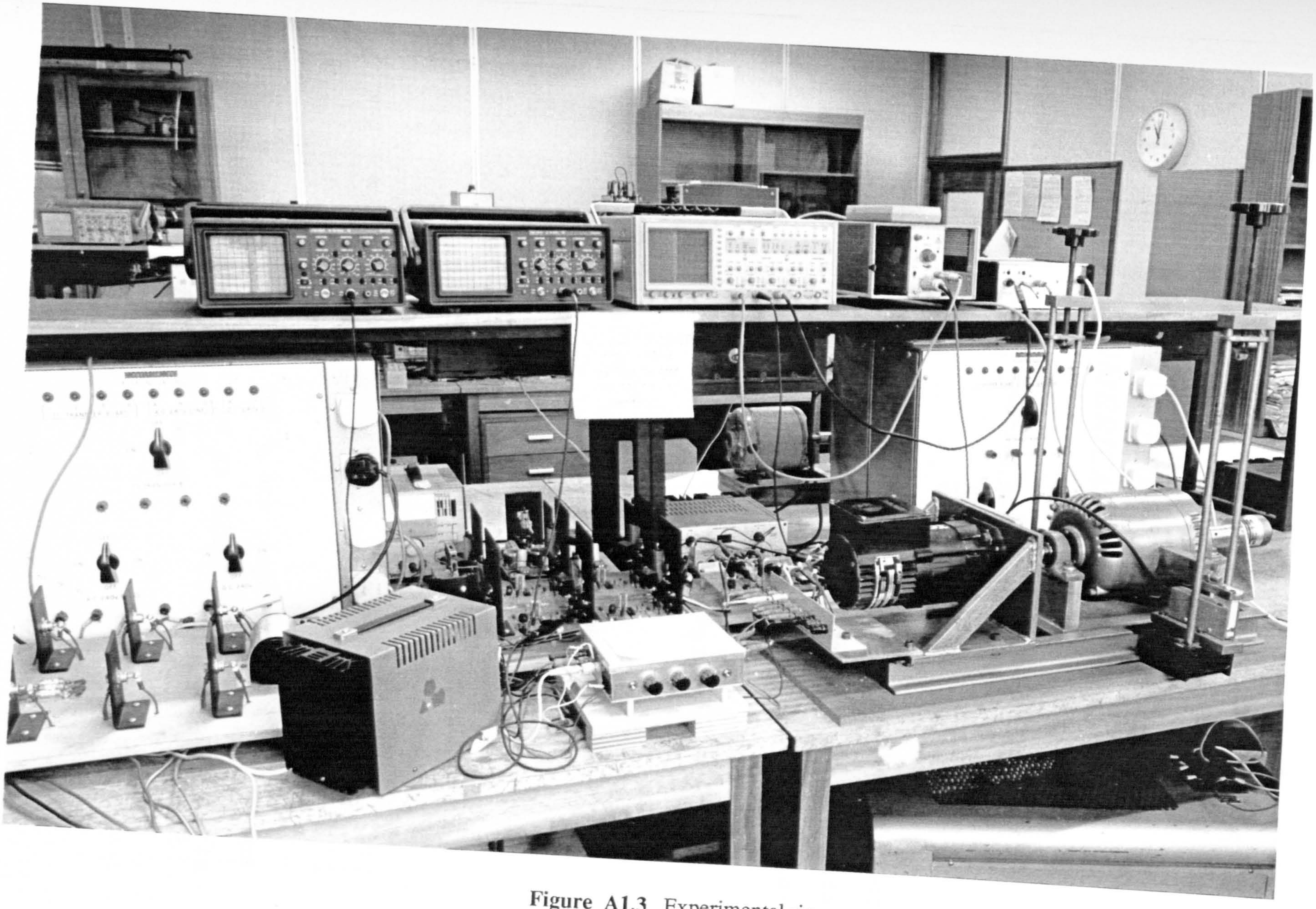

Figure A1.3 Experimental rig

APPENDIX A2

FOURTH-ORDER RUNGE-KUTTA NUMERICAL INTEGRATION

A differential equation of the form

$$\frac{dI}{dt} = f(t, I)$$

is readily solved on a step-by-step basis using the 4-th Order Runge-Kutta method[42,43]. The $(n+1)th$ value I_{n+1} is obtained from the previous nth value I_n by applying the formula

$$I_{n+1} = I_n + \frac{1}{6}(K_1 + 2K_2 + 2K_3 + K_4)$$

where

$$K_1 = h.f(t_n, I_n),$$

$$K_2 = h.f(t_n + \frac{1}{2}h, I_n + \frac{1}{2}K_1),$$

$$K_3 = h.f(t_n + \frac{1}{2}h, I_n + \frac{1}{2}K_2),$$

$$K_4 = h.f(t_n + h, I_n + K_3),$$

and h is the integration step length.

The quantities t_n and I_n are respectively the time and the current at the start of an integration step, and I_{n+1} is the current at the end of the step.

APPENDIX A3

SHAFT ENCODER SPECIFICATION LEINE AND LINDE LTD

MODEL 63 INCREMENTAL ENCODER WITH MARKER PULSE*)

*) Also available without marker pulse (Model 53).

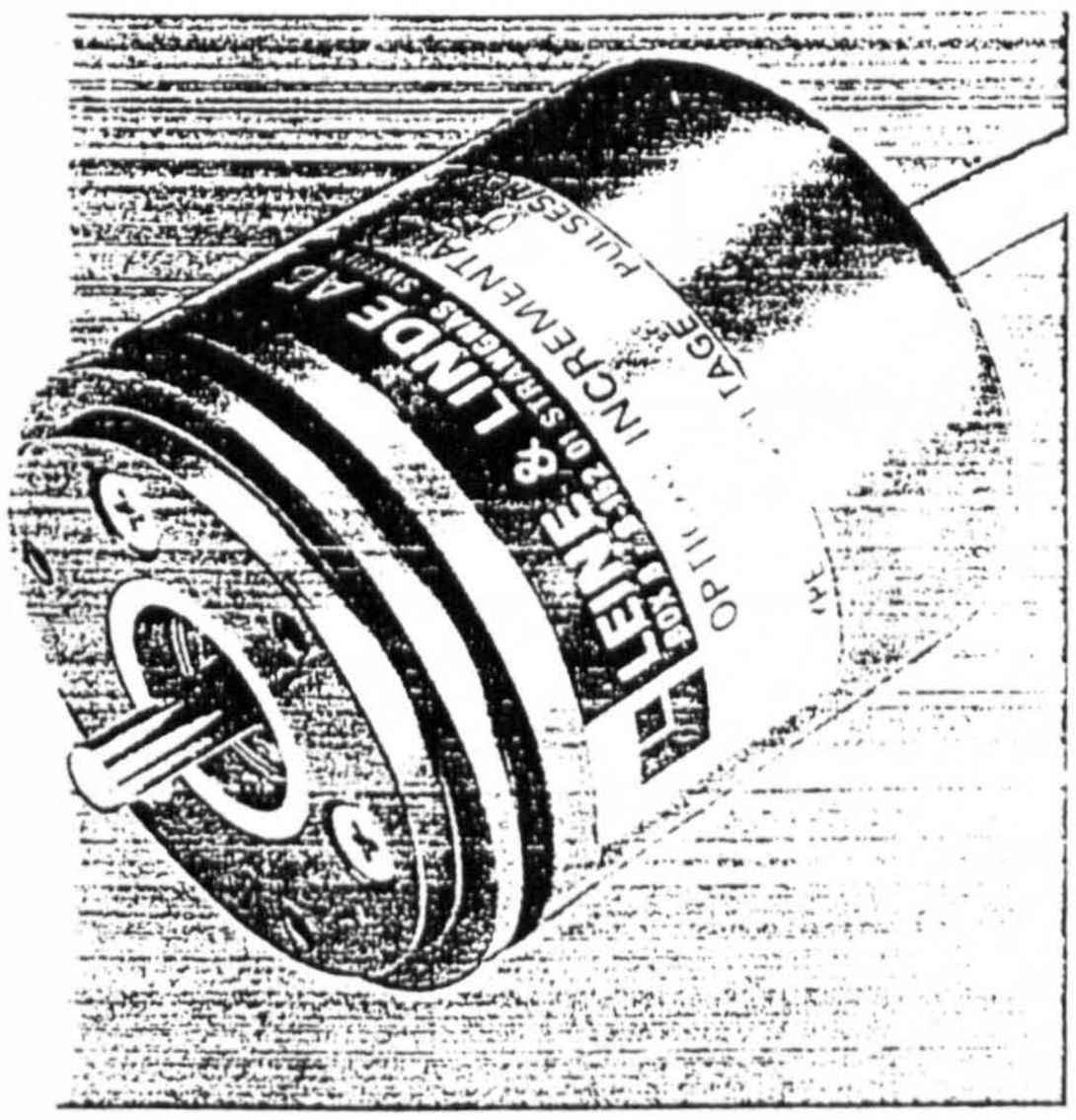

Rugged photo-electric encoder for industrial applications

- Light emitting diodes for long life. Push-pull photo diode circuit has high noise-immunity and high tolerance to temperature variations and component ageing.
- Marker pulse channel gives one pulse per revolution for use as zero reference.
- Single supply, 5—24 VDC. No separate lamp supply required.
- Complementary output signals permit use of differential lines to give high immunity to interference on long lines.
- Housing is splash proof. Optional shaft seal makes entire encoder dust and spray proof according to IP65 classification.
- Four shaft/bearing options:
  - **60** 6 mm shaft
  - **06** 6 mm shaft with screw flat
  - **63** 6,35 mm (1/4") shaft
  - **10** 10 mm shaft with screw flat.
- Rugged housing with 2 mm walls. Shock and vibration proof electronics, plastic disc and grating.
- Cable or connector to the rear or to the side.
- Line driver standard by 5 V.

STANDARD PULSE RATES

The following rates (pulses per revolution) are available. *These rates can be doubled by counting* both the positive *and negative flank of the pulse. If this is performed on both* channels a quadrupling of the nominal pulse rate will be achieved.

This doubling or quadrupling can be made in an electronic counter, in computer soft ware or in a signal converter supplied by us.

5 000	2 048	1 080	635	360	200	60
4 096	2 000	1 024	625	300	180	50
4 000	1 800	1 000	600	256	150	
3 600	1 600	900	512	250	128	
2 540	1 440	800	508	254	127	
2 500	1 270	750	500	250	125	
2 160	1 250	720	400	240	100	

SPECIAL MODELS

For special orders, our manufacturing technique enables us to offer fast delivery of non-standard pulse rates up to 5 000.

ELECTRICAL SPECIFICATIONS

Opto components	Light emitting diodes and photo diodes		
	Line driver		
Supply current V	5 ±5 %	12—18	18—30
Current drain at no load typ. (max) mA	130 (180)	50 (70)	50 (70)
Sink current min mA	40	50	50
Source	40	35	35
Max pulse frequency kHz better than	200	100	100
	(5 V 400 kHz optional)		
Low output level max V	0.5	1.5	1.3
High output level	Load dependent, see data sheet of resp IC-circuit		
Output signals	Complementary (1, $\bar{1}$, $\bar{2}$, 2, 0, $\bar{0}$)		
Cable length	1.5 m (8 core screened, $2 \times 0.34\ mm^2 + 6 \times 0.22\ mm^2$) extra length optional		
Cable colour code	A Signal 1 green	G Signal 0 brown	
	B Signal $\bar{1}$ white	H Signal $\bar{0}$ violet	
	C Signal $\bar{2}$ black	E +E volt	red
	D Signal 2 yellow	F 0 volt	blue
Temperature range	—40°C to +60°C		

OUTPUT CIRCUIT OF ENCODER

Supply current V	5	12—18	18—30
IC-circuit (active pull up)	SN 75114	see circuit diagram	see circuit diagram
Resistance	—	270Ω	270Ω

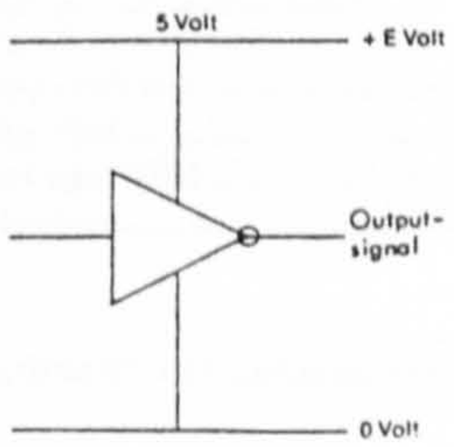

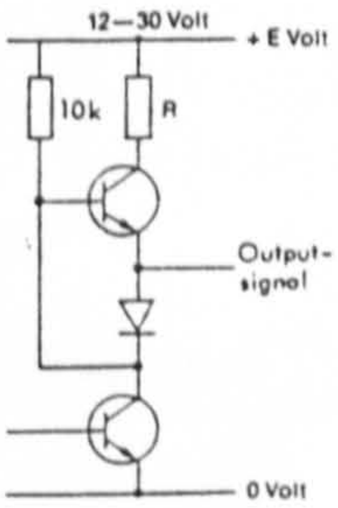

OUTPUT SIGNALS

Bidirectional encoders: Two 90° phased (quadrature) square waves permit direction-sensing. Signal 2 comes before signal 1 at clock-wise rotation (seen from shaft end). One 0-pulse.

The 0-pulse is synchronized with channel 1 and 2 and is high once per revolution at the same time as channels 1 and 2 are high.

SIGNAL SEQUENCE

Clock-wise rotation, seen from shaft end.

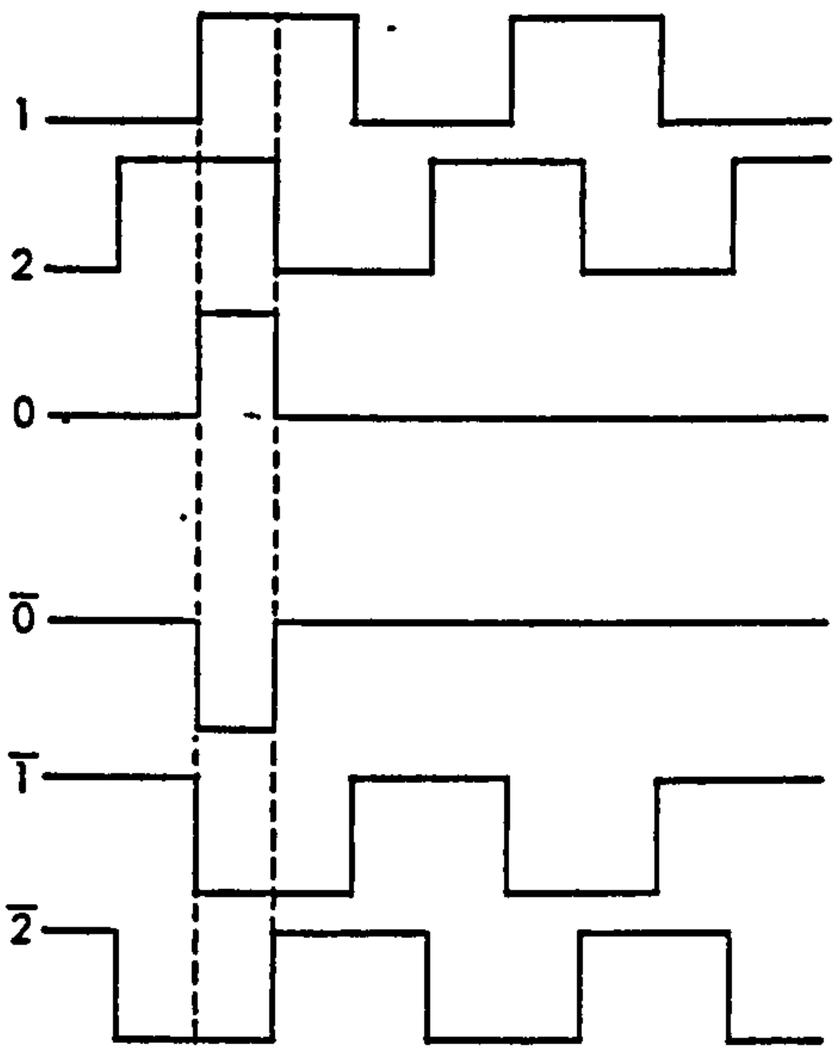

BEARING LIFE 6 and 10 mm shaft

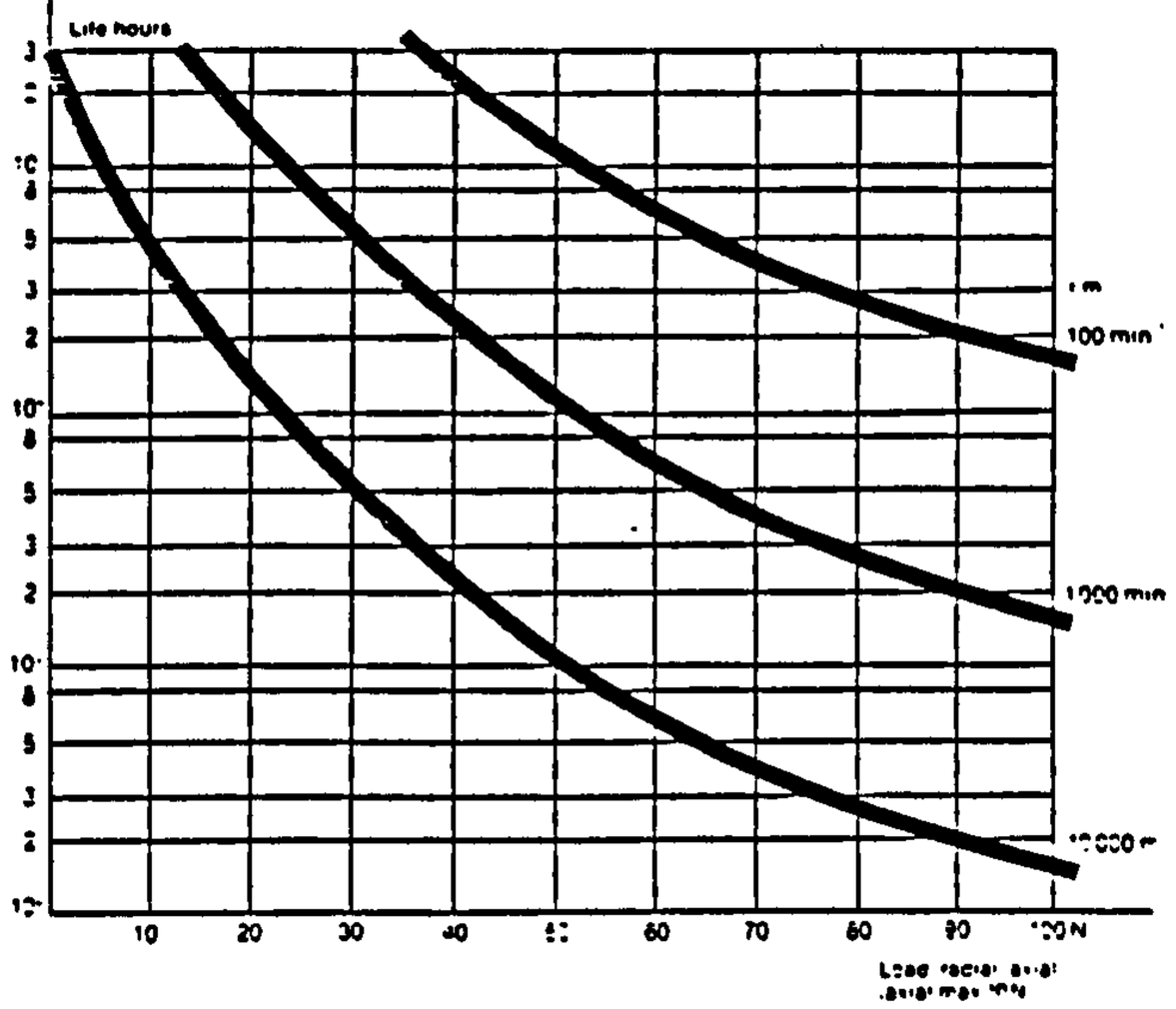

ACCURACY

Electrical degrees are used as the unit of measurement to specify the accuracy of the encoder. 360 electrical degrees are defined as the mechanical shaft angle that corresponds to one signal cycle. (360 mechanical degrees divided by the pulse rate of the encoder.)

The dividing error specifies the largest deviation from the nominal distance between two pulse edges from the same or from different signal channels and consists of mechanical angle and electronic reproduction errors. The dividing error does not increase when the encoder is turned through more than one complete turn, that is, the error is non-cumulative.

When measured at arbitrary edges of different channels:

Max dividing error = ±50 electrical degrees.

Channel separation specifies the distance between adjacent edges of different channels:

Channel separation = 90 ±25 electrical degrees.

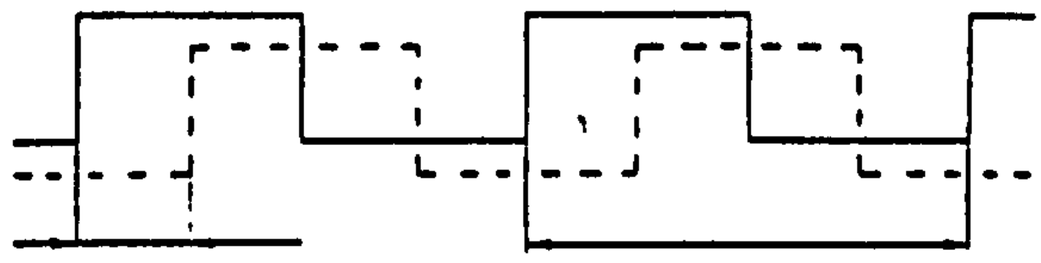

Channel separation 360° el.degrees (1 pulse)

MECHANICAL SPECIFICATIONS

Case	Anodized aluminium	
Shaft	Stainless steel	
Bearings	Permanently lubricated stainless steel bearings	
Code disc	Plastic disc with photographically generated pattern	
Sealing	Dust and moisture proof, except shaft bearing. Optional shaft seal classifies encoder as IP65	
Shaft type	06, 60, 63	10
diameter mm	6	10
Max shaft load		
radial max N	10	20
axial max N	10	10
Torque max Nm	$2 \cdot 10^{-3}$	$4 \cdot 10^{-3}$
Moment of inertia max kgm²	$14 \cdot 10^{-7}$	$18 \cdot 10^{-7}$
Rpm max	12 000	12 000
Bearing life h	50 000	50 000
Weight kg	0.4	0.4
Pulse rate max	5 000	5 000
Vibration	better than 10 g	
Shock	better than 75 g	

ORDER NUMBERING SYSTEM

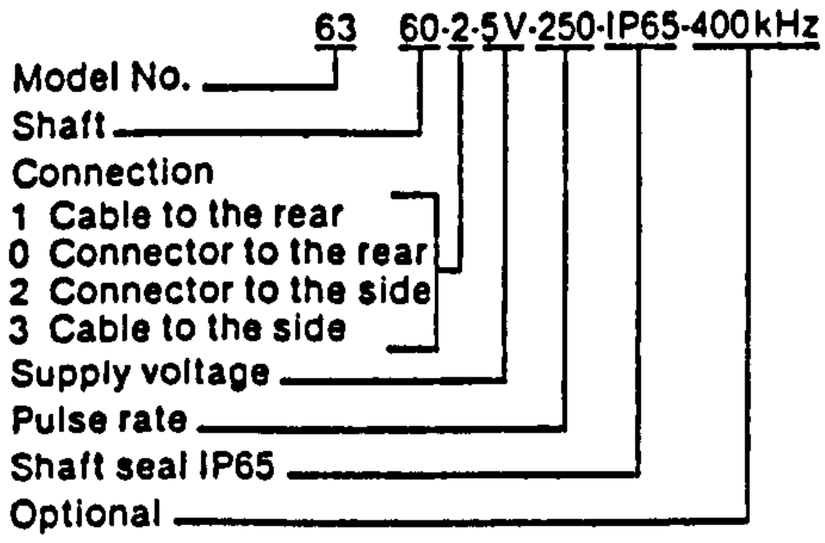

Specifications subject to change without notice.

APPENDIX A4

The 11th International Conference on Electric Vehicle, Florence, Italy,
27-30 September 1992

CURRENT PROFILING FOR TORQUE PULSATION MINIMISATION IN *BRUSHLESS DC MOTOR DRIVES*

J G Kettleborough, I R Smith, K Al-Hadithi & V V Vadher
Loughborough University of Technology, UK

ABSTRACT

Most mathematical models for rotating electrical machines assume that the machine windings are balanced and sinusoidally distributed, and that the generated emf waveforms are sinusoidal. The Trapezoidal Type Brushless DC motor, which is becoming popular for battery powered electric vehicle applications, has windings which are far from sinusoidally distributed and a generated emf whose waveform is almost trapezoidal. Consequently, it is not possible to investigate reliably the harmonic torque and speed ripple occurring in the machine, particularly at low speed, using one of these models. To overcome this problem a phase reference frame may be used, since it does not rely on the above assumptions. This paper outlines the use of the phase reference frame for the analysis of a brushless DC motor and the resulting model is used in a study of the factors affecting torque and speed pulsations experienced by the drive. Particular attention is paid to profiling the motor phase current, to produce a smooth motor torque. Experimental results from a practical drive system are shown to compare well with simulation results.

INTRODUCTION

An important item of plant in an electric vehicle is the drive motor and lately, the permanent magnet Trapezoidal Type Brushless DC motor (BDCM) has become popular for this application, due to its higher power/weight ratio, smaller inertia and lesser maintenance requirements. A typical system is shown in Figure 1, where the three coils *a*, *b*, and *c* represent the machine stator windings, and *d* and *q* represent rotor damper circuits, which may or may not be present, depending on the machine design. The active rotor is usually a rare-earth permanent magnet. The stator is supplied from a 3-phase inverter bridge, comprising typically MOSFET switches (1 to 6) and inverse parallel diodes (D1 to D6) to commutate the current between phases as different combinations of switches turn on and off. The conduction pattern of the switches is controlled by a rotor position sensor, which turns pairs of devices on in a defined pattern according to the rotor position.

With this type of motor, the stator windings are far from sinusoidally distributed and the emfs generated in the phase windings are almost trapezoidal. Consequently, the popular dqO and $\alpha\beta 0$ reference frames are unsuitable for modelling the system, due to their simplifying assumptions, and a phase reference frame was chosen to investigate the machine's electrical behaviour [1].

Under normal operating conditions, the magnetic circuit for this type of machine operates in the linear region of its demagnetisation curve, since the very high reluctance of the rare-earth magnets have a linearising effect similar to an airgap and, consequently, saturation was neglected in the model. It could however be included, by expressing the stator winding flux linkages as functions of both the rotor angle and the machine currents [2]. To simplify the analysis further, slot effects and hysteresis and eddy currents in the magnetic circuit were neglected.

Although the inverter switching devices are assumed to be ideal, with no impedance or forward voltage drop when conducting and an infinite impedance when non-conducting, the model developed is sufficiently flexible to incorporate alternative device representations, as well as the turn-on and turn-off times for the devices.

A tensor approach is used [3], to define automatically the circuit topology [4] as the conduction pattern of the inverter switches changes and consequently the different circuit equations which apply. The system equations are solved by numerical integration, to obtain the time variation of flux linkages and currents in the mesh reference frame and the corresponding branch voltages and currents are obtained by further transformations.
A description of the model now follows.

DRIVE SYSTEM MODEL

The use of tensors necessitates the definition of branch and mesh reference frames and the transformation between the two frames.

Branch reference frame.

The branch reference frame is concerned with the voltages across and currents through the individual windings or branches of the circuit shown in Figure 1. The matrix voltage equation relating to this reference frame is

$$\begin{bmatrix} V_a \\ V_b \\ V_c \\ V_d \\ V_q \\ V_s \end{bmatrix} = \begin{bmatrix} R_a & & & & & \\ & R_b & & & & \\ & & R_c & & & \\ & & & R_d & & \\ & & & & R_q & \\ & & & & & R_s \end{bmatrix} \begin{bmatrix} I_a \\ I_b \\ I_c \\ I_d \\ I_q \\ I_s \end{bmatrix} + p \begin{bmatrix} \psi_a \\ \psi_b \\ \psi_c \\ \psi_d \\ \psi_q \\ \psi_s \end{bmatrix} \qquad (1)$$

where a, b, c, d, and q relate to the machine windings, s is the supply impedence and $p=\frac{d}{dt}$
Equation 1 may be written in the abbreviated form

$$V_b = R_b I_b + p\psi_b \qquad (2)$$

where V_b is the branch voltage vector, I_b the branch current vector, R_b the branch resistance matrix and ψ_b the branch total flux linkage vector given by

$$\begin{bmatrix} \psi_a \\ \psi_b \\ \psi_c \\ \psi_d \\ \psi_q \\ \psi_s \end{bmatrix} = \begin{bmatrix} L_{aa} & L_{ab} & L_{ac} & L_{ad} & L_{aq} & O \\ & L_{bb} & L_{bc} & L_b & L_{bq} & O \\ & & L_{cc} & L_{cd} & L_{cq} & O \\ & & & L_{dd} & O & O \\ & & & & L_{qq} & O \\ & & & & & L_{ss} \end{bmatrix} \begin{bmatrix} I_a \\ I_b \\ I_c \\ I_d \\ I_q \\ I_s \end{bmatrix} + \begin{bmatrix} \psi_{pa} \\ \psi_{pb} \\ \psi_{pc} \\ \psi_{pd} \\ \psi_{pq} \\ \psi_{ps} \end{bmatrix} \qquad (3)$$

where L_{xx} is the self inductance of winding x (x=a,b,c,d,q), L_{xy} the mutual inductance between windings x and y (x, y = a, b, c, d, q) and ψ_{px} the flux linkages with winding x due to the permanent magnet

In abbreviated form equation (3) is

$$\psi_b = L_b I_b + \psi_{pb} \tag{4}$$

where L_b is the branch inductance matrix and ψ_{pb} the vector of branch flux linkages due to the permanent magnet.

Re-arranging equation (4) and combining with equation (2)

$$V_b = R_b L_b^{-1}(\psi_b - \psi_{pb}) + p\psi_b$$

Mesh reference frame

This is concerned with the meshes formed when conducting switches connect the motor phases to the DC supply. During normal operation, six discrete switching states occur in a defined sequence, with only two switches conducting at any instant. A typical conduction pattern is shown in Figure 1, with switches S1 and S2 forming one mesh, together with the permanent meshes formed by the damper circuits d and q. The application of Kirchhoff's voltage law to these meshes results in three mesh differential equations which may be expressed as the mesh matrix differential equation

$$p\psi_m = V_m - R_m L_m^{-1}(\psi_m - \psi_{pm}) \tag{5}$$

where V_m is the impressed mesh voltage vector, I_m the mesh current vector, $\psi_m = L_m I_m + \psi_{pm}$ the mesh total flux linkages vector, ψ_{pm} the mesh flux linkage vector due to the permanent magnet and R_m *and* L_m are respectively the mesh resistance and inductance matrices.

Equation 5 may be integrated numerically to give a new flux linkage vector ψ_m and a step-by-step solution may be obtained.

Branch/mesh transformation

The mathematical model has to generate automatically the relevant mesh equations as the switch and diode conduction pattern changes and this is achieved by defining a transformation between the branch and mesh reference frames. The relationship between the mesh currents shown in Figure 1 and the branch currents may be obtained by inspection as

$$\begin{bmatrix} I_a \\ I_b \\ I_c \\ I_d \\ I_q \\ I_s \end{bmatrix} = \begin{bmatrix} +1 & 0 & 0 \\ 0 & 0 & 0 \\ -1 & 0 & 0 \\ 0 & +1 & 0 \\ 0 & 0 & +1 \\ +1 & 0 & 0 \end{bmatrix} \begin{bmatrix} I_{mq} \\ I_{m2} \\ I_{m3} \end{bmatrix} \tag{6}$$

where ±1 denotes whether the mesh current has the same or the reversed sense as the branch current and a 0 that there is no mesh current in that branch. Equation 6 may be written in the abbreviated form $I_b = CI_m$ where C is the branch/mesh current transformation matrix. Assuming power invariance between reference frames

$$(V_b - p\psi_m)^t I_b = (V_m - p\psi_m)^t I_m$$

it can be shown that [5]

$$R_m = C^t R_b C \text{ and } L_m = C^t L_b C \qquad \psi_m = C^t \psi_b \text{ and } \frac{dL_m}{d\theta} = C^t \frac{dL_b}{d\theta} C$$

and that

$$V_m = C^t V_b$$

Where the superscript t denotes transpose.

In the mathematical model, C is changed automatically whenever there is a change in the conduction pattern. The last two columns of C represent the permanent meshes of the damper circuits d and q and these remain unaltered. The first column (if two devices are conducting) or the first two columns (if three devices are conducting, such as occurs during commutation) are dynamic and change with the conduction pattern. The elements of these columns are obtained from the master matrix shown in Figure 2, which holds the meshes relating to all practical combinations of switches and/or diodes. For the case shown in Figure 1, mesh (1) would be extracted from the master matrix and inserted in column 1 of C, as shown in Equation 6.

System mechanical equation

The equation relating to the various system torques is

$$T_e = J\frac{d\omega}{dt} + D\omega + T_L \tag{7}$$

where T_e is the electromagnetic torque, J the combined motor and load inertia, $\frac{d\omega}{dt}$ the rotor angular velocity, D the friction constant and T_L the load torque.

The electromagnetic torque is given by

$$T_e = P\left\{\left(I_m^t \frac{dL_m}{d\theta} I_m\right) + \left(I_m^t \frac{d\psi_{pm}}{d\theta}\right)\right\}$$

where P is the number of pairs of poles.

Equation 7 may be re-arranged in the form

$$\frac{d\omega}{dt} = J^{-1}(T_e - D\omega - T_L)$$

which may be integrated numerically to give a step-by-step solution for the rotor speed ω.

Computer implementation

A computer program was written to predict the motor performance, using the techniques described in the previous sections. The solution process is described by the following algorithm.

a) The branch resistance matrix is formed. This fixed matrix is assembled once only, at the

beginning of the simulation.

b) The mesh resistance matrix is determined from $R_m = C^t R_b C$. This matrix is dynamic and changes with the switch conduction pattern.

c) The time varying branch inductance matrix L_b is determined. This matrix is formed at every integration step, since its elements vary with the angular position of the rotor.

d) The mesh inductance matrix is determined from $L_m = C^t L_b C$ and its inverse is obtained.

e) The impressed mesh voltage vector is obtained from $V_m = C^t V_b$.

f) The branch flux linkage vector ψ_{pb} due to the permanent magnet rotor is obtained using the relationships given in the Appendix.

g) The mesh flux linkage vector due to the permanent magnet rotor is obtained from $\psi_{pm} = C^t \psi_{pb}$.

h) Equation (5) is integrated numerically using the 4th-Order-Runge-Kutta method, to obtain a new value for the flux linkage vector ψ_m.

i) The mesh current vector is obtained from $I_m = L_m^{-1} (\psi_m - \psi_{pm})$.

j) The branch current vector is obtained from $I_b = CI_m$.

k) The rate-of-change of branch inductance matrix $\frac{dL_b}{d\theta}$ is obtained from the derivative of the branch inductance matrix with respect to rotor position.

l) The mesh rate-of-change of inductance matrix is obtained from

$$\frac{dL_m}{d\theta} = C^t \frac{dL_b}{d\theta} C$$

m) The mesh current derivative vector pI_m is determined from

$$pI_m = L_m^{-1} (V_m - R_m I_m - \frac{dL_m}{d\theta} \cdot \omega I_m - p\psi_{pm})$$

n) The branch current derivative vector pI_b is determined from

$$pI_b = CpI_m$$

o) The branch voltage vector is obtained from

$$V_b = R_b I_b + L_b pI_b + \frac{dL_b}{d\theta} \omega I_b + p\psi_{pb}$$

p) The new electromagnetic torque is obtained from equation (8) and the new angular velocity is obtained by integrating numerically equation (9).

The solution advances by one integration step, the initial conditions are updated and procedures (c) to (p) are repeated until the end of the simulation. At the end of each step, the system is tested for discontinuities (turn-on or turn-off of diodes or MOSFETs) which have occurred in the bridge conduction pattern. If a change occurs, the following procedure is implemented.

1) The instant to the time of the discontinuity is obtained using linear interpolation.
2) Equation (5) is re-integrated from the start of the integration step up to the point of discontinuity.
3) A new current transformation matrix C is assembled.

4) New mesh matrices are formed according to the new circuit topology.
5) Equation (5) is integrated from the point of discontinuity to the end of the integration step.
6) The system is tested for further changes in the bridge conduction pattern. If any occur, operation (1) to (6) are repeated. If not, the solution proceeds with operations (c) to (p) over the next integration step.

PREDICTED AND EXPERIMENTAL PERFORMANCE

A program was written in Fortran 77 and run on a mainframe computer. The parameters for the BDCM model obtained by test from the actual machine are given in the Appendix.

Figures 3 and 4 show respectively the predicted and experimental steady-state performance for the drive, with a supply voltage $V_s = 24V$, load torque $T_L = 0.7Nm$ and steady-state speed $n = 222rpm$. The close agreement between the two sets of results gives confidence in the models ability to predict the drive performance. Note in both sets of line-voltage waveforms (Figures 3(c) and 4(c)) the sudden dips in the voltage to zero. These occur at intervals during which one switch is turning-on and another is turning-off. There is then a period during which both devices are on and this causes a short circuit between two lines, or a commutation notch. In the next section, it is shown that these notches have an undesirable affect on the motor torque and speed and the computer program is used to show how the motor phase current may be altered to eliminate this affect.

Figures 5 and 6 respectively show the predicted and experimental transient performance as the motor is started from rest, for the same conditions described above. Again, there is good correspondence between the two sets of results.

TORQUE RIPPLE MINIMISATION

The emf generated in a BDCM is ideally trapezoidal, with a flat-top spanning 120° electrical and, since the electromagnetic torque T_e is proportional to the product of this emf and the stator current [6], a rectangular stator current waveform is needed to produce a constant torque. In practice, both the generated emf and the stator current waveforms differ from the ideal, and the torque exhibits a ripple which is periodic and dependent on the rotor position and the commutation events. At high speeds, these effects are masked by the drive inertia, but at low speed they can seriously degrade the drive performance. The computer program was used to study the factors effecting this torque ripple and the ways by which this might be reduced and in particular, the optimum phase current waveform to produce a smooth torque was determined.

Factors affecting torque ripple

The major factors effecting the torque ripple are the non-ideal shape of the phase emf waveforms and the commutation events.

The idealised and actual phase voltage waveforms are shown in Figures 7 (a) and (b). The actual waveform results from the fact that the airgap flux-density distribution is not rectangular, but has rounded corners due to fringing, and consequently the emf waveform has fluctuations as shown. The actual phase emf waveform is accurately represented in the model, since the flux linkages variation with the rotor position due to the permanent magnet were obtained experimentally and represented in the computer program as a harmonic series.

During commutation, the winding inductance prevents the phase current from changing instantaneously and consequently the waveform has rounded edges as shown in Figure 8 (a) rather than the theoretical rectangular waveshape. This phenomenon is inherently predicted by the computer program.

Current profiling simulations

Figure 8 shows the phase current, motor torque and speed waveforms for a load torque of 0.6Nm an average speed of 102rpm. For this condition there is no compensation, and the torque and speed pulsations are clearly evident. During the period that switches 1 and 2 both conduct, as shown in Figure 1, the instantaneous motor torque is

$$T_e = \frac{I_{m1}}{\omega} (e_a - e_c)$$

where I_{m1} is the current in mesh 1.

It was shown in Figure 7 (b) that the phase voltages are not flat topped. Consequently, to maintain T_e constant, the mesh current has to be adjusted in proportion to the term $1/(e_a - e_c)$ during the period that switches 1 and 2 bothconduct. This is achieved in the program (and in practice) by introducing a current control loop with pulse-width-modulation control of the inverter switches to force the motor phase current to follow the above proportionality. Figure 9 shows the waveforms for the same conditions as Figure 8, but it is now evident that the torque and speed ripples are considerably reduced. Note the new phase current waveshape, that exhibits the above mentioned adjustment.

There are still torque and speed pulsations evident in Figure 9 and these clearly occur at commutation instants. A current boost during commutation was therefore introduced into the control loop, together with the current profiling, and Figure 10 shows the effect of this on the waveforms. The slight increase in phase current at commutation has virtually eliminated the torque and speed ripple. The high frequency ripple evident in the current and torque waveforms of Figures 9 and 10, but absent from Figure 8, is due to the PWM switching of the inverter.

CONCLUSIONS

The paper has presented a mathematical model for a BDCM drive and has demonstrated that good correspondence is obtained between theoretical predictions and practical results. Having established confidence in the model, it was then used to investigate the minimisation of torque ripple using current profiling. The results obtained show that the method can effectively eliminate torque and speed pulsations in the drive.

REFERENCES

[1] Smith I R, Snider L A: "Prediction of transient performance of an isolated synchronous generator", IEE Proceedings, Vol 119, No 9, Sept 1972, pp 1309-1318.

[2] Nehl T W, Demerdash N A, Fovad F A: "Impact of winding inductances and other parameters on the design and performance of brushless dc motors", IEEE Trans on Power Apparatus and Systems, PAS-104, No 8, Aug 19885, pp 2206-2213.

[3] Kron G: "Tensors for circuits", Dover Publications, Second Edition, 1959.

[4] Kettleborough J G, Smith I R, Fanthome B A: "Simulation of a dedicated aircraft generator supplying a heavy rectified load", IEE Proceedings, Vol 130, Part B, No 6, Nov 1983, pp 431-435.
[5] Happ H: "Diakoptics and networks", Academic Press, First Edition, 1971.
[6] Jahns T M: "Torque production in permanent-magnet synchronous motor drives with rectangual current excitation", IEEE Trans on Industry Applications, Vol 1A-20, No 4, July/August 1984, pp 803-813.

APPENDIX

The experimental BDCM had the following nameplate rating:
3 phase, 6 pole, 1.3kW, 2400 rpm

The phase parameters are as follows:

$L_{ad}, L_{aq}, L_{bd}, L_{q}, L_{cd}, L_{cq} = 0$ (*Assuming no dampers*)

where θ is the angle in electrical radians between the axes of the a-phase and the rotor pole as defined in Figure 1.

$$R_a, R_b, R_c = 1.28\Omega$$
$$R_d, R_q = 0 \text{ (Assuming no dampers)}$$
$$R_s = 10m\Omega$$
$$L_{aa} = (9.85 - 045 \cos\theta)\ mH$$
$$L_{bb} = (9.85 - 0.45 \cos 2(\theta + 2\pi/3))\ mH$$
$$L_{cc} = (9.85 - 0.45 \cos 2(\theta - 2\pi/3))\ mH$$
$$L_{dd}, L_{qq} = 0 \text{ (Assuming no dampers)}$$
$$L_{ss} = 10mH$$
$$L_{ab} = (-1.95 - \cos 2(\theta - 2\pi/3))$$
$$L_{ac} = (-1.95 - \cos 2(\theta + 2\pi/3))$$
$$L_{bc} = (-1.95 - \cos 2\theta)$$

The elements of the branch flux linkage vector ψ_{pb} are

$$\psi_{pa} = 0.18\ (\cos\theta + 0.08 \cos 3\theta + 0.01 \cos 5\theta)$$

$$\psi_{pb} = 0.18\ (\cos\theta + 2\pi/3) + 0.08 \cos 3(\theta + 2\pi/3) + 0.01 \cos 5(\theta + 2\pi/3))$$

$$\psi_{pc} = 0.18\ (\cos(\theta - 2\pi/3) + 0.08\cos 3\ (\theta - 2\pi/3) + 0.01 \cos 5(\theta - 2\pi/3))$$

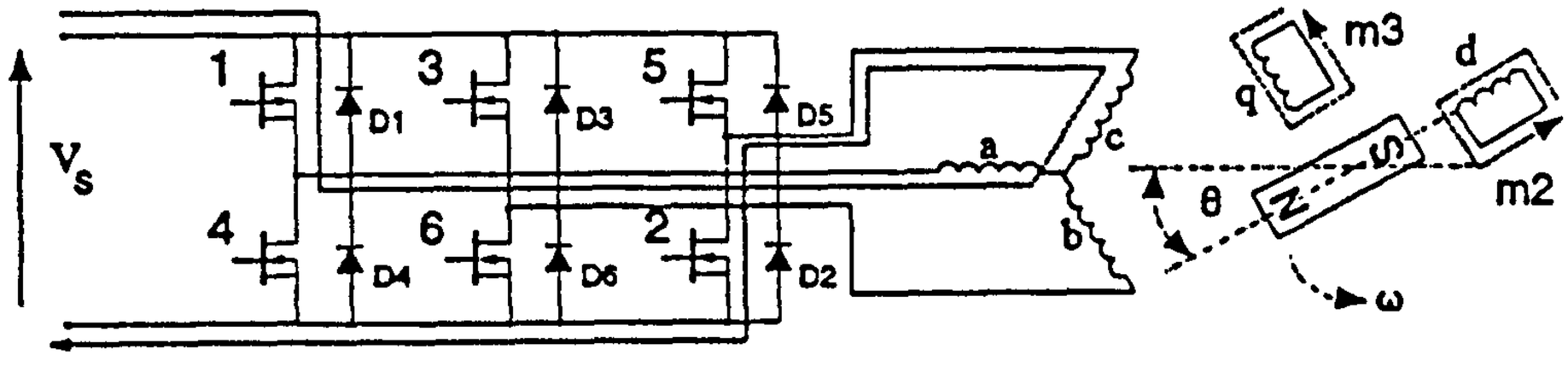

Figure 1 Brushless DC Motor Drive

Conducting Device	1 2	3 2	3 4	5 4	5 6	1 6	1 D3	1 D5	3 D1	3 D5	5 D1	5 D3	4 D6	4 D2	6 D4	6 D2	2 D4	2 D6
Mesh No.	1	2	3	4	5	6	7	8	9	10	11	12	13	14	15	16	17	18
Branch																		
a	1		-1	-1		1	1	1	-1		-1		-1	-1	1		1	
b		1	1		-1	-1	-1		1	1		-1	1		-1	-1		1
c	-1	-1		1	1			-1		-1	1	1		1		1	-1	-1
d																		
q																		
s	1	1	1	1	1	1												

Figure 2 Master Matrix

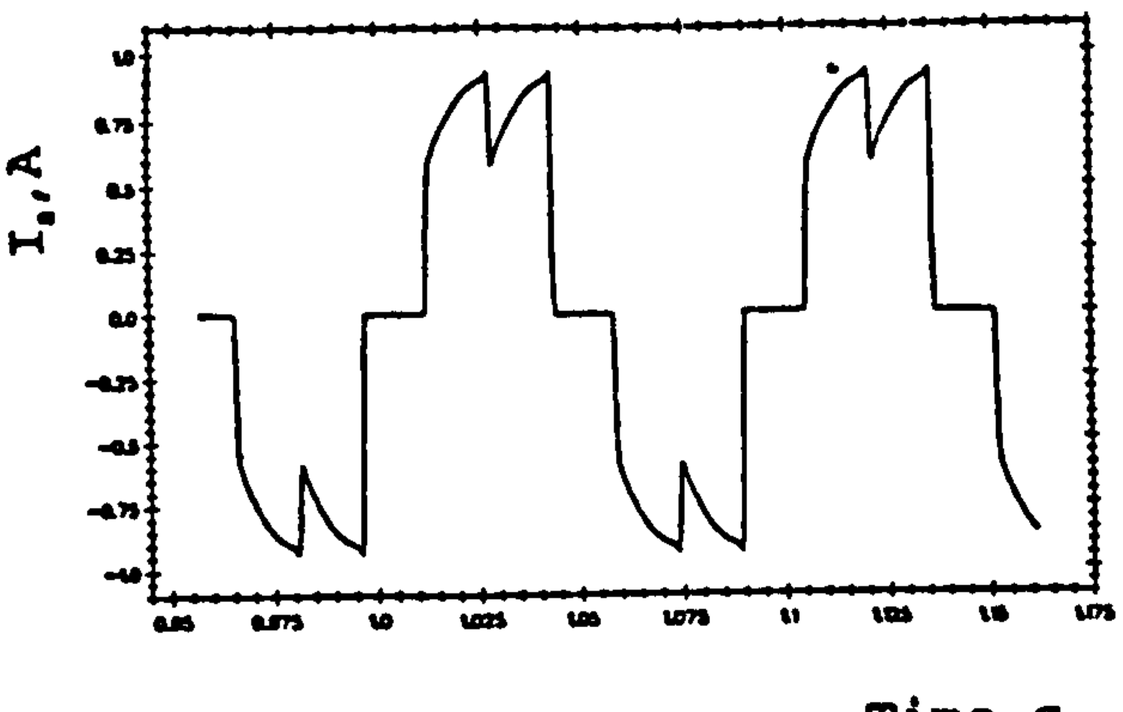

(a) Phase Current

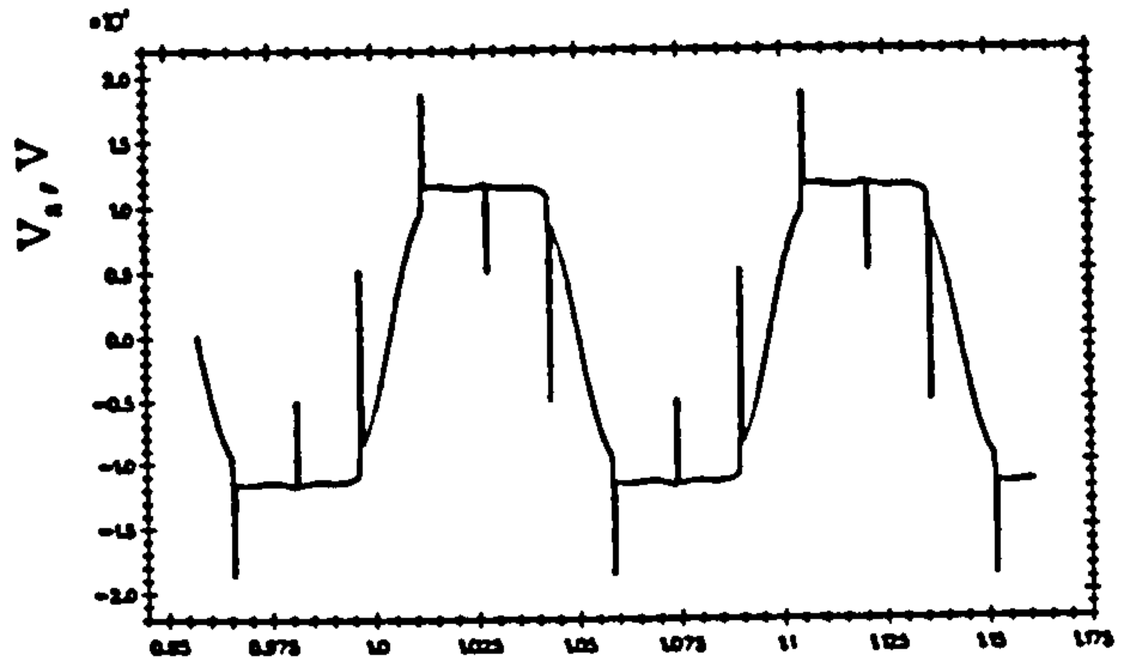

(b) Phase Voltage

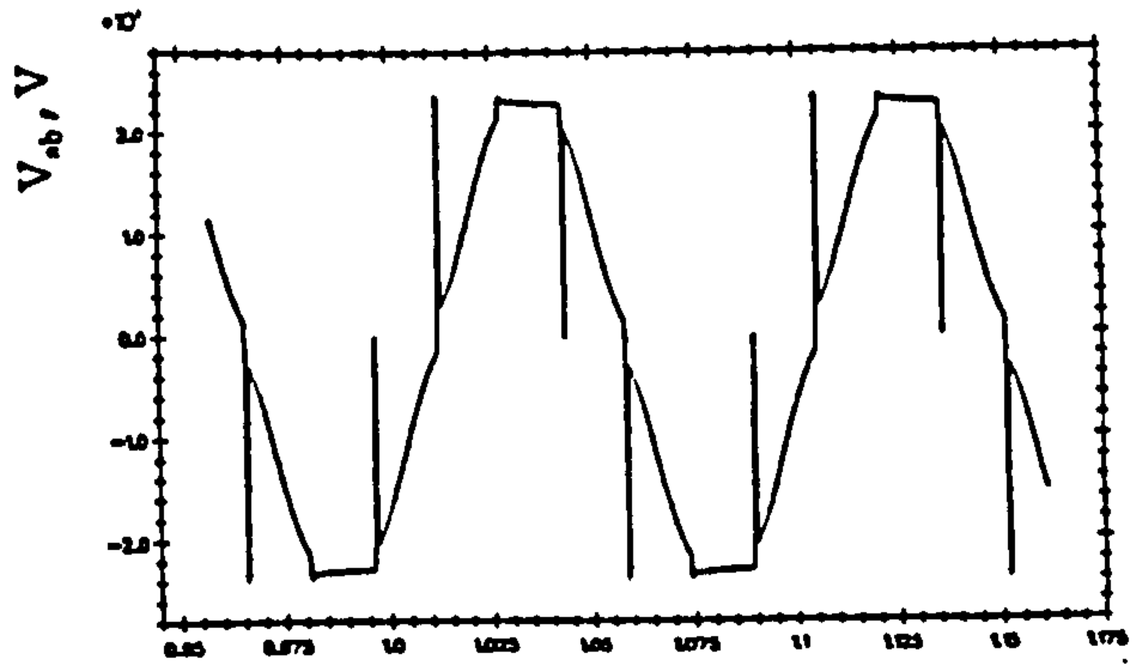

(c) Line Voltage

Figure 3 Predicted Steady-state Performance

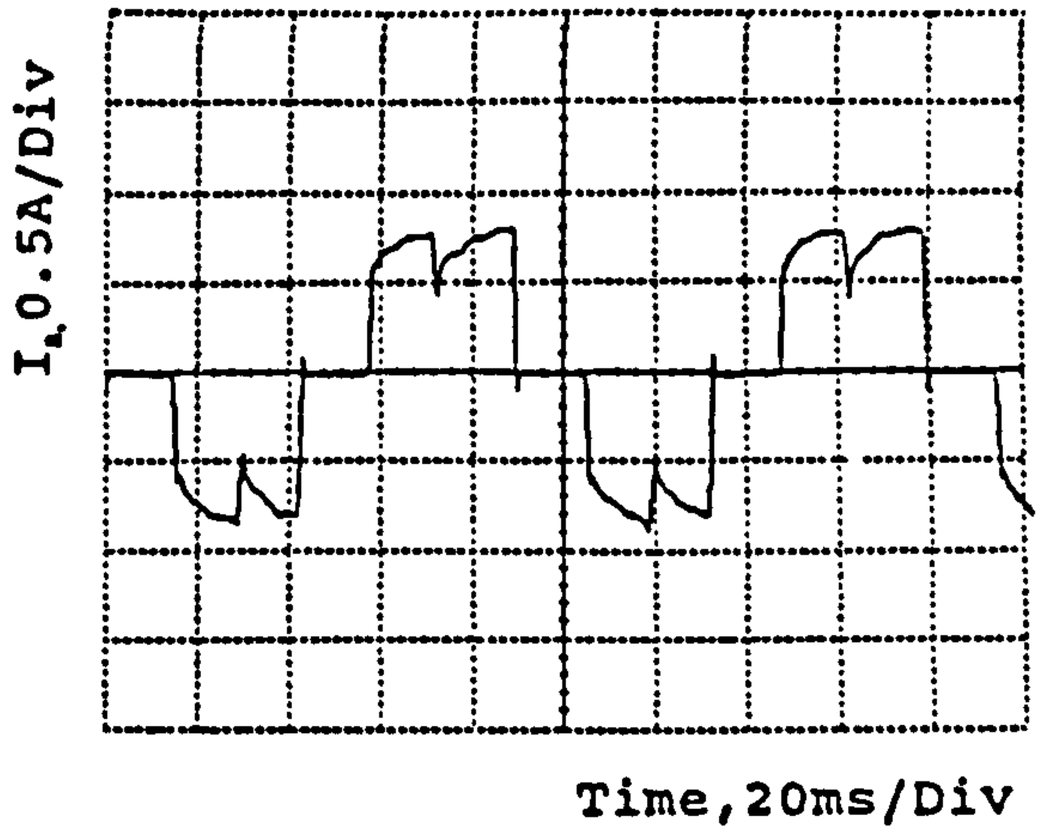

(a) Phase Current

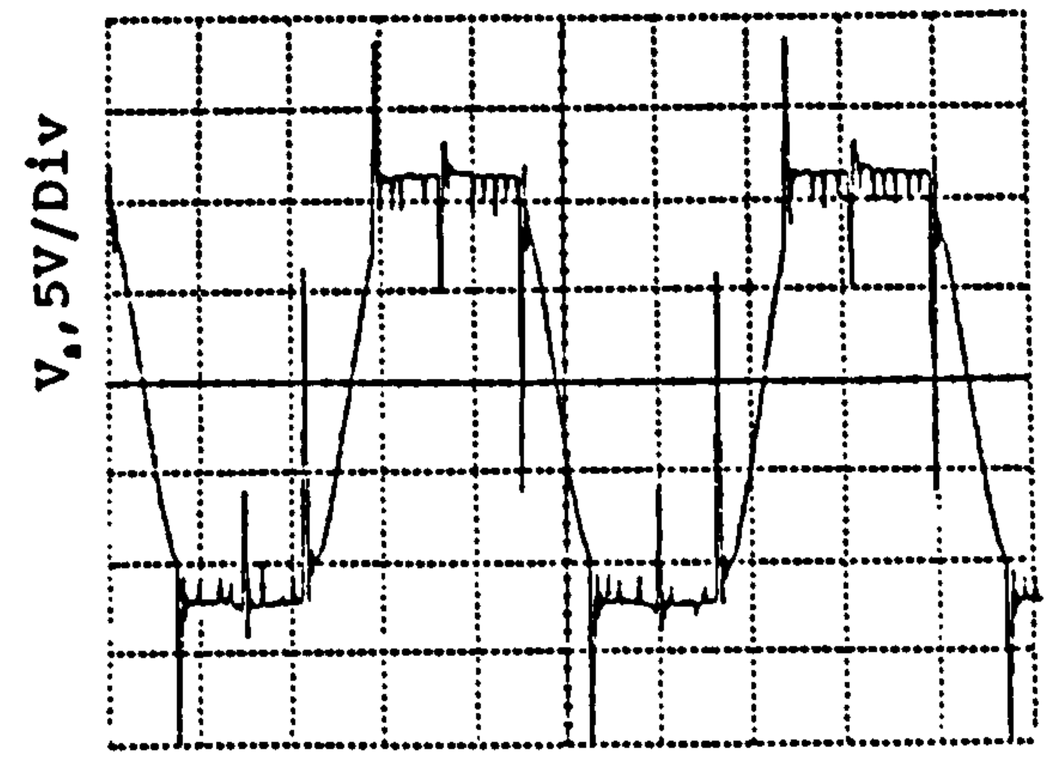

(b) Phase Voltage

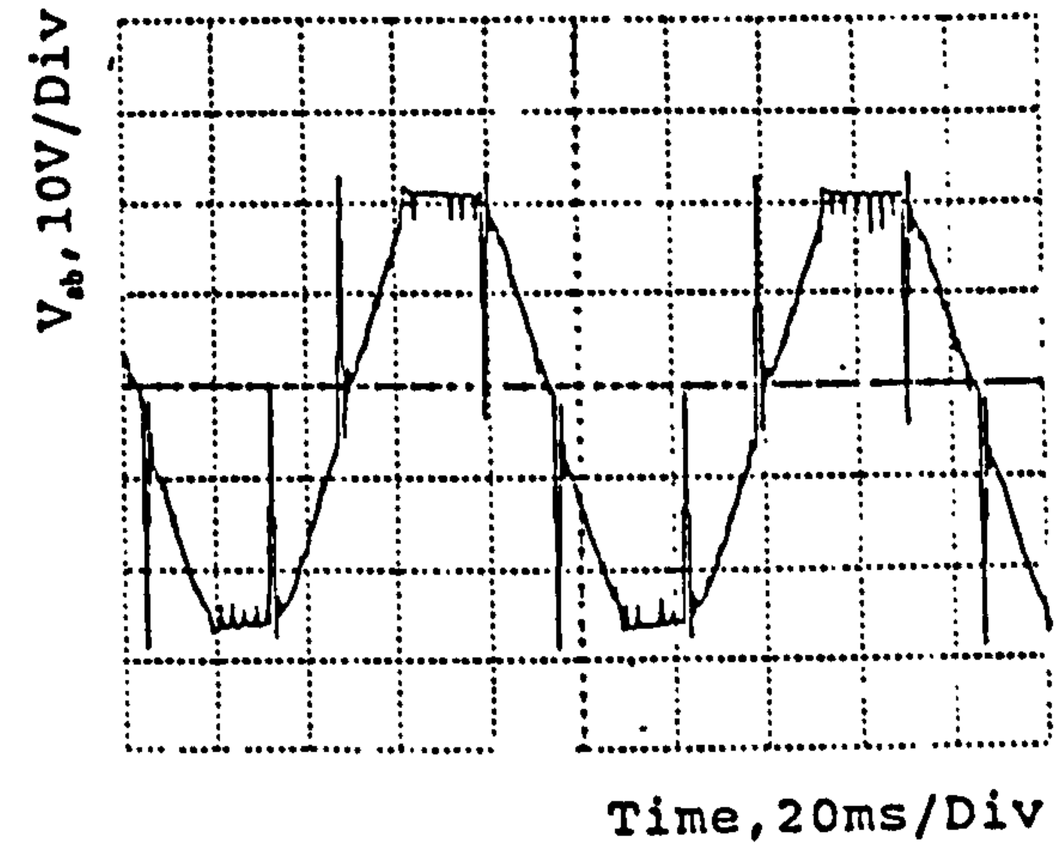

(c) Line Voltage

Figure 4 Experimental Steady-state Performance

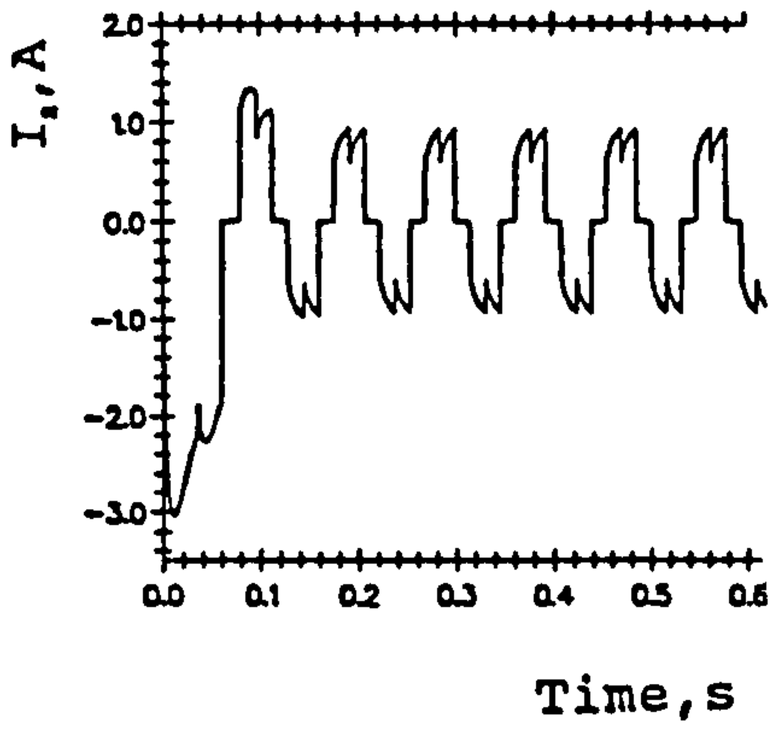

(a) Phase Current

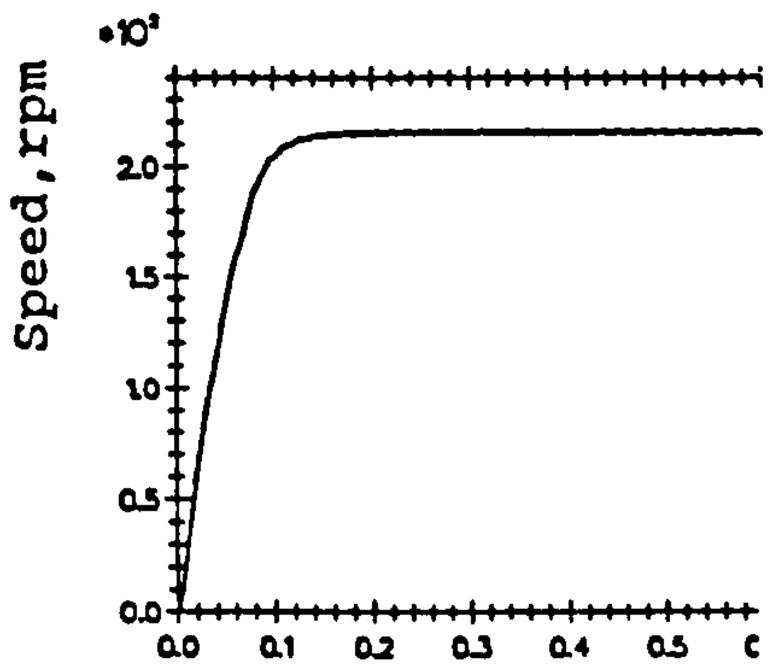

(b) Rotor Speed

Figure 5 Predicted Transient Performance

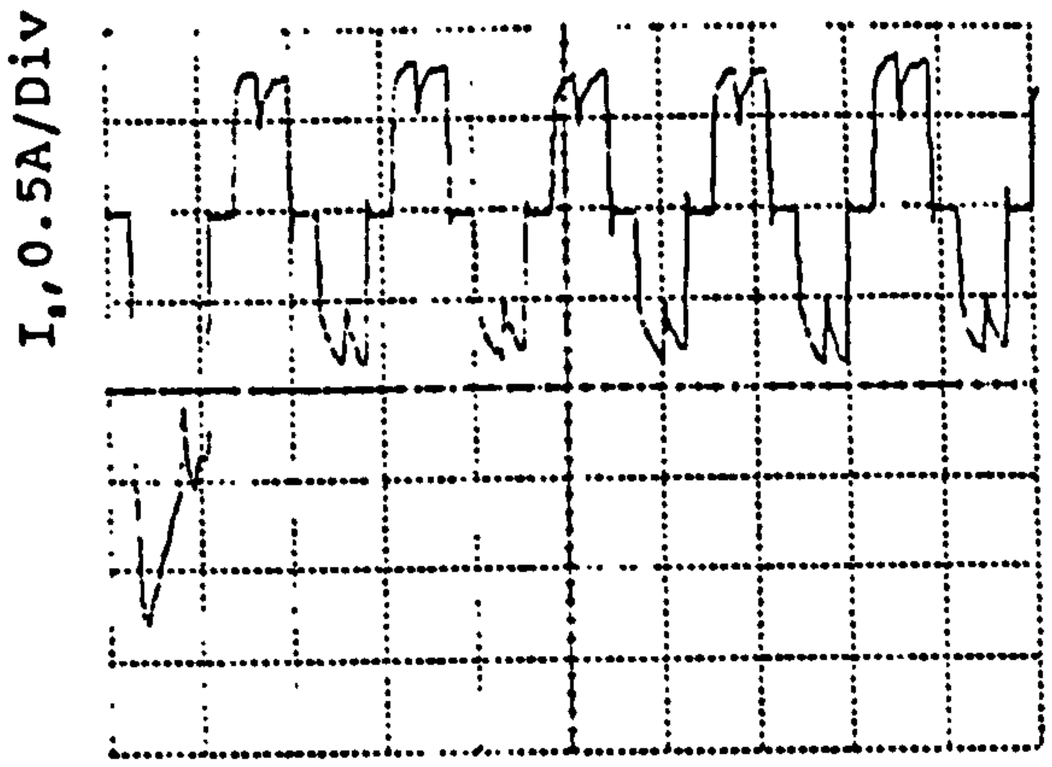

(a) Phase Current

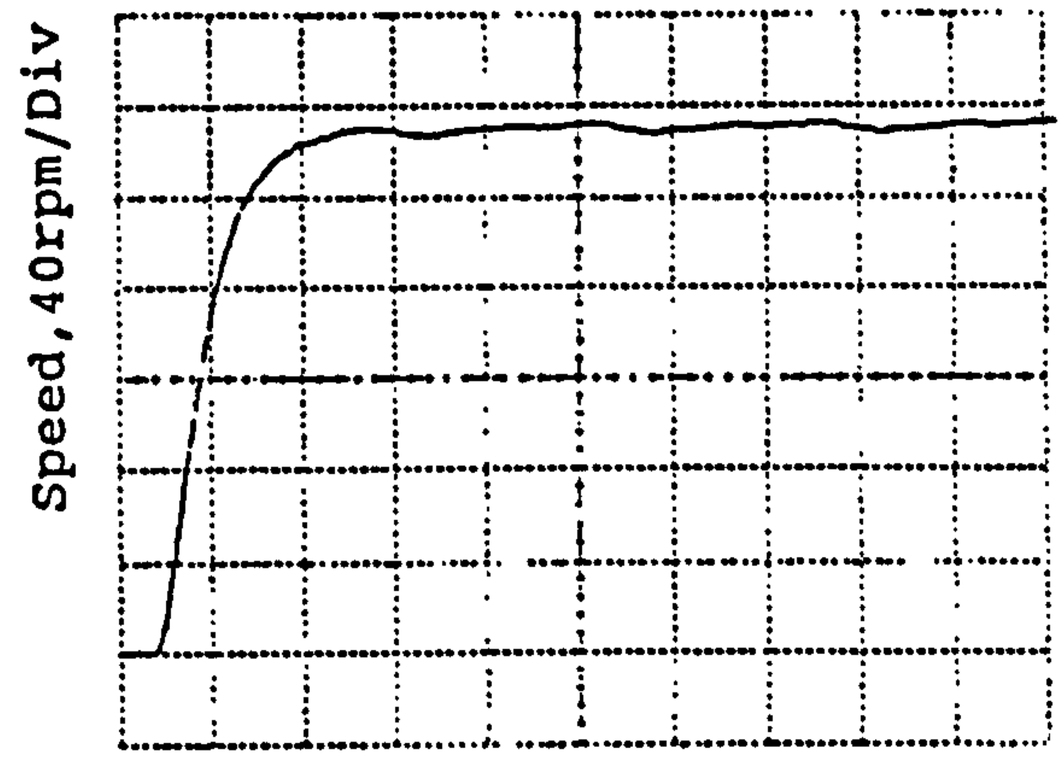

(b) Rotor Speed

Figure 6 Experimental Transient Performance

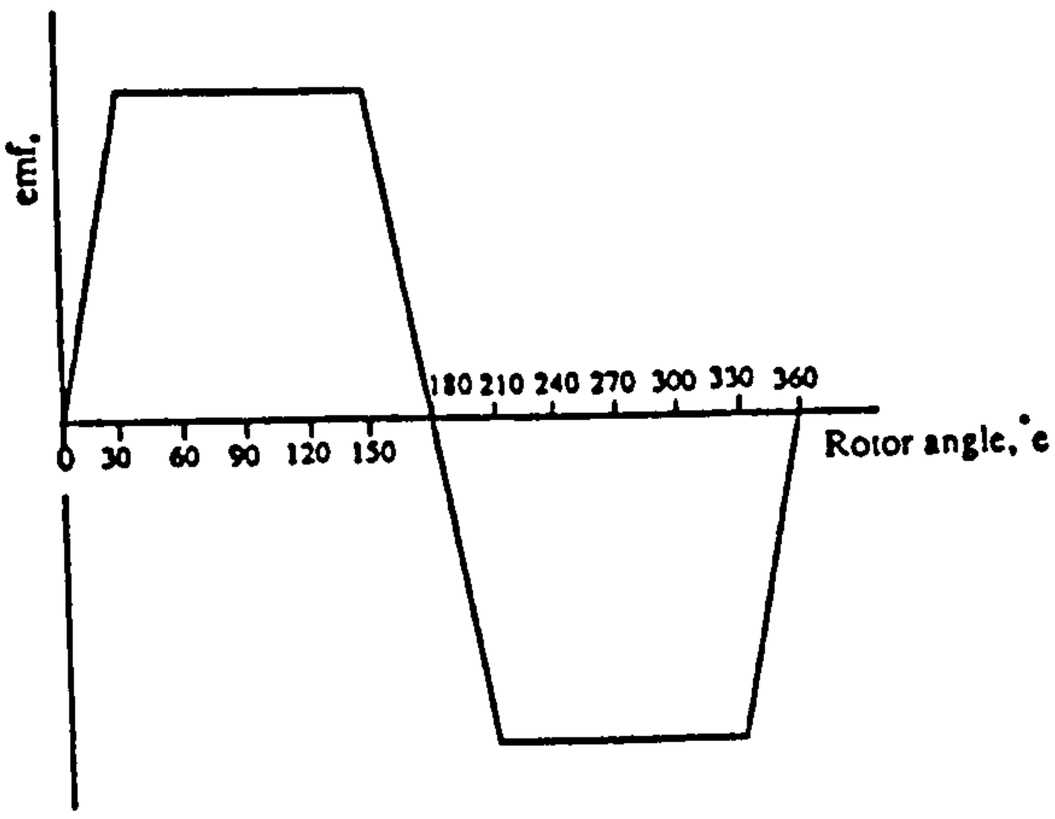

(a) Idealised

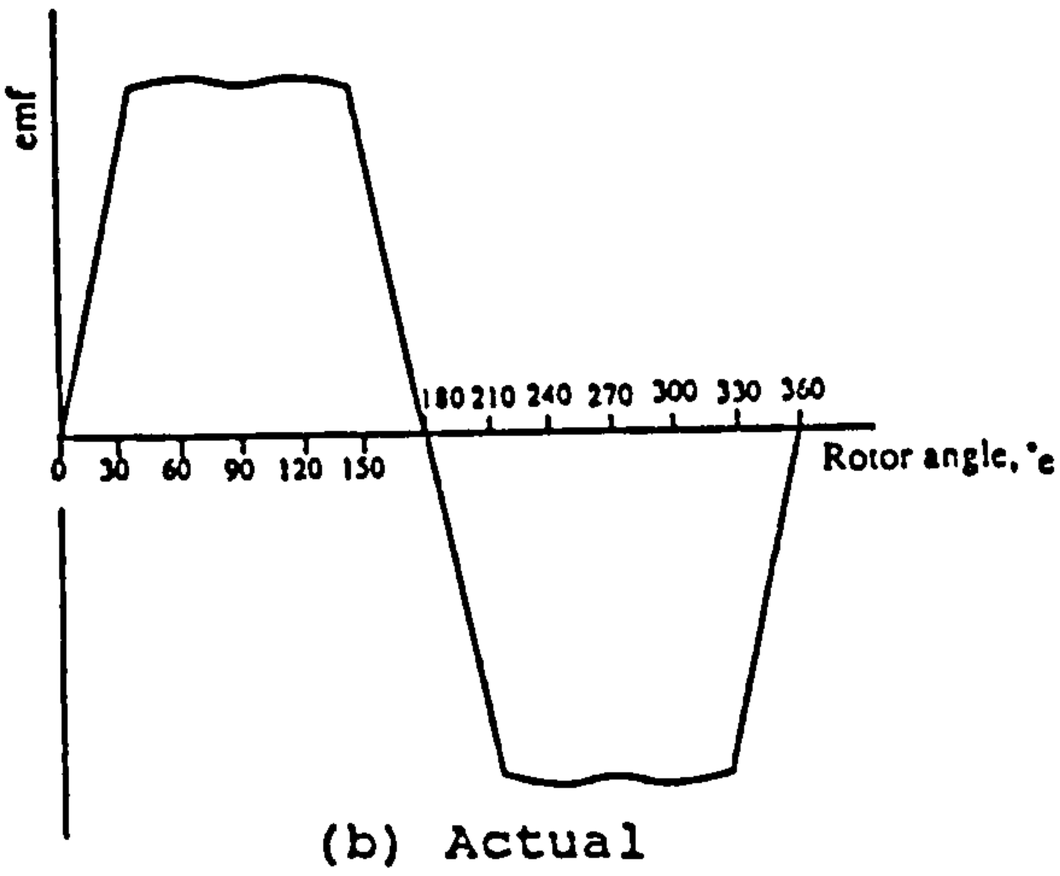

(b) Actual

Figure 7 Generated Phase Voltage

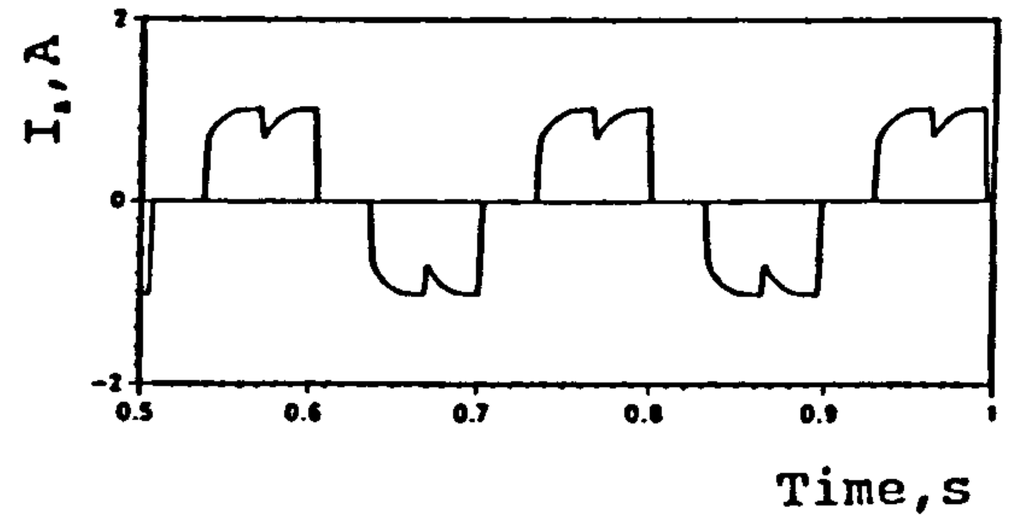

(a) Phase Current

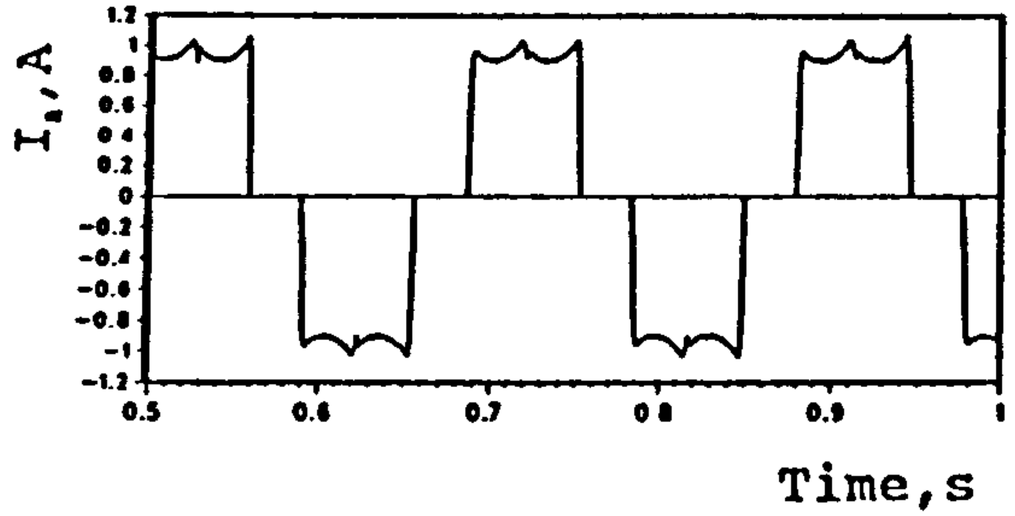

(a) Phase Current

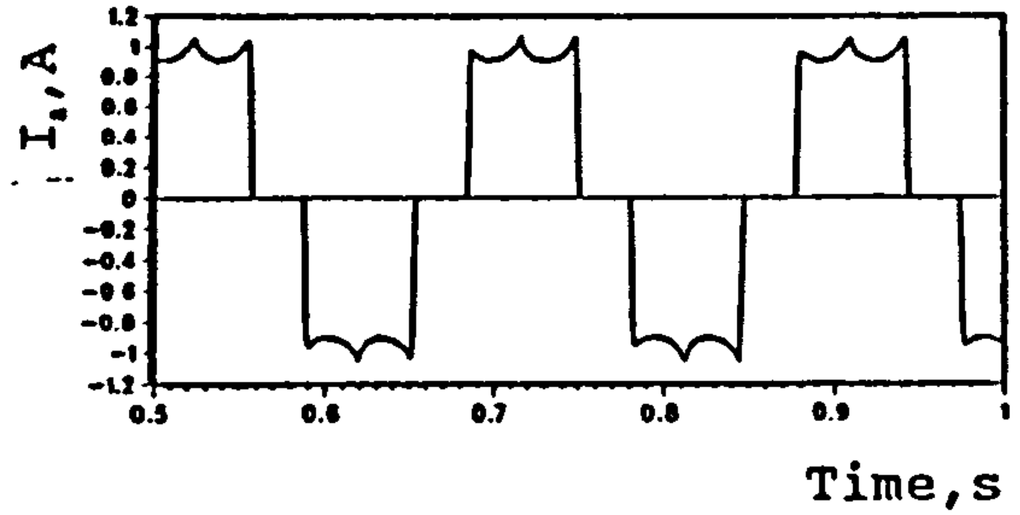

(a) Phase Current

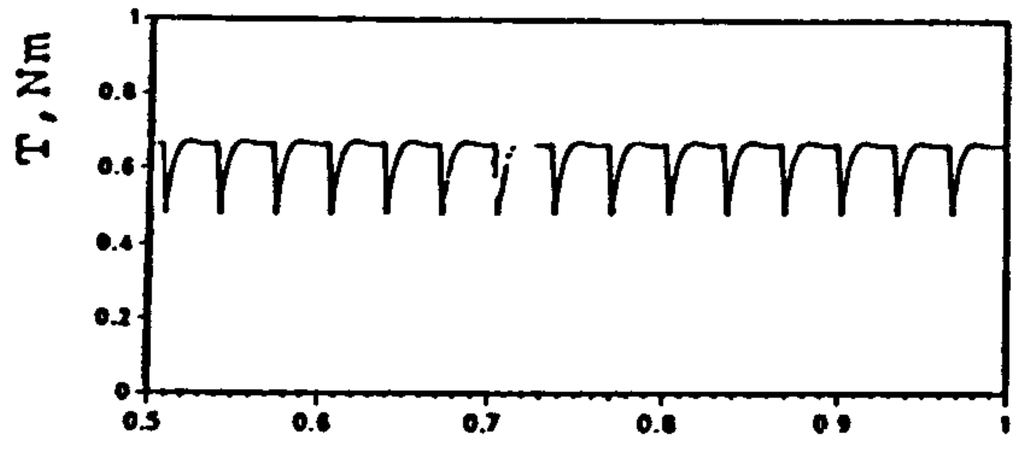

(b) Motor Torque

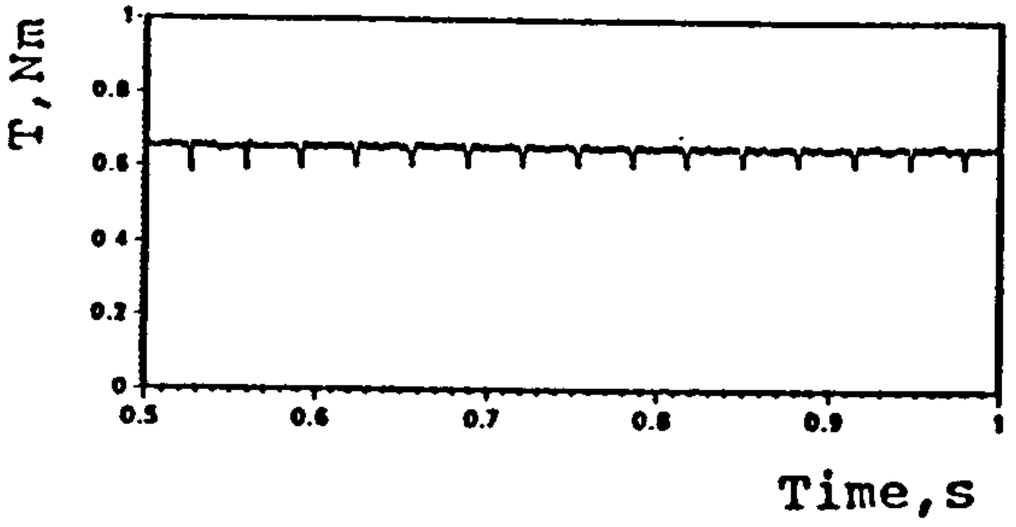

(b) Motor Torque

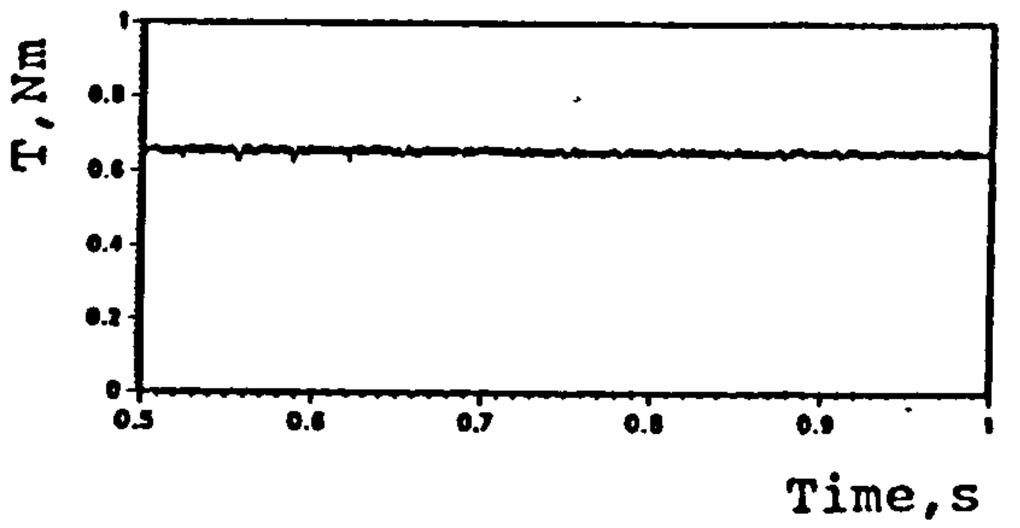

(b) Motor Torque

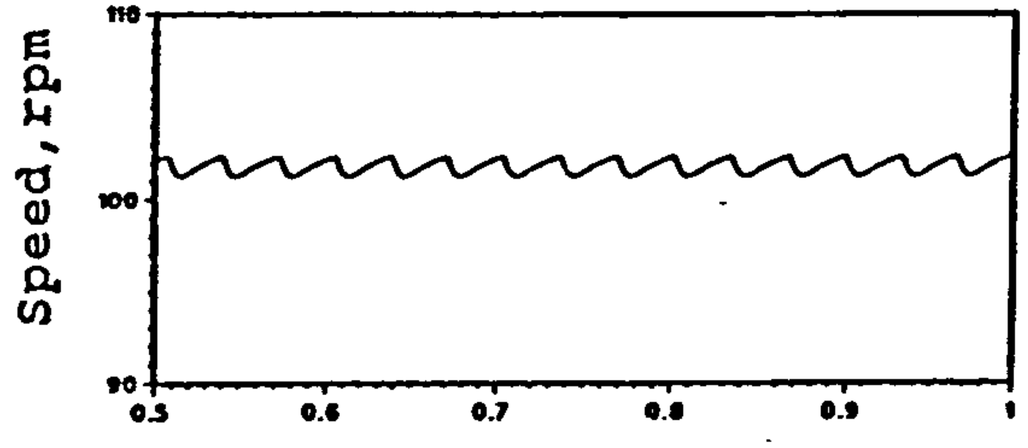

(c) Rotor Speed

Figure 8 Uncompensated Performance

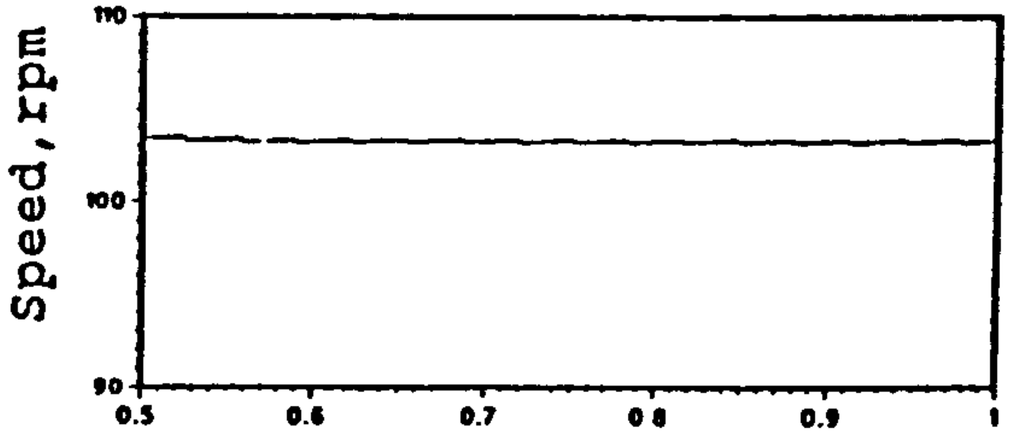

(c) Rotor Speed

Figure 9 With Current Profiling

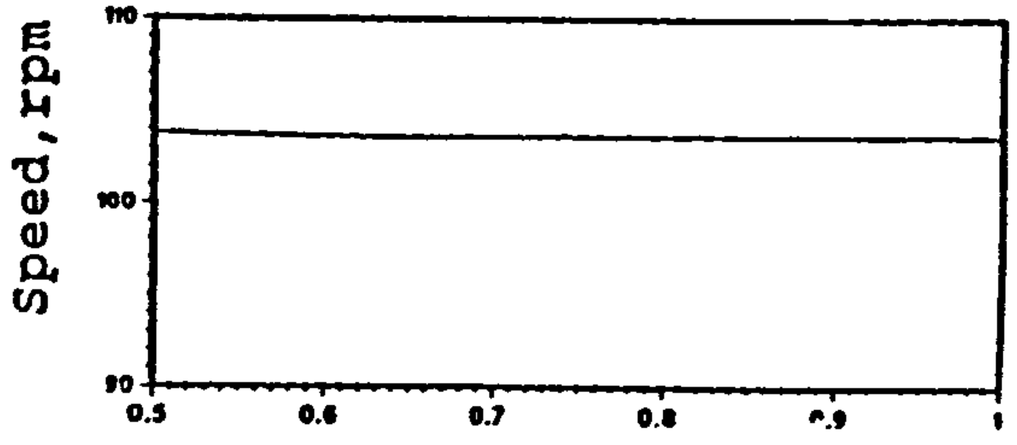

(c) Rotor Speed

Figure 10 Current Profiling and Current Boost